Table of Contents

ELECTRONIC STRUCTURE OF METALS AND SEMICONDUCTORS: BULK, SURFACE, AND INTERFACE PROPERTIES

Steven Gwon Sheng Louie

Materials and Molecular Research Division, Lawrence Berkeley Laboratory
and Department of Physics, University of California
Berkeley, California 94720

ABSTRACT

A theoretical study of the electronic structure of various metals and semiconductors is presented with the emphasis on understanding the properties of these materials when they are subjected to extreme conditions and in various different configurations.

Among the bulk systems studied, the properties of cesium under high pressure are discussed in terms of the electronic structure calculated at various cell volumes using the pseudopotential method. Local fields or umklapp processes in semiconductors are studied within the random phase approximation (RPA). Specifically the dielectric response matrix $\epsilon_{\underset{\sim}{G}\underset{\sim}{G}'}(\underset{\sim}{q}=0,\omega)$ is evaluated numerically to determine the effects of local-field corrections in the optical spectrum of Si. Also, some comments on the excitonic mechanism of superconductivity are presented and the role of local fields is discussed. The pseudopotential method is next extended to calculate the electronic structure of a transition metal Nb. The calculation is performed self-consistently with the use of a non-local ionic potential determined from atomic spectra. Finally the theory of the superconducting transition

temperature T_c is discussed in the strong-coupling formulation of the BCS theory. The Eliashberg equations in the Matsubara representation are solved analytically and a general T_c equation is obtained.

In addition to the above study of bulk properties, a new method is developed using pseudopotentials in a self-consistent manner to describe non-periodic systems. The method is applicable to localized configurations such as molecules, surfaces, impurities, vacancies, finite chains of atoms, adsorbates, and solid interfaces. Specific applications to surfaces, metal-semiconductor interfaces and vacancies are presented here.

For surfaces, the new scheme is employed to calculate the electronic structure of the Si(111) surface for three different structural models (ideal, relaxed and reconstructed). Surface states are identified and analyzed throughout the two-dimensional Brillouin zone. Charge densities and electronic density of states are presented and discussed. The effects of relaxation on the electronic structure of the GaAs (110) surface are also investigated. Similar studies are carried out for metal surfaces with the Al (111) surface and the Nb(001) surface considered as prototypes for the simple s-p metal and the transition metal surfaces.

For metal-semiconductor interfaces, the electronic structure of a series of four interfaces of increasing semiconductor ionicity is studied. The series consists of interfaces of Al (modeled by a jellium core potential) in contact with the (111) surface of Si and the (110) surfaces of GaAs, ZnSe and ZnS. The different types of

states existing near the interfaces are identified and analyzed in terms of a local density of states and their individual charge densities. The calculated Schottky barrier heights are in good agreement with experiments. In addition, a model involving metal-induced states in the semiconductor band gaps near the interface is presented for the ionicity-dependent behavior of the metal-semiconductor Schottky barrier heights.

Finally, as an example of vacancies in semiconductors, the electronic structure of a neutral vacancy in the Si crystal is calculated for the ideal and two model reconstructed geometries. Vacancy states are identified and their charge densities are presented.

I. INTRODUCTION

We present a theoretical study on the electronic structure of various metals and semiconductors. Particular emphasis is placed on understanding the changes in the properties of these systems when they are subjected to extreme conditions and in various different configurations. The pseudopotential method has been employed extensively to calculate the bulk, surface and interface electronic structure of the systems studied. Superconductivity is discussed both in the weak-coupling and the strong-coupling formulation of the BCS theory.

We begin in Section II with the discussion of the bulk properties of solids. The electronic structure of cesium under high pressure is examined in Sec. IIA. The calculated results indicate that many of the properties of Cs under pressure arise from the changes in the characteristics of the conduction electrons which become increasely d-like as the volume contracts. Local fields or umklapp processes in semiconductors are discussed next in Sec. IIB. An expression for the dielectric response matrix $\epsilon_{\underline{G}\underline{G}'}(\underline{q},\omega)$ in the random phase approximation (RPA) is derived via a diagrammatic approach. The matrix $\epsilon_{\underline{G}\underline{G}'}(\underline{q}=0,\omega)$ is then evaluated to study the effects of local-field corrections in the optical spectrum of Si. Some comments on the excitonic mechanism of superconductivity which involves a metal-semiconductor interface are presented and the role of local fields is discussed. Section IIC is on bulk Nb. We show that, with the inclusion of a non-local d-potential, the pseudopotential method can be extended to calculate the electronic

structure of transition metals. The calculations were performed self-consistently with the Nb^{+5} ionic core pseudopotential determined from atomic spectra. In Sec. IID we explore the theory of the superconducting transition temperature. The Eliashberg equations in the Matsubara representation are solved analytically using a self-consistent, variational procedure. An expression for the superconducting transition temperature T_c is derived. Unlike the McMillan equation, this T_c equation is shown to be a valid solution of the Eliashberg equations for all electron-phonon coupling strength and for different shapes of the electron-phonon interation spectrum, $\alpha^2F(\omega)$.

The remaining three sections are on non-periodic systems. In Sec. IIIA a new method which extends the pseudopotential scheme to localized configurations is presented. These calculations are done self-consistently and the approach is applicable to problems such as atomic and molecular states, solid surfaces, impurity and vacancy states, finite chains, adsorbates, and solid interfaces. Our results on the semiconductor surfaces are presented in Sec. IIIB. Specifically, we have studied the electronic structure of the Si(111) surface using three different structure models - the ideal structure, a relaxed structure and a (2×1) reconstructed structure. The effects of relaxation on the GaAs (110) surface are also studied. In Sec. IIIC we examine the metal surfaces with the Al(111) surface and the Nb(001) surface considered as prototypes for the simple s-p metal and the transition metal surfaces. In all of the cases studied, surface states with different characteristics are found to exist over a wide range of

energies; and our results are in general agreement with available experimental data when the appropriate restructuring of the surface is included.

In Section IV we apply our method to study the metal-semiconductor interfaces. The interfaces studied are interfaces of Al (modeled by a jellium core potential) in contact with the (111) surface of Si and the (110) surfaces of GaAs, ZnSe and ZnS. The electronic structure of the Al/Si interface is discussed in some detail in Sec. IVA and the results for the metal-zincblende semiconductor interfaces are presented in Sec. IVB. Metal-semiconductor Schottky barrier heights in very good agreement with experiments were obtained. Our results indicate that, within the jellium-semiconductor model, intrinsic semiconductor surface states do not play a dominant role in determining the Schottky barrier heights. In particular the intrinsic surface states which existed in the fundamental gaps of the semiconductors for the "free" surface case are found to be removed by the presence of the metal (r_s = 2.07) and new types of metal-induced gap states (MIGS) occur in this energy range. In Sec. IVC the role of ionicity in metal-semiconductor Schottky barriers is investigated. We show that the variations in the experimental barrier heights for different metals in contact with various semiconductors can be understood quantitatively in terms of a simple model involving the MIGS in the semiconductor band gap.

Finally, in Section V we study the electronic properties of vacancies in covalent semiconductors. Specifically we have calculated

the electronic structure of a neutral vacancy in the Si crystal using the method discussed in Sec. IIIA. The energies of the localized vacancy states and their corresponding charge density distributions were obtained. In addition to the ideal structure, the effects of structural reconstruction on the Si vacancy states were also investigated through the use of two model reconstructed structures.

II. BULK

A. Electronic Structure of Cesium under Pressure

In this section we present some calculations on the electronic properties of cesium under high pressure. The calculations are based on the pseudopotential method.[1] We have calculated the band structure, the density of states, and the charge density of the conduction electrons at cell volumes V equal to 0.5 V_o, 0.4 V_o and 0.3 V_o where V_o is the cell volume at normal pressure. The conduction electron density of states is further separated into contributions from s-, p- and d-like components. In addition, the topology of the Fermi surfaces at the above volumes was determined.

The present calculations were performed to try to gain some information about the many interesting properties of cesium under pressure. Experiments[2-5] show that cesium undergoes three phase transitions in the pressure range of one to fifty kilobars. At room temperature and under hydrostatic pressures, X-ray[3] and neutron diffraction[4] measurements show that there are three discontinuities in the volume versus pressure curve. The first discontinuity occurs at 23.7 kbar ($V/V_o = 0.63$). At this pressure cesium undergoes a transition from a bcc structure (CsI) to a fcc structure (CsII) with a small reduction in volume. The next discontinuity occurs at 42.2 kbar ($V/V_o = 0.45$). The latter transition is a first order isostructural transition. The structure of the new phase, CsIII, is fcc as in CsII but the volume drops by 9%. The third transition, CsIII to CsIV, occurs at 42.7 kbars

(V/V_o = 0.41) where the cell volume of cesium drops by 2.4%. The structure of CsIV has not been determined.

The above transitions are also evident in resistivity versus pressure measurements.[3,5,6] The resistivity as a function of pressure decreases initially, reaches a minimum at 8 kbar. It then increases with increasing pressure with a discontinuous rise at 23.7 kbar where bcc CsI transforms to fcc CsII; it becomes anomalously large near 42 kbar. Two spikes in the resistivity were observed at 42.2 kbar and 42.7 kbar; they correspond to the CsII-III and the CsIII-IV transitions respectively. The resistivity data are also interesting at higher pressures. The resistance of cesium drops steadily after the 42.7 kbar transition, and there is a second anomalous region near 120 kbar where the resistivity rises steeply to a maximum.[6]

The bulk modulus of cesium also behaves anomalously at the higher pressures.[7] Below the 42.7 kbar transition and above 120 kilobars, the bulk modulus is a linearly increasing function of pressure. In between, however, cesium becomes anomalously stiff; the bulk modulus increases abruptly and reaches a value at 120 kbar which is two orders of magnitude higher than its value at 43 kbar. Finally, cesium has the interesting property that it becomes superconducting at low temperature and high pressure.[8] The superconducting transition temperature is found to be 1.5°K at 120 kbar and the transition temperature is a decreasing function of pressure.

The CsI-II transition at 23.7 kbar was first explained by Bardeen[9] and later confirmed by experiment.[3] The isostructure

transition at 42.2 kbar ($V/V_o = 0.45$) is more complicated. Previous theoretical investigations[10-12] have attributed it to the change of the character of the conduction electrons from 6s to 5d, which occurs when the lattice is compressed to critical volume. This idea was first proposed by Sternheimer[10] in 1950. However his model gives the mixing of the s- and d-waves at lower pressure than the observed value.

Recent calculation by Yamashita and Asano[13] has shown that the cesium d-bands are broader than those obtained by Sternheimer. Using the APW method, Yamashita and Asano have calculated the band structure of cesium as a function of various cell volumes and they have examined the Fermi surfaces at those volumes. Calculations of total energy versus volume[14,15] have also been done which show a first order isostructural transition but at too low pressure.

As noted by McWhan,[4] recent experimental and theoretical evidence indicate a continuous s-d transition rather than an abrupt one as previously believed. The present calculation is the first attempt using the pseudopotential method to look at the isostructural transition of cesium. A band structure is calculated throughout the Brillouin zone which yields a detailed calculation of the density of states and of the electronic charge density. The calculation is described below in section 1, the results are given in section 2, and some discussion of the results is presented in section 3.

1. Methods of Calculation

a. Band structure. In applying the pseudopotential method to obtain the electronic band structures, we have used the pseudopotential

Hamiltonian[1]

$$H = \frac{p^2}{2m} + V_p \tag{1}$$

where V_p is a weak pseudopotential which is taken to be a superposition of atomic pseudopotentials. V_p which is energy dependent can be decomposed into a local and a non-local component

$$V_p = V_L(E) + V_{NL}(E) \ . \tag{2}$$

However, for a limited energy range, the energy dependence may be ignored.

In the case of cesium, for the local pseudopotential, we used Animalu's[16] screened model potential form factors. The form factors are defined as

$$V(\underset{\sim}{G}) = \frac{1}{\Omega} \int V_a(\underset{\sim}{r}) \ e^{-i\underset{\sim}{G}\cdot\underset{\sim}{r}} \ d^3\underset{\sim}{r} \tag{3}$$

where V_a is the local atomic pseudopotential, $\underset{\sim}{G}$ is a reciprocal lattice vector, and Ω is the primitive cell volume. To compute the energy bands at high pressure, i.e. different primitive cell volume and different $\underset{\sim}{G}$'s, the form factors must be appropriately scaled. We scaled the form factors in the following way. Let Ω' and $\underset{\sim}{G}'$ be the primitive cell volume and the reciprocal lattice vector at a new pressure, then the new form factors are given by

$$V'(\underset{\sim}{G}') = \frac{1}{\Omega'} \int V_a(\underset{\sim}{r}) \ e^{-i\underset{\sim}{G}'\cdot\underset{\sim}{r}} \ d^3\underset{\sim}{r}$$

$$= \frac{\Omega}{\Omega'} V(\underset{\sim}{G}') \ . \tag{4}$$

The atomic pseudopotential is weak because the repulsive potential from the orthogonalization terms cancels the strong atomic potential. However the cancellation is different for the different angular momentum components of the conduction electron wavefunction. In using a local pseudopotential one has assumed that the cancellation is the same for each angular momentum component.

In cesium the core has configuration

$$(1s)^2(2s)^2(2p)^6(3s)^2(3p)^6(3d)^{10}(4s)^2(4p)^6(5s)^2(4d)^{10}(5p)^6 \qquad (5)$$

The cancellation for $\ell=0$ and 1 is expected to be good over the whole core. For $\ell=2$ there is some cancellation arising from the 3d and 4d core states, but it can only cancel the atomic potential up to the n=4 shell. It leaves the potential in the n=5 shell uncancelled and the d-component of the conduction electrons will see a deeper attractive potential.

At normal pressure the conduction electron wavefunction is mostly s-like; the ℓ-dependent effect will not be important. However, at high pressures, there is a large s-d mixing. The ℓ-dependent part of the potential is then very important. To account for the incomplete cancellation, we have added a non-local correction to the local form factors of the form

$$V_a^{NL}(\underset{\sim}{r}) = A_2 \exp(-r^2/R^2)P_2 \quad .^{17} \qquad (6)$$

A_2 is the well depth, R is the well size, and P_2 is a projection operator acting on the d-component of the wavefunction.

Since there was no experimental information on the band structure of cesium at high pressure, A_2 and R were determined by adjusting them to fit our band structure at $V/V_o = 0.5$ to the band structure calculated by Yamashita and Asano[13] at the same volume. With some further adjustments of V_L, we obtained a good fit for the values $A_2 = -3.2$ rydbergs and R = 1.275 Å. The largest discrepancy is 0.5 eV at the point L in the Brillouin zone. The scaled local form factors and the d-potential for the various cell volumes are given in Table I. (ξ is in units of $2\pi/a$ where a is the lattice constant.) We have not scaled the size and the depth of the d-well since we assumed these are properties of the atomic core and the d-well is very localized. Even at $V/V_o = 0.15$, the radius of the inscribed sphere is larger than R. Thus the same d-well was used in the band structure calculation at $V/V_o = 0.5$, 0.4 and 0.3. The most important band structure effects for V/V_o's come from the d-potential and the scaling of V_L is not critical.

b. Density of states. Once the band structure has been obtained, the density of states N(E) may be calculated from

$$N(E) = \frac{2}{N} \sum_{\underset{\sim}{k}} \sum_{n} \delta(E-E_n(\underset{\sim}{k})) \qquad (7)$$

where N is the number of primitive cells and N(E) is normalized to the number of states per atom. To calculate the s, p and d contributions to the density of states, we define the ℓ-character of a wavefunction $\psi_{n\underset{\sim}{k}}(\underset{\sim}{r})$ in the following quantity

$$C_\ell(n,\underline{k}) = \frac{\int \psi^*_{n\underline{k}}(\underline{r}) P_\ell \psi_{n\underline{k}}(\underline{r}) d^3\underline{r}}{\sum_{\ell=0}^{2} \int \psi^*_{n\underline{k}}(\underline{r}) P_\ell \psi_{n\underline{k}}(\underline{r}) d^3\underline{r}} \tag{8}$$

where the integrals are to be taken over the inscribed sphere. By assuming that the fractional mixing of the various angular momentum components of the wavefunction outside of the inscribed sphere is the same as those in the inside, the partial density of states may be calculated and

$$N_\ell(E) = \frac{2}{N} \sum_{\underline{k}} \sum_{n} C_\ell(n,\underline{k}) \; \delta(E-E_n(\underline{k})) \tag{9}$$

with

$$N(E) = N_s(E) + N_p(E) + N_d(E) \; . \tag{10}$$

This is a reasonable definition for the partial density of states because the inscribed sphere contains 75% of the primitive cell volume.

Equations (7) and (9) were numerically evaluated using the Gilat-Raubenheimer technique.[18] At volume $V/V_o = 0.5$, a grid of 125 points in the fcc irreducible Brillouin zone was used in the calculation. At volumes $V/V_o = 0.4$ and $V/V_o = 0.3$, a grid of 308 points was used. The reason for the grid size variation is that 308 points were needed for the charge density calculation at volumes $V/V_o = 0.4$ and $V/V_o = 0.3$.

c. Electronic charge density. From the density of states we obtained the Fermi energy E_F by the following normalization

$$1 = \int^{E_F} N(E) \; dE \; . \tag{11}$$

The band charge density of the conduction electron in a given band, n, may then be calculated from

$$\rho_n(\underset{\sim}{r}) = 2e \sum_{\substack{\underset{\sim}{k}\in BZ \\ E_n(\underset{\sim}{k}) \leq E_F}} \psi^*_{n\underset{\sim}{k}}(\underset{\sim}{r})\, \psi_{n\underset{\sim}{k}}(\underset{\sim}{r}) \qquad (12)$$

and the total charge density is

$$\rho(\underset{\sim}{r}) = \sum_n \rho_n(\underset{\sim}{r}) \ . \qquad (13)$$

To obtain sufficient convergence for the charge density calculation, the wavefunctions $\psi_{n\underset{\sim}{k}}$ were expanded in a basis set of about 85 plane waves. And because the Fermi surfaces at $V/V_o = 0.4$ and $V/V_o = 0.3$ are more distorted than the Fermi surface at $V/V_o = 0.5$, to insure good convergence, a grid three times the size of the grid at $V/V_o = 0.5$ was used.

2. Results

The scaled form factors, d-well parameters, and lattice constants used in the calculations are listed in Table I. At all three volumes $V = 0.5\ V_o$, $0.4\ V_o$ and $0.3\ V_o$, the structure is assumed to be fcc.

a. Calculated band structures. The band structures of cesium at $V/V_o = 0.5$, 0.4 and 0.3 are shown in Fig. 1. They were calculated with a matrix size determined by the cutoff energies[19] $E_1 = 19.1$, $E_2 = 40.1$; the non-local d-well was not included in the Löwdin perturbation scheme.[19] The values for the d components of the wavefunctions are indicated along the symmetry directions. In all three cases the bottom band is mostly s-like near Γ and is mostly d-like near X and K in the

Brillouin zone. There is approximately equal mixing of s- and d-character near the point L. The second band is almost completely d-like; it has a small amount of p-mixing near L_2, which becomes completely p-like at the L point.

Our calculated band structures for contracted volumes are in qualitative agreement with those obtained by Yamashita and Asano.[13] The volume dependence of the band structure behaves in a reasonable way in both calculations; i.e., the energies in the region near X for the first two bands drop with decreasing volume with respect to Γ_1. The X_3 state drops below the Fermi level at $V/V_o \sim 0.45$. The L_2,-L_1 gap increases as the volume decreases. The second band doubled its width when the volume changes from 0.5 V_o to 0.3 V_o.

b. Calculated densities of states. The densities of states and the separate s, p and d components (as defined in section 1.b) are shown in Figs. 2-4. The origin of the energy scale is taken to be at $E(\Gamma_1) = 0$ for all three volumes $V/V_o = 0.5$, 0.4 and 0.3.

As seen from Fig. 2, even at $V/V_o = 0.5$, there is a large d component in the density of states below the Fermi level. The contribution of the d-waves to the density of states increases with decreasing volume for states below the Fermi level. This is consistent with the s-d transition arguments originally proposed by Sternheimer.[10] However, the transition appears to be continuous rather than abrupt. To make this quantitative, we have calculated the total number of states or the fractional amount of charge distributed among the s, p and d states in the inscribed sphere

by integrating the partial densities of states, i.e.

$$Q_{\ell} = \int^{E_F} N_{\ell}(E)dE \ . \qquad (14)$$

The results are presented in Table II. The d component of the total charge, Q_d, changes from 0.21 to 0.31 then to 0.54 as the volume changes from V/V_o = 0.5 to 0.4 to 0.3. Here our results differ quantitatively from those of Ref. 13 where a higher d-mixings was found at the above volumes. These authors find that the mixing ratio of the d-component changes from 0.47 to 0.70 as the volume decreases from V/V_o = 0.5 to 0.4. The differences may arise because of the different band structure methods involved.

At the Fermi energy, both the density of states and the contribution from the d-waves, $N(E_F)$ and $N_d(E_F)$, increase with decreasing volumes. $N(E_F)$ increases from 1.64 to 1.91 and $N_d(E_F)$ increases from 0.56 to 0.86 as the volume changes from V/V_o = 0.5 to 0.3. (The density of states is in units of states/eV-atom.) This increase in the density of states at the Fermi energy may be related to the fact that Cs becomes superconducting at high pressures (and low temperatures).

c. Electronic charge densities in the (100) plane. The charge densities of the conduction electrons in cesium are shown for the (100) plane in Figs. 5-7. The separate charge densities for the two lowest bands and the total charge density are given.

At volume V/V_o = 0.5, the Fermi level is below the second band. Hence the charge density of the bottom band is the total conduction electron charge density. The charge density is shown in a contour plot

in Fig. 5 in units of e/Ω where $\Omega = a^3/4$ is the volume of the primitive cell. Near the atomic site the charge density is spherically symmetric about the cesium atom. It has a maximum of 1.81 at the atomic site and decreases to a minimum of 0.65 half way along the lines connecting the atom to the second nearest neighbors. This arises from the fact that the occupied states are at the lower energies of band 1 and they are therefore mostly s-like.

At volume $V/V_o = 0.4$, a portion of the second band around X_3 is below the Fermi level. Therefore the total charge density has contributions from both band 1 and band 2. They are shown separately in Fig. 6. As seen from Fig. 6(a), the charge density of the first band is no longer spherically symmetric about the Cs atoms. The distortion arises from the increase in d-mixing in band 1 near X which comes from the lowering of band 2 in this region. The X_1 wavefunctions are mainly $d_{3z^2-r^2}$ and the charge density is moved out from the atomic sites consistent with the signature of the $d_{3z^2-r^2}$ symmetry which can be seen from the shapes of the contours. The charge density of the second band has the interesting feature that charges are concentrated along the nearest neighbor direction with local maxima occurring about halfway between the atoms. This is not too surprising since the charge density of band 2 arises from states in the region around X_3 where the wavefunctions are principally d_{xy}. At $V/V_o = 0.4$, the contribution of band 2 to the total charge is very small (~2%) and the total charge distribution is mainly that of the first band.

More charge is moved away from the atomic sites as the volume decreases. At $V/V_o = 0.3$, (see Fig. 7), the total charge density has a uniform background density of ~0.7 with local maxima along the lines connecting the nearest neighbor atoms. In the (100) plane the charge density of band 1 is uniform except for the four lobes from the $d_{3z^2-r^2}$ states. Because of the further lowering of X_3, the second band now contributes 15% to the total charge. As seen from Fig. 7(b), the charge density of band 2 is almost completely d_{xy}. This gives the total charge density of cesium at $V/V_o = 0.3$ a strikingly covalent-bonding-like character.

d. Fermi surfaces. We have examined the Fermi surface of cesium at $V/V_o = 0.5$, 0.4 and 0.3. The resulting Fermi surfaces are less distorted than those given in Ref. 13, but the qualitative behavior as a function of volume is approximately the same. They are shown in Figs. 8-10.

As seen from Fig. 8, the Fermi surface at $V/V_o = 0.5$ differs considerably from the characteristic spherical behavior usually seen in the alkali metals. Sizable necks have formed around the points L and X. Since a large portion of the UXW plane is below the Fermi level, this plane contains the region in the Brillouin zone where most of the occupied d-like states are concentrated. As the volume decreases to $V/V_o = 0.4$, the occupied conduction electron states shift towards the zone edge, i.e. towards states with larger k-values. Figure 9 shows that at $V/V_o = 0.4$ a larger portion of the UXW plane is below the Fermi level and contributions from the second band appears around X.

However, we do not find the contribution near W and K which is found in Ref. 13. A new sheet arises from the fact that X_3 drops below the Fermi level; it is almost completely d-like. As the volume decreases to 0.3 V_o (the Fermi surface is shown in Fig. 10), $E(X_1)$, $E(X_3)$ and $E(L_1)$ are all lower than $E(\Gamma_1)$; thus most of the occupied states are now concentrated around X and L instead of Γ. A small pocket is formed around K.

3. Discussion

In summary, our calculation is generally consistent with previous calculations. The conduction electrons become more d-like as the volume decreases (see Table II). From our band structure calculation, X_3 drops below the Fermi level at a volume $V \sim 0.45\ V_o$. This may be related to the first order isostructural transition of Cs at $V/V_o = 0.45$. According to Lifshitz,[20] as each band drops below E_F there is a discontinuity in the slope of the density of states as a function of volume. This could lead to a first order isostructural transition, but the quantitative aspects of this approach have not been determined.

At a volume $V = 0.5\ V_o$, we get a charge density resembling that expected of an alkali metal; i.e. the conduction electrons are s-like. However, at volumes smaller than 0.4 V_o the picture is quite different. Cesium becomes a transition metal. Covalent bonding charge begins to build up along the line joining the nearest neighbor atoms and we would expect a stiffening of the lattice. This change is consistent with the anomalous behavior in the bulk modulus. McWhan[7] noted that almost all of the pretransition elements and many of the d- and f-transition

elements near the beginning of each series have this type of abrupt increase in the bulk moduli. This behavior is associated with the transfer of electrons from bands of mainly s and p character to bands of mainly d character.

It is interesting to compare our charge density of cesium at $V/V_o = 0.3$ to those of NbC and NbN. The charge densities of band 5 in NbC and NbN[21] have the same type of covalent bonding character along the Nb-Nb direction as in the charge density of cesium at very high pressure. Both NbC and NbN have high superconduction transition temperatures, T_c, which are associated with the occurrence of anomalies in the phonon dispersion curves of these compounds.[22,23] These anomalies have been attributed to interactions involving charge density with d_{xy} symmetry.[24] Thus it is conceivable that the mechanism which caused high transition temperature in NbN and NbC is responsible for Cs becoming superconducting under high pressure. The covalent nature of the bonding appears to be intimately connected[25] with the occurrence of superconductivity.

We have also explored the pressure dependence of the Knight shift in cesium. McWhan and Gossard[26] have measured the Cs^{133} nuclear resonance frequency shifts $\Delta\nu/\nu$ at 4.2°K at pressures up to 50 kbar. They found that the increase in $\Delta\nu/\nu$ with pressure observed in previous experiments[27] extends to higher pressure, with $\Delta\nu/\nu$ (30 kbar) $\gtrsim 2\Delta\nu/\nu$ (1 kbar). At 50 kbar, however, $\Delta\nu/\nu$ drops by 25% relative to the 30 kbar value. The Hamiltonian[28] for the interaction of the jth nuclear spin in a solid with the conduction electrons is

$$H_{enj} = \gamma_e \gamma_n \hbar^2 \underset{\sim}{I} \cdot \sum_i \left(\frac{8\pi}{3} \underset{\sim}{s}_i \delta(\underset{\sim}{r}_{ij}) + \frac{3\underset{\sim}{r}_{ij}(\underset{\sim}{s}_i \cdot \underset{\sim}{r}_{ij}) - \underset{\sim}{s}_i r_{ij}^2}{r_{ij}^5} + \frac{\underset{\sim}{\ell}_i}{r_{ij}^3} \right) \qquad (15)$$

where $\underset{\sim}{r}_{ij} = \underset{\sim}{r}_i - \underset{\sim}{R}_j$ and $\underset{\sim}{r}_i$ is the position of the ith electron, $\underset{\sim}{R}_j$ is the position of the jth nucleus, and γ_e and γ_n are the gyromagnetic ratios of the electron and nucleus, respectively. One usually considers only the hyperfine contact interaction and neglects core-polarization effects, then the isotropic Knight shift is given by

$$K = \frac{\Delta H}{H} = A \sum_{\underset{\sim}{k}} |\psi_{\underset{\sim}{k}}(0)|^2 \delta(E_{\underset{\sim}{k}} - E_F) \qquad (16)$$

where A is a constant in which the many body effects have been absorbed.

To make a rough estimate of the Knight shift as a function of pressure in cesium, we calculated $\sum_{\underset{\sim}{k}} |\psi_{\underset{\sim}{k}}(0)|^2 \delta(E_{\underset{\sim}{k}} - E_F)$ at various cell volumes. Relative to its value at one bar, $\sum_{\underset{\sim}{k}} |\psi_{\underset{\sim}{k}}(0)|^2 \delta(E_{\underset{\sim}{k}} - E_F)$ increases to a maximum ≈ 2 at $V/V_o = 0.4$ (~40 kbar) and then decreases slowly as the volume contracts further. This result shows the same qualitative trend as observed in Ref. 26. The discrepancy in the rate which K drops at high pressures may result from the d core-polarization effect since the d-electron paramagnetism produces negative frequency shift terms through core polarization mechanism.

Further, following a suggestion by Heine,[29] we have explored the effects of screening on the crystal potential. As the volume decreases the screening by the s and p electrons becomes less efficient. And, as the potential gets stronger, the d-character of the conduction electrons becomes more dominant. In turn since the d-electrons are less

efficient in screening, the d-well deepens further. A "run-away" situation can then occur resulting in a phase transition. In order to examine this possibility we have calculated the electron-electron interaction in the Hartree-Fock-Slater sense using the pseudocharge density in the manner of Appelbaum and Hamann.[30] We find at each volume that the exchange term dominates. At high pressure, the Hartree-Fock potential is positive and a maximum at the atomic site; and is negative and a minimum at the "bonding" region. This lends support to Heine's speculation which may be a possible scheme for understanding the phase transition in the 42 kbar region.

B. Local Fields in Semiconductors

Recently much effort has been made to understand the role of microscopic electric fields on various physical properties of crystalline solids.[31-43] In this section we shall examine some of the effects of local-field corrections in semiconductors. In particular we will discuss the optical spectrum of Si and the role of umklapp processes in the proposed excitonic mechanism of superconductivity.

Within the linear response theory, a small perturbing electric field of frequency ω and wavevector $\underset{\sim}{q}+\underset{\sim}{G}$ in a crystal will establish responses with frequency ω and wavevectors $\underset{\sim}{q}+\underset{\sim}{G}'$, where $\underset{\sim}{G}$ and $\underset{\sim}{G}'$ are reciprocal lattice vectors. The microscopic fields of wavevectors $\underset{\sim}{q}+\underset{\sim}{G}'$ are generated from the applied perturbing field through umklapp processes. In the case of cubic crystals, the dielectric responses of the solid for longitudinal fields may be described by a matrix in $\underset{\sim}{G}$ and $\underset{\sim}{G}'$,[44]

$$\sum_{\underset{\sim}{G}'} \varepsilon_{\underset{\sim}{G},\underset{\sim}{G}'}(\underset{\sim}{q},\omega) E(\underset{\sim}{q}+\underset{\sim}{G}',\omega) = E_{pert}(\underset{\sim}{q}+\underset{\sim}{G},\omega) \ , \tag{17}$$

where E is the total field in the crystal and E_{pert} is the applied perturbing field. Microscopic-field effects (or local-field effects) are traditionally ignored by assuming the off-diagonal elements of the dielectric response matrix to be zero. However the off-diagonal elements can be important when considering local-field corrections to optical spectra,[31-33] plasmon dispersion in metals,[34,35] valence-electron density,[36] and lattice dynamics[37-41] in semiconductors and insulators.

An expression for the dielectric response matrix, $\varepsilon_{\underset{\sim}{G},\underset{\sim}{G}'}(\underset{\sim}{q},\omega)$, has been derived, within the RPA, by Adler and Wiser.[44] In section 1 below we present an alternate derivation of the dielectric matrix using the diagramatic approach. The optical properties of Si and the excitonic mechanism of superconductivity are discussed in sections 2 and 3 respectively.

1. The Dielectric Response Matrix

The unperturbed one-particle Green function for an electron in a crystal is defined by

$$G_o(1,2) = -i \langle 0|T\{\psi(1)\psi^+(2)\}|0\rangle \Omega \tag{18}$$

where T is the time order operator, Ω is the crystal volume and $\psi(i)$ the field operator at space-time $(\underset{\sim}{r}_i, t_i)$ is given by

$$\psi(i) = \sum_{n,\underset{\sim}{k}} \phi_{n,\underset{\sim}{k}}(r_i) C_{nk}(t_i) \Omega$$

with $\phi_{n,\underset{\sim}{k}}$ and $C_{n,k}$ are Bloch states and their corresponding destruction operators. Hence

$$G_o(1,2) = -i \sum_{\substack{n,\underset{\sim}{k} \\ n',\underset{\sim}{k}'}} \phi_{n,\underset{\sim}{k}}(\underset{\sim}{r}_1)\phi^*_{n',\underset{\sim}{k}'}(\underset{\sim}{r}_2)\langle 0|T\{C_{n,\underset{\sim}{k}}(t_1)C^+_{n,\underset{\sim}{k}}(t_2)|0\rangle \Omega .$$

And since for Fermions

$$-i\langle 0|T\{C_{n,\underset{\sim}{k}}(t_1)C^+_{n',\underset{\sim}{k}'}(t_2)\}|0\rangle =$$

$$\begin{cases} -i(1-f_{n\underset{\sim}{k}})e^{-i\varepsilon_{n\underset{\sim}{k}}(t_1-t_2)}\,\delta_{n\underset{\sim}{k},n'\underset{\sim}{k}'} & \text{for } t_1 > t_2 \\ if_{n\underset{\sim}{k}}\, e^{-i\varepsilon_{n\underset{\sim}{k}'}(t_1-t_2)}\,\delta_{n\underset{\sim}{k},n'\underset{\sim}{k}'} & \text{for } t_1 \leq t_2 \end{cases}$$

where $f_{n\underset{\sim}{k}}$ is the Fermi-Dirac distribution function, we have, in energy space,

$$G_o(\underset{\sim}{r}_1,\underset{\sim}{r}_2,\varepsilon) = \Omega \sum_{n\underset{\sim}{k}} \phi_{n\underset{\sim}{k}}(\underset{\sim}{r}_1)\phi^*_{n\underset{\sim}{k}}(\underset{\sim}{r}_2)\,\frac{e^{i\varepsilon\delta}}{\varepsilon - \varepsilon_{n\underset{\sim}{k}} + i\eta_{n\underset{\sim}{k}}}$$

where $\delta \to +0$ and $\eta_{n\underset{\sim}{k}} > 0$ (< 0) if $\varepsilon_{n\underset{\sim}{k}} > E_F$ $(< E_F)$. Also since $\phi_{n\underset{\sim}{k}}$ are Bloch states, periodic translation symmetry implies that G_o is a matrix $G^o_{\underset{\sim}{G},\underset{\sim}{G}'}(\underset{\sim}{q},\varepsilon)$ in momentum (Fourier) space with indexes $\underset{\sim}{G},\underset{\sim}{G}'$ being reciprocal lattice vectors and $\underset{\sim}{q}$ restricted in the first Brillouin zone, i.e.

$$G_o(\underset{\sim}{q}+\underset{\sim}{G},\ \underset{\sim}{q}+\underset{\sim}{G}',\ \varepsilon) = G^o_{\underset{\sim}{G},\underset{\sim}{G}'}(\underset{\sim}{q},\varepsilon)$$

$$= \sum_{n\underset{\sim}{k}} \frac{1}{\Omega}\int \phi_{n\underset{\sim}{k}}(\underset{\sim}{r}_1)\phi^*_{n\underset{\sim}{k}}(\underset{\sim}{r}_2)e^{i(\underset{\sim}{q}+\underset{\sim}{G})\cdot\underset{\sim}{r}_1}\, e^{-i(\underset{\sim}{q}+\underset{\sim}{G}')\cdot\underset{\sim}{r}_2}\, d\underset{\sim}{r}_1 d\underset{\sim}{r}_2 \times \frac{e^{i\varepsilon\delta}}{\varepsilon - \varepsilon_{n\underset{\sim}{k}} + i\eta_{n\underset{\sim}{k}}} \quad (19)$$

Similarly each interaction line in a periodic medium is a matrix in $\underset{\sim}{G}$ and $\underset{\sim}{G}'$. The Dyson equation for the interaction between two electrons now becomes

$$\bar{\bar{V}} = \bar{\bar{v}} + \bar{\bar{v}}\bar{\bar{P}}\bar{\bar{V}} \tag{20}$$

where $\bar{\bar{V}}$ is the screened interaction with $V_{\underset{\sim}{GG}'}(\underset{\sim}{q},\omega) = V(\underset{\sim}{q}+\underset{\sim}{G}, \underset{\sim}{q}+\underset{\sim}{G}', \omega)$, $\bar{\bar{v}}$ is the bare Coulomb interaction with $v_{\underset{\sim}{GG}'}(\underset{\sim}{q},\omega) = v(\underset{\sim}{q}+\underset{\sim}{G})\delta_{\underset{\sim}{GG}'}$ and $\bar{\bar{P}}$ is the irreducible polarizability.

From Eq. (20), the dielectric matrix is given by

$$\varepsilon_{\underset{\sim}{GG}'}(\underset{\sim}{q},\omega) = \delta_{\underset{\sim}{GG}'} - \sum_{\underset{\sim}{G}''} v_{\underset{\sim}{GG}''}P_{\underset{\sim}{G}''\underset{\sim}{G}'} = \delta_{\underset{\sim}{GG}'} - v(\underset{\sim}{q}+\underset{\sim}{G})\, P_{\underset{\sim}{GG}'}(\underset{\sim}{q},\omega) \ . \tag{21}$$

Hence we only need to evaluate $P_{\underset{\sim}{GG}'}$ to obtain the dielectric matrix. The diagram for the irreducible polarization in the RPA is given in Fig. 11. The physical interpretation of the diagram is the following: At space-time 1, the electron gains $\underset{\sim}{q}+\underset{\sim}{G}$ from the interaction. Between 1 and 2, the electron can loose or gain any $\underset{\sim}{G}$-vectors due to the lattice background. Finally, at 2, the electron looses $\underset{\sim}{q}+\underset{\sim}{G}'$ to the interaction.

We may now evaluate $P_{\underset{\sim}{GG}'}$ using the Feynman rules[45]

$$P_{\underset{\sim}{GG}'}(\underset{\sim}{q},\omega) = 2i \sum_{\underset{\sim}{pKL}} \int \frac{dp_o}{2\pi} G_o(\underset{\sim}{p}+\underset{\sim}{K},\underset{\sim}{p}+\underset{\sim}{L}+\underset{\sim}{G}',p_o)G_o(\underset{\sim}{p}-\underset{\sim}{q}+\underset{\sim}{L},\underset{\sim}{p}-\underset{\sim}{q}+\underset{\sim}{K}-\underset{\sim}{G},p_o-\omega) \tag{22}$$

where the factor of 2 is for the spin of the electron and $\underset{\sim}{K}$ and $\underset{\sim}{L}$ are reciprocal lattice vectors. Let us first consider the $\underset{\sim}{p}+\underset{\sim}{K}$, $\underset{\sim}{p}+\underset{\sim}{L}$ sum. Defining $\underset{\sim}{p}_1 = \underset{\sim}{p}+\underset{\sim}{K}$, $\underset{\sim}{p}_2 = \underset{\sim}{p}+\underset{\sim}{L}$ then

$$A = \sum_{p_1,p_2} G_o(p_1,p_2+G',p_o)G_o(p_2-q,\ p_1-q-G,\ p_o-\omega)$$

$$= \sum_{\substack{nk\\ n'k'}} \int \phi^*_{n'k'}(r_1)e^{i(q+G)\cdot r_1}\ \phi_{nk}(r_1)d^3r_1 \int \phi^*_{nk}(r_2)e^{-i(q+G')\cdot r_2}\ \phi_{n'k'}(r_2)d^3r_2$$

$$\times\ \frac{e^{ip_o\delta}\ e^{i(p_o-\omega)\delta}}{(p_o-\varepsilon_{nk}+i\eta_{nk})(p_o-\omega-\varepsilon_{n'k'}+i\eta_{n'k'})}$$

Again, using periodic translation symmetry, we have k' equal to $k+q+K$ where K is a reciprocal lattice vector which brings $k+q$ back to the first Brillouin zone. Hence we have

$$A = \sum_{\substack{nn'\\ k}} \langle n'k+q|e^{i(q+G)\cdot r}|nk\rangle\langle nk|e^{-i(q+G')\cdot r}|n'k+q\rangle$$

$$\times\ \frac{e^{ip_o\delta}\ e^{i(p_o-\omega)\delta}}{(p_o-\varepsilon_{nk}+i\eta_{nk})(p_o-\omega-\varepsilon_{n'k+q}+\eta_{n'k+q})}$$

Performing the integral over p_o, we have

$$i\int_{-\infty}^{\infty}\frac{dp_o}{2\pi}\ \frac{e^{ip_o\delta}\ e^{i(p_o-\omega)\delta}}{(p_o-\varepsilon_{nk}+i\eta_{nk})(p_o-\omega-\varepsilon_{n'k+q}+i\eta_{n'k+q})}$$

$$= \frac{f_{n'k+q}-f_{nk}}{\varepsilon_{n'k+q}-\varepsilon_{nk}-\omega+i\delta}$$

and therefore

$$P_{GG'}(q,\omega) = 2\sum_{\substack{k\\ nn'}} \frac{(f_{n'k+q}-f_{nk})\langle n'k+q|e^{i(q+G)\cdot r}|nk\rangle\langle nk|e^{-i(q+G')\cdot r}|n'k+q\rangle}{\varepsilon_{n'k+q}-\varepsilon_{nk}-\omega+i\delta}$$

Substituting $P_{GG'}$ into Eq. (31), we obtain the following expression[44] for the dielectric matrix

$$\epsilon_{GG'} = \delta_{GG'} - \frac{4\pi e^2}{\Omega|q+G|^2} \; 2 \sum_{k\,nn'} \frac{f_{n'k+q} - f_{nk}}{\epsilon_{n'k+q} - \epsilon_{nk} - \omega + i\delta}$$

$$\times \langle n'k+q|e^{i(q+G)\cdot r}|nk\rangle \langle nk|e^{-i(q+G)\cdot r}|n'k+q\rangle \; . \qquad (23)$$

(NOTE: we have set $\hbar=1$ in this section.)

2. Local-field Effects in the Optical Spectrum of Si

Two recent Physical Review Letters[31,32] have been published on local-field corrections to the optical spectrum of diamond; however, the two calculations give quite different results. By inverting the dielectric response matrix, Van Vechten and Martin,[31] using the pseudopotential method, and Hanke and Sham,[32] using a linear combination of atomic orbital (LCAO) method, have calculated the macroscopic dielectric function for diamond in the random phase approximation (RPA). Van Vechten and Martin find that local-field effects shift the strength of the imaginary part of the dielectric function, $\epsilon_2(\omega)$, to the energy region just above the main optical peak. This behavior increases the discrepancy between the calculated $\epsilon_2(\omega)$ and experiment. In an attempt to improve agreement with experiment, Van Vechten and Martin included the effects of dynamical correlation in their calculation of $\epsilon_2(\omega)$ via a one-parameter model. Hanke and Sham, on the other hand, find that local-field effects weaken the strength of $\epsilon_2(\omega)$ in the energy region from the main peak ($\sim$ 12 eV) to 20 eV and that the positions of the

prominent peaks in $\varepsilon_2(\omega)$ are shifted in the opposite direction needed to achieve good accord with experiment by approximately 0.5 eV. Hanke and Sham then include exchange effects (beyond the RPA) into their calculation of the macroscopic dielc tric function and are able to achieve better agreement with experiment.

To gain some new insights into the effect of local-field corrections to optical spectra of covalent solids, we present here a calculation of the dielectric function of silicon with local-field effects included. Using an extremely accurate band structure from the empirical pseudopotential method, we have calculated the RPA dielectric response matrix, $\varepsilon_{\underset{\sim}{G},\underset{\sim}{G}'}(\underset{\sim}{q}=0,\omega)$, for silicon and inverted it to obtain the macroscopic frequency dependent dielectric function. We find that (1) local-field corrections do not shift the prominent peak positions of $\varepsilon_2(\omega)$ and that (2) local-field corrections do improve the calculated dielectric function as compared to experiments at energies higher than the main optical peak. In particular, agreement with measured energy-loss spectra is significantly better when local-field effects are included.

In analyzing the optical spectrum, the incident light of frequency ω may be viewed as a perturbing field of vanishingly small wavevector. The macroscopic dielectric function is given by[44]

$$\varepsilon(\omega) = \lim_{\underset{\sim}{q}\to 0} \frac{1}{[\varepsilon^{-1}(\underset{\sim}{q},\omega)]_{\underset{\sim}{G},\underset{\sim}{G}}} \quad , \tag{24}$$

where ε^{-1} is the inverse of the matrix $\varepsilon_{\underset{\sim}{G},\underset{\sim}{G}'}$. We use here a symmetric form of the dielectric response matrix

$$\varepsilon_{\underset{\sim}{G},\underset{\sim}{G}'}(\underset{\sim}{q},\omega) = \delta_{\underset{\sim}{G},\underset{\sim}{G}'} - \frac{4\pi e^2}{\Omega|\underset{\sim}{q}+\underset{\sim}{G}||\underset{\sim}{q}+\underset{\sim}{G}'|} \sum_{\underset{\sim}{k}nn'} \frac{f_0[E_{n'}(\underset{\sim}{k}+\underset{\sim}{q})]-f_0[E_n(\underset{\sim}{k})]}{E_{n'}(\underset{\sim}{k}+\underset{\sim}{q})-E_n(\underset{\sim}{k})+\hbar\omega+i\hbar\alpha}$$

$$\times \langle \underset{\sim}{k}+\underset{\sim}{q},n'|e^{i(\underset{\sim}{q}+\underset{\sim}{G})\cdot\underset{\sim}{r}}|\underset{\sim}{k},n\rangle\langle \underset{\sim}{k},n|e^{-i(\underset{\sim}{q}+\underset{\sim}{G}')\cdot\underset{\sim}{r}}|\underset{\sim}{k}+\underset{\sim}{q},n'\rangle \ , \qquad (25)$$

where Ω is the crystal volume, f_0 is the Fermi-Dirac distribution function, and $|\underset{\sim}{k},n\rangle$ and $E_n(\underset{\sim}{k})$ are eigenstates and eigenvalues of the unperturbed Hamiltonian. $\varepsilon_{\underset{\sim}{0},\underset{\sim}{0}}(\underset{\sim}{q},\omega)$ is just the usual Cohen-Ehrenreich dielectric function (no local-field effects).[46] Equation (25) differs from Eq. (23) and from the definition of $\varepsilon_{\underset{\sim}{G}\underset{\sim}{G}'}$ in Refs. 43 and 44 by a factor of $|\underset{\sim}{q}+\underset{\sim}{G}|/|\underset{\sim}{q}+\underset{\sim}{G}'|$. The difference arises from whether the electric field or the potential is used in Eq. (17). Both approaches lead to the same macroscopic dielectric function.

To evaluate the required matrix elements and eigenvalues in Eq. (25), we have calculated a band structure for silicon using the empirical pseudopotential method.[1] The resulting band structure[47] is in excellent agreement with the optical gaps and photoemission experiments. Each $\varepsilon_{\underset{\sim}{G},\underset{\sim}{G}'}(q=0,\omega)$ was evaluated in energy intervals of 0.125 eV up to 100 eV. The summation over wavevector was performed by evaluating the wavefunctions and eigenvalues on a grid of 308 $\underset{\sim}{k}$-points in the irreducible zone. The matrix size of the dielectric response matrix involved in the inversion for Eq. (24) was chosen to be 59 × 59, containing $\underset{\sim}{G}$-vectors through the set (222). Symmetry can be invoked to reduce the number of $\varepsilon_{\underset{\sim}{G},\underset{\sim}{G}'}$ elements which need be calculated to 72. Convergence of the macroscopic dielectric function was confirmed by inversion of $\varepsilon_{\underset{\sim}{G},\underset{\sim}{G}'}$

including sets of $\underset{\sim}{G}$-vectors through (111), (200), (220), (311), and (222) respectively.

In order to establish the accuracy of the calculated $\varepsilon_{\underset{\sim}{G},\underset{\sim}{G}'}$, we have tested our results using the sum rules as derived by Johnson,[48]

$$\int_0^\infty \omega \, \mathrm{Im}\, \varepsilon_{\underset{\sim}{G},\underset{\sim}{G}'}(\underset{\sim}{q},\omega)\,d\omega = \frac{\pi}{2}\,\omega_p^{\,2}\left[\frac{\rho(\underset{\sim}{G}-\underset{\sim}{G}')}{\rho(\underset{\sim}{0})}\right]\,\hat{e}(\underset{\sim}{q}+\underset{\sim}{G})\cdot\hat{e}(\underset{\sim}{q}+\underset{\sim}{G}')\ , \qquad (26)$$

where $\omega_p^{\,2} = 4\pi ne^2/m$ is the plasma frequency, $\rho(\underset{\sim}{G})$ are the Fourier transforms of the valence-electron density, and $\hat{e}(\underset{\sim}{q}+\underset{\sim}{G})$ is a unit vector in the $\underset{\sim}{q}+\underset{\sim}{G}$ direction. In Table III we list our calculated results for the specific cases $\underset{\sim}{G} = \underset{\sim}{G}'$ and $\underset{\sim}{G} = 0$, $\underset{\sim}{G}' \neq 0$. The integral appearing in Eq. (26) was evaluated over a 100 eV range in intervals of 0.125 eV. Our results demonstrate good internal consistency except for the diagonal elements for the higher $\underset{\sim}{G}$-vectors. This arises from the fact that $\mathrm{Im}\, \varepsilon_{\underset{\sim}{G},\underset{\sim}{G}'}(q=0,\omega)$ becomes more extended in frequency as $|\underset{\sim}{G}|$ increases and that the integrand in Eq. (26) is linearly weighted with frequency. Better results can be obtained if we extend our integrations beyond the 100 eV range. As far as the optical properties are concerned, this high energy behavior is unimportant, and our values for $\varepsilon_{\underset{\sim}{G},\underset{\sim}{G}'}$ in the region considered should be very accurate.

The calculated imaginary part of the macroscopic dielectric function with (Adler-Wiser) and without local-field (Cohen-Ehrenreich) corrections, $\varepsilon_2(\omega)$ and $\mathrm{Im}\, \varepsilon_{\underset{\sim}{0},\underset{\sim}{0}}(\omega)$ respectively, is given in Fig. 12 together with the experimental measurement of Philipp and Ehrenreich.[49] From Fig. 12 we see that local-field corrections do not alter the

prominent peak positions, although they do alter the strength of the dielectric function. Compared with the usual Im $\varepsilon_{\underline{Q},\underline{Q}}(\omega)$, $\varepsilon_2(\omega)$ has less strength at energies below the main optical peak, thus increasing the discrepancy with experiment. At energies higher than the main optical peak, the strength of $\varepsilon_2(\omega)$ is reduced from that of Im $\varepsilon_{\underline{Q},\underline{Q}}(\omega)$ until approximately 7 eV. Beyond this point $\varepsilon_2(\omega)$ is larger than Im $\varepsilon_{\underline{Q},\underline{Q}}(\omega)$: an event which must transpire if the well known sum rules[44] are to be satisfied. This behavior results in an overall improvement in $\varepsilon_2(\omega)$ at higher energies as compared with experiment. Excitonic effects, particularly on the lower energy side of the main optical peak, which are not included in our calculation, should further improve the agreement between our $\varepsilon_2(\omega)$ result and experiment in the low energy region. The effect of these electron-hole interactions tends to increase the oscillator strength, hence the strength of $\varepsilon_2(\omega)$, at the lower energies.[32,50]

Another improvement of $\varepsilon(\omega)$ arising from local-field effects at higher energies is reflected in the calculated energy-loss spectrum of silicon as indicated in Fig. 13. We note a drastic decrease in the magnitude of the peak of Im $(\frac{1}{\varepsilon(\omega)})$ through the inclusion of local-field effects, and a shifting of the peak by approximately 1.2 eV to lower energies.[51] Both these effects result in significantly better agreement with experiments.[49,52] However, effects other than local-field corrections,[53] might also be responsible for at least some of the discrepancy between experiment and the calculated Im$(1/\varepsilon_{\underline{Q},\underline{Q}}(\omega))$.

In conclusion we remark that there are now three calculations on the effect of local-field corrections to the optical spectra of covalent solids using the RPA formalism. All three calculations give different results indicating that work remains to be done to establish firmly the influences of local-field effects.

3. Some Comments on the Excitonic Mechanism of Superconductivity

Allender, Bray and Bardeen[54] (ABB) have explored the possibility of using electronic polarizability to induce Cooper pair formation and superconductivity in a system consisting of a thin metal layer on a semiconductor surface, i.e. a Schottky barrier. The process considered involves the tunneling of metal electrons at the Fermi surface into the semiconductor gap where they interact by exchanging "virtual excitons".[55]

Shortly after ABB introduced their model, Inkson and Anderson[56] (IA) used a dielectric function approach to estimate the pairing interaction, and reported that the attractive interaction between electron pairs was stronger in the metal side of the Schottky barrier than in the semiconductor side. In reply ABB[57] questioned the detailed structure of the IA semiconductor dielectric function and its appropriateness with respect to the ABB model.

In this section we deal mainly with the IA objection to ABB and discusses the pairing interaction in general. It is shown that the IA model for the metallic dielectric function does yield a more attractive pairing interaction than their model semiconductor dielectric function; however, the pairing interactions differ from those calculated here. It is also demonstrated that a

semiconductor dielectric function based on a pseudopotential band calculation does not yield an attractive interaction. It is proposed that if an attractive interaction is possible via the exchange of excitons, umklapp processes or local fields are necessary.

a. Calculation. Following ABB, the N(0)V parameter of BCS can be written as

$$N(0)\ V = \lambda_{ex} - \mu \tag{27}$$

where λ_{ex} is the attractive electron-electron coupling constant arising from exciton exchange and μ is the repulsive Coulomb-parameter.

In analogy with the phonon induced[25] effective interaction ABB arrive at the following expression

$$-N(0)V = \mu\left[1 - \frac{\beta\omega_p^2}{\epsilon(\vec{q})\omega_g^2}\right] = \mu - \lambda_{ex}\ , \tag{28}$$

where ω_p is the electron plasma frequency in the semiconductor, ω_g is the average semiconductor gap, $\epsilon(\vec{q})$ is a wavevector dependent dielectric constant for a metal of equal electron density and β is a numerical factor which accounts for the decay of the metallic electron wave functions into the semiconductor and the fraction of time the metal electrons spend in the semiconductor. ABB introduce a screening factor, a, and the exciton coupling constant becomes

$$\lambda_{ex} = ab\xi\ \omega_p^2/\omega_g^2 \tag{29}$$

In favorable cases, ABB estimate $\lambda_{ex} \sim 0.2$-0.5. These values would give substantial increases in the superconducting transition temperatures

of metal films.

IA approach the pairing interaction from a different point of view. They argue that the total interaction, attractive exciton and repulsive coulomb, can be treated using the wavevector and frequency dependent dielectric function, $\varepsilon_s(\vec{q},\omega)$, appropriate to the semiconductor. They express the <u>total</u> interaction as

$$V_t(\vec{q},\omega) = \frac{4\pi e^2}{\vec{q}^2 \varepsilon_s(\vec{q},\omega)} \quad . \tag{30}$$

The IA form for ε_s is

$$\varepsilon^{IA}_s = 1 + \frac{A}{1 + AB} \tag{31}$$

where $A = \varepsilon_o - 1$, $B = \frac{q^2}{k^2} - \frac{\omega^2}{\omega_p^2}$, ε_o is the static electronic dielectric constant, and k^{-1} and ω_p are the screening length and plasmon energy of an equivalent electron density metal.

If $\varepsilon_o \to \infty$, then it is expected that $\varepsilon^{IA}_s \to \varepsilon^{IA}_m = 1 + B^{-1}$, a dielectric function appropriate for a metallic system. Therefore using the above expressions,

$$\frac{1}{\varepsilon^{IA}_s} \approx \frac{1}{\varepsilon^{IA}_m} + \frac{1}{\varepsilon_o} \tag{32}$$

for $\varepsilon_o \gg 1$. Equations (30) and (32) show that the total interaction in the semiconductor is equal to the total interaction in a metal plus an added <u>repulsive</u> term. IA therefore conclude that the semiconductor is less favorable than the metal for superconductivity.

To obtain the N(0)V parameter or the frequency-dependent kernel of the BCS equation, $K(\delta)$,[58] it is necessary to do a Fermi surface average of the wavevector dependent interaction, V_t,

$$K(\delta) \sim \int_{|\vec{k}-\vec{k}'|}^{|\vec{k}+\vec{k}'|} q\, V_t\,(q,\delta)\, dq \qquad (33)$$

where $\delta = \hbar\omega/E_F$, and $\vec{k}$ and $\vec{k}'$ are the initial and scattered electron wavevector, i.e., $\vec{k}' = \vec{k} + \vec{q}$. It is $K(\delta)$ which must have attractive regions for the pairing interaction to be positive. It is not sufficient to have negative regions of the wavevector dependent interactions, V_t.

To calculate $K(\delta)$,[59] we assume a metal-semiconductor interface with electron densities appropriate to Al and Si, i.e. $r_s \sim 2$ and $\varepsilon_o \sim 10$. We first evaluate $K(\delta)$ for the IA model dielectric function. ε^{IA}_s and ε^{IA}_m. In Fig. 14(a) the kernels appropriate to ε_s and ε_m are displayed. The IA metal kernal is more favorable for superconductivity since it is less repulsive at low frequencies and the attractive region is larger than the attractive region obtained using the IA semiconductor dielectric function. This is in accord with the IA calculations.

However, a more relevent question is how good are the IA approximations to begin with. The ε^{IA}_m is constructed to approximate the frequency and wavevector dependent dielectric function for a metal. ε^{IA}_m coincides with the RPA or Lindhard[60] dielectric function for $\vec{q} = 0$ and for $\omega = 0$, $\vec{q} \ll k_F$. A better approximation for the metal kernel would be to use the Lindhard dielectric function in V_t. The results (Fig. 14(b)) show that $K(\delta)$ is <u>repulsive</u> for all δ. Thus the

attractive region found using ϵ^{IA}_{m} is a result of their model and is not found in the more realistic Lindhard model.

It is also possible to do a more realistic calculation of $K(\delta)$ using the numerical values for the $\epsilon(\vec{q},\omega)$ of Ge. The calculation[61] for the Ge $\epsilon(\vec{q},\omega)$ was based on a pseudopotential calculation of the energy band structure and wavefunctions, and is therefore expected to be more realistic than ϵ^{IA}_{s}. The results which appear in Fig. 14(c) indicate that $K(\delta)$ is repulsive for all frequencies.

b. Discussion and Conclusions

So we have explored the IA objection to the ABB model based on ϵ^{IA}_{s} and ϵ^{IA}_{m} and we have shown that the kernel of the BCS equation, $K(\delta)$, (and therefore the BCS parameter $N(0)V$), is repulsive for all frequencies if the total interaction used is based on a realistic semiconductor dielectric function. What does this imply about ABB?

In their reply to IA, ABB emphasized that the reason that IA did not obtain a favorable result was that the pole of ϵ^{IA}_{s} did not have the proper $\vec{q}$ dependence. However, as we have shown, the problems are more serious than this and in fact ϵ^{IA}_{s} is more favorable for superconductivity than the more realistic Ge calculation.

The essential point is that the peak in the dielectric function will give a zero in $K(\delta)$. A qualitative reason for this is that the peak in the dielectric function signals a transverse excitation (electron-hole or excitonic resonance) and in this approximation the electrons are not coupling to this mode. The strongest coupling comes near the zero of the dielectric function i.e. plasmon exchange. A similar effect

occurs in the electron-phonon interaction. Electrons interact only with longitudinal modes unless umklapp processes are invoked. In the exciton case the coupling could arise via local-field effects.

One method of including local-field effects in the dielectric function is through the use of a dielectric tensor $[\frac{1}{\epsilon}]_{\vec{G}\vec{G}'}$. IA addressed themselves to this problem and calculate the frequency dependence of some off-diagonal terms in the dielectric tensor. They conclude that the dielectric tensor still has a pole at ω_g and that the coupling to the excitons is still zero, i.e. the kernel will be zero at ω_g. Two problems arise: (1) The formalism for using the dielectric tensor to evaluate the kernel and pairing interaction is not adequately discussed. For the phonon case, a generalized susceptibility will have a pole at the transverse phonon frequencies, yet it is known that electrons couple to transverse phonon modes (via umklapps). (2) It is not clear that the approximate calculations for the IA dielectric tensor are sufficiently accurate to rule out attractive pairing interactions.

The ABB approach circumvents (1) by computing λ_{ex} using Eq. (28). We presume that ABB have assumed that local fields are included in this expression. This coupling constant is large for small ω_g, but small ω_g usually implies small local fields in covalent systems. ABB suggest PbTe which is partially ionic to overcome this problem.

It would be useful in estimating the coupling to use a local-field semiconductor dielectric function which was computed for a realistic semiconductor for ω and q. To our knowledge the only semiconductor local field dielectric function[62] in the literature is given as a

function of ω, but for $\vec{q} = 0$. To show why this approach or some other is desireable to obtain reliable values for λ_{ex} we can make estimates assuming the ABB form to be correct for the interaction including local fields.

If we take the Phillips - Van Vechten[63] model for the dielectric function and identify ω_g with the Phillips average gap, then

$$\varepsilon_o = 1 + \frac{\omega_p^2}{\omega_g^2} \tag{34}$$

and assuming Eq. (29) to be valid, we obtain

$$\lambda_{ex} = ab\mu(\varepsilon_o - 1) \ . \tag{35}$$

ABB estimate $a \sim \frac{1}{5}$ to $\frac{1}{3}$, $b \sim 0.2$, $\mu \sim \frac{1}{3}$ to $\frac{1}{2}$ and using $\varepsilon_o \sim 5$ to 30, then $\lambda_{ex} \sim .05$ to 1.0. Leaving out phonons this would give estimates of the transition temperature from zero (repulsive total N(0)V) to extraordinarily large values. Estimates for b by ABB are consistent with recent self-consistent Schottky barrier calculations[64] for the penetration of metallic electrons. The parameters a and μ can be evaluated more carefully, but it would still be more reassuring to use a total local-field dielectric function and/or some other method to estimate N(0)V for the exciton interaction.

In conclusion, our calculation of the total semiconductor kernel yields a repulsive interaction. This together with the IA arguments would suggest that the ABB results should be reconsidered; however, we feel that the umklapp contribution should be included explicitly before a firm conclusion is reached.

C. Electronic Structure of Bulk Nb

We present in this section a self-consistent calculation of the electronic structure of bulk niobium using the pseudopotential method. Early non-self-consistent band structure calculations have been done for Nb using the modified orthogonalized plane wave method (MOPW),[65] the augmented plane wave method (APW),[66] and the empirical pseudopotential method.[67] All these calculations are in good agreement with each other and with Fermi surface experiments.[68] Using a Slater-Koster parametrization of the APW band structure,[66] Pickett and Allen[69] have recently calculated a joint density of states for Nb which agrees reasonably well with the imaginary part of the dielectric function $\varepsilon_2(\omega)$ obtained from experimental reflectivity data.[70] A self-consistent APW calculation done by Anderson et al.,[71] however, gives results differing significantly from the other calculation particularly at the point H.

In the following we will first discuss our method of calculation and then present our results on the band structure and density of states of bulk Nb. The obtained results are consistent with experiments[68,70,72] and with previous non-self-consistent calculations. In addition, we will present charge distributions for the total valence electrons and also for states in particular energy ranges.

1. Methods of Calculation

The electronic structure of Nb was calculated from a pseudopotential Hamiltonian

$$H = \frac{p^2}{2m} + V_{ps} + V_H + V_x \qquad (36)$$

where V_{ps} is a weak pseudopotential taken to be a superposition of Nb^{+5} ionic pseudopotentials

$$V_{ps}(\underset{\sim}{r}) = \sum_{\underset{\sim}{R}_n} V_{ps}^{ion}(\underset{\sim}{r} - \underset{\sim}{R}_n) \ . \tag{37}$$

And for the ionic potentials we have used a ℓ-dependent non-local pseudopotential of the form

$$V_{ps}^{ion} = \sum_{\ell=0}^{2} V_\ell(r) P_\ell \tag{38}$$

where P_ℓ are projection operators for the various angular momentum components. The non-local nature of the Nb^{+5} pseudopotential accounts for the differences in the repulsive potentials that each angular momentum component of the electron wavefunction sees as a result of core orthogonalization.

The potentials V_s, V_p and V_d were obtained by fitting the experimental spectroscopic term values of the Nb^{+4} ion (i.e. the Nb^{+5} plus one electron system).[73] In addition, we demanded that when V_{ps}^{ion} was used to calculate the Nb neutral atom self-consistently, it would reproduce the eigenvalues and the positions of the wavefunction maxima calculated by Herman and Skillman.[74] A comparison of our results with those from experiment and Herman and Skillman is given in Table IV. Figure 15 is a plot of our V_s, V_p and V_d ionic pseudopotentials. It can be seen that the d-electrons feel a much weaker core orthogonalization repulsion than the s and p electrons.

In our self-consistent scheme, the ionic pseudopotential is screened with a Hartree-like screening potential V_H and a local exchange potential of the Slater type V_x obtained from the pseudocharge density $\rho(\underline{r})$ by

$$\nabla^2 V_H(\underline{r}) = -4\pi e^2 \rho(\underline{r}) \tag{39}$$

and

$$V_x(r) = -3\alpha e^2 \left(\frac{3}{8\pi}\right)^{1/3} \rho^{1/3}(\underline{r}) \tag{40}$$

where α, the exchange parameter, is chosen to be 0.79. The iteration process is started with approximating the $V_{ps} + V_H + V_x$ term in the Hamiltonian (Eq. 36) by a potential constructed from a superposition of the self-consistently screened atomic pseudopotentials. With this starting Hamiltonian, the valence charge density is calculated and the screening potentials V_H and V_x are derived. The new V_H and V_x are then put back into the Hamiltonian. The process is repeated until self-consistency in the screening potentials is reached.

In the present calculation, plane waves with a maximum reciprocal-lattice vector corresponding to an energy of 10.2 Ry were used in the basis set. This corresponds to about 80 plane waves in the expansion of the eigenfunctions; another 60-80 plane waves were included by second-order perturbation theory. In the iteration towards self-consistency, eigenvalues and eigenvectors were calculated for a grid of 8 special points in the irreducible part (1/48) of the bcc Brillouin zone.[132] The Fermi level E_F was then determined by

$$2 \sum_{k_i} \sum_{n} \omega_{k_i} \theta(E_F - E_n(k_i)) = z \qquad (41)$$

where z is the number of electrons per primitive cell, ω_{k_i} is the appropriate weight for each special point and θ is the Heaviside step function. Finally the valence charge density was determined from the wavefunctions of the occupied states.

After self-consistency has been obtained, we further calculated the energies and wavefunctions of 285 k-points in the irriducible zone. With these results, we obtained the detailed band structure, density of states, and valence charge density for bulk Nb. The charge distributions for states under the various peaks in the density of states curve were also examined.

2. Results

The calculated band structure $E_n(k)$ for Nb plotted along the symmetry directions of the bcc Brillouin zone is shown in Fig. 16. This result is in good agreement with previous band calculations.[65-67] Table V compares some of the principal energy levels of the present band structure with those of previous calculations. The main differences are: the lowest Γ_1 level for the present calculation is ~0.8 eV lower than the previous results and the $\Gamma_{12} - \Gamma_{25'}$ gap is ~0.8 eV wider.

Figure 17 shows the calculated density of states (DOS) together with the DOS from Matheiss' APW calculation.[66] The two curves are in quite good agreement and are consistent with the photoemission data of Eastman.[72] Table VI gives the positions of the peaks in the DOS of the present calculation in comparison with previous results and

experiment. Also our calculated value for $N(E_F)$ is 1.1 states/eV-atom which is a very good agreement with the empirical value of 0.91 states/eV-atom obtained by McMillan.[75]

The valence charge density in the (110) and (100) planes are shown in Fig. 18. The positions of the Nb atoms are indicated by the dots. The charge density is zero at the atomic nuclei because of the highly repulsive core. It then rises up sharply to form lobes around the atoms showing a distinct d-like character. The distance of the peaks of the charge density from the atoms in the crystal agrees well with the position of the peaks of the d-electrons in the isolated Nb atom. In addition to the lobes, there is a uniform charge background distributed in the space between the atoms.

Plotting the charge distributions for states under the various peaks in the DOS reveal that they have quite different characters. The charge distribution for states under the lowest peak A with energies from -6.5 to -2.0 eV is shown in Fig. 19(a). The charge distribution is mainly s-like with a small admixture of $d_{3z^2-r^2}$ character. The charge distributions for peak B (-2.0 to -0.75 eV) and peak C (-0.75 to 0.60 eV), shown in Fig. 19(b) and 19(c) respectively, are very similar with the charge concentrated mainly in the bonding d-like lobes along the line joining two neighboring atoms. The charge for the highest and unoccupied peak D (0.6 to 5.85 eV) has a distinct $d_{3z^2-r^2}$ and $d_{x^2-y^2}$ character around the atomic sites.

We have also determined the Fermi surface of Nb from the calculated band structure. The calculated Fermi surface is in satisfactory

agreement with previous calculations and with experiment except for one point. The Fermi surface in the present calculation does not cut across the Σ symmetry line (Γ - N) in contrast to Mattheiss' result[66] and to de Haas van Alphen experiments.[68] It can be seen from our band structure in Fig. 16 that, along the Σ direction, the third band just miss cutting the Fermi level by ~0.1 eV. This discrepancy can be easily resolved by a very slight change in the potential.

3. Conclusions

In conclusion we have present a calculation of the band structure of Nb using a self-consistent pseudopotential method and obtain results which are in good agreement with Matheiss' APW calculation and are consistent with experimental results.[68,70,72] This demonstrates the applicability of the self-consistent pseudopotential method in calculating the electronic structure of transition metals. We shall use this same Nb^{+5} ionic pseudopotential later to study the surface properties of Nb.

D. Theory of the Superconducting Transition Temperature

There has been recent interest and controversy concerning the theoretical formulation[75-79] for calculating the superconducting transition temperature, T_c, especially for strong electron-phonon coupling. The most widely used approach was developed by McMillan[75] who, using the interaction spectrum $\alpha^2F(\omega)$ for Nb as a model, numerically solved the linearized gap equation in the strong-coupling formulation[80,81] of the BCS theory[82] and obtained an interpolation formula for T_c. However, Allen and Dynes[79] have shown recently from their detailed

numerical studies of the Eliashberg equations that the McMillan T_c equation is not valid for large electron-phonon interaction parameter, i.e. $\lambda > 2$. More recently Leavens[83] has questioned the large λ asymptotic form of the Allen-Dynes result and has stated that these results are incorrect.

In this section the Eliashberg equations[80] expressed in the Matsubara representation are solved analytically using a self-consistent, variational procedure. An expression for T_c is thus derived from these equations and the results are compared with exact numerical solutions. It is shown that our T_c equation is valid for all ranges of electron-phonon coupling strength and for different shapes of $\alpha^2F(\omega)$. Both our analytical and numerical results concur with the observation made by Allen and Dynes[79] on the asymptotic limit of T_c for very strong coupling i.e. $T_c \sim \sqrt{\lambda \langle \omega^2 \rangle}$, where λ and $\langle \omega^n \rangle$ are defined by

$$\lambda = 2\int \frac{\alpha^2F(\omega)}{\omega}\, d\omega \tag{42}$$

and

$$\langle \omega^n \rangle = \frac{2}{\lambda} \int \alpha^2F(\omega)\omega^{n-1}\, d\omega \ . \tag{43}$$

As will be described later, our results indicate that the discrepancies pointed out by Leavens were resulted from an imprecise definition of the condition for the asymptotic limit by Allen and Dynes.

1. The Eliasberg Equations

In the Matsubara representation the gap equation is given in the form[76,79]

$$\sum_{n\geq 0}^{\infty} (K_{mn} - \rho(T)\delta_{mn})\,\bar{\Delta}_n = 0 \ , \tag{44}$$

where

$$K_{mn} = \lambda_{m-n} + \lambda_{m+n+1} - 2\mu - \delta_{mn}[2m+1+\lambda_0+2\sum_{\ell=1}^{m}\lambda_\ell] \ , \tag{45}$$

and

$$\lambda_n = 2\int_0^\infty \frac{d\omega\alpha^2F(\omega)\omega}{\omega^2+(2\pi nT)^2} \ . \tag{46}$$

λ_0 is just the electron-phonon parameter defined in Eq. 42, μ is the Coulomb parameter which is related to the better known μ^* by

$$\mu^* = \mu/[1 + \mu\,\ell n(\omega_e/\sqrt{\langle\omega^2\rangle})] \ , \tag{47}$$

and $\bar{\Delta}_n$ is a modified gap parameter evaluated at the imaginary frequency $i\omega_n = i(2n+1)\pi T$. $\bar{\Delta}_n$ becomes $\Delta_n/|\omega_n|$ at $T = T_c$ where Δ_n has the meaning of the usual gap parameter. In this formulation T_c is that value of T for which the maximum eigenvalue of Eq. 44 is zero, i.e. $\rho_{max}(T_c) = 0$.

Allen and Dynes[79] have calculated T_c using an iterative procedure in which T_c, μ and the shape of $\alpha^2F(\omega)$ is held fixed and λ is solved so that $\rho_{max}(T_c) = 0$. Alternately, an equivalent but perhaps more appealing method is to fix $\alpha^2F(\omega)$ (i.e. λ_n) and μ and study $\rho_{max}(T)$. This is illustrated in Fig. 20 for the case of Pb.

We now show that, in addition to the numerical results, a general and relatively simple analytical expression for T_c can be obtained from the Eliashberg equations.

2. A General T_c Equation

All the detailed information about the superconductivity mechanisms is contained in λ_n and μ. On the other hand, we need only a few moments of $\alpha^2F(\omega)$ to get an accurate approximation for λ_n. Specifically, they are λ, $\langle\omega^2\rangle$ and ω_{log} which is defined by[79]

$$\omega_{log} = \lim_{n\to 0} \langle\omega^n\rangle^{1/n} = \exp\left(\frac{2}{\lambda}\int_0^\infty \frac{d\omega}{\omega}\,\alpha^2F(\omega)\,\ln\omega\right) . \tag{48}$$

λ gives the strength of the electron-phonon interaction and $\sqrt{\langle\omega^2\rangle}$ together with ω_{log} provide information about the shape of $\alpha^2F(\omega)$. We find that λ_n can be approximated very accurately for the commonly studied $\alpha^2F(\omega)$ spectra (Pb, Hg, etc) by the expression

$$\lambda_n = \lambda \frac{n_o^2}{n_o^2 + 1.6\beta\, n_o n + n^2} \tag{49}$$

where $\beta = \left(\sqrt{\langle\omega^2\rangle}/\omega_{log}\right) - 1$ and $n_o = \sqrt{\langle\omega^2\rangle}/2\pi T$ is the phonon cutoff in units of $2\pi T$. For the Einstein spectrum β is zero and Eq. (49) is exact. β is 0.161 for Pb and 0.690 for Hg.

To obtain an expression for T_c, we construct the following trial gap function

$$\bar{\Delta}_n = \frac{\Delta_n}{|\omega_n|} = \begin{cases} a\left(\dfrac{1}{1+2^{n-n_o}} - b\right)\dfrac{1}{(2n+1)\pi T_c} & n \le N \\ 0 & n > N \end{cases} \tag{50}$$

where $N = n_o\omega_e/\sqrt{\langle\omega^2\rangle}$ and ω_e is the Coulomb cutoff, e.g. $\omega_e \sim$ band width or electronic plasma frequency. The parameters n_o and b (hence T_c) are to be determined by the two linear equations

$$\sum_{n=0}^{N} K_{0n}\bar{\Delta}_n = 0 \tag{51}$$

and

$$\sum_{n=0}^{N} K_{Nn}\bar{\Delta}_n = 0 \ . \tag{52}$$

The trial gap function Δ_n is a Fermi-like function which changes most rapidly near the phonon cutoff and reduces to the two-square well model in the limit of small T_c, i.e. $n_o \gg 1$.

Since in general $\omega_e \gg \sqrt{\langle \omega^2 \rangle}$, Eq. (52) yields

$$b(1 + 2\mu \sum_{n=0}^{N-1} \frac{1}{2n+1}) = 2\mu \sum_{n=0}^{\infty} (\frac{1}{1+2^{n-n_o}})(\frac{1}{2n+1}) \tag{53}$$

and, for large N, we get

$$b(n_o) = \frac{2\mu \sum_{n=0}^{\infty} (\frac{1}{1+2^{n-n_o}}) (\frac{1}{2n+1})}{1 + \mu \left(\ln \left(n_o \frac{\omega_e}{\sqrt{\langle \omega^2 \rangle}}\right) + 1.9635\right)} \ . \tag{54}$$

Using Eqs. (45), (49), (51) and (54), we finally obtain the following relation for n_o

$$\frac{1}{\lambda}(1 + b') = F(n_o, \beta, \mu) \tag{55}$$

where F is a simple series

$$F(n_o,\beta,\mu) = -1 + \sum_{n=0}^{\infty} \left\{ \frac{n_o^2}{n_o^2 + 1.6\beta n_o n + n^2} + \frac{n_o^2}{n_o^2 + 1.6\beta n_o (n+1) + (n+1)^2} \right\}$$

$$\times \left(\frac{1}{1+2^{-n_o}} - b \right)^{-1} \left(\frac{1}{1+2^{n-n_o}} - b \right) \frac{1}{2n+1} \tag{56}$$

and

$$b' = b(n_o) \left(\frac{1}{1+2^{-n_o}} - b \right)^{-1} . \tag{57}$$

Equation (55) gives n_o and hence is our new T_c equation since $n_o = \sqrt{\langle \omega^2 \rangle} \,/\, 2\pi T_c$. $F(n_o,\beta,\mu)$ is a very rapid convergent series for parameters of interest and can be evaluated using a hand calculator. Therefore, for given β, μ and λ, one can readily solve for n_o and hence T_c from Eq. (55).

The transition temperatures obtained from Eq. (55) are in excellent agreement with the exact numerical solutions of Eq. (44). In Fig. 21 the calculated T_c using the new T_c equation for β=0.0, 0.161 and 0.690 (corresponding to the Einstein, Pb and Hg spectra) and $\mu^* = 0.1$ are shown. In this figure the exact results obtained by diagonalizing matrices of the size of ~64×64 are indistinguishable from the results obtained from Eq. (55). Also shown in Fig. 21 is the T_c from the McMillan equation and the two experimental data points for Pb and Hg.[84] As seen in Fig. 21, the McMillan equation has the spurious effect of saturating at large λ. In Fig. 22, the experimental T_c for six elemental superconductors with considerable different λ and different shapes of $\alpha^2F(\omega)$ are compared with the calculated values using Eq. (55)

and the appropriate measured values of λ, μ^* and β.[84] The agreement is rather remarkable considering the simple assumptions in our derivation of the T_c equation. The parameters used and the calculated results are presented in more details in Table VII. We have also computed T_c for the 23 alloys and amorphous metals given in Table I of reference 79; the agreement between the calculated and measured values is comparable to the results in Fig. 22.

We next examine the asymptotic limits of T_c using our model. For simplicity we shall only consider the case of $\mu = 0$ (i.e. $b = 0$). $F(n_o,\beta, \mu=0)$ is a monotonically increasing function of n_o with

$$F(n_o,\beta,\mu=0) \rightarrow \begin{cases} 1.3140\ n_o^2 & \text{for} \quad n_o \rightarrow 0 \\ \ell n n_o + 0.9635 + c(\beta) & \text{for} \quad n_o \rightarrow \infty \end{cases} \tag{58}$$

where $c(\beta)$ is a constant for a fixed β. In the limit of weak and strong coupling, we obtain: a) $\frac{1}{\lambda} \gg 1$ implies that $F(n_o,\beta,\mu=0)$ is very large and using Eq. (58) we have

$$T_c = 1.13\ \sqrt{\langle\omega^2\rangle}\ e^{-\frac{1+\lambda}{\lambda}}\ f(\beta) \tag{59}$$

where $f(\beta)$ is a factor of order unity (for $\beta = 0$, $f = 1/\sqrt{2}$).

b) $1/\lambda \ll 1$ implies that $F(n_o,\beta)$ is very small and again using Eq. (58), we obtain

$$T_c = 1.824\ \sqrt{\lambda\ \langle\omega^2\rangle}\ . \tag{60}$$

Our expression for T_c therefore reduces to the familiar McMillan exponential form for small λ and goes to an asymptotic form identical to that obtained numerically by Allen and Dynes for very large λ.

Returning to the questions raised by Leavens,[83] we concur with the conclusion that large λ alone does not imply that the asymptotic regime has been reached. We agree that the condition $\lambda > 10$ given in Eq. (24) of Allen and Dynes[79] is not sufficient, however the main conclusions of Allen and Dynes are <u>not</u> incorrect. The crucial point is that the n dependence of λ_n is essential in determining the asymptotic region. This depends on the shape of $\alpha^2F(\omega)$ and hence our β parameter. For example, in the case cited in Ref. 83, an interaction spectrum with $\alpha^2F(\omega) = \delta(\omega - 0.2) + 10\delta(\omega - 10)$ will have $\lambda = 12$ and $\beta = 9.64$. In our model, these values give a $T_c \sim 0.16 \sqrt{\langle\omega^2\rangle}$ which does not voilate the inequality $T_c \leq 0.116\lambda \langle\omega\rangle$ discussed in Ref. 83 and is not in the asymptotic limit.

In conclusion we have derived an T_c equation which has been demonstrated to be valid for all ranges of coupling strength and for different shapes of $\alpha^2F(\omega)$. In our model, T_c depends on $\langle\omega^2\rangle$, λ, μ^* and β. Information about these quantities can be obtained from $\alpha^2F(\omega)$ through tunneling measurements, the phonon spectrum $F(\omega)$ for $\langle\omega^2\rangle$ and β, heat capacity measurements for λ and isotope effect measurements for μ^*. Conversely the measured T_c can be used to obtain information on λ and μ^* via Eq. (55). For example, Eq. (55) will be useful for studying the dependence of T_c on the shape of $\alpha^2F(\omega)$ (i.e. β) which depends on phenomena such as phonon softening.

III. SURFACE

A. Self-consistent Pseudopotential Method for Non-periodic Systems

In view of their technological significance, non-periodic systems such as solid surfaces, solid-solid interfaces and vacancies in solids have been subjects of intensive investigations both experimentally and theoretically in the past few years.[85-87] However, the properties of these systems are still far from being well understood.

In this section we introduce a powerful yet simple method for calculating the electronic structure of non-periodic systems. The method is an extension of the self-consistent pseudopotential procedure discussed in Sec. IIC to localized configurations. This approach is applicable to problems such as atomic and molecular states, solid surfaces, localized impurity and vacancy states, finite chains or layers, adsorbates, and interfaces between solids. The scheme has many of the advantages of the standard pseudopotential calculations in that it uses a simple plane wave expansion and the starting potential can be obtained from bulk experimental data. We shall discuss the method in general in this section and specific applications to surfaces, interfaces, and vacancies will be discussed in subsequent sections.

The method discussed here is straightforward and initially involves putting the local configuration of interest into the structure factor. In the pseudopotential formulation, the crystalline pseudopotential form factors, $V(\underline{G})$, are written in terms of atomic potential form factors, $V_a(\underline{G})$ through the structure factor $S(\underline{G})$,

$$V(\underline{G}) = \sum_{\tau_a} S(\underline{G}) V_a(\underline{G})$$

$$S(\underline{G}) = e^{i\underline{G}\cdot\underline{I}_a} \qquad (61)$$

where $\underline{G}$ is a reciprocal lattice vector and $\underline{I}_a$ are the basis vectors to the various atoms in a primitive cell. The basic scheme is to include in $S(\underline{G})$ the essential features of the local configuration. In the case of a molecule, the structure factor can be constructed to create a cell with a molecule and sufficient empty space around the molecule to provide isolation from the next molecule when the cell is repeated. For a surface, usual periodicity can be retained in two dimensions and a slab of space can be inserted to provide a surface in the third dimension. The impurity or vacancy problem requires a cluster of host atoms surrounding the site of interest. Ultimately the cell chosen is repeated indefinitely to allow the use of the pseudopotential method. A similar approach specifically designed for surfaces has been used by Kleinman et al.[88] to calculate some properties of Al and Li surfaces.

Self-consistency[30,89] is essential in obtaining realistic solutions since the calculations will start with potentials derived for bulk calculations. It is necessary to allow the valence electrons to react to the boundary conditions imposed by the local configuration and the resulting readjustment and screening is a fundamental part of the problem. Also, the self-consistent screening potential has to be completely general and is not necessarily a superposition of atomic potentials. Self-consistency is restricted to the valence electrons since a fixed ion core pseudopotential is used. Changes in the core

electrons due to feedback from valence electrons are neglected since they are localized in a limited region around the ion cores and not significant for determining the valence-electron and bonding properties of the system.

In the scheme described above, the configuration of atoms and spaces can be as complex as desired. The ultimate limitation on the number of atoms is the amount of computer time necessary to generate the eigenvalues and eigenfunctions through solution of the secular equation. The basis set is formed by Bloch waves expanded in terms of free electron eigenfunctions.

The starting potential can be an ionic model potential fit to atomic term values and screened appropriately or a potential obtained from measurements on bulk solid state properties. In both cases the results are the same once self-consistency is reached. The problems with the method come mainly via the artificial long-ranged symmetry imposed, but most of the consequences can be dealt with. Some examples are: the interaction between configurations; establishing a zero of energy; the fact that the potential which should depend continuously on wavevector, $\underset{\sim}{q}$, is approximated by form factors at $\underset{\sim}{q}$'s equal to the $\underset{\sim}{G}$'s of the chosen lattice structure; and the symmetry of the configuration to some extent suggests the choice of lattices. Most of the above potential problems are eliminated or reduced by taking large enough cells and cells of the appropriate structure or symmetry.

The steps in our self-consistent procedure are shown in Fig. 23. The self-consistent loop is initiated with a starting potential which

is usually taken to be an empirical pseudopotential from a crystalline calculation. From the resulting total valence charge density $\rho(\underline{r})$, a Hartree-like screening potential is derived via the Poisson equation,

$$V_H(\underline{G}) = \frac{4\pi e^2 \rho(\underline{G})}{\Omega_c |\underline{G}|^2} \quad , \tag{62}$$

and an exchange potential of the Slater type[90]

$$V_x(\underline{r}) = -\alpha \left(\frac{3}{2\pi}\right)(3\pi^2)^{1/3} e^2 \rho(\underline{r})^{1/3} \tag{63}$$

is calculated. The sum of V_H and V_x is then the total screening potential for the valence electrons. This screening potential is added to an ionic pseudopotential V_{ion} generated by the ionic cores of the atoms to form a new total pseudopotential for the next iteration. New screening potentials are derived and the process is repeated until self-consistency is reached. The use of a statistical exchange of the above form for atoms, molecules and solids has been discussed widely in the literature[90] and been proven to yield satisfactory results.

We note that there are no adjustable parameters related to the properties of the localized configurations in the calculations. The only parameters went into the calculations are (1) the structure, i.e. the position of the atoms, and (2) the ionic potentionals, V_{ion}. V_{ion} can be determined from atomic spectra as discussed in Sec. IIC. As for the structure, one has to go to experiments for guidance. More details on the method will be presented when we discuss the individual applications in the following sections.

B. Semiconductor Surfaces

1. Si(111) Surfaces: Unreconstructured (1×1) and Reconstructed (2×1) Model Structures

In this section we present self-consistent pseudopotential calculations on Si(111) surfaces. Three different surface models have been studied and the resulting calculated density of states curves and electronic charge density distributions have been examined to extract the essential physical features of the various models. In each case the calculations were carried to self-consistency following the procedure presented in the preceding section. The requirement of self-consistency proves to be absolutely necessary to account for the modified screening in the surface region.

The three different models for the Si (111) surface studied are:

a) An unrelaxed, unreconstructed surface, in which all surface atoms remain at their exact "bulk" positions,

b) A relaxed surface, in which the outermost atomic layer is rigidly relaxed inwards by an amount of $\Delta = 0.33$ Å. These two models have been studied by Appelbaum and Hamann[91] in the only previously existing self-consistent approach to the problem, and their results are basically confirmed by our calculations. In addition we find new types of surface states and are able to present density of states curves. The third model we studied is

c) A (2×1) reconstructed surface, in which atoms of the outermost atomic layer are alternatively moved inward and outward to form a (2×1) planar unit cell. This model has been refined in a second step as first proposed by Haneman[92] by moving atoms of the second atomic layer

slightly laterally, the effect of which was small compared to the effect of the "buckling" at the first step. The predominant result of this (2×1) reconstruction is the splitting of the "dangling-bond" surface state in the gap into two separate peaks corresponding to two separate surface bands one of which is occupied. This essential feature is in good agreement with experiments[93] and is not obtained in the other two models.

The method used to obtain the electronic surface structure in a self-consistent fashion has been discussed in Sec. IIIA and will be presented in some more detail in Sec. IVA when we discuss the metal-semiconductor interfaces, therefore we only review the essential features here.[94] The local configuration in the present case is a 12-layer slab of Si, simulating two non-interacting surfaces. The slab is placed in a periodic lattice spaced ~4 layers apart to prevent interaction between the different slabs (or surfaces). This artifact has the enormous advantage that the system can now in principle be treated as any periodic crystal and that the pseudopotential method in its standard form can be applied. A self-consistent treatment, however, is necessary to achieve the correct screening of the atoms in the neighborhood (~3 to 4 atomic layers) of the surfaces.

One problem which arises when simulating surfaces by finite slabs of atoms periodically repeated, is spurious structure in the density of states due to the "unreal" periodicity of slabs perpendicular to the surfaces. Spurious two-dimensional singularities occur. Their number increases with the number of atomic layers per slab. For the "true"

surface case these singularities become "dense" and disappear. For finite slab calculations all structures in the density of states have to be investigated in this spirit. Similar problems are encountered when simulating an amorphous material by large unit cells periodically repeated.[95]

As discussed in Sec. IIIA the calculations are initiated with an empirical pseudopotential carried over from crystalline calculations. From the resulting total charge density, screening and exchange potentials are derived and added to an atomic Si^{+4} ion-potential.[94,96] New screening and exchange potentials are derived and the process is repeated until self-consistency (stability of the eigenvalues or stability of the input versus output potentials within 0.1 eV) is reached. For the ideal and relaxed structures, a density of states curve has been computed from 336 k-points in the two-dimensional Brillouin zone at each iteration to guarantee a precise location of the Fermi level. The total charge density could then be derived from all states with energies below the Fermi level. Plane waves with a maximum reciprocal-lattice vector corresponding an energy of 2.7 Ry were used in the basis set. This corresponds to about 180 plane waves for the twelve-layer (1×1) structure. Another 340 plane waves up to an energy cutoff of 6 Ry were included by second-order perturbation theory. From the self-consistent calculation an ionization potential of about $\phi = 4.0$ eV was obtained for the relaxed surface. We shall discuss the calculations for the (2×1) structure in detail later.

In Fig. 24 the crystal structure of Si is viewed in perspective along the [110] direction. The [111] direction is vertical. A horizontal (111) surface is obtained by cutting all vertical bonds in a plane. An excellent overall impression of the behavior of the electronic states at the Si (111) surface can be obtained by considering the total, self-consistent valence charge distribution, as presented in Fig. 25 for the unrelaxed surface model. The figure shows charge density contours in a (110) plane cutting the (111) surface at right angles (see Fig. 24). The plotting area starts midway between two films and extends about 4 1/2 atomic layers into the bulk. The atomic (unrelaxed) positions are indicated by dots. Moving deeper into the crystal, the charge distribution closely resembles the Si bulk charge densities; near the surface, it decays rapidly into the "vacuum". This rapid decay assures the required "vacuum" and hence the decoupling of the films. No surface states can be recognized on this plot, since only a small number of them exists in a continuum of decaying bulk-like states.

Figure 26 displays the two-dimensional band structure of a twelve layer Si (111) film based on the self-consistent potential for the relaxed surface model. The band structure is presented for surface $\underline{k}$-vectors $\underline{k}_{\parallel}$ between $\bar{\Gamma}(0,0)$, $\bar{M}(1/2,0)$, $\bar{K}(1/3,1/3)$ and $\bar{\Gamma}(0,0)$ in the hexagonal Brillouin zone. The 24 valence bands can be roughly divided into 3 bulk groups, representing the 6 low-lying s-like bands, 6 bands of mixed s- and p-character, 11 p-like bands and one separate p-like dangling-bond band in the fundamental gap. The three groups of bands,

would with increasing film thickness approach continua separated by several gaps in which most of the surface states appear.

Let us first discuss the dangling bond bands in the fundamental gap. Suppose a Si bulk crystal is cut every 12 layers parallel to the (111) plane and the pieces are gradually separated from each other. With increasing distance one state each would split away from both the valence-bands and the conduction bands to meet about at half-gap to form the two fold degenerate dangling bond surface band corresponding to the broken bonds on either side of the Si films. In Fig. 26 the two bands are not exactly degenerate corresponding to some weak interaction (~0.2 eV) still present between opposite surfaces of the 12 layer films. If the surfaces are unrelaxed and unreconstructed the two dangling bond bands show almost no dispersion parallel to the surface, i.e. they would appear extremely flat in the band structure plot. If the outermost atomic layer is relaxed inward, the dangling bond band shows an increased dispersion parallel to the surface together with a slight overall shift of the bands (see Fig. 27).

In contrast to the dangling bond surface band which exists throughout the two-dimensional Brillouin zone independent of relaxation, other surface states show up only in parts of the two-dimensional Brillouin zone and some depend on relaxation. They are indicated at the high symmetry points Γ, K and M by dots in Fig. 26. A region of particular interest is around the point K. Strongly localized surface states exist in the gap between -7 eV and -9 eV independent of surface relaxation. These states merge into the continuum at M and become

strong surface resonances. A similar behavior is found around K between -2 eV and -4 eV. Even though the existence of these surface states does not depend upon relaxation, their exact energy position is a function of relaxation. Other surface states appear only after relaxation like the splitting away of the lowest valence band pair between -9.5 eV and -12.5 eV throughout the zone. All these findings have qualitatively also been obtained in a recent analytical model calculation by Yndurain and Falicov.[97]

Density of states curves for the self-consistent results for the unrelaxed and relaxed surface models are presented in Fig. 27. Since these curves represent the total density of states for a 12 layer slab, their overall features strongly resemble those of the Si bulk density of states. The results for the (2×1) reconstructed surface (insert) are obtained for a 6 layer slab. They shall be discussed later together with 12 layer (2×1) reconstructed surface calculations. To locate structures associated with surface states (no distinction is made in the present case between bona fide surface states and strong surface resonances), we investigated the charge density distributions for small energy intervals scanning the entire width of the valence bands. As already mentioned, because of the existence of artificial two-dimensional singularities not all sharp structures in the density of states correspond to surface states. The locations of surface states and strong surface resonances (for the relaxed case) are indicated by arrows in Fig. 27. Their labelling corresponds to the regions around high symmetry $\underline{k}$-points in the two-dimensional Brillouin zone, from which

they originate (see dots and labelling in Fig. 26). The surface state energies are given in Table VIII and compared to experimental data obtained from UPS measurements on (2×1) and (7×7) reconstructed surfaces. Also indicated in Table VIII are the results of the self-consistent pseudopotential calculation of Appelbaum and Hamann (AH)[91] and of the empirical tight-binding calculation of Pandey and Phillips (PP)[98] on unreconstructed relaxed Si(111) surfaces.

We now examine some of the individual surface states. In particular we investigate the points Γ(center) and K(corner) of the two-dimensional hexagonal Brillouin zone. Model calculations[97] indicate that K rather than M (edge midpoint) is a point of special interest to study surface states.

We first discuss the results at Γ. Below the energy zero which was chosen to coincide with the bulk valence band edge E_V we find (in agreement with Appelbaum and Hamann[91] and Pandey and Phillips[98]) three surface states. Two of them are degenerate and close to E_V representing the transverse back bonds with charge localized between the first and second atomic layer. The third state is localized at the bottom of the valence bands and is predominantly s-like around the outermost atoms. With the "dangling bond" state above E_V, which we shall discuss later, there are four surface states at Γ which agrees with the classical tight binding concept.[98] The situation, however is different at K. We find only one "pure" transverse back bond K_{tb}, the remaining states $K_{\ell b}$ and $K_{\ell b}$, having more longitudinal or s-like character. The interesting feature is that some states $K_{\ell b}$, (at -2.0 eV and -9.7 eV)

have most of their charge localized between the second and third layer in contrast to the state $K_{\ell b}$ (at -8.5 eV) which is a mixture of s-like and p-like states at the outermost atoms giving rise to a charge distribution between the first and second layer. In Fig. 28 we show a contour map of the charge of the state $K_{\ell b}$, at -2.0 eV. We would like to stress the fact that surface states apparently can "penetrate" into the second longitudinal bond which puts a limitation on the position of a "matching plane"[91] separating the surface region from the bulk. The appearance of surface states at K in the second longitudinal bond increases the number of surface states from four to five which has been predicted by model calculations[97] but which is in contrast to the findings of Pandey and Phillips.[98] At the point M the situation is similar but less pronounced with some of the surface states merging into the bulk continuum.[97]

Let us now examine the surface states in the energy gap above E_V. As shown in Fig. 27 we find for the unrelaxed, unreconstructed surface one very flat surface band about mid gap. This almost dispersionless band is half occupied, placing the Fermi level right at the peak. The charge distribution of these (either occupied or empty) mid gap surface states is very much "dangling bond"-like exhibiting a pronounced p-like charge centered at the outermost atoms. When the last atomic layer is relaxed inward, the back bonds get stronger resulting in a mixing of the "dangling bond" states with lower lying back bond states. This increases the interaction between the individual "dangling bonds" via the second atomic layer and the dispersion of the surface band

increases. In fact, the resulting density of states exhibits the asymmetric shape of critical points expected for a planar triangular network of s- or π-like orbitals. The critical points are labelled K_d and Γ_d in Fig. 27 indicating their origin in $\underline{k}$-space. A charge density plot for the states K_d is shown in Fig. 29. It exhibits the very pronounced "dangling bond" character. The unoccupied states Γ_d show a stronger mixing with back bonds. As for the unrelaxed case there is only <u>one</u> surface band which is half occupied. This changes qualitatively when we consider the (2×1) reconstructed surface.

We have used the Haneman model[92] in calculating the electronic structure of the metastable (2×1) phase of the Si (111) surface. The structural parameters entering our (2×1) reconstructed surface model are the following: alternating rows of atoms have been raised by 0.18 Å and lowered by 0.11 Å, and second layer atoms have been shifted laterally as indicated by the arrows in Fig. 30 such as to approximately preserve the length of the back bonds. This choice of parameters may not represent an optimum choice. In particular, since these parameters represent an overall <u>outward</u> relaxation of the outermost atomic layer, some surface states which depend on inward relaxation like the states $\Gamma_{\ell b}$ at the bottom of the valence bands will become delocalized. Our main interest in this study however is the behavior of the electronic states in the vicinity of the gap and their dependence on the <u>character</u> of the reconstruction (buckling with preserving the length of back bonds). The planar unit cell now contains 4 atoms. First preliminary calculations have been done on six-layer slabs separated by 3 bond

lengths of empty space. The corresponding density of states in the vicinity of the valence band edge, obtained from 72 $\underline{k}$-points in the two-dimensional Brillouin zone is shown as an insert in Fig. 27. As expected, qualitative changes compared to the unreconstructed (1×1) case occur. Doubling the real space unit cell in one dimension corresponds to folding back the Brillouin zone in certain directions. Thus <u>two</u> surface bands appear separated by a gap resulting from the potential perturbation of the reconstruction. This behavior is reflected by the density of states in Fig. 27 showing two peaks which now correspond to two different bands. In Fig. 27 the density of states does not vanish between the two peaks, thus leaving the surface semi-metallic. In fact the gap between the two surface bands is comparable or smaller than their dispersion. We believe that this behavior is an artifact of only including 6 layers per slab. The surface states on opposite surfaces of the slab show too much interaction, consequently causing the semimetallic behavior.

To obtain more quantitative results (2×1) calculations with 12 layers per slab have been performed. Because of the large matrix size (about 320 plane waves were included to obtain the same convergence as for the unreconstructed cases), the self-consistent calculations were based on a two-point scheme ((0,0)Γ and (1/2,1/2)K'). For the final self-consistent potential several $\underline{k}_{\parallel}$-points along high symmetry directions have also been included. A band structure showing the bands in the vicinity of the fundamental gap is presented in Fig. 31. The two dangling bond surface bands are split by a gap of $\geq$ 0.27 eV

throughout the zone. They show some dispersion of only about 0.2 eV. The Fermi-level falls between the two bands, thus creating a semiconducting surface. To obtain a density of states curve for these bands a four term Fourier expansion for the band energy $E(k_{\parallel})$ has been fitted to the calculated band structure at the four $k_{\parallel}$-points Γ, M', $\tilde{M}$ and K', and subsequently evaluated over a fine grid of $k_{\parallel}$-points of the two-dimensional Brillouin zone. The results are shown in Fig. 32 (bottom). Two structures are found separated by about 0.4 eV corresponding to the two surface bands. The lower surface band which overlaps with states arising from bulk and other surface bands is centered at about $E = E_V = 0$. Experimental photoemission data[93] show structure at somewhat lower energy ($E \approx -0.5$ eV). Further lowering of the calculate surface band and better agreement with experiment can probably be obtained by using a different choice of atomic displacement parameters. Our results, however, show the definite trend of splitting the dangling bond surface bands combined with an overall lowering because of the buckling structure.

Also indicated in Fig. 32 (top) is a joint density of states (JDS) for optical transitions between the lower and the upper surface bands. Matrix-element effects have not been considered in this plot. The JDS curve can be qualitatively compared to infrared absorption measurements[99] (broken line). A quantitative comparison is not reasonable because of the ad hoc choice of atomic displacement parameters and because of probable strong excitonic effects. It is also instructive to calculate the charge density distributions for states inside the two peaks in

the density of states of Fig. 32 (bottom). The corresponding charge (or hypothetical charge for the unoccupied upper band) is displayed in Fig. 33 in a (210) plane intersecting the surface at right angle. This plane corresponds to the (110) plane of the unreconstructed surface. The buckling raises the surface atom on the left hand side and lowers the surface atom on the right hand side. Due to lateral shifts the second layer atoms are slightly moved out of the (210) plane. The states show very interesting real space behavior. Electrons in states originating from the lower peak labelled d_{out} are located predominantly on those atoms which have been raised and avoid those atoms which have been lowered. Conversely the wavefunctions for unoccupied states of the peak labelled d_{in} are concentrated around those atoms which have been lowered. The surface thus exhibits a (2×1) pattern of nearly two-fold occupied dangling bond states centered at every second row of atoms. Roughly speaking the unpaired dangling electron of every second surface atom (in) is transferred to its neighboring atom (out) where it pairs up with another electron, thus creating an ionic semi-conducting surface. This result thus provides an explanation to the absence of electron spin resonance signal from a clean Si (111) surface.[100]

In summary, we have applied the self-consistent pseudopotential method for local "non-periodic" configurations discussed in Sec. IIIA to several Si (111) surface models. Three different surface models have been studied including unreconstructed, relaxed and unrelaxed (1×1) surfaces which also have been investigated by Appelbaum and Hamann[91] in the only previously existing self-consistent calculation.

Their results are basically consistent with our calculations. In addition new types of surface states corresponding to the longitudinal back bonds between the second and third atomic layer are found and complete density of states curves are presented. A buckled (2×1) surface model such as proposed by Haneman (with preserved back bond lengths) has been used to study the (2×1) reconstructed surface. The salient experimental results on (2×1) Si (111) surfaces can be understood on the basis of this model. Upon reconstruction the dangling bond band is split and lowered considerably in energy. The surface is found to be semiconducting thus producing an infrared absorption peak at low energies and eliminating the electron spin resonance signals from the surface.

2. Relaxation Effects on the (110) Surface of GaAs

We continue our study of semiconductor surfaces in this section with the (110) surface of GaAs. Numerous theoretical calculations[101-105] have been performed for the ideal (110) surface of GaAs. Employing a variety of techniques these calculations provide a consistent picture of the intrinsic surface states occurring near the Fermi level. Occupied anion derived states are found to exist near the valence band maximum and empty cation derived states exist in the semiconductor band gap. Although early experimental work[93(a),105-108] seemed to lend support for this interpretation more recent work has yielded contrary evidence.

With respect to the empty cation states, Eastman and Freeouf[106] have made partial yield photoemission measurements on a series of zincblende (110) surfaces. They observed a correlation between the

position of the empty cation states, measured to lie within the band gap, and Schottky barriers. Based upon suggestions first put forth by Bardeen,[109] they asserted that the empty cation states play a prominent role in the determination of the Schottky barrier height. However, recent theoretical studies[110] have shown that semiconductor surface states are not present at the metal-semiconductor interface in the energy range of the band gap, and it is the metal induced gap states (MIGS) that are related to the properties of Schottky barriers.

In addition, recent studies on GaSb[111] and GaAs[112] have suggested that there exist no empty surface states within the band gap. Evidence for a higher placement of empty cation states comes from a model for (110) surface relaxation as proposed by Rowe and coworkers.[113] In order to account for the insensitivity of the cation surface states to metal overlayers[106,113] and oxygen adsorbates,[105,114] they proposed that the surface cations must relax inward. This type of relaxation is expected to move the cation states to higher energy relative to the bulk valence band maximum.[106]

Early experimental evidence[93(a)] for filled anion states occurring near the valence band maximum has also been questioned.[105,115,116] The theoretical calculations indicate a strong and narrow surface band near the valence band maximum; however, recent photoemission is in poor agreement with this result.[116] The photoemission work suggests that only a rather broad surface feature, possibly obscured by bulk valence band states, is compatible with the experimental data.

Thus, to assess the effects of relaxation on the GaAs (110) surface we have considered a model similar to the one proposed by Rowe, et al.[113] In this model we allow the cations to relax inward to form an sp^2 configuration and the anions to relax outward such that the bond lengths are preserved. A very similar model has been used in the previous section to account for the reconstruction occurring for the (111) Si surface.[92,117] We find that the empty cation states are moved to higher energies; however, the leading edge of these states still lies within the band gap. In addition, the character of the cation states is dramatically changed. The charge density is not localized outward along the cation dangling bonds as for the ideal surface, but inward between the first and second surface layers. This could account for the insensitivity of these states to metal overlayers and gas adsorbates. With respect to the filled states the unrelaxed As dangling bond states move to lower energies and become obscured by bulk states in agreement with the recent photoemission work.[116]

To calculate the electronic structure for the proposed model, we consider an eleven layer slab of GaAs with the (110) surface exposed to vacuum on both sides. The slab is repeated in a super-lattice and the electronic structure is calculated following the self-consistent procedure described in Sec. IIIA. The ionic pseudopotentials (determined by model calculations and bulk considerations) used are the same as those given in Ref. 104.

In Fig. 34 a local density of states (LDOS) is presented for the relaxed surface. The histogram density of states was prepared by

weighting each eigenvalue contribution to a given energy interval by the corresponding charge density localized within the specified layer.[64,104] The first layer corresponds to the surface layer; the fifth layer deep within the bulk. The result for the first layer for an ideal surface is also displayed in Fig. 34. The local density of states for a given layer has the physical significance of giving the probability of finding an electron of a given energy E in that specified layer. Prominent peaks arise from surface states on the GaAs (110) surface are shown in Fig. 34 as shaded areas in the LDOS.

In contrast to Si surface calculations,[91,94,97,98] the lower surface states on GaAs are not significantly altered by relaxation. However, this is not the case for the anion and cation dangling bond surface states occurring near the band gap. These states are significantly altered in both in energy position and charge localization. The filled anion states are lowered in energy by nearly 1 eV as compared to the ideal case. Since strong bulk contributions occur within the same region, this result could account for the absence of filled surface state contributions in the recent photoemission work.[116] The lowered energy position for the filled states is a natural outcome of the bond angle deviations occurring at the surface anion site. Within our model relaxation, the sp^3 anion bonding configuration is made more s-like, hence, lowering the energy of the states. This behavior is analogous to the buckled Si reconstruction as suggested by Haneman.[92,117]

As expected the empty cation states show the opposite trend; they move to higher energies with the sp^2 configuration.[113] A detailed

density of states for the cation derived empty surface states for both the ideal and relaxed surface is given in Fig. 35. This density of states was constructed by a Fourier interpolation scheme between 20 $\underline{k}$-points in the surface Brillouin zone. The band gap in GaAs is 1.4 eV, thus the center of mass of the empty surface band density of states has moved above the conduction band minimum. However, the threshold of the calculated surface band remains in the band gap. The minimum of this band occurs along the $\langle 001 \rangle$ bulk direction and is a result of significant mixing between anion and cation states along this direction. Our results are only compatible with the Eastman and Freeouf[106] data provided either the center of mass is exciton shifted downward in energy or the threshold of the surface band is exciton enhanced.

It is possible that a relaxation model could be constructed in which the threshold is raised, but it appears within the limits of our calculation that this would require an unphysical stretching of the anion-cation bonds along the surface layer. This conjecture is based upon the result that the threshold appears to be insensitive to changes in the bond lengths as calculated by relaxing the cation but not altering the positions of the surface anions.

Finally, in Fig. 36 we display the pseudocharge density for the cation surface states. For the ideal surface[104] these states protrude into the vacuum region and would be expected to interact strongly with surface adsorbates. In the relaxed case we would not expect this to occur as the states are localized inward between the first and second

surface layers. These states are predominantly p-like at the cation site with considerable s-like admixture. The strengthening of the back lobe of the p-like orbital by inward relaxation is to be expected by analogous behavior calculated for relaxed Si surface states.[91]

In summary we have self-consistently determined the electronic structure of a model relaxed GaAs (110) surface. We final that this model can account for the insensitivity of the empty cation derived surface states to metal overlayers, and the lack of evidence for occupied anion surface states in recent photoemission measurements. Also with relaxation of the surface, the empty cation derived surface band becomes more dispersive. The center of mass lies above the conduction band minimum; however, the threshold of the surface band remains within the bulk band gap.

C. Metal Surfaces

Theoretical progress in the understanding of the electronic properties of metal surfaces has lagged considerably behind that of semiconductor surfaces in recent years. Simple s-p metal surfaces lack the wealth of interesting experimental data which have attracted the theorists to work on semiconductor surfaces. On the other hand, although transition metal surfaces are of great interest because of their possible technological applications, the complexity of the d-electrons has made realistic calculations on these surfaces prohibitively difficult. Thus far, the only self-consistent calculations on simple metal surfaces are those on the jellium model[118] and on monovalent metals[119,120] which do not have occupied surface states

hence preclude them from participating in the self-consistent screening; and, as of yet, there are no fully self-consistent calculation for the electronic structure of transition metal surfaces.

As an attempt to improve the above situation, we have performed self-consistent calculations on the electronic structure of a polyvalent s-p metal surface (the Aℓ(111) surface) and that of a transition metal surface (the Nb(001) surface). Because of the greater interest in transition metal surfaces, emphasis will be placed on the Nb(001) surface in the discussions.

1. Aℓ (111) Surface

We followed the procedure discussed in Sec. IIIA to calculate, using self-consistent pseudopotentials, the electronic structure of a (111) surface of aluminum. The local configuration in the present case consisted of a twelve layer Aℓ slab with a vacuum region of three interlayer distances for each surface over which the wavefunctions of the slab are allowed to decay. As in the semiconductor surface calculations, the $Aℓ^{+3}$ ionic pseudopotential used is a Heine-Animalu core potential[121] which has been fitted to a 4-parameter curve in Fourier space

$$V_{ion}(q) = \frac{a_1}{q^2}(\cos(a_2 q) + a_3)e^{a_4 q^4} \tag{64}$$

with parameters $a_1 = -0.7758$, $a_2 = 1.0468$, $a_3 = -0.13389$, and $a_4 = -0.02944$. The units are such that if q is entered in atomic units, V(q) is given in Ry. The potential has been normalized to an atomic volume of 112.36 $(a.u.)^3$.

At each iteration in the self-consistent process, the required screening potential and the Fermi level, E_F, were determined by calculating the eigenvalues and eigenvectors over a grid of 294 points in the two dimensional Brillouin zone. The final calculated value for E_F was 0.85 Ry above the conduction band minimum in good accord with the bulk value of 0.86 Ry. The obtained value for the work function ϕ is 0.38 Ry, which unfortunately cannot be compared directly to the experimental value of 0.31 available for polycrystalline Aℓ.[122,123]

Let us now discuss the surface states on the Aℓ (111) surface. To determine the existence of surface states we have examined the charge density for all eigenvalues below E_F at high symmetry points in the two dimensional zone. Our results indicate the existence of surface states below E_F at Γ and at K in agreement with the results of previous non-self-consistent calculations by Caruthers, Kleinman and Alldredge,[124] but not with that of Boudreaux.[125] At Γ one surface state occurs at 0.33 Ry below E_F and at K we find two surface states at 0.15 Ry and 0.07 Ry below E_F.

Among the three surface states, the most localized (in real space) state is the upper state at K at 0.07 Ry. The charge density distribution for this state is shown in Fig. 37. The top figure shows the charge density averaged parallel to the surface and plotted as a function into the bulk. The bottom figure is a contour plot for the charge in the (110) plane. This state occurs in a rather large energy gap in the projected band structure[124] and its decay is more rapid than the other state at K at 0.15 Ry or the surface state at Γ. As seen from

Fig. 37, the charge density of this state is localized in a "cavity" near the surface formed by the first and second atomic layers. Since this state occurs quite near E_F and is localized strongly near the surface, it is expected to be chemically active.[124]

The surface state at 0.15 Ry at K is not as localized as the upper state discussed in the previous paragraph, and is quite sensitive to the surface potential. As with the 0.07 Ry state at K it has charge localized in the cavity regions, but peaks further from the surface. Finally, the surface state at Γ, which occur in the bulk band gap at L in the three dimensional zone, decays very slowly falling only by 10% from the peak value at the surface to the mid-point of the slab.

2. Nb(001) Surface

We would like to discuss in some detail in this section the electronic structure of a transition metal surface. A self-consistent pseudopotential calculation is presented for the (001) ideal surface of Nb. To our knowledge, this is the first fully self-consistent calculation for a transition metal surface. The band structure and real space distribution of the electrons near the surface are determined. Surface states of different angular momentum character are found to exist over a wide range of energies and over different portions of the two-dimensional Brillouin zone. Our calculations predict strong surface features in the density of states in the range of 0-2 eV above the Fermi energy.

Previous calculations[85,126-129] on transition metal surfaces can be roughly divided into three groups: (1) Greens-function calculations[127]

of the density of states of semi-infinite crystals using a d-function tight-binding Hamiltonian (i.e. neglecting the effects of sp-d hybridization), (2) band calculations on semi-infinite crystals by matching wavefunctions across a potential barrier constructed to represent the surface,[128] and (3) band calculations on thin films using multiple-scattering, tight-binding or OPW methods.[129]

Although the above calculations have provided useful information about band narrowing and some properties of surface states, their limitations have motivated us to attempt the present calculation. Some of the limitations of these calculations are: None of these calculations are fully self-consistent; tight-binding calculations usually involve a limited basis set and some important effects of dehybridization at the surface are neglected; and Greens-function calculations provide only information about the surface density of states without giving surface bands and their $\underline{k}$-space distribution. Pseudopotential calculations when carried out in a self-consistent fashion (Sec. IIIA) will avoid most of these shortcomings.

The remainder of this section is organized as follows: In section a the methods of calculation are discussed. In section b the results for the electronic structure of the Nb(001) surface are presented together with the projected band structure of bulk Nb on the (001) surface. And in the final section c a summary and some discussion are presented.

a. Calculations. Let us first discuss the calculation on the projected band structure (PBS). Since bona-fide surface states can only occur in the gaps of the projected bulk part of the two-dimensional

(2D) band structure,[130] a knowledge of the projected band structure of the three-dimensional (3D) bulk crystal on a crystal face will be extremely helpful in analyzing surface states on that surface. For this reason we have projected the bulk band structure of Nb on the (001) surface using a method similar to that discribed in Ref. 131 by Caruthers and Kleinman.

For the (001) face of the bcc lattice, the surface lattice vectors are $\underline{a} = a_c\hat{x}$, $\underline{b} = a_c\hat{y}$, where a_c is the bcc cubic lattice constant and $\hat{x}$, $\hat{y}$, $\hat{z}$ are the usual cubic unit vectors. The 2D Brillouin zone (BZ) for this surface unit cell is then a square (Fig. 38 top) with primitive reciprocal lattice vectors $\underline{K}_x = 2\pi/a_c\hat{x}$ and $\underline{K}_y = 2\pi/a_c\hat{y}$. To obtain the PBS, we construct the smallest 3D unit cell of the bcc lattice which is compatible with the 2D surface unit cell and determine the 3D band structure of Nb according to this new unit cell. The allow energies at a point $\underline{k}_{\parallel} = (k_x, k_y)$ in the 2D BZ are then the energy eigenvalues at all the points $(\underline{k}_{\parallel}, k_z)$ such that $-K_z/2 \leq k_z \leq K_{z/2}$ where K_z is the primitive reciprocal lattice vector along the $\hat{z}$-direction for the new 3D unit cell. In the present case, the new unit cell is just the bcc cubic cell and the new BZ is a cube inscribed in the standard BZ (Fig. 38 bottom). Also the band structure $E_n(\underline{k})$ for the new cell can be easily obtained by folding back the eigenvalues in the standard BZ into the new zone. For this purpose we have used the band structure calculated in Sec. IIC. The PBS for the (001) surface of Nb were obtained from the eigenvalues of 285 $\underline{k}$-points in the irreducible part (1/48) of the standard BZ.

In calculating the surface electronic structure, we employed the self-consistent method developed in Sec. IIIA. A nine-layer slab of Nb with the (001) surfaces exposed to both sides is used to simulate two noninteracting surfaces. The slab is placed in a periodic superlattice with the slabs separated by a distance equivalent to 6 atomic layers of Nb. Screening is achieved using a Hartree potential derived via Poisson's equation and a Slater-type exchange potential. The only input to the calculation consists of the structure (i.e. the atomic positions) and a fixed ionic pseudopotential for the Nb^{+5} ion cores.

The Nb^{+5} ionic potential used here is the same potential used in Sec. IIC which is a ℓ-dependent nonlocal pseudopotential of the form

$$V = \sum_{\ell=0}^{2} V_\ell P_\ell \tag{65}$$

where P_ℓ are projection operators for the various angular components of the electron wavefunction. The potentials V_s, V_p, V_d were obtained by fitting the spectroscopic term values of the Nb^{+4} ion (i.e. the Nb^{+5} plus one electron system) and they are depicted in Fig. 15. When used in self-consistent atomic and bulk band structure calculations, this Nb^{+5} ionic pseudopotential has proven to yield results agree well with experiment and other calculations. (See Sec. IIC.)

In the present calculation we have used the same convergence criteria as in the bulk calculation (Sec. IIC). The electronic wavefunctions were expanded in a basis set consisting of approximately 1000 plane waves; an additional 1000 plane waves were treated by second-order perturbation techniques. Using symmetry, the Hamiltonian

matrix was reduced to two ~ 500×500 matrices since the central plane of the slab is a reflection plane. Because of the large matrix size, the self-consistent calculations were based on a three special-point scheme.[132] However, for the final self-consistent potential, a total of 15 $\underline{k}$-points in the irreducible part (1/8) of the 2D square Brillouin zone has been included.

With the results at the 15 $\underline{k}$-points, we obtained the self-consistent valence charge density, the local density of states for the electrons near the surface,[64] and the charge densities for the various surface states. The surface states were identified by examining the charge density for all eigenvalues below the vacuum level at the 15 $\underline{k}$-points.

b. Results. The PBS for the Nb(001) surface is shown in Fig. 39. We have scanned the entire irreducible part of the square zone by examining $\underline{k}$-points along lines parallel to the $\bar{\Sigma}$ line ($\bar{\Gamma}$ to $\bar{M}$) in equal intervals. Each small figure in Fig. 39 shows the PBS along one of such lines. For example, Fig. 39(a) is the PBS along the $\bar{\Sigma}$ line whereas Fig. 39(i) corresponds to the one point $\bar{X}$. As seen from the figures there are a number of absolute gaps in the PBS. Symmetry gaps which we will discuss later are not shown in these figures. We note that the absolute gaps tend to be located well far away from the zone center $\bar{\Gamma}$ and tend to be the widest at off high-symmetry points.

From the PBS one therefore expects most of the surface states to occur away from the zone center and have energies in the wider gaps. Our surface results indeed show that most of the prominent surface

states occur in the big gap, G1, positioned just above to Fermi level E_F between 0 and 3 eV and in the smaller gap, G2, positioned between -2 and -1 eV. The $\underline{k}$-space extension of these two major gaps in the PBS is shown in Fig. 40.

Let us now proceed to the surface results. Figure 41 shows the total, self-consistent valence charge density for the Nb (001) surface. The charge density distribution on the (110) plane is plotted in Fig. 41(a) and that on the (100) plane is plotted in Fig. 41(b). We find that, after only a few layers into the bulk, the charge density is virtual identical to the bulk charge density presented in Fig. 18 in Sec. IIC. Some of the noticable changes in the charge distribution near the surface are that the atoms on the second layer have a slightly higher charge density which can be understood in terms of the Friedel oscillations and that the charge density at the surface atoms become less directional and more s-like.

The local density of states (LDOS) curves[104] are presented in Fig. 42. The first layer corresponds to the surface layer; the fifth layer at the center of the slab. As stated in section (a), fifteen $\underline{k}$-points in the irreducible part of the 2DBZ were used to calculate the LDOS. In addition, to ascertain the surface features, a difference curve obtained by subtracting the LDOS at the center of the slab from the LDOS at the surface is present in Fig. 43.

Away from the surface in layer 5, the LDOS strongly resembles the bulk Nb spectrum given in Fig. 17; slight differences arise because of the use of a smaller number of $\underline{k}$-points and also because of some influence of the surfaces. The observed changes at the surface layer

are mostly due to surface states and partly due to distortions of the bulk-state wavefunctions at the surface. (In this section we shall make no distinction between bona fide surface states and strong surface resonances.) Narrowing of the rms width of the LDOS is observed for the surface layer. The regions A, B, C and D shown in Figs. 42 and 43 indicate the regions where some of the prominent surface bands are found.

The increase in the density of states at the surface layer in the energy range of 0 to 2 eV arises mainly from the contributions of three surface bands (T1, T2 and T3). These three surface bands occur in the absolute energy gap G1 located just above the Fermi level in the two-dimensional projected band structure (PBS). As seen from Fig. 40 the G1 gap encompasses nearly 70% of the irreducible zone extending from $\bar{M}$ to over 2/3 of the way to $\bar{\Gamma}$ along the $\bar{\Sigma}$ direction and similarly to nearly touching $\bar{X}$ along the $\bar{Y}$ direction. The existence of these surface bands in the above gap is not very sensitive to the potential used. Their dispersion is ~ 2.5 eV for two of the bands (T2 and T3) and ~ 0.4 for the other (T1). The increase in the density of states at the surface layer in the energy region D, on the other hand, arises from occupied surface states in the smaller gap G2.

Figure 44 shows the various calculated surface bands along the high symmetry lines together with the PBS. Also indicated in Fig. 44 are some of the symmetry gaps along the symmetry lines. (Symmetry gaps are gaps at high symmetry points or along symmetry lines in the PBS in which bulk states of a given symmetry are forbidden but where states of other symmetry may exist.) In Fig. 44 vertical crosshatching is used

to show the extend of bulk states with $\bar{\Delta}_1$, $\bar{Y}_{1,2}$ and $\bar{\Sigma}_1$ symmetry; horizontal crosshatching is used to show the extent of bulk states with $\bar{\Delta}_2$ and $\bar{\Sigma}_2$ symmetry; and the dash curves are the surface (bona-fide or strong resonance) bands.

Let us first discuss the surface states in the G1 gap. There are four surface bands in this gap. Three of them are the T1, T2 and T3 surface bands. As discussed earlier the T1 band is very flat in $\underline{k}$-space, where as the T_2 and T_3 bands are relatively dispersive. The extent of these states encompasses a large fraction of $\underline{k}$-space. The fourth band of surface states is found at ~ 3.0 eV in a small region near $\bar{M}$.

The T2 and T3 surface states yield similar charge distributions. These two bands follow each other closely in $\underline{k}$-space with a typical energy separation of ~0.5 eV which vanishes near $\bar{M}$. The character[133] of the two bands is for the most part $d_{zx,zy}$ with admixtures of d_{xy} and $d_{x^2-y^2}$ depending on the value of $\underline{k}$. For example along $\bar{\Sigma}$ the T2 band is of $\bar{\Sigma}_1$ symmetry (see Table IX). Its character is therefore mainly of $d_{z(x+y)}$ with admixture of d_{xy}. The T3 band along this direction is however of $\bar{\Sigma}_2$ symmetry and its character is therefore mostly of $d_{z(x-y)}$ with admixture of $d_{x^2-y^2}$. At the point $\bar{M}$ the two bands merge to a two-fold degenerate state with mainly $d_{zx,zy}$ character. The band T1, on the other hand, is almost solely of $d_{3z^2-r^2}$ character throughout $\underline{k}$-space. Finally the upper, fourth band existed only near $\bar{M}$ is mostly of $d_{x^2-y^2}$ character. In terms of spectral weights, the

T2 and T3 states are mainly concentrated in energy regions B and C whereas the T1 states are concentrated in region A.

A natural, but perhaps over-simplified interpretation of the above surface bands is that the T2 and T3 surface states are states principally derived from the two bonding orbitals d_{zx} and d_{zy} of the surface atoms which are broken by the formation of the surface. They split off as two surface bands into the above discussed band gap from the bonding and anti-bonding part of the spectrum. Similarly the T1 surface states are $d_{3z^2-r^2}$ orbitals which split off from the anti-bonding part of the spectrum and move down into the band gap to form one surface band.

There are other surface states near the Fermi level. For example, at $\bar{\Gamma}$, a surface state of $d_{3z^2-r^2}$ character is found in a $\bar{\Gamma}_1$ symmetry gap at 0.2 eV. Also found near E_F is an unoccupied surface band in a $\bar{\Delta}_1$ symmetry gap in the PBS along the $\bar{\Delta}$ direction and, just below this Δ_1 gap, an occupied band of strong surface resonances. The two bands merge and become weak surface resonances at $\bar{\Gamma}$. Since the state at $\bar{\Gamma}$ and those in the above two bands are well defined surface states only at their respective symmetry points, they do not contribute much to the LDOS.

In Fig. 45, the charge densities of the states in regions A, B and C are presented. These include both bulk and surface states. We note that the charge for all three regions are highly localized on the first layer indicating that these regions are essentially composed of surface states. Since T1 states are dominant in region A, the charge density plot for this region (Fig. 45(a)) shows a strong charge

lobe protruding out into the vacuum region along the z-direction perpendicular to the (001) surface. Although it cannot be seen from the plot, the charge density is completely symmetric about the z-axis giving the charge distribution a striking $d_{3z^2-r^2}$ character. In contrast, the charge densities for regions B and C have their maxima protruding out into the vacuum region at a 45° angle with respect to the normal; they are nearly symmetric with respect to the z-axis. Therefore they are mostly of $d_{zx,zy}$ character with some admixture of d_{xy} and $d_{x^2-y^2}$ character. From Fig. 45, one can also see the reason for the rather large dispersion for the T2 and T3 states. The charge densities for these states overlap quite strongly between neighboring surface atoms where as there are virtually no overlap of charges for the T1 states.

Other prominent surface states found are two occupied surface bands in the energy region D. Similar to the T1, T2 and T3 states, they appear in an absolute gap, the G2 gap, in the PBS (Fig. 44). But, unlike the former states, they are not dangling-bond-like. The $\underline{k}$-space extension of this lower gap (Fig. 40) consists of a strip extending from midway along the $\bar{\Sigma}$ line to the point $\bar{X}$. The surface charge distributions for the states in the upper band T4 are primarily d_{xy}-like, whereas the states in the lower band T5 are primarily $d_{x^2-y^2}$-like. However, the charge distributions for these states do change significantly over different parts of $\underline{k}$-space. In some regions charge is shifted from the first layer to the second layer.

To illustrate some of the characteristics of the individual surface states, we have plotted the charge density distributions for the five surface states at the point $\underline{k} = (3/8,1/4)\ 2\pi/a_c$. This $\underline{k}$-point was chosen for the reasons that all five surface bands T1-T5 extend to this point and that it is a general point in the 2DBZ. Figure 46 shows the charge density distribution for the T1 state at E = 1.6 eV. The charge distribution on the surface atom is $d_{3z^2-r^2}$-like and has virtually no overlap with the charge from nearby surface atoms. Figure 47 shows the charge density distribution for the T2 state at E = 0.8 eV. Comparing the charge distribution on the (110) plane (Fig. 47(a)) with that on the (100) plane (Fig. 47(b)), we see that the charge distribution on the surface atom is of $d_{zx,zy}$ character with an admixture of d_{xy} character. Overlap of charges along the (010) direction is considerable which is consistent with the large dispersion of the T2 band. Figure 48 shows the charge density distribution for the T3 state at E = 0.4 eV. The charge distribution is again $d_{zx,zy}$-like. But unlike the T2 state, it has an admixture of $d_{x^2-y^2}$ charge distribution. Again the overlap of charges along the (010) direction is appreciable. Figure 49 shows the charge density distribution for the occupied T4 state at E = -1.7 eV. The charge density for this state is not as highly localized on the surface atoms as the states in the G1 gap. The charge extends into the second layer and is mostly of d_{xy}-character with a small admixture of $d_{xz,zy}$ character. Finally, the charge density distribution for the state T5 at E = -2.0 eV is presented in Fig. 50. The charge is localized on the second-layer atoms, but extends quite far into the slab.

Analysis of the T5 band show that this band changes character as it move towards to point $\bar{X}$. At $\bar{X}$ the charge density distribution is $d_{x^2-y^2}$-like and localized on the outermost Nb atoms.

c. Summary and Conclusions. In summary we have calculated the electronic structure of the (001) ideal surface of niobium using a self-consistent pseudopotential method. Surface states are identified and analyzed throughout the two-dimensional Brillouin zone. When compared to the semiconductor surface states, the surface states on the Nb(001) surface are much more complex both in their extent in k-space and in their charge density distributions.

Our results also show that most prominent surface bands appear in gaps of the PBS which are located well away from the zone center. Since we do not expect the positions of the gaps in the PBS for the (001) surface of most transition metals to change by much, this situation will likely to occur on other transition metal surfaces and therefore it is not adequate to analyze the surface properties of transition metals by just examining the $\bar{\Gamma}$ point.

Finally, to our knowledge there is no published experimental data on the (001) surface of Nb; measurements[134,135] have been done on the (001) surfaces of Mo and W. A rigid-band interpretation of our results can be made for Mo and W provided that screening at the surface does not significantly alter the energies of the surface states. We also note that spin-orbit interactions are not necessary for the existence of the surface states discussed.[136]

IV. METAL-SEMICONDUCTOR INTERFACE

In this section we study the electronic structure of metal-semiconductor interfaces.

Experimentally the behavior of the Schottky barrier height ϕ_b for metal-semiconductor (m/s) interfaces as a function of the metal electronegativity is found to be dramatically different depending on whether the semiconductor is covalent or ionic.[137] For covalent semiconductors ϕ_b is approximately constant for all metals, whereas for ionic semiconductors, ϕ_b is strongly dependent on the metal contact. Furthermore the transition from covalent behavior to ionic behavior appears to be a rather sharp transition which occurs at a critical ionicity.

While there have been a number of theories and speculations[109,138-141] and various mechanisms have been proposed to explain these properties of the barriers, a definitive explanation has yet to emerge because of the lack of detailed information on the microscopic nature of m/s interfaces. A necessary step toward understanding the properties of Schottky barriers should therefore involve a systematic study of the electronic structure of a series of m/s interfaces as a function of increasing semiconductor ionicity. Our present work is motivated by these considerations.

The interfaces studied in this section are interfaces of Al (modeled by a jellium core potential with $r_s = 2.07$) in contact with the ideal (111) surface of Si and the ideal (110) surfaces of GaAs,

ZnSe and ZnS. We find that, within the jellium-semiconductor model, the electronic structure of the four interfaces under investigation is qualitatively similar. Moreover we find that the experimentally observed variation in ϕ_b for different metals in contact with semiconductors of different ionicity can be understood quantitatively in terms of a simple model involving metal-induced states in the semiconductor band gap.

The remainder of the section is organized as follows: In Section A the methods of calculation and the electronic structure of the metal-Si interface are discussed in some detail. In Section B the results for the electronic structure of the metal-zincblende semiconductor interfaces are presented. In Section C the ionicity-dependent behavior of the Schottky barrier height is examined. And in the final Section D some discussion and conclusions are presented.

A. Al/Si Interface

In this section we present self-consistent pseudopotential calculations on the electronic structure of a metal-Si interface. The calculations model an Al-Si interface with a jellium potential representing the aluminum ion potential in contact with the Si (111) surface. This model describes an ideal or intimate interface, i.e. there is no oxide layer between the two materials. A local density of states (LDOS) which displays the density of states as a function of distance away from the interface has been calculated for this Al-Si junction. Various states which exist near the interface are identified and discussed in terms of the LDOS and their charge densities. Our

calculated interface barrier height is found to be in excellent agreement with recent experimental results.[142] To our knowledge, this is the first realistic self-consistent calculation for a metal-semiconductor interface.

Metal-semiconductor interfaces are of great importance because of their rectifying properties which are crucial to the operation of many electronic devices. Much experimental efforts have been devoted to the study of their properties. With the advent of recent ultra-high vacuum techniques, ideal interfaces can now be fabricated and studied systematically,[142-146] and the detailed electronic structure at the interface can be probed using modern photoemission techniques.[144-146] On the theoretical side, metal-semiconductor interfaces have been the subject of much discussions and speculations.[109,138-141,147-149] Many models have been proposed to explain the interface properties. However, regretably, past theoretical investigations into their electronic structure have been mostly qualitative or semi-quantitative. A clear picture of the electronic structure at a metal-semiconductor interface has yet to emerge.

Experimentally, the electrical barrier height ϕ_B (Schottky barrier) at a metal-semiconductor interface can be accurately determined using many different methods (I-V, C-V, photoelectric, etc.). To avoid confusion over n- and p-type semiconductors, we measure here the barrier height from the Fermi level E_F to the semiconductor conduction band. For covalent semiconductors such as Si and Ge, the barrier height is found to be virtually independent of the metal contact and

of the doping in the semiconductor.[137,142,149] Bardeen[109] attributed this behavior of the barrier height to a high density of surface states in the semiconductor band gap; i.e. the filling or emptying of these surface states pins the Fermi level to a nearly constant value. Heine,[138] on the other hand, pointed out that semiconductor surface states cannot exist in the semiconductor gap if this energy range is inside the metallic band. He suggested that the pinning of the Fermi level is due to states of a different type in the semiconductor gap. These states are composed of the states from the tails of the metallic wavefunctions decaying into the semiconductor side.

Theories[139,141] which do not explicitly involve extra states in the semiconductor gap have also been proposed to explain the barrier height behavior. Inkson,[139] using a model dielectric function formulation, proposed that the pinning of the Fermi level is due to the narrowing of the semicondcutor gap at the interface. According to Inkson, the screening of the valence and conduction bands of the semiconductor is different near the interface. This causes the valence band to bend up and the conduction band to bend down and eventually the bands merge together at the interface for a covalent semiconductor. In addition, Phillips[141] claimed that polarizability effects play the dominant role at the metal-semiconductor interface. He suggested that it is the elementary excitations and chemical bonding at the interface which determine the behavior of the Schottky barrier.

The purpose of the present work is to study the electronic structure of a metal-covalent semiconductor interface in detail using

the Al-Si junction as a prototype and to gain some insights into the nature of metal-semiconductor Schottky barriers. The model and methods of calculation present here can be applied to general metal-semiconductor contacts. The main features of this calculation which are absent in previous work are (1) a realistic interface is constructed through a jellium-semiconductor model and (2) the calculation is self-consistent. It is noted that, as in all previously existing self-consistent surface calculations, self-consistency in the present context means self-consistency in the electronic responses to a given structural model.

In the remainder of this section we shall first discuss in section 1 in some detail the model for the interface and the steps in the self-consistent calculations. In section 2 the results for the electronic structure of the Al-Si interface are presented. And in the final section 3 some discussion and conclusions are presented.

1. Calculations

Our model for an ideal metal-semiconductor interface consists of jellium in contact with a semiconductor described in the pseudopotential formalism. Present experimental and theoretical methods do not allow a detailed determination of the geometry at the metal-semiconductor interface; however, we believe that the important properties of the interface are dominated by the properties of the free electrons residing next to the semiconductor surface. The present model is expected to contain all of the essential features of a metal-semiconductor interface.

The method we have employed to calculate the electronic structure of the Al-Si interface is similar to the method which we have used in Sec. III for the surface calculations. The main difficulties in calculating the electronic structure of solid interfaces are:

(1) Periodicity along the direction perpendicular to the interface is absent. Therefore the established methods for bulk calculations which depend on the periodicity of crystalline solid cannot be used.

(2) Self-consistency is essential in obtaining realistic solutions. It is necessary to allow the electrons to react to the boundary conditions imposed by the interface and the resulting readjustment and screening is a fundamental part of the problem.

The essence of our method is to retain (artificial) periodicity perpendicular to the interface and thus allow the use of well established tools in pseudopotential crystal calculations to calculate the interface electronic structure. In addition, the method goes beyond the usual pseudopotential approach through the requirement of self-consistency.

For the present calculation, we consider a unit cell consisting of a slab of Si with the (111) surfaces exposed to a jellium of Al density on both sides. This cell is then repeated and the electronic structure of the system is calculated self-consistently. The basic idea consists of considering periodic interfaces which are separated by large distances, and then obtaining the essential features of a single interface by calculating the electronic structure of this periodic system. The unit cell used consists of 12 layers of Si plus an equivalent distance of jellium. It is spanned in two dimensions by the

shortest lattice vectors parallel to the Si (111) surface i.e. hexagonal lattice vectors with the length of 7.26 a.u. and by a long c-axis of length c = 71.1 a.u. The volume of the cell is equal to 3241 $(a.u.)^3$.

With the above geometry, the jellium edge is one-half of a Si-Si bond length away from the atoms on the Si (111) surface. This is a physically reasonable choice since the length of a Al-Si bond is approximately the same as a Si-Si bond. To simulate non-interacting interfaces, the Si and the Al slab sizes have to be chosen such that (a) the bulk properties of the materials are adequately reproduced and (b) the surfaces from opposite side of the same slab do not interact appreciably. Calculations on the Si (111) surface[94] and various test calcualtions on jellium slabs of Al density showed that the assumed slab thickness which is equivalent to 12 layers of Si satisfies the above requirements well.

The electronic structure of this "periodic" system can now be solved in a self-consistent manner using pseudopotentials. The steps leading to a self-consistent solution are shown in Fig. 23. We expand the electron wavefunctions in plane waves with reciprocal lattice vectors, $\underline{G}$:

$$\psi_{n\underline{k}}(\underline{r}) = \sum_{\underline{G}} a_{\underline{k}}{}^{n}(\underline{G}) e^{i(\underline{k}+\underline{G})\cdot\underline{r}} \quad . \tag{66}$$

This leads to a matrix eigenvalue equation of the usual kind

$$\sum_{\underline{G}'} (H_{\underline{G},\underline{G}'} - E\delta_{\underline{G},\underline{G}'}) a_{\underline{k}}(\underline{G}') = 0 \tag{67}$$

which is solved by standard methods.[1] Here, the Hamiltonian matrix elements are of the form

$$H_{\underline{G},\underline{G}'} = \frac{\hbar^2}{2m} |\underline{k}+\underline{G}|^2 \delta_{\underline{G},\underline{G}'} + V_{ps}(\underline{G},\underline{G}') \tag{68}$$

where $V_{ps}(\underline{G},\underline{G}')$ are the pseudopotential matrix elements. In general the pseudopotentials are non-local and energy dependent.[1] However, for bulk Si and Si surfaces, local pseudopotentials are known to yield satisfactory results. Therefore local pseudopotentials will be used throughout for the present calculation.

The self-consistent cycle is initiated by the following potential

$$V_{start}(\underline{G}) = S(\underline{G}) V^{Si}_{emp}(|\underline{G}|) + V^{Al}_{start}(\underline{G}) \ . \tag{69}$$

The first term is the starting potential for the Si slab and the second term is the starting potential for the Al slab. The Si structure factor

$$S(\underline{G}) = \frac{1}{M} \sum_{\tau_i}^{M} e^{-i\underline{G}\cdot\underline{\tau}_i} \tag{70}$$

describes the positions of the Si atoms in the unit cell. $V^{Si}_{emp}(|\underline{G}|)$ are Si atomic pseudopotential form factors derived from empirical bulk calculations.[47] Since empirical form factors are only known for discrete $\underline{G}$ vectors and the $\underline{G}$ vectors are different for different crystal structures, a continuous extrapolation is performed to obtain the form factors corresponding to the new $\underline{G}$ vectors in the interface problem. We fitted a curve of the form

$$V(q) = \frac{a_1(q^2-a_2)}{\exp[a_3(q^2-a_4)]+1} \qquad (71)$$

to the 3 form factors for bulk Si V(111) = -0.2241 Ry, V(200) = 0.0551 Ry, V(311) = 0.0724 Ry and renormalized it for the different unit cell volume. The four parameters a_i in Eq. (71) are given in Table X. The potential is normalized to an atomic volume of 270 $(a.u.)^3$ and the units are in Ry if q is entered in a.u.

A starting potential for the Al slab is less obvious. We assumed that in zeroth order, the Al electronic charge is uniform and confined completely inside the Al slab. Then the Hartree part of the electron screening will cancel the positive jellium background and the starting potential for the Al slab can be taken to contain only an exchange term

$$V^{Al}_{start}(\underline{G}) = -\alpha\left(\frac{3}{2\pi}\right)(3\pi^2)^{1/3}\, e^2\, \rho^{1/3}_{jel}(\underline{G}) \qquad (72)$$

where $\alpha = 0.79$ and $\rho^{1/3}_{jel}(\underline{G})$ are the Fourier components of the jellium density to the one-third power. Here we have replaced the non-local Hartree-Fock exchange potential, $V_x(r,r')$, by the statistical exchange model of Slater.[90,150] The choice of $\alpha = 0.79$ will be discussed later. In principle, for a self-consistent calculation, the starting potentials should be unimportant. However, in practice, a good starting potential reduces the number of iterations needed enormously.

From Eq. (67) we obtain the band structure $E_n(\underline{k})$ and the pseudo-wavefunctions $\psi_{n\underline{k}}(\underline{r})$. To perform the next step in the self-consistent

loop, the total valence charge density

$$\rho(\underline{r}) = 2 \sum_{n} \sum_{\underline{k}} \psi^{*}_{n\underline{k}}(\underline{r})\psi_{n\underline{k}}(\underline{r}) \qquad (73)$$
$$E_n(\underline{k}) \leq E_F$$

has to be accurately determined. This requires good convergence in the electron wavefunctions and a precise location of the Fermi level. To assure good convergence, the electronic wavefunction were expanded in a basis set consisted of approximately 270 plane waves. This expansion corresponds to a kinetic energy cutoff[1] $E_1 = |\underline{G}_{max}|^2 \approx 2.7$ Ry. In addition, another 300 plane waves were included via Löwdin's perturbation scheme.[1] The total valence charge density was evaluated at 21 $\underline{k}$-points in the irreducible part (1/12) of the two-dimensional hexagonal Brillouin zone with the Fermi level determined by demanding charge neutrality in the unit cell. That is, the Fermi level is determined by filling the eigen levels in the Brillouin zone until the number of occupied levels correspond to the number of electrons in the unit cell required by charge neutrality.

We note that, for our "periodic" system, we should in principle evaluate the total charge over the whole 3-dimensional Brillouin zone. However, for a large elongated cell as in the present case, the energies and wavefunctions are quite independent of the $\underline{k}$-vectors along the c-direction. As we shall see later, the final charge density away from the interface is in good accord with bulk calculations thus indicating that our sampling in $\underline{k}$-space is sufficiently fine and the

wavefunctions are converged.

Once the valence charge density $\rho(\underline{r})$ is known in terms of its Fourier components $\rho(\underline{G})$, the Hartree-Fock type screening potentials V_H and V_x can be evaluated easily. V_H, the so-called Hartree screening potential, is the repulsive Coulomb potential seen by an electron and is generated by all the valence electrons. It is related to the valence charge density by Poisson's equation

$$\nabla^2 V_H(\underline{r}) = -4\pi e^2 \rho(\underline{r}) \tag{74}$$

and can be written as a Fourier series

$$V_H(\underline{r}) = \sum_{\underline{G}} V_H(\underline{G}) e^{i\underline{G}\cdot\underline{r}} \tag{75}$$

with

$$V_H(\underline{G}) = \frac{4\pi e^2 \rho(\underline{G})}{|\underline{G}|^2} \quad . \tag{76}$$

Physically overall charge neutrality in the solid requires that $V_H(\underline{G}=0) = -V_{ion}(\underline{G}=0)$ where V_{ion} is the ionic potential generated by the positive Si^{+4} ion cores and by the positive jellium slab. Therefore, for the present calculations, we can arbitrarily set $V_H(\underline{G}=0) = V_{ion}(\underline{G}=0) = 0$. Numerically, however, the divergent character of $V_H(\underline{G})$ and $V_{ion}(\underline{G})$ for small $\underline{G}$-values causes some problem with the stability of the self-consistency process. This is discussed in detail in Ref. 94. The Hartree-Fock exchange potential was approximated using the Slater exchange model, as we have done for the Al starting potential. In $\underline{G}$-space, the exchange potential then has the form

$$V_x(\underline{G}) = -\alpha\left(\frac{3}{2\pi}\right)(3\pi^2)^{1/3}e^2\rho^{1/3}(\underline{G}) \tag{77}$$

where $\alpha = 0.79$ and $\rho^{1/3}(\underline{G})$ are Fourier components of $\rho^{1/3}(\underline{r})$. The justification for the present value for α is that this choice of α will bring Slater's exchange in an approximate agreement with Wigner's[151] interpolation formula at the average valence charge density of Al and Si. Thus, from the total charge density, the electronic screening potential

$$V_{SCR}(\underline{r}) = \sum_{\underline{G}} (V_H(\underline{G}) + V_x(\underline{G}))e^{i\underline{G}\cdot\underline{r}} \tag{78}$$

is obtained at each iteration in the self-consistent loop.

After the screening potential is determined, the self-consistent process is continued by adding V_{SCR} to an ionic potential V_{ion} to form a potential for the next iteration. The ionic potential consists of two terms

$$V_{ion}(\underline{G}) = S(\underline{G})V_{ion}^{Si}(\underline{G}) + V_{ion}^{Al}(\underline{G}) \tag{79}$$

where the first term is generated by the Si^{+4} ionic cores and the second term is generated by the Al slab. $S(\underline{G})$ is the Si structure factor as defined in Eq. (70).

First let us discuss V_{ion}^{Al}. This is just the Coulombic potential generated by repeated slabs of uniform positive charge. For an origin at the center of a metallic slab, V_{ion}^{Al} has the form

$$V_{ion}^{Al}(\underline{G}) = \frac{-8\pi e^2 n_+ \sin G_z a/2}{C\,G_z^3}\,\delta_{G_x 0}\,\delta_{G_y 0} \tag{80}$$

where a is the width of the jellium slab, C is the length of the unit cell along the direction (z) perpendicular to the interface and n_+ is the positive background density.

For the Si ion core potential, we have used an atomic model potential which was fitted to atomic term values by Abarenkov and Heine.[96] The repulsive cores of the ionic model potentials as given by Abarenkov and Heine are nonlocal (i.e. ℓ-dependent). For the present calculation, a local, "on the Fermi sphere" approximation[1] has been made and the Fourier transform of the resulting local potential was fitted to a 4-parameter curve

$$V_{ion}^{Si}(q) = \frac{b_1}{q^2}\left[\cos(b_2 q) + b_3\right]\exp(b_4 q^4) \quad . \tag{81}$$

The values of the b_i's are given in Table X. The normalization and the units for Eq. (81) are the same as those for Eq. (71). Using the parameters given in Table X, this ionic core potential has proven to yield excellent results in bulk and surface self-consistent calculations.[94]

With the above V_{ion}, the first two cycles of the self-consistent loop were performed using

$$V_{IN}^{(1)}(r) = V_{start}(r)$$

$$V_{IN}^{(2)}(r) = V_{ion}(r) + V_{SCR}^{(1)}(r) \quad . \tag{82}$$

However, due to the divergent character of V_H and V_{ion} mentioned earlier, an input potential V_{IN} which deviates from the truly

self-consistent potential will lead to an output potential which "overshoots" and is further away from the true potential. Therefore further iterations based on a straightforward extension of Eq. (82) would not yield a converging potential. This unstable behavior of the screening potential especially for very small $\underline{G}$-vectors is commonly found in surface calculations.[94,118,120] The procedure to deal with these instabilities is to compute adjusted input potentials $V_{IN}^{(n)}(\underline{G})$ for $n > 2$ from preceding input and output potentials. This can be done by obtaining the input potential of the nth iteration from a linear combination of input and output potentials of the (n-1)th iteration or from inspecting V_{OUT} versus V_{IN} graphs separately for each small $\underline{G}$. A detailed discussion of this problem and the procedures to overcome it are given in Ref. 94. The criterion for self-consistency is now the stability of the adjusted input screening potential as compared to the output screening potential calculated from Eq. (78). In the present calculation, the final self-consistent potential is stable to within 0.01 Ry.

After self-consistency has been reached, the electronic structure of the interface can then be analyzed in terms of charge densities. For this purpose, charge densities have been calculated as a function of different energy intervals and different $\underline{k}$-points in the Brillouin zone. In addition, we performed a local density of states (LDOS) calculation for the Al-Si interface. This LDOS which displays the density of states in real space, facilitates the identification and illustrates the characteristics of the various kinds of states at the

interface. Analogous to the projected density of states in tight binding calculations, the LDOS for a given region in real space is given by

$$N_i(E) = \sum_{k_\parallel, n} \int_{\Omega_i} |\psi_{k_\parallel, n}(\underline{r})|^2 \, d^3\underline{r} \, \delta[E - E_n(k_\parallel)] \tag{83}$$

where $k_\parallel$ is the wavevector parallel to the interface, n is the band index, $\psi_{k_\parallel, n}$ is the electronic wavefunction and Ω_i is the volume of the chosen region. Physically $N_i(E)$ can be interpreted as the probability that an electron with energy, E, is found in the region i.

2. Results

In this section our results for the Al-Si interface are discussed. We find that four different types of states can exist near the Al-Si interface. Aside from the usual states which are bulk-like in both materials, there are states with energy below the Al conduction band which are bulk-like in the Si side but decay rapidly in the Al side. Also, in the two-dimensional Brillouin zone, we find extra metal induced gap states (MIGS) in the semiconductor energy gaps whenever the range of the gap is inside the metallic band. They are somewhat similar to the states suggested by Heine, i.e. they are bulk-like in Al and decay rapidly in Si. However, at the Si surface, these MIGS retain the characteristics of the "free-surface" Si surface states which existed in the absence of the metal. It is these states which pin the Fermi level and dominate the properties of the Al-Si junction. In addition, we find truly localized interface states which decay in both directions away from the interface. These appear in the Si energy gaps in the energy range below the Al conduction band.

First let us examine the total, self-consistent valence charge density. The total charge density is a good indicator of the quality of the present work. For the present calculations to adequately represent non-interacting interfaces, the charge densities away from the interface should resemble the bulk densities of the two materials. Figure 51 displays the total valence charge density in a (110) plane along with the function $\bar{\rho}_{total}(z)$ which is the total charge density averaged parallel to the interface with z being the direction perpendicular to the interface. For the purpose of discussing the charge densities and the local density of states, we have also divided the unit cell into 12 equal regions (slices) as shown partially in Fig. 51(b). The jellium edge is indicated by the double dashed line. Only the charge within a few angstroms from the interface is significantly perturbed from the bulk values. The charge densities in region I and II and regions V and VI are in good accord with bulk densities.[47,152] The slight differences between the present Si charges away from the interface and those calculated in Refs. 47 and 152 are due to the difference in the cutoff energy E_1.

From Fig. 51(b) one sees the well known Fridel oscillations in the Al charge density and there is a net transfer of charge from aluminum to silicon. On the Al side, regions I and II each contain 7.9% of the total charge in the unit cell where as region III contains only 7.6%. On the Si side, regions V and VI each contain 8.8% of the total charge but region IV contains 9.1%. Thus approximately 0.3% of the total charge in the unit cell has been transferred from region III

to region IV. A dipole potential with an electric field pointing toward the Si side is hence set up at the interface. This is a consequence of equalizing the Fermi levels in the two materials. As seen from Fig. 51(a), the Al charge is spilling into the empty "channels" in the Si charge density and into the dangling bond sites. The charge density at the dangling bond sites in the present case is significantly higher than a sum of the jellium electron charge density and the Si charge density from the free surface calculations. This indicates the formation of a metallic-covalent like bond between Si and a jellium of Al density.

Figure 52 displays the self-consistent pseudopotential V_{sc} in a (110) plane along with $\bar{V}_{sc}(z)$ which is V_{sc} averaged parallel to the interface. The total charge density discussed earlier is the self-consistent response to this potential. The potential on the Al side is flat and does not show pronounced Fridel oscillations. Similar behaviors have been found in self-consistent calculations on the Al surface using the jellium model.[118] In the course of self-consistency, the Si potentials on the first two layers are made slightly deeper than the Si potentials further away from the interface. As expected, the perturbation to the Si potentials due to the presence of the metal appears to be much less than the perturbation due to the free surface.[94]

Now let us discuss the local density of states (LDOS) as defined in Eq. (83). We have calculated the LDOS for the six regions indicated in Fig. 51 by using twenty-one points in the irreducible part of the two-dimensional zone. The histograms of the LDOS for the six regions

are shown in Fig. 53. To facilitate comparisons, the density of states of bulk Si from Ref. 47 is superimposed on the LDOS of regions IV to VI and a free electron density of states (i.e. $N(E) \sim \sqrt{E}$) is superimposed on the LDOS of regions I to III. The Fermi level is indicated by the dashed line. Most of the interesting features appear in the LDOS of region IV. To investigate the energy positions of the extra states and their origins, we subtracted the LDOS of region VI from the LDOS of region IV to obtain a difference local density of states (DLDOS). The result is presented in Fig. 54. The positive portion of the histogram indicates an addition of states in that particular energy range in region IV and the negative portion of the histogram shows a depreciation of states.

The LDOS reveals much information about the electronic structure of the interface. From the position of the Fermi level and the position of the conduction band edge of the semiconductor, one can calculate the barrier height at the interface. We obtained a barrier height of 0.6 ± 0.1 eV for the Al-Si interface which is in excellent agreement with the recent experimental result of 0.61 eV. There are other experimental values for the Al-Si barrier height ranging from ~0.55 eV to ~0.70 eV. (See for example Ref. 149) However, we believe that the value from Ref. 142 is the best for an ideal Al-Si interface because of the ultra-high vacuum conditions used in this particular experiment.

The various types of states which appear near the interface can be seen from the LDOS. States with energy below -11.1 eV (i.e. below

the onset of the Al conduction band) are bulk-like in Si and do not penetrate into the bulk of Al. Of course there are states with higher energy which can behave similarly. For example, at the $\underline{k}$-point K, states with energy up to -6.5 eV are below the Al conduction band. To illustrate this type of states, the charge density for all states with energy below -11.5 eV is presented in Fig. 55. On the Si side, the charge density contours strongly resemble the charge density contours for the bottom band of bulk Si[47] whereas the charge on the Al side is completely zero. The slightly higher charge density at the first two layers is most likely due to Friedel oscillations.

From the LDOS of region IV (Fig. 53) or the DLDOS (Fig. 54), we see that the dips in the bulk Si density of states which are due to gaps in the Si band structure are being filled up by either interface states or MIGS at the interface. The extra states centered at ~-8.2 eV are partially interface states and partially MIGS whereas the states centered at ~-5.0 eV and states in the optical gap are MIGS.

The MIGS in the optical gap are of particular importance because the density of these states sensitively influences the position of the Fermi level with respect to the semiconductor band edges. These states have a charge density which is metallic in the Al slab, becomes dangling-bond-like at the Si surface, and decay rapidly to zero in the Si slab. The charge density for these states in the thermal gap, i.e. states with energy between 0 and 1.2 eV, is plotted in Fig. 56 along with $\bar{\rho}(z)$ which is the same charge density averaged parallel to the interface. The dangling bond surface states which exist at these

energies for the free surface case have been matched to the continuum of metallic states. Thus, as seen from Fig. 56(a), the charge is quite uniform in the Al slab but retains the dangling bond character at the Si surface. We note that the charge density displayed in Fig. 56 is for all states with energy in the thermal gap. The decaying rates are different for states at different energies. The charge for states near midgap decays most rapidly into the Si side.

An examination of the LDOS of region IV from -1.0 to 2.0 eV indicates that there is an apparent asymmetry in the distribution of extra states about the optical gap. A plausible physical explanation is the following: The states in the optical gap are derived from the valence band and the conduction band. Note the large depreciation of states near -1.8 eV and near +4.0 eV. (See Fig. 54) Since these MIGS are dangling-bond-like (i.e. p_z-like) in region IV and the top of the Si valence band is p-like whereas the bottom of the conduction band is s-like, bulk states from the top of the valence band will be "robbed" to form the MIGS while only states higher in the conduction band will be strongly affected by the formation of the MIGS. Therefore the depreciation of bulk state densities will be larger at the top of the Si valence band than at the bottom of the conduction band. This results in the apparent asymmetry.

The interface states centered at -8.5 eV, labelled S_K in Fig. 53, appear near the point K in the two-dimensional hexagonal Brillouin zone. At first sight, localized states should not appear because there are aluminum states in this energy range. This appearance of interface

states is a band structure effect. Near the point K in $\underline{k}$-space, the Si two-dimensional band structure has a gap between -7.2 eV and -9.5 eV which is below the Al conduction band. In Fig. 57 we show a schematic diagram of the projected band structure of the bottom two bands of Si together with the projected band structure of Al. The Fermi levels of the two materials have been set equal. The lowest gap at K is the gap that we are discussing. Silicon surface states existing in this gap cannot be matched with any Al states because there are no Al states with the same energies and $\underline{k}$-vectors. A contour map of the charge density of the interface states at K at -8.5 eV is shown in Fig. 58. The charge density is s-like and highly localized on the outermost Si atoms. The charge is almost completely confined in region IV. Similar states with the same energy and character have been found in Si surface calculations. However the charge for states found in surface calculations are less localized.

3. Summary and Discussions

We have studied the electronic structure of a metal-covalent semiconductor interface using an Al-Si system as a prototype. A jellium-semiconductor model has been constructed for the Al-Si interface. The electronic structure of the interface was then calculated using a method involving self-consistent pseudopotentials. The model and methods of calculation used in the present section have wider application than just the Al-Si system; these techniques can be extended straightforwardly to calculate the electronic structure of other metal-semiconductor interfaces.

Four different types of states are found to exist near the interface. The characteristics of these states have been analyzed in details in terms of their charge densities. Our local density of states results indicate a high density of MIGS in the Si thermal gap near the Al-Si interface. This implies a pinning of the Fermi level by these MIGS which is consistent with experimental results. It is important to note that, in the present calculation, we have used a statistical exchange model for the exchange potential. Hence both the valence bands and conduction bands see the same screening potential. Also, from examining the structure of the local density of states, there does not seem to be a merging of the valence band with the conduction band near the interface. Therefore, the pinning of the Fermi level can be explained without invoking Inkson's argument of merging of the bands due to difference in the screening of the valence band and the conduction band at the interface. Furthermore, it is not very meaningful to talk about a band picture as a function of distance away from the interface on such a microscopic scale.

The present calculation is for a high density metal, Al, in contact with Si. For metals with a low density of s-p electrons, interface states can coexist with MIGS in the energy range of the Si optical gap such as in the -7.2 to -9.5 eV gap in the present calculation. Under such conditions, one expects that an even higher density of extra states will appear near midgap and the Fermi level is again pinned in the thermal gap. This may be an explanation of why surface states continue to exist in the GaAs gap when an overlayer of Cs[145,146]

or Pd[144] is placed on GaAs. Both Cs and Pd are metals of low s-p electron densities.

B. Metal-Zincblende Semiconductor Interfaces

In this section we extend the analysis in Sec. IVA to the metal-zincblende semiconductor interfaces. The interfaces studied are interfaces of Al (modeled by a jellium core potential) in contact with the ideal (110) surfaces of GaAs, ZnSe and ZnS.

1. Calculations

As in Sec. IVA we are considering intimate m/s interfaces and approximate the system by replacing the metal with a jellium model and describing the semiconductor in the pseudopotential formalism. Since the methods of calculation have discussed at length in Sec. IVA, we shall only briefly describe some of the essential features of the method and will be mainly concerned with the parameters needed in the calculations.

The calculations were carried out by constructing an elongated unit cell which, in two dimensions, is spanned by the shortest lattice vectors parallel to the appropriate semiconductor surface and, in the third dimension, by a long c axis extending over M atomic layers of the semiconductor and N layers of equivalent thickness of jellium metal. (Here the thickness of one layer is the interatomic distance between planes of semiconductor atoms parallel to the interface; and, the length of the c axis is therefore equal to M + N interplane distances.) The numbers used were M = 11 and N = 7 for m/GaAs and m/ZnSe and M = 11 and N = 9 for m/ZnS.

There are no adjustable parameters in the calculations. The only input consists of the structure (i.e., the geometry of the interface) and the ionic pseudopotentials of the semiconductor ion cores which are determined from atomic spectra. Since we use a jellium-semiconductor model, the structure is determined by the crystal structure of the semiconductors except for the placement of the edge of the positive jellium core. This edge has been taken to be at a distance of one-half of an interlayer distance away from the outermost semiconductor atoms. The ion core potentials V_{ion} used are local pseudopotentials whose Fourier transforms are of the form given in Eq. (81) with the parameters, b_i, fitted to a Heine-Abarenkov core potential.[104] In addition to the ionic core potentials, a starting potential is needed to initiate the self-consistent loop (Fig. 23). For this purpose we have used the empirical pseudopotentials V_{emp} obtained from bulk calculations with Fourier transforms expressed in a 4-parameter curve given by Eq. (71). The parameters b_i and a_i for the various semiconductors used in the calculations are listed in Table XI and XII respectively.

Using the same convergence criteria as in Sec IVA, a basis set of approximately 500 plane waves was employed in expanding the wavefunctions in the calculations. An additional ~1200 plane waves were also included via Lowdin's perturbation scheme.[1] The total valence charge density $\rho(\underline{r})$ needed for each iteration was determined by a five point sampling over the irreducible part of the rectangular zone. The points included the symmetry points Γ, X, X' and M and one general point in the center of the irreducible zone.[153] This set of points

yields an accurate charge density and, at the same time, allows the use of symmetrized plane waves to reduce the sizes of the Hamiltonian matrices and hence the computation time for diagonalization.

2. Results

In this section, the electronic structure of the three metal-zincblende semiconductor interfaces is presented.

We have chosen the interfaces m/Si, m/GaAs, m/ZnSe, and m/ZnS to study because the semiconductors composing this series are of the same crystal structure and of increasing ionicity. Within our model, we find that the calculated electronic structure of the four m/s interfaces is qualitatively very similar. In all four cases, as found in Sec. IVA, the intrinsic surface states which existed in the fundamental gaps of these semiconductors[104] are removed by the presence of the metal and new types of states occur in this energy range. These metal-induced gap states (MIGS) are bulk-like in the metal and decay rapidly into the semiconductor with some of the characteristics of the semiconductor-vacuum surface states (which exist in the absence of the metal) weakly retained at the semiconductor surface. In addition, truly localized interface states which have charge densities decaying in both directions away from the interface are found for energies near the lower part of the semiconductor valence band.

Before we discuss the individual states, let us examine the self-consistent, valence charge densities for the three metal-zincblende semiconductor interfaces. They are shown in Figs. 59 to 61. In each figure the total valence charge density is displayed in two different

planes containing the two types of semiconductor surface atoms. The units are normalized to one electron per unit cell. Several interesting features are seen from the figures: (1) Charge densities in the bulk configuration are essentially the same as those found in the third layer into the semiconductor showing that the significant influence of the interface is quite short range (i.e. in the order of 2 to 3 atom layers). (2) Owing to the stronger potential of the anions, charge is increasingly localized on the anions as the ionicity of the semiconductor increases. And (3), for all three interfaces, the charges on the outermost semiconductor atoms are slightly higher than the charges on the atoms deeper in the slab. This probably results from the presence of the metal which lowers the potential of the surface atoms.

In Fig. 62 the local density of states for the m/GaAs system is displayed for four regions. Each region contains one atomic layer. Region D is at the center of the semiconductor slab. Region C is the layer containing the outermost semiconductor atoms. Region B is adjacent to region C on the metallic side. The boundary between C and B defines the interface. And finally region A is at the center of the metallic slab. The LDOS was evaluated according to Eq. (83) with 5 $\underline{k}$-points in the irreducible zone to calculate the histograms.[154] The LDOS for the m/ZnSe and m/ZnS interfaces are calculated in the same manner; these are shown in Figs. 63 and 64 respectively. Although the number of $\underline{k}$-points used is too small to reproduce a nice $\sqrt{E}$ curve for the free-electron-gas density of states on the metallic side, it yields

most of the prominent features of interest. A LDOS curve of much finer quality for the m/Si interface was obtained in Sec. IVA with the use of 21 $\underline{k}$-points in the irreducible zone.

The region of most physical interest is region C whose LDOS essentially describes the energy spectrum of the electrons on the semiconductor surface. The darkly shaded areas in Figs. 62 to 64 indicate the MIGS in the semiconductor thermal gaps. Also indicated (by the lighter shaded areas) are the energies of the localized interface states. The MIGS in the thermal gaps have, as we shall show in the next section, a large influence on the Fermi level E_F and thus play a dominant role in determining the behavior of the m/s Schottky barriers.

Figure 65 displays the charge profiles $\bar{\rho}(z)/\bar{\rho}(0)$ of the penetrating tails of the MIGS in the thermal gap for the four m/s interfaces studied as a function of distance z into the semiconductor. Here $\bar{\rho}(z)$ is the charge density for the MIGS averaged over the states in the thermal gap and averaged parallel to the interface with z = 0 at the interface. We note that the overall behavior of the charge profiles for Si and GaAs is quite similar and that the average penetration distances are considerably shorter than previously believed. The differences in the short range oscillations in the charge profiles mostly arise from the difference in the atomic arrangement between the two types of semiconductor surfaces (Si (111) and GaAs (110)).

We shall only discuss and illustrate the interface states at the m/ZnS interface to avoid redundancy. The characteristics of the

interface states for the other two systems are qualitatively similar. The lowest lying interface states at the m/ZnS interface (see Fig. 64) are localized strongly on the outermost sulfur atoms and have s-like character in their charge distribution. These states split off from the bottom valence band of ZnS and form a narrow interface band extending over the whole Brillouin zone. The corresponding charge density given in Fig. 66 is extremely localized on the sulfur surface atoms with practically zero charge on the zinc atoms. A surface band, very similar to this s-like interface band, has been found in calculations on the (110) surface of zincblende semiconductors.[155] The surface states are, however, located at higher energies in the antisymmetric gap instead of at the bottom of the spectrum. These s-like interface state are therefore intrinsic to the semiconductor surface with energies shifted because of the presence of the metal.

Two additional interface bands are found at ~-5 eV below the ZnS valence band maximum. Unlike the previously discussed states, these interface states exist over a rather small region in $\underline{k}$-space at the zone edge around the point M. The charge distribution differs from the s-like state since it is p-like around the outermost sulfur atoms. The charge density for a state at M in the lower of the two interface bands is given in Fig. 67. Figure 67(a) shows the charge density contours in a $(1\bar{1}0)$ plane containing the surface Zn atoms. Figure 67(b) shows the charge density contours in a (110) plane parallel to the interface containing both types of semiconductor surface atoms. As seen from the figure, the charge is highly localized on the outermost

semiconductor layer with the maxima of the p-like lobes lying in the (110) plane. The other interface state at M belonging to the higher of the two bands has a very different charge distribution which is displayed in Fig. 68. The charge is again p-like around the S atom. However, the charge lobes for this state are pointing along the back-bond direction between the first layer S atoms and the second layer Zn atoms. Surface states somewhat similar to these states are also found in surface calculations.[155]

Our results are consistent with recent experiments on metal overlayers which have provided information on the electronic structure of m/s interfaces in the energy range of the semiconductor band gap. Rowe et al.[113] have found that the intrinsic surface states on the (111) and (100) semiconductor surfaces are removed by metallic overlayers and extrinsic metal-induced states are found within the band gap. Their findings on the Ge (110) surface is however somewhat ambiguous. Similar extrinsic metal-induced states are found but they are weaker and the intrinsic surface states appear not to completely removed by the thin metallic overlayers.

C. Ionicity and the Theory of Schottky Barriers

In this section some of the properties of m/s Schottky barriers and their relation to the calculated electronic structure are examined.

The calculated barrier heights for the four m/s interfaces studied are presented in Table XIII together with the measured ϕ_b.[142,149] The calculated values were obtained by determining the position of the conduction band minimum of the bulk semiconductor relative to the

Fermi level E_F via the local density of states. Considering the sizes of the thermal gaps of the more ionic crystals, the agreement obtained between theory and experiment is quite good.

Empirically the barrier height $\phi_b(m,s)$ obeys the relation[137]

$$\phi_b(m,s) = S(s)X_m + \phi_0(s) \tag{84}$$

where X_m is the Pauling-Gordy electronegativity[156] of the metal and S and ϕ_0 are constants depending on the semiconductor. As an example, the experimental barrier heights[142,149] for our four semiconductors are presented in Fig. 69 as a function of the X_m of various metals. Moreover the slope or "index of interface behavior" S is found to be a smooth function of $\Delta X = X_A - X_B$, the electronegativity difference of the anions and cations in the semiconductor. Since ΔX provides a measure of the ionicity of the semiconductor, S is also a function of the semiconductor ionicity. For ϕ_b expressed in units of electron volts, S is small ~0.1 for semiconductors with $\Delta X < 0.5$ but S is ~1.0 for semiconductor with $\Delta X > 0.9$. In addition, there is a well defined and rather sharp transition in the value of S at ΔX ~0.7 to 0.8 (see Fig. 70).

As we have discussed earlier, the standard explanation for S relies on the Bardeen model which attributes this behavior of ϕ_b to the density of surface states existing in the semiconductor band gap. However arguments had been presented by Heine[138] which showed that semiconductor surface states do not exist in the fundamental gap for most m/s interfaces and many alternate theories have since been proposed.[138-141]

Physically the barrier height is determined by the requirement that in equilibrium the Fermi levels of two materials in contact are equal. This is achieved by creating an electric dipole potential Δ at the interface. Hence, in the one-electron theory, the density of the MIGS in the semiconductor thermal gap and their penetration into the semiconductor will strongly influence the behavior of ϕ_b. The extent of their penetration can be measured by a penetration depth δ defined by $\bar{\rho}(\delta)/\bar{\rho}(0) = 1/e$. From Fig. 65 δ is equal to ~3.0 Å and ~2.8 Å for Si and GaAs respectively. As the ionicity of the semiconductor increases, δ however rapidly reduces to ~1.9 Å for ZnSe and to ~0.9 Å for ZnS.

The other quantity which is relevent to the behavior of ϕ_b and related to the MIGS is the surface density of states $D_s(E)$. For energies in the semiconductor thermal gap, we define

$$D_s(E) = A^{-1} \int_A \int_0^\infty N(E,\underline{r}) dz dA, \quad 0 \leq E \leq E_g , \tag{85}$$

where A is the interface area, $N(E,\underline{r})$ is the LDOS as defined in Eq. (83) and the integral over z is to be evaluated from the interface to deep into the bulk of the semiconductor. Thus $-eD_s(E)$ gives the density of localized surface charge per unit energy on the semiconductor surface. The calculated $D_s(E)$ are depicted in Fig. 71. The averaged D_s near the center of the gap for Si and GaAs which both have about the same S is approximately the same. Two trends which can be observed from Fig. 14 are that $D_s(E)$ decreases for more ionic semiconductors and $D_s(E)$ has a relatively flat minimum over the center region of the

gap. The D_s for m/ZnSe is essentially identical to that of m/ZnS except its magnitude is ~30% higher. Hence it is omitted from Fig. 71.

From an electrostatic point of view, the fact that both δ and D_s decrease for more ionic semiconductor crystals implies that the change in Δ with respect to a change in E_F will be small for ionic semiconductors and larger for covalent semiconductors. Therefore we expect from the calculated δ and D_s that S will be large for ionic crystals and small for covalent crystals.

To estimate the influence of δ and D_s on the barrier height, we use the following simple model to calculate S(s). Cowley and Sze[157] had used a somewhat similar approach to obtain the interface density of states in terms of the experimentally determined S. In this model, δ and D_s are assumed to be quantities intrinsic to the semiconductor (i.e. they are independent of the metal contacts) and also D_s is taken to be approximately constant over the central portion of the thermal gap. Calculations on metal-Si interfaces using surface Green function methods have shown that D_s is approximately constant for a wide range of metals.[140,158] In this model, we have also made use of the empirical relation that the metal work function ϕ_m is linear in X_m, i.e. $\phi_m = AX_m + B$ with $A = 2.27$ and $B = 0.34$ for ϕ_m expressed in electron volts.[156,159]

For a semiconductor of electron affinity χ_s in contact with a metal, the electric dipole potential established at the interface is

$$\Delta = \chi_s + \phi_b - AX_m - B \ . \qquad (86)$$

The change in Δ for a metal of slightly different X_m in contact with the same semiconductor is therefore

$$d\Delta = d\phi_b - AdX_m \quad . \tag{87}$$

Using simple electrostatic arguments, another expression for $d\Delta$ is

$$d\Delta = -4\pi e^2 D_s \delta_{eff} d\phi_b \tag{88}$$

where δ_{eff} is the effective distance between the center of mass of the negative charge transferred to the semiconductor due to the change in ϕ_b and the center of mass of the positive charge left behind in the metal. This distance is the true distance divided by the appropriate dielectric screening function ε, i.e. $\delta_{eff} = (t_m/\varepsilon_m + t_s/\varepsilon_s)$. We may approximate t_s by our calculated δ and t_m/ε_m by the typical screening length in a metal which is $\sim$0.5 Å. Equations (4), (7) and (8) then yield the following S[160]

$$S = \frac{2.3}{1+4\pi e^2 D_s (0.5+\delta/\varepsilon_s)} \quad . \tag{89}$$

The dielectric screening for potential fluctuations in the distance of the order of δ has been found to be $\approx$2 by Walter and Cohen[161] for our four semiconductors. Hence we may evaluate S using the calculated values of δ and D_s and $\varepsilon_s = 2$. They are presented in Table XIII together with the experimentally determined S. The agreement between theory and experiment is surprisingly good for this very simple model.

Although our results are for intrinsic semiconductors at zero temperature, the calculated ϕ_b and S will be essentially the same as those for doped semiconductors at finite temperature. The argument is as follows, for typical doping density of $n \leq 10^{17}$ cm^{-3}, a small charge accumulation of $\sim 10^{12}$ electrons/cm^2 at the semiconductor surface will result in band bending on the order of volts. Hence, with $D_s \sim 10^{14}$/eV-cm^2, only a slight change (~0.01 eV) in E_F at the interface is needed to account for the band bendings caused by impurities or thermally excited electrons.

We have also examined the sensitivity of our results to the only uncertain parameter in the calculations, i.e. the placement of the jellium core edge. Our results appear to be quite insensitive to this parameter. In the case of the m/Si interface, a change of 25% in this parameter left ϕ_b and δ essentially unchanged and only changed D_s by a few percent. A similar observation has been made by Louis et al.[140,160] They have performed non-self-consistent calculations on m/s interfaces using a Green function method.

D. Discussion and Conclusions

Using a self-consistent pseudopotential method, we have studied the electronic structure of a series of m/s interfaces of increasing semiconductor ionicity. Our results are consistent with recent experiments on metal overlayers[113] which indicated that the intrinsic surface states on the semiconductor surfaces are removed by metallic overlayers and extrinsic metal-induced states are found within the energy range of the band gap. Hence, contrary to the Bardeen model

and the recent speculations made by Eastman and Freeouf,[106] intrinsic semiconductor surface states do not appear to play a dominant role in determining ϕ_b. Detailed experimental information on the electronic structure of these m/s is however not available at present for comparison.

We have also examined the question of ionicity in the behavior of Schottky barrier heights. A simple model involving the MIGS has been constructed to estimate S. We find that both ϕ_b and S can be satisfactorily determined using the self-consistent pseudopotential results for the more covalent semiconductors and somewhat less accurately for the more ionic semiconductors. Our results suggest that the important properties of Schottky barriers are mostly incorporated in the one-electron, jellium-semiconductor type of model. Other effects not included in the present calculations such as many-body effects and bonding between metal and semiconductor atoms are most likely necessary before complete agreement between theory and experiments for the more ionic semiconductors can be achieved.

V. VACANCIES IN SEMICONDUCTORS: A Si NEUTRAL VACANCY

Despite numerous theoretical investigations, the detailed electronic structure of deep defect states in semiconductors remains essentially an unsolved problem.[162] The main difficulties arise from the fact that deep levels in the semiconductor gap imply a strongly localized defect potential often combined with structural reconstruction in the vicinity of the defect. Consider the case of an isolated neutral vacancy (V^0) in Si. Several different methods of calculation have been employed leading to quite different results. Among them defect molecule calculations[163,164] have provided only qualitative information about the Si vacancy levels; as of yet no connection with the band structure has been established. Results from one-electron methods using clusters of Si atoms such as the Extended Hückel Method strongly depend on the size of the cluster, the basis functions used, and the boundary conditions imposed.[165,166] Finally, studies considering the vacancy as a perturbation on the perfect Si crystal give results ranging from having only resonant vacancy states in the Si conduction band[167] to having localized states anywhere in the forbidden gap depending on an arbitrary scaling of the perturbing vacancy pseudopotential.[168]

Experimentally the energy levels for the neutral vacancy (V^0) in Si are not well determined. However, they are believed to be deep (at least a few tenths of an eV) in the forbidden gap.[169,170] Moreover, from electron paramagnetic measurements,[169] it is found that both the

singly positive (V^+) and negative (V^-) charged states of the Si vacancy undergo a structural reconstruction. For the V^+ state, a tetragonal Jahn-Teller distortion is observed; and for the V^- state, a mixed tetragonal and trigonal distortion is found. A similar type of reconstruction is expected for the V^o state.

In this section the electronic structure of a neutral vacancy in Si is studied using the self-consistent pseudopotential method developed in Sec. IIIA. To study the effect of local reconstruction we have considered three different structural models for the Si vacancy: the ideal undisturbed structure and two differently reconstructed structures. Self-consistency in the present context means the self-consistent electronic response to a given structural model. Among the above mentioned methods for calculating the electronic properties of a semiconductor vacancy, only the defect molecule calculations are self-consistent in this spirit. To our knowledge, the present work is the first calculation of a Si vacancy in which bulk band structure effects are included and which at the same time is self-consistent.

In the present calculations, the lattice vacancies are repeated periodically to form a superlattice of vacancies embedded in the infinite Si crystal and the electronic structure of this periodic system is calculated self-consistently. Hence the vacancy levels are spread into bands with dispersion in $\underline{k}$-space. The amount of dispersion provides a measure of the localization of the vacancy states. It is found that localized vacancy states in the gap and strong resonance states in the valence band existed for the three structural models.

The characteristics of these states have been studied by analyzing their charge densities. In addition, a tight-binding model has been fitted to the vacancy bands for the ideal case. From the fitted tight-binding parameters, the "dispersionless" energies of vacancy levels which correspond to isolated vacancies can be extracted.

The remainder of this section is organized as follows: In Section A the steps in the self-consistent calculations and the tight-binding model are discussed. In Section B the results for the electronic structure of the Si neutral vacancy for three structural models are presented and discussed. In the final Section C some conclusions are presented.

A. Calculations

In this section a description is given of the self-consistent calculations, carried out for the three structural models of the neutral Si vacancy. In addition a tight-binding model used to fit the vacancy bands for the ideal vacancy is presented.

1. Self-consistent Pseudopotential Calculations

As discussed in Sec. III A, the method employed here for the calculation of a local configuration consists of periodically repeating the particular local configuration to form a superlattice. Self-consistent pseudopotentials are then used to compute the electronic structure. The steps leading to a self-consistent solution to the vacancy problem are schematically shown in Fig. 23. The method has been applied successfully to the calculation of a Si diatomic molecule[172] and to the calculations of crystalline surfaces (Sec. III) and solid

interfaces (Sec. IV). A detailed discussion of the method has been given in Sec. IIIA and Sec. IVA; it therefore will only be briefly described below.

Two essential features of the method are: (1) Self-consistency in the potential is required to allow for the correct electronic screening around the vacancy site and (2) periodicity is retained artificially which permits the use of standard pseudopotential techniques.

For the present case of a Si vacancy, the infinite Si crystal is divided into large fcc unit cells each containing 54 atoms. Neutral vacancies are simulated by removing an identical atom from each cell. The different structural models involve different reconstructions for the positions of the atoms surrounding the vacancy site. Test runs with various cell sizes indicated that at least 54-atom unit cells are needed to quantitatively provide the essential physics of the system. In the 54-atom unit cell neighboring vacancies are separated by six Si-Si bonds. The self-consistent loop (see Fig. 23) is initiated with an empirical pseudopotential carried over from crystalline calculations. From the resulting total charge density, a Hartree screening potential and an exchange potential of the Slater type are derived and added to an atomic Si^{+4} ion-pseudopotential to form a new total pseudopotential for the next iteration. New screening and exchange potentials are derived and the process is repeated until self-consistency (stability of input vs. output potentials within 0.005 Ry) is reached.

The self-consistent cycle is initiated using the followng starting potential

$$V_{start}(\underline{G}) = S(\underline{G})V_{emp}^{Si}(|\underline{G}|) \tag{90}$$

where $\underline{G}$ are reciprocal lattice vectors and the Si structure factor

$$S(\underline{G}) = \frac{1}{M}\sum_{\tau_i}^{M} e^{-i\underline{G}\cdot\underline{I}_i} \tag{91}$$

describes the positions of the atoms in the large 54-atom unit cell. $V_{emp}^{Si}(|\underline{G}|)$ are the Si atomic pseudopotential form factors fitted to empirical bulk calculations.[47] They are derived from a continuous extrapolation of the form

$$V_{cmp}^{Si}(q) = \frac{a_1(q^2-a_2)}{\exp[a_3(q^2-a_4)]+1} \tag{92}$$

where the four parameters a_i are given in Table XIV. The potential $V_{emp}^{Si}(q)$ is normalized to an atomic volume of 137.6 $(a.u.)^3$ with units in Ry if q is entered in a.u. Using this starting potential, the band structure $E_n(\underline{k})$ and the wavefunctions $\psi_{n\underline{k}}(\underline{r})$ can then be calculated using standard methods,[1] i.e. expanding the electron wavefunction in plane waves with reciprocal lattice vectors and diagonalizing the Hamiltonian matrix to obtain electronic energy $E_n(\underline{k})$ and the electronic wavefunction $\psi_{n\underline{k}}$.

To perform the next step in the self-consistent loop, the total valence charge density

$$\rho(\underline{r}) = \sum_{\underline{k}} \rho_{\underline{k}}(\underline{r}) = 2 \sum_{\underline{k}} \sum_{n} |\psi_{n\underline{k}}(\underline{r})|^2 \tag{93}$$

has to be evaluated. There are 106 occupied bands in the band structure scheme (no spin-orbit interaction). For reasonable convergence of the wavefunctions, a matrix size of the order of 750 by 750 is needed when the Hamiltonian is expanded in plane waves. This corresponds to a kinetic energy cutoff[1] $E_1 = |\underline{G}^2_{max}| \approx 2.7$ Ry. In addition, another ~800 plane waves were included via Löwdin's perturbation scheme[1] to further improve the accuracy of the eigen-energies. To avoid a full Brillouin zone evaluation of the total charge density at each iteration of the self-consistent process, the total charge density $\rho(\underline{r})$ is approximated by the charge density evaluated at one point $\underline{k} = \Gamma$. The point Γ was chosen because, among the high symmetry points, $\rho_\Gamma(\underline{r})$ provides a good representation of $\rho(\underline{r})$ for crystalline Si. At the bond and atomic sites, $\rho_\Gamma(\underline{r})$ of bulk Si is within 10% of the charge density given by a full zone calculation. The choice of high symmetry points is necessary because the Hamiltonian matrix can then be reduced by using symmetrized plane waves.

Once $\rho(\underline{r})$ is known, the Hartree screening potential V_H and the Hartree-Fock-Slater exchange potential V_x are evaluated using

$$V_H(\underline{G}) = \frac{4\pi e^2 \rho(\underline{G})}{|\underline{G}|^2} \tag{94}$$

and

$$V_x(\underline{G}) = -\alpha\left(\frac{3}{2\pi}\right)(3\pi^2)^{1/3} e^2 \rho^{1/3}(\underline{G}) \tag{95}$$

where $\alpha = 0.79$ and $\rho(\underline{G})$ and $\rho^{1/3}(\underline{G})$ are the Fourier components of $\rho(\underline{r})$ and $\rho^{1/3}(\underline{r})$ respectively. Justification for the use of the Slater exchange potential and the choice of α are discussed in detail in Ref. 94. V_H and V_x together form the electronic screening potential of the system. They are then added to an ionic potential

$$V_{ion}(\underline{G}) = S(\underline{G})V_{ion}^{Si}(\underline{G}) \tag{96}$$

to form an input potential for the next iteration. For V_{ion}^{Si}, we have used a local approximation of a Abarenkov-Heine atomic model potential[96] which is fitted to the following 4-parameter potential

$$V_{ion}^{Si}(q) = \frac{b_1}{q^2}\left[\cos(b_2 q)+b_3\right]\exp(b_4 q^4) \ . \tag{97}$$

The values of the b_i's are given in Table XIV. The normalization and the units for Eq. (97) are the same as those for Eq. (92).

The calculation is continued by repeating the whole cycle. However, due to the divergent character of V_H and V_{ion} for small $\underline{G}$'s, self-consistency cannot be achieved straightforwardly by using the output screening potential from one iteration as the input screening potential for the next iteration. An alternative procedure to the one suggested in Ref. 94 is used in the present calculations. The input screening potential of the nth iteration is taken to be a weighted linear combination of the input and output screening potentials of the $n-1^{th}$ iteration. The criterion for self-consistency is the stability of the subsequent output screening potentials. In the present

calculations, the final self-consistent potentials are stable to within 0.005 Ry.

2. Tight-binding Model

In this subsection a tight-binding model[173] for interacting p-like atomic states in a fcc lattice is described. This model will be used later to analyze the vacancy levels of the Si vacancy in the ideal crystal structure. We consider a fcc array of atoms which have 3-fold degenerate p-like atomic levels (P_x,P_y,P_z). Then Bloch functions of the form

$$\psi_1(\underline{k}) = \frac{1}{\sqrt{N}} \sum_n e^{i\underline{k}\cdot\underline{R}_n} P_x(\underline{r}-\underline{R}_n)$$

$$\psi_2(\underline{k}) = \frac{1}{\sqrt{N}} \sum_n e^{i\underline{k}\cdot\underline{R}_n} P_y(\underline{r}-\underline{R}_n)$$

$$\psi_2(\underline{k}) = \frac{1}{\sqrt{N}} \sum_n e^{i\underline{k}\cdot\underline{R}_n} P_z(\underline{r}-\underline{R}_n) \qquad (98)$$

are constructed and the band structure $E_n(\underline{k})$ is given by diagonalizing

$$\begin{pmatrix} \langle\psi_1|H|\psi_1\rangle - E & \langle\psi_1|H|\psi_2\rangle & \langle\psi_1|H|\psi_3\rangle \\ \langle\psi_2|H|\psi_1\rangle & \langle\psi_2|H|\psi_2\rangle - E & \langle\psi_2|H|\psi_3\rangle \\ \langle\psi_3|H|\psi_1\rangle & \langle\psi_3|H|\psi_2\rangle & \langle\psi_3|H|\psi_3\rangle - E \end{pmatrix} \qquad (99)$$

where $\underline{k}$ is the wavevector, $\underline{R}_n$ are the lattice positions and H is the crystal Hamiltonian. Assuming only nearest neighbor interactions, the Hamiltonian matrix can be expressed in terms of three parameters: (1) u, the energy of the isolated atomic states, (2) σ, the interaction

energy between parallel orbitals centered at neighboring atoms which point along the line connecting the atoms, and (3) π, the interaction energy between parallel orbitals centered at neighboring atoms which are perpendicular to the line connecting the atoms. Denoting $\underline{k} = (\xi_1,\xi_2,\xi_3)$ with ξ_i in units of $2\pi/a$ where a is the lattice constant of the fcc superlattice, the matrix elements are given by:

$$\begin{aligned}
\langle\psi_1|H|\psi_1\rangle &= u+(\sigma+\pi)[\cos\pi(\xi_1+\xi_2)+\cos\pi(\xi_1-\xi_2)+\cos\pi(\xi_1-\xi_3) \\
&\quad + \cos\pi(\xi_1+\xi_3)]+2\pi[\cos\pi(\xi_2+\xi_3)+\cos\pi(\xi_2-\xi_3)] \\
\langle\psi_2|H|\psi_2\rangle &= u+(\sigma+\pi)[\cos\pi(\xi_2+\xi_3)+\cos\pi(\xi_2-\xi_3)+\cos\pi(\xi_2-\xi_1) \\
&\quad + \cos\pi(\xi_2+\xi_1)]+2\pi[\cos\pi(\xi_3+\xi_1)+\cos\pi(\xi_3-\xi_1)] \\
\langle\psi_3|H|\psi_3\rangle &= u+(\sigma+\pi)[\cos\pi(\xi_3+\xi_1)+\cos\pi(\xi_3-\xi_1)+\cos\pi(\xi_3-\xi_2) \\
&\quad + \cos\pi(\xi_3+\xi_2)]+2\pi[\cos\pi(\xi_1+\xi_2)+\cos\pi(\xi_1-\xi_2)] \\
\langle\psi_2|H|\psi_1\rangle &= (\pi-\sigma)[\cos\pi(\xi_1-\xi_2) - \cos\pi(\xi_1+\xi_2)] \\
\langle\psi_3|H|\psi_1\rangle &= (\pi-\sigma)[\cos\pi(\xi_1-\xi_3) - \cos\pi(\xi_1+\xi_3)] \\
\langle\psi_3|H|\psi_2\rangle &= (\pi-\sigma)[\cos\pi(\xi_2-\xi_3) - \cos\pi(\xi_2+\xi_3)] \; . \qquad (100)
\end{aligned}$$

For some high symmetry k-points, the eigenvalues can be obtained easily without diagonalizing the 3×3 matrix, Eq. (99). At $\underline{k} = (0,0,0)$, $\langle\psi_i|H|\psi_i\rangle = u + 4\sigma + 8\pi$ and $\langle\psi_i|H|\psi_j\rangle = 0$ for $i \neq j$. Therefore, the energies for the three bands are degenerate at Γ and have the energy

$$E(\underline{k}=\Gamma) = u + 4\sigma + 8\pi \; . \qquad (101)$$

At $\underline{k} = X = (1,0,0)$ one has $\langle \psi_1|H|\psi_2\rangle = u-4\sigma$, $\langle \psi_2|H|\psi_2\rangle = u-4\pi$, $\langle \psi_3|H|\psi_3\rangle = u-4\pi$ and $\langle \psi_i|H|\psi_j\rangle = 0$ for $i \neq j$. Thus two energy eigenvalues exist at X: one is singly degenerate

$$E_1(\underline{k}=X) = u-4\sigma \tag{102}$$

the other is doubly degenerate

$$E_2(\underline{k}=X) = u-4\pi \tag{103}$$

B. Results and Discussions

1. Ideal Structure

The first structural model used to study the electronic structure of a neutral Si lattice vacancy is the "ideal" structure. In this structure, the atoms surrounding the vacancy site remain in their cyrstalline positions after the vacancy is created. A portion of the Si crystal structure is shown in Fig. 72(a). Every Si atom is tetrahedrally coordinated and the valence electrons form covalent bonds linking the neighboring atoms. As a results of creating a vacancy, four bonds are broken (see Fig. 72(b)). The electrons which previously participated in the broken bonds will tend to localize around the vacancy site and localized vacancy levels are expected to appear among the energy eigenvalues of bulk Si. In the present calculations, we have found both vacancy states deep in the Si thermal gap and strong resonant states embedded in the bulk bands.

Before discussing the individual vacancy states, first the total, self-consistent valence charge density as given by the approximations

discussed in Sec. A shall be examined. A necessary condition for the present calculations to represent non-interacting Si vacancies is that the charge density away from the vacancy site should closely resemble the charge density of bulk Si. Figure 73 displays the total valence charge density in a (110) plane for the ideal structure. The vacancy site is located at the center of the unit cell (open circle) and the atoms are indicated by full dots. Note that, for the center chain of atoms, both an atom and the associated covalent bonds are missing. The top and bottom chains are complete. Their charge densities are in good accord with densities obtained from bulk calculations[47] (which illustrates the local nature of the lattice perturbation).

As mentioned earlier, vacancy levels which are dispersionless in $\underline{k}$-space for an isolated vacancy will appear as bands in the present periodic model. For the ideal structure, three vacancy bands in the Si thermal gap and one strong resonant band in the energy range of the valence bands are found. More weak resonant states corresponding to perturbed back bonds may exist in the valence bands. Figure 74 shows the energies of the vacancy bands at $\underline{k} = \Gamma$. The top figure depicts the positions of the $\underline{k}$=0 vacancy states with respect to the Si bulk density of states.[47] The three states in the gap are degenerate in energy at Γ. In the bottom figure, the energy levels at Γ for several runs in the self-consistent procedure are shown. The first row shows the energy levels of bulk Si in the 54-atom unit cell structure. The empirical pseudopotential from Ref. 47 is used. There are 108 occupied valence bands separated from the conduction bands by the Si thermal

gap (shaded area in Fig. 74). The second row shows the energy levels for the 53-atom unit cell (i.e. 53 Si atoms plus one vacancy) calculated using the empirical pseudopotential. The last row shows the energy levels for the 53-atom unit cell using the final self-consistent potential. The vacancy states are indicated by the arrows. Note that the final self-consistent vacancy levels appear significantly deeper in the forbidden gap than those calculated from the empirical pseudopotential. However, the energy of the resonant state at E ~ -8.2 eV is pinned in energy by the minimum of the density of states and changes only slightly in the course of achieving self-consistency.

In Fig. 75(a) the charge density contour map for the vacancy states in the gap is displayed. The plotting plane is the same as in Fig. 73 ((110) plane) and the plotting area is enclosed by the two horizontal dashed lines in Fig. 73. As expected from the fact that these states appear deep in the gap, their charge density is fairly localized around the atoms surrounding the vacancy site. There is practically no charge built up on the atoms of neighboring chains, however, some charge overlap between vacancy states within the same chain is present. The charge distributions are dangling-bond-like, i.e. mostly p-like with a small mixture of s character. Figure 75(b) shows the charge density contour plot for the resonant state in the valence band. Again the charge density is highly localized on the atoms surrounding the vacancy site. However, for this state, the charge distribution is mostly s-like around the atoms. Although these plots are calculated for states at Γ, they are representative for the

vacancy states, since it is found that the charge distributions of the vacancy states are virtually identical for all $\underline{k}$-points in the fcc Brillouin zone.

The origin of the vacancy states can be understood using a simple molecular orbital picture.[174] In this model, one assumes that in first order only the electrons in the broken bonds are significantly perturbed and that the wavefunctions of the vacancy states can be represented by a combination of atomic orbitals. Specifically, each molecular orbital (a single-electron vacancy state) is expressed as a linear combination of the dangling bond orbitals (a,b,c,d) of the four atoms next to the vacancy site. Because of the symmetry of a Si vacancy in the ideal structure, the molecular orbitals must transform under the operation of the group T_d according to irreducible representations of that group. Suitable single-electron wavefunctions thus are

$$\begin{aligned} v &= a + b + c + d \quad a_1 \\ t_x &= a + b - c - d \\ t_y &= a - b - c + d \quad t_2 \\ t_z &= a - b + c - d \end{aligned} \tag{104}$$

The resonant vacancy state at $E \sim -8.2$ eV has the symmetry of the state a_1, whereas the three states in the Si gap can be associated with the above t_2 states. This simple picture which correctly describes the symmetry of the vacancy states found, does not of course account for the dehybridization of sp^3 hybrids around the vacancy. The dehybridization into s-like and p-like states is, however

appreciable as seen from Fig. 75. Moreover the simple model does not include possible resonant state due to perturbed back bonds.

The dispersions of the vacancy states in k-space which in a tight-binding picture are caused by the interactions between vacancies in the superlattice shall now be examined. The dispersion for the resonant vacancy state at E ~ -8.2 eV is found to be verv small (~0.1 eV). This is confirmed by Fig. 75(b) in which virtually no overlap between orbitals centered at neighboring vacancy sites is found. However, the dispersion of the three vacancy states in the gap is appreciable which can be seen by the presence of charge between neighboring vacancy sites (see Fig. 75(a)). This result indicates that the 54-atom unit cell chosen is not large enough to completely decouple the individual vacancies. In Fig. 76 symmetries and dispersions of the states in the gap along the Δ direction from Γ to X are shown schematically. In the ideal structure the three states are degenerate in energy at Γ with E = 0.9 eV. Along Δ, they split into one non-degenerate band (Δ_3) and one two-fold degenerate band (Δ_5). At X the energy values are $E_2(X)$ = 0.7 eV for the two-fold degenerate states and $E_1(X)$ = -0.3 eV for the non-degenerate state (all energies are given with respect to the valence band maximum).

An estimation of the position of the energy levels for a single non-interacting vacancy is obtained using the tight-binding model described in Sec. A.2. Assuming that the dispersions of the vacancy bands in the Si gap are completely due to nearest neighbor interactions among the "p-like" single-electron vacancy states, the energy levels

u for an isolated vacancy can be obtained by solving Eq. (101), (102), and (103) simultaneously. This yields the following expression for u:

$$u = [E(\Gamma) + E_1(X) + 2E_2(X)]/4 \ . \qquad (105)$$

Using the calculated values for $E(\Gamma)$, $E_1(X)$ and $E_2(X)$, the energy for the three-fold degenerate vacancy state in the gap for an isolated vacancy is $u = 0.5$ eV. At present no experimental data are available which allow comparison of this calculated value.

The radial dependence of the various one-electron potentials of interest for the ideal neutral Si lattice vacancy are displayed in Fig. 77. Non-spherical contributions to the potentials are negligibly small in the ideal structure. As described in the previous section the self-consistent calculations are based on a lattice of Si^{4+} ionic potentials V_{ion} with one vacant lattice site (solid curve). The long range Coulomb tail of this missing Si^{4+} ion is completely screened by the Hartree-exchange potential V_{HX} of four defect electrons (dashed line) as calculated from the total, self-consistent valence charge distribution. The resulting vacancy potential V_{SC} (dotted line) is of short range similar to the empirical Si pseudopotential V_{emp} (dashed dashed dotted dotted line) as used in crystal calculations. Compared to V_{emp}, however, V_{SC} shows a more repulsive core and a deeper well around 1Å. A similar difference has been obtained in recent self-consistent surface calculations.[94] Also shown for comparison is the self-consistent pseudopotential V_{SC} (atom) obtained for an isolated atom by a calculation based on the same ionic Si^{4+} potential V_{ion}

(dashed dotted curve). Even though the vacancy and the atomic potentials show comparable amplitudes for the repulsive core and the attractive bonding region, the self-consistent atomic potential is of considerably longer range and extends up to about 4 Å. This difference is due to the presence of covalent bonds in the crystalline case or dangling bonds in the vacancy case which lead to an increased electron density between 1 and 2 Å and thus to a stronger screening decreasing the effective range of the potential.

2. Reconstructed Structures

Results presented in the previous subsection indicated that, in the ideal structure, there are three vacancy states in the Si thermal gap which are degenerate in energy. For a neutral vacancy, only one of the three states (neglecting spin) is occupied. This situation is unstable with respect to Jahn-Teller distortions[175] which lead to structural changes. Indeed, as discussed earlier, the charged V^+ and V^- states for the Si vacancy are observed to undergo Jahn-Teller distortions which produce an uniaxial asymmetry in the electronic wavefunction along the cubic [100] direction. Although there exists no experimental data on the detailed structure of a neutral vacancy at present, it is generally believed that a similar type of distortion takes place for the neutral vacancy.

To study the effects of Jahn-Teller distortions on the vacancy levels, the electronic structure of a neutral vacancy is calculated for two differently reconstructed structural models. The first reconstructed structure is obtained by shortening the distance between

atoms d and g and between atoms e and f in Fig. 72(b) by an amount equal to $\delta = 0.48\ d_0$ where d_0 is the crystalline value of the Si-Si bond length. This is done by symmetrically moving the atoms toward each other along the connecting line. This type of distortion produces an asymmetry along the cubic [100] direction. The estimated value for δ is chosen to be in approximate agreement with the displacement found by Swalin[176] in his study of vacancy formation using Morse potentials. This value does not present an optimum choice, it merely represents a trial value. Figure 78 shows the total self-consistent charge density for this reconstructed structure (Rec I). As for the ideal case the charge density away from the vacancy is very much bulk-like. However the charge density near the vacancy site differs significantly from that obtained for the ideal structure. There appears bond like charge between the two atoms which have been moved closer to each other whereas the stretched back bonds become considerably weaker.

The effects of Rec I on the resonant vacancy level are small; its energy remains at ~-8.0 eV. The effects of the distortion on the vacancy states in the gap, on the other hand, are significant. They are shown schematically in the center portion of Fig. 76. The three-fold degeneracy at Γ is lifted by the uniaxial distortion. The lower band (labelled Δ_3) remains in the gap, whereas the two-fold degenerate band (labelled Δ_5) merges with the conduction band structure. The highest fully occupied band is now Δ_3, separated by a finite gap from unoccupied states indicating that no further symmetry reduction (i.e. Jahn-Teller distortion) is needed to stabilize the system. In

addition, a new (empty) vacancy band, labelled Δ_1, appears in the gap. This state is induced by the chosen vacancy reconstruction and has its wavefunction localized at the vacancy site. Rec I has the net effect of moving the four atoms surrounding the vacancy site closer towards the vacancy site. This distortion stretches and weakens the back bonds. Some back bonding charge as a consequence is spread out and transferred to the second nearest back bonds, which causes an increased vacancy-vacancy interaction in the present model. This effect is also recognizable from the increased dispersion of the Δ_3 vacancy band between Γ and X (see Fig. 76, middle). In analogy to the Si (111) surface, Rec I corresponds to an outward relaxation and therefore seems unlikely to occur.[177]

To study the effects of an opposite movement of atoms, another reconstructed structure, Reconstruction II (Rec II) is considered. The type and symmetry of distortions for this structural model is identical as for Rec I except for $\delta = -0.48\ d_0$, which corresponds to a contraction of back bonds and a net relaxation away from the vacancy site. Figure 79 shows the total, self-consistent charge density for Rec II. As compared to Fig. 78, charge has been removed from the immediate vacancy region and has been transferred into the back bonds.

As for Rec I, the distortion does not significantly affect the resonant vacancy level at about -8.0 eV. The behavior of the vacancy bands in the gap is shown on the right portion of Fig. 76. For Rec II, only one vacancy band (Δ_3) exists in the Si thermal gap. This band is fully occupied and separated by a finite gap from empty states.

Thus, the type of distortion of Rec II which lowers cubic symmetry leads to a Jahn-Teller stable situation. The strengthening of back bonds localizes the vacancy induced charge fluctuations which results in a decrease of dispersion of the vacancy bands along Δ (see Fig. 76). In contrast to Rec I, no empty vacancy state is found in the gap of Si. The Δ_5 vacancy levels become resonant levels with the conduction bands.

While the exact atomic positions of the reconstructed vacancy environment are still unknown, Rec II-type relaxations are expected to occur most likely. Analogies to the Si (111) surface relaxation[177] support this model. More experimental, spectroscopic information about the neutral Si vacancy is needed to clarify the situation.

C. Conclusions

The neutral lattice vacancy in Si has been studied embedded in a large 54-atom super cell using a self-consistent pseudopotential formalism. The method allows us to calculate self-consistently the response of valence electrons to an arbitrary arrangement of ionic cores. Thus three different structural models of the atoms surrounding the vacancy have been investigated. These models are: the ideal undistorted Si structure, (Rec I) a uniaxial [100] distortion of the four atoms closest to the vacancy with a net relaxation <u>towards</u> the vacancy site and (Rec II) a uniaxial [100] distortion with a net relaxation <u>away</u> from the vacancy site.

In each model one strong resonant, virtually dispersionless band is found around -8.0 eV in the valence band region. Its character is predominantly s-like on the four atoms surrounding the vacancy. In

addition vacancy bands appear in the fundamental gap, strongly influenced by the structural model used. In the ideal undistorted Si structure a threefold degenerate vacancy band is found with an estimated energy center of 0.5 eV above the valence band edge. This level is onefold (neglecting spin) occupied which causes Jahn-Teller instabilities. Spin-resonant experiments on charged V^+ and V^- vacancies indicate the existence of a uniaxial [100] Jahn-Teller type distortion, which can be assumed to also exist for the neutral vacancy. Both reconstruction models Rec I and Rec II result in a uniaxial [100] distortion. In both cases (inward and outward relaxation) one vacancy level is split away to lower energies resulting in a Jahn-Teller stable situation. Analogous considerations to the Si (111) surface relaxations favor model Rec II in which the four atoms surrounding the vacancy are relaxed away from the vacancy site, resulting in an increase in strength of back bonds. The studies presented have about the type of vacancy reconstruction existing in Si do not allow conclusive results and call for more experimental, spectroscopic information.

REFERENCES

1. M. L. Cohen and V. Heine, Solid State Phys. 24, 37 (1970).
2. P. W. Bridgman, Proc. Am. Acad. Arts Sci. 72, 207 (1938); ibid. 76, 55 (1948); ibid. 81, 165 (1952).
3. H. T. Hall, L. Merrill and J. D. Barnett, Science 146, 1297 (1964).
4. D. B. McWhan, G. Parisot and D. Bloch, J. Phys. F 4, L69 (1974).
5. D. B. McWhan and A. L. Stevens, Solid State Comm. 7, 301 (1969).
6. H. G. Drickamer, Solid State Phys. 17, 1 (1965); Rev. Sci. Inst. 41, 1667 (1970).
7. D. B. McWhan, Science 176, 751 (1972).
8. J. Wittig, Phys. Rev. Lett. 24, 812 (1970).
9. J. Bardeen, J. Chem. Phys. 6, 372 (1938).
10. R. L. Sternheimer, Phys. Rev. 78, 235 (1950).
11. E. S. Alekseev and R. G. Arkhipov, Fiz. Tver. Tela 4, 1077 (1962); Sov. Phys. Solid St. 4, 795 (1962).
12. H. Brooks, Trans. Met. Soc. AIME 227, 546 (1963).
13. J. Yamashita and S. Asano, J. Phys. Soc. Japan 29, 264 (1970).
14. F. W. Averill, Phys. Rev. B4, 3315 (1971); ibid. B6, 3637 (1972).
15. J. B. Conklin, F. W. Averill and T. M. Hattox, J. de Phys. (Paris) 33, C3-213 (1972).
16. A. O. E. Animalu, Technical Report 3, Solid State Theory Group, Cavendish Lab., Cambridge (1965).
17. J. R. Chelikowsky and M. L. Cohen, Phys. Rev. Lett. 31, 1582 (1973).
18. G. Gilat and L. J. Raubenheimer, Phys. Rev. 144, 390 (1966).

19. See Ref. 1 for a discussion of E_1, E_2 and the Löwdin perturbation.

20. I. M. Lifshitz, Z. Expt. Theor. Phys. 38, 1569 (1960); Sov. Phys. JETP 11, 1130 (1960).

21. D. J. Chadi and M. L. Cohen, Phys. Rev. B 10, 496 (1974).

22. H. G. Smith, in Superconductivity in d- and f-band Metals, ed. D. H. Douglass, Amer. Inst. of Physics, N.Y. (1972), p. 321.

23. H. G. Smith and W. Glaser, Phys. Rev. Lett. 25, 1611 (1970); ibid. 29, 353 (1972).

24. W. Weber, H. Bilz and U. Schröder, Phys. Rev. Lett. 28, 600 (1972).

25. M. L. Cohen and P. W. Anderson, in Superconductivity in d- and f-Band Metals, ed. D. H. Douglass, Amer. Inst. of Physics, N.Y. (1972), p. 17.

26. D. B. McWhan and A. C. Gossard, Bulletin of the American Physical Society 18, 422 (1973).

27. G. B. Benedek and T. Kushida, J. Phys. Chem. Solids 5, 241 (1958); H. T. Weaver and A. Narath, Phys. Rev. B1, 973 (1970).

28. A. Abragam, The Principles of Nuclear Magnetism (Oxford University Press, London, 1961).

29. V. Heine, private communication.

30. J. A. Appelbaum and D. R. Hamann, Phys. Rev. B8, 1777 (1973).

31. J. A. Van Vechten and R. M. Martin, Phys. Rev. Lett. 28, 446 (1972); ibid. 28, 646(E)(1972).

32. W. R. Hanke and L. J. Sham, Phys. Rev. Lett. 33, 582 (1974).

33. T. K. Bergstresser and G. W. Rubloff, Phys. Rev. Lett. 30, 794 (1973).

34. N. H. March and M. P. Tosi, Proc. R. Soc. A 330, 373 (1972).

35. K. C. Pandey, P. M. Platzman, P. Eisenberger, and E. N. Foo, Phys. Rev. B9, 5046 (1974).

36. E. Tosatti, C. Calandra, V. Bortolani, and C. M. Bertoni, J. Phys. C5, L299 (1972).

37. L. J. Sham, Phys. Rev. 188, 1431 (1969).

38. R. M. Pick, M. H. Cohen, and R. M. Martin, Phys. Rev. B1, 910 (1970).

39. R. M. Martin, Phys. Rev. 186, 871 (1969).

40. W. R. Hanke, Phys. Rev. B8, 4585, 4591 (1973).

41. C. M. Bertoni, V. Bortolani, C. Calandra, and E. Tosatti, Phys. Rev. Lett. 28, 1578 (1972) and Phys. Rev. B9, 1710 (1974).

42. D. L. Johnson, Phys. Rev. B9, 4475 (1974).

43. J. C. Inkson, J. Phys. C7, 1571 (1974).

44. S. L. Adler, Phys. Rev. 126, 413 (1962); N. Wiser, Phys. Rev. 129, 62 (1963).

45. J. R. Schrieffer, Theory of Superconductivity, W. A. Benjamin, Inc., Reading, Massachusetts (1964).

46. H. Ehrenreich and M. H. Cohen, Phys. Rev. 115, 786 (1959).

47. James R. Chelikowsky and Marvin L. Cohen, Phys. Rev. B 10, 5095 (1974).

48. D. L. Johnson, Phys. Rev. B9, 4475 (1974).

49. H. R. Philipp and H. Ehrenreich, Phys. Rev. 129, 1550 (1963).

50. J. C. Phillips, Solid State Phys. 18, 55 (1966).

51. Our calculated $\mathrm{Im}(1/\varepsilon_{\underline{Q},\underline{Q}}(\omega))$ differs from that of J. P. Walter and M. L. Cohen, Phys. Rev. B5, 3101 (1972). Their result yielded a broader peak with a corresponding reduction in peak height. We feel that our result, which involved the use of a more accurate integration scheme for $\mathrm{Im}\ \varepsilon_{\underline{Q},\underline{Q}}(\omega)$ and did not involve the use of a tail function in obtaining $\mathrm{Re}\ \varepsilon_{\underline{Q},\underline{Q}}(\omega)$ from $\mathrm{Im}\ \varepsilon_{\underline{Q},\underline{Q}}(\omega)$, to be superior.

52. H. Dimigen, Z. Physik 165, 53 (1961).

53. For example, it is possible that the use of OPW matrix elements could also shift the position of the energy-loss peak (M. Schlüter, private communication). Also see J. P. Van Dyke, Phys. Rev. B5, 1489 (1972).

54. J. Bardeen, this conference; and D. Allender, J. Bray and J. Bardeen, Phys. Rev. B7, 1020 (1973).

55. Excitonic states are not essential to the argument; for most of the models considered, the excitations are not excitons but unbound electron-hole pairs. We will not distinguish between these in this paper.

56. J. C. Inkson and P. W. Anderson, Phys. Rev. B8, 4429 (1973).

57. D. Allender, J. Bray and J. Bardeen, Phys. Rev. B8, 4433 (1973).

58. e.g. M. L. Cohen, Phys. Rev. 134, A511 (1964).

59. In all cases, it is the real part of the kernel which is being computed.

60. J. Lindhard, Kgl. Danske Videnskab. Selskab, Mat.-Fys. Medd. 28, 8 (1954).

61. S. J. Sramek and M. L. Cohen, Phys. Rev. B6, 3800 (1972).

62. S. G. Louie, J. R. Chelikowsky and M. L. Cohen, Phys. Rev. 28, 8 (1974).

63. J. C. Phillips. Rev. Mod. Phys. 42, 317 (1970).

64. S. G. Louie and M. L. Cohen, Phys. Rev. B13, 2461 (1976).

65. R. A. Deegan and W. D. Twose, Phys. Rev. 164, 993 (1967).

66. L. F. Mattheiss, Phys. Rev. B1, 373 (1970).

67. C. Y. Fong and M. L. Cohen, Phys. Lett. 44A, 375 (1973).

68. M. H. Halloran, J. H. Condon, J. E. Graebren, J. E. Kunzler and F. S. L. Hsu, Phys. Rev. B1, 366 (1970).

69. W. E. Pickett and P. B. Allen, Phys. Rev. B11, 3599 (1975).

70. J. H. Weaver, D. W. Lynch and C. O. Olson, Phys. Rev. B7, 4311 (1973).

71. J. R. Anderson, D. A. Papconstantopoulos, J. W. McCaffrey and J. E. Schirber, Phys. Rev. B 7, 5115 (1973).

72. D. E. Eastman, Solid State Commun. 7, 1697 (1969).

73. C. E. Moore, Atomic Energy Levels, Vol. II, Circ. Nat. Bur. Std. 467 (1952).

74. F. Herman and S. Skillman, Atomic Structure Calculations, Prentice-Hall, Inc. (1963).

75. W. L. McMillan, Phys. Rev. 167, 331 (1968).

76. G. Bergmann and D. Rainer, Z. Phys. 263, 59 (1973).

77. W. Kessel, Z. Naturforsch. A29, 445 (1974).

78. C. R. Leavens, Solid State Commun. 13, 1607 (1973).

79. P. B. Allen and R. C. Dynes, J. Phys. C 8, L158 (1975) and Phys. Rev. B 12, 905 (1975).

80. G. M. Eliashberg, Zh. Eksp. Teor. Fiz. 38, 966 (1960); 39, 1437 (1960) [Sov. Phys. - JETP 11, 696 (1960); 12, 1000 (1961)].

81. D. J. Scalapino, R. J. Schrieffer, and J. W. Wilkins, Phys. Rev. 148, 263 (1966).

82. J. Bardeen, L. N. Cooper, and J. R. Schrieffer, Phys. Rev. 108, 1175 (1957).

83. C. R. Leavens, Solid State Commun. 19, 395 (1976).

84. A tabulation of the experimental parameters used in this section is available in Ref. 5 and in J. M. Rowell, W. L. McMillan and R. C. Dynes, J. Phys. Chem. Ref. Data (to be published).

85. See for example the April issue of Physics Today 1975.

86. See for example the Nov./Dec. issue of J. Vac. Sci. Technol., 1974.

87. J. A. Appelbaum and D. R. Hamann, Rev. Mod. Phys. 48, 479 (1976).

88. G. P. Alldredge and L. Kleinman, Phys. Rev. Lett. 28, 1264 (1972), and G. P. Alldredge and L. Kleinman, Phys. Rev. B10, 559 (1974).

89. J. P. Walter and M. L. Cohen, Phys. Rev. B2, 1821 (1970).

90. J. C. Slater in Quantum Theory of Molecules and Solids (McGraw-Hill, N.Y. 1974), vol. 4.

91. J. A. Appelbaum and D. R. Hamann, Phys. Rev. Lett. 31, 106 (1973) and Phys. Rev. Lett. 32, 1433 (1974).

92. A. Taloni and D. Haneman, Surf. Science 10, 215 (1968).

93. (a) D. E. Eastman and W. D. Grobman, Phys. Rev. Lett. 28, 1378 (1972); (b) L. F. Wagner and W. E. Spicer, Phys. Rev. Lett. 28, 1381 (1972); (c) J. E. Rowe and H. Ibach, Phys. Rev. Lett. 32, 421 (1974); (d) J. E. Rowe, M. J. Traum, and N. V. Smith, Phys. Rev. Lett. 33, 1333 (1974).

94. A detailed discussion of the method and the calculated results on the Si (111) surfaces can be found in M. Schlüter, J. R. Chelikowsky, S. G. Louie and M. L. Cohen, Phys. Rev. B12, 4200 (1975).

95. J. D. Joannopoulos and M. L. Cohen, Phys. Rev. B7, 2644 (1973).

96. I. V. Abarenkov and V. Heine, Phil. Mag. 12, 529 (1965).

97. F. Yndurain and L. M. Falicov, J. Phys. C 8, 147 (1975); and 8, 1563 (1975).

98. K. C. Pandey and J. C. Phillips, Phys. Rev. Lett. 32, 1433 (1974).

99. G. Chiarotti, S. Nannarone, R. Pastore and P. Chiaradia, Phys. Rev. 4, 3398 (1971).

100. D. E. Haneman, private communications.

101. J. D. Joannopoulos and M. L. Cohen, Phys. Rev. B10, 5075 (1974).

102. C. Calondra and G. Santoro, J. Phys. C. 8, L86 (1975).

103. N. Garcia, Solid State Commun. 17, 397 (1975).

104. J. R. Chelikowsky and M. L. Cohen, Phys. Rev. B 13, 826 (1976).

105. P. E. Gregory, W. E. Spicer, S. Ciraci and W. A. Harrison, Appl. Phys. Lett. 25, 511 (1974).

106. D. E. Eastman and J. L. Freeouf, Phys. Rev. Lett. 33, 1601 (1974), and ibid 34, 1624 (1975).

107. R. Ludeke and A. Koma, Phys. Rev. Lett. 34, 817 (1975).

108. J. M. Dinan, L. K. Galbraith and T. E. Fischer, Surf. Sci. 26, 587 (1971).

109. J. Bardeen, Phys. Rev. 71, 717 (1947).

110. S. G. Louie and M. L. Cohen, Phys. Rev. Lett. 35, 866 (1975), and Phys. Rev. B 13, 2461 (1976). S. G. Louie, J. R. Chelikowsky and M. L. Cohen, to be published.

111. P. W. Chye, I. A. Babalola, T. Sukegawa, and W. E. Spicer, Phys. Rev. Lett. 35, 1602 (1975).

112. A. Huijser and J. Van Laar, Surf. Sci. 52, 202 (1975).

113. J. E. Rowe, S. B. Christman and G. Margaritonde, Phys. Rev. Lett. 35, 1471 (1975).

114. R. Dorn, M. Lüth, and G. J. Russel, Phys. Rev. B10, 5049 (1974).

115. H. Fraithzheim and M. Ibach, Surf. Sci. 47, 713 (1975).

116. P. E. Gregory and W. E. Spicer, Phys. Rev. B. 13, 725 (1976).

117. D. Haneman, Phys. Rev. 121, 1093 (1961).

118. N. D. Lang and W. Kohn, Phys. Rev. B1, 4555 (1970), B3, 1215 (1971) and N. D. Lang, Solid State Physics 28, 225 (1973).

119. J. Appelbaum and D. Hamann, Phys. Rev. B6, 2166 (1972).

120. G. P. Alldredge and L. Kleinman, Phys. Rev. B10, 559 (1974).

121. A. O. E. Animalu and V. Heine, Philos. Mag. 12, 249 (1965).

122. J. C. Riviere, Solid State Surface Science, ed. M. Green (Marcel Dekker, New York) 1, 1969.

123. While anisotropy for ϕ in metals is small it can typically amount to 0.05 Ry (see Ref. 122) from the loosely packed faces to the more densely packed faces.

124. E. Caruthers, L. Kleinman and G. P. Alldredge, Phys. Rev. B10, 1252 (1974), B9, 3325, 3330 (1974), and B8, 4570 (1973).

125. D. S. Boudreaux, Surf. Sci. 28, 344 (1971).

126. B. Feuerbacher and R. F. Willis, J. Phys. C 9, 169 (1976). This is a review article on photoemission and electron states at clean surfaces. It provides quite an extensive and up-to-date list of

references for both theoretical and experimental work on transition metal surfaces.

127. R. Haydock, V. Heine, M. J. Kelly, and J. B. Pendry, Phys. Rev. 29, 869 (1972); R. Haydock, V. Heine, and M. J. Kelly, J. Phys. C. 5, 2845 (1972); R. Haydock and M. J. Kelly, Surf. Sci. 38, 139 (1973); J. W. Davenport, T. L. Einstein, and J. R. Schrieffer, Proceedings of the 2nd International Conference on Solid Surfaces, Kyoto, Japan, 1974; M. C. Desjonqueres and F. Cyrot-Lackmann, J. Phys. (Paris) 36, L45 (1975) and J. Phys. F, 5 1368 (1975).

128. S. J. Gurman and J. B. Pendry, Phys. Rev. Lett. 31, 637 (1973).

129. B. R. Cooper, Phys. Rev. Lett. 30, 1316 (1973); R. V. Kasowski, Phys. Rev. Lett. 33, 83 (1974) and Solid State Comm. 17, 179 (1975); E. Caruthers and L. Kleinman, Phys. Rev. Lett 35, 738 (1975); D. G. Dempsey, L. Kleinman, and E. Caruthers, Phys. Rev. B12, 2932 (1975); S. J. Gurman, J. Phys. F 5, L194 (1975).

130. V. Heine, Proc. Phys. Soc. 81, 300 (1963).

131. E. Caruthers and L. Kleinman, Phys. Rev. B10, 376 (1974).

132. D. J. Chadi, Ph. D. Thesis (unpublished). S. L. Cunningham. Phys. Rev. B10, 4988 (1974).

133. In discussing the character of the surface states in this section, we are concerned only with the main d-character of the wavefunctions.

134. L. W. Swanson and L. C. Crouser, Phys. Rev. Lett. 19, 1179 (1967); E. Al Khouri Nemek, R. C. Cinti and J. B. Hudson, J. Phys. (Paris), 35, L179 (1974).

135. E. W. Plummer and J. W. Gadzuk, Phys. Rev. Lett. 25, 1493 (1970); B. Feuerbacher and B. Fitton, Phys. Rev. Lett. 29, 786 (1972) and Phys. Rev. Lett. 30, 923 (1973).

136. K. Sturm and R. Feder, Solid State Comm. 14, 1317 (1974).

137. S. Kurtin, T. C. McGill, and C. A. Mead, Phys. Rev. Lett. 22, 1433 (1969); C. A. Mead and T. C. McGill, unpublished (1976).

138. V. Heine, Phys. Rev. 138, A1689 (1965).

139. J. C. Inkson, J. Phys. C: Solid State Phys. 5, 2599 (1972) and 6, 1350 (1973).

140. F. Yndurain, J. Phys. C: Solid State Phys. 4, 2849 (1971); F. Flores, E. Louis, and F. Yndurain, J. Phys. C. 6, L465 (1973); E. Louis, F. Yndurain, and F. Flores, Phys. Rev. B13, 4408 (1976).

141. J. C. Phillips, Phys. Rev. B1, 593 (1970), and J. Vac. Sci. Technol. 11, 947 (1974).

142. A. Thanailakis, J. Phys. C 8, 655 (1975).

143. A. Thanailakis in Conference Series 22, Metal-semiconductor Contacts, M. Pepper, ed., the Inst. of Phys., Bristol and London (1974).

144. J. L. Freeouf and D. E. Eastman, Phys. Rev. Lett 34, 1624 (1975).

145. W. E. Spicer, P. E. Gregory, P. W. Chye, I. A. Babalola, and T. Sukegawa, Appl. Phys. Lett. (to be published).

146. P. E. Gregory and W. E. Spicer, Phys. Rev. B12, 2370 (1975).

147. A. J. Bennett and C. B. Duke, Phys. Rev. 160, 541 (1967); Phys. Rev. 162, 578 (1967).

148. B. Pellegrini, Phys. Rev. B7, 5299 (1973).

149. S. M. Sze, Physics of Semiconductor Devices, New York and London: Wiley (1969).

150. J. C. Slater, Phys. Rev. 81, 385 (1951), W. Kohn and L. J. Sham, Phys. Rev. 140, A1133 (1965).

151. E. P. Wigner, Phys. Rev. 46, 1002 (1934).

152. J. P. Walter and M. L. Cohen, Phys. Rev. B4, 1877 (1971).

153. Notation for the high symmetry points is as in Quantum Theory of Solids by C. Kittel, John Wiley & Sons, Inc., New York, 1964.

154. Each non-zero histogram bin was constructed by averaging its value with 25% of the neighboring bins to remove some of the unphysical sharp structure resulting from the small number of $\underline{k}$-points used.

155. See for example Ref. 104 and reference therein.

156. L. Pauling, The Nature of the Chemical Bond, 3 ed., Cornell University Press, 1960.

157. A. M. Cowley and S. M. Sze, J. Appl. Phys. 36, 3212 (1966).

158. For metals with very low density of s-p electrons, localized interface states may occur in the thermal gap and thus changes the character of D_s.

159. W. Gordy and W. J. O. Thomas, J. Chem. Phys. 24, 439 (1956).

160. E. Louis, et al. have used an expression similar to Eq. 89 to analyze their results in Ref. 140. In their paper however the relation between ϕ_m and X_m was neglected which produced a larger discrepancy between their calculated S and experimentally determined values. They have also used a different dielectric screening.

161. J. P. Walter and M. L. Cohen, Phys. Rev. B2, 1821 (1970).

162. A. B. Roitsin, Sov. Phys. Semicond. 8, 1 (1974).

163. F. P. Larkins, J. Phys. Chem. Solids 32, 965 (1971).

164. F. P. Larkins and A. M. Stoneham, J. Phys. C 4, 143, 154 (1971).

165. F. P. Larkins, J. Phys. C 4, 3065, 3077 (1971).

166. R. P. Messmer and G. D. Watkins in Radiation Damage and Defects in Semiconductors, Conf. Series No. 16, the Institute of Physics, London and Bristol (1972), p. 255.

167. D. Rouhani, M. Lannoo and P. Lenglart, Int. Conf. on Radiation Effects in Semicond., Albany, New York, USA, 24-28 Aug. 1970 (London, England: Gordon & Breach 1971), p.15.

168. J. Callaway and A. J. Hughes, Phys. Rev. 156, 860 (1967).

169. G. D. Watkins, Proc. Seventh Intern. Conf. on Physics of Semiconductors, Paris, 1964, Vol. 3, Radiation Damage in Semiconductors, Dunod, Paris; Academic Press, New York (1965), p.97.

170. J. A. Naber, C. E. Mallon and R. E. Leadon, Proceedings of the Int. Conf. on Radiation Damage and Defects in Semiconductors, Reading, Berks., England, 19-21 July 1972 (London, England: Inst. Phys. 1973), p.26.

171. A superlattice of vacancies has been considered by Messmer and Watkins for vacancies in diamond in Ref. 166. They used the Extended Hückel Method and their calculation is not self-consistent.

172. M. L. Cohen, M. Schlüter, J. R. Chelikowsky and S. G. Louie, Phys. Rev. B12, 5575 (1975).

173. J. C. Slater and C. F. Koster, Phys. Rev. 94, 1498 (1954).

174. Watkins and coworkers have used this type of simple picture to understand the EPR data on the Si vacancies.

175. H. A. Jahn and E. Teller, Proc. Roy. Soc. A161, 220 (1937).

176. R. A. Swalin, Phys. Chem. Solids 18, 290 (1961).

177. J. A. Appelbaum and D. R. Hamann, Phys. Rev. Lett. 32, 225 (1974); J. C. Phillips, Surf. Sci. 44, 290 (1974).

FIGURE CAPTIONS

Fig. 1. Calculated band structure at three volumes for fcc Cs along several axes of high symmetry in the Brillouin zone. The energy is given in eV and the energy origin is taken to be at Γ_1. The values for the volumes were (a) $V/V_o = 0.5$, (b) $V/V_o = 0.4$, (c) $V/V_o = 0.3$. The numbers along the bands indicate the d-character of the wavefunction.

Fig. 2. Density of states for Cs at $V/V_o = 0.5$ in units of states/eV atom. s, p, and d denote the components of the density of states from the three angular momentum states.

Fig. 3. Density of states for Cs at $V/V_o = 0.4$. See Fig. 2.

Fig. 4. Density of states for Cs at $V/V_o = 0.3$. See Fig. 2.

Fig. 5. Electronic charge density for the occupied states of Cs at $V/V_o = 0.5$ in the (100) plane. The charge density is in units of e/Ω where Ω is the primitive cell volume.

Fig. 6. Electronic charge densities for the occupied states of Cs at $V/V_o = 0.4$ in the (100) plane. (a) Band 1, (b) Band 2, (c) Sum of band 1 and band 2.

Fig. 7. Electronic charge densities for the occupied states of Cs at $V/V_o = 0.3$ in the (100) plane. (a) Band 1, (b) Band 2, (c) Sum of band 1 and band 2.

Fig. 8. A section of the Fermi surface of Cs at $V/V_o = 0.5$. The hatched region represents the occupied states.

Fig. 9. A section of the Fermi surface of Cs at $V/V_o = 0.4$. The hatched region represents the occupied states. The cross hatched region represents the component of the Fermi surface coming from band 2.

Fig. 10. A section of the Fermi surface of Cs at $V/V_o = 0.3$. See Fig. 9.

Fig. 11. The irreducible polarization propagator in the RPA for periodic systems.

Fig. 12. Calculated $\epsilon_2(\omega)$ for Si, with (dashed curve) and without (dotted curve) local-field effects, compared with experiment (solid curve) from Ref. 49.

Fig. 13. Calculated energy-loss spectra for Si, with (dashed curve) and without (dotted curve) local-field effects, compared with experiment (solid curve) from Ref. 49.

Fig. 14. The frequency dependent kernel K(δ) (N(0)V parameter) for a screened Coulomb interaction using the semiconductor and metallic dielectric function model of Inkson and Anderson. Parameters appropriate for Aℓ and Si were used. (b) The frequency dependent kernel K(δ) (N(0)V parameter) for a screened Coulomb interaction using the Lindhard dielectric function (parameters are appropriate for Aℓ). (c) The frequency dependent kernel K(δ) (N(0)V parameter) for a screened Coulomb interaction using a dielectric function calculated from a pseudopotential band structure for Ge.

Fig. 15. Nb^{+5} ionic pseudopotentials. V_s, V_p and V_d plotted as a function of r.

Fig. 16. Electronic band structure of Nb. Energy scale is zeroed at E_F.

Fig. 17. Density of states for bulk Nb. (a) Present calculation and (b) Mattheiss' calculation from Ref. 66.

Fig. 18. Contour plots of total valence charge distribution of bulk Nb in the (a) (110) plane and (b) (100) plane. The charge density is normalized to 1 electron per unit cell.

Fig. 19. Partial charge densities for states in the energy ranges (a) -6.5 to -2.0 eV, (b) -2.0 to -0.75 eV (c) -0.75 to 0.60 eV and (d) 0.60 eV to 5.85 eV. The charge density for each energy range is normalized to 1 electron per unit cell and is plotted on the (110) plane.

Fig. 20. The pair-breaking parameter ρ_1 as a function of temperature from the solutions of the gap equation, Eq. (44).

Fig. 21. $T_c/\sqrt{\langle\omega^2\rangle}$ plotted versus λ. The solid curves are results calculated using the new T_c equation (Eq. 55) for various shapes of α^2F. The same curves also represent the exact solutions of the Eliashberg equations (see text) since the two results are indistinguishable on the scale of the plot. The dash curve is the McMillan equation using the prefactor $\sqrt{\langle\omega^2\rangle}/1.20$ instead of $\theta_D/1.45$. The experimental points are taken from tunneling data.[84]

Fig. 22. Calculated T_c from Eq. (55) plotted versus experimental T_c for six elemental superconductors. The experimental values are taken from tunneling data.[84]

Fig. 23. Steps in the self-consistent procedure for the calculation of the electronic structure of localized configurations.

Fig. 24. Perspective view of the Si crystal structure projected on a (110) plane. The [111] direction is vertical. The (111) surface is obtained by cutting the vertical bonds in a horizontal plane.

Fig. 25. Total valence charge distribution for an unrelaxed Si (111) surface. The charge is plotted as contours in a (110) plane intersecting the (111) surface at right angles. The plotting area starts in the vacuum and extends about 4-1/2 atomic layers into the crystal. The atomic positions and bond directions are indicated by dots and heavy lines respectively. The contours are normalized to electrons per Si bulk unit cell volume $\Omega_0 = \frac{a^2 c}{4}$.

Fig. 26. Two-dimensional band structure of a twelve layer Si (111) film (relaxed surface model). The energy is plotted as a function of $k_{\parallel}$ in the two-dimensional hexagonal Brillouin zone. The various surface states or strong surface resonances at high symmetry points are indicated by dots and labelled according to the description in the text.

Fig. 27. Density of states curves for the self-consistent results on twelve layer films for the relaxed (broken line) and unrelaxed (solid line) surface geometry. Surface states are indicated by arrows and labelled according to Fig. 26. Inserted is the density of states in the vicinity of the

fundamental gap for a six layer (2×1) reconstructed surface model.

Fig. 28. Charge density contours in a (110) plane cutting the relaxed (111) surface of the longitudinal back bond state $K_{\ell b}$.

Fig. 29. Charge density contours of the occupied part K_d of the dangling bond states for the relaxed surface model.

Fig. 30. Schematic representation of the ideal and (2×1) reconstructed Si (111) surface. The reconstruction is done according to Haneman's model[92] and leaves the surface buckled as indicated by arrows. The slight lateral shifts of second layer atoms are also indicated by arrows.

Fig. 31. Two-dimensional band structure around the fundamental gap for a (2×1) reconstructed Si (111) twelve layer film. The folded back Brillouin zone is indicated in the insert.

Fig. 32. Calculated joint density of states curve for low energy transitions between dangling bond bands of (2×1) Si (111) (top). Also indicated is the experimental absorption $\varepsilon_2(\omega)$ as obtained in Ref. 99. The bottom figure shows the regular density fo states for the two dangling bond bands (d_{in} and d_{out}) of (2×1) Si (111).

Fig. 33. Charge density contour plots for the dangling bond states d_{out}(top) and d_{in} (bottom) of (2×1) Si (111). The charge is plotted in a (210) plane of (2×1) Si which corresponds to the (110) plane of (1×1) Si. The raised and lowered atoms are marked by arrows.

Fig. 34. Local density of states in arbitrary units for a relaxed (110) surface of GaAs. The local density of states at the surface layer for the ideal case is also displayed.

Fig. 35. Density of states (in arbitrary units) of the empty cation derived surface band for both the ideal and relaxed cases.

Fig. 36. Pseudocharge density of the cation surface states for a relaxed surface. The charge density contour map is normalized to one electron per unit cell, $\Omega_c = 812$ Å^3.

Fig. 37. The top figure shows the charge density averaged parallel to the surface and plotted as a function into the bulk for the surface state at K at 0.07 Ry. The bottom figure shows the charge density for this state in the (110) plane. The charge density is normalized to 1 electron per unit cell.

Fig. 38. Brillouin zone for the 2-dimensional square lattice and the 3-dimensional bcc lattice.

Fig. 39. Projected bulk band structure for the (001) surface of Nb. (see text)

Fig. 40. Extents of the two major absolute gaps in the projected band structure of the Nb (001) surface.

Fig. 41. Total valence charge density of the Nb (001) surface plotted on (a) the (110) plane and (b) the (100) plane. The charge density is normalized to one electron per unit cell.

Fig. 42. Calculated local density of states curves for the Nb (001) surface.

Fig. 43. Difference curve for the local density of states at the Nb (001) surface. (See text)

Fig. 44. Surface bands (dashed curves) and the projected band structure for the Nb (001) surface.

Fig. 45. Charge-density contour plots for the three energy regions (a) region A, (b) region B, (c) region C. (see text) The charge density for each region is normalized to 1 electron per unit cell and is plotted for a (100) plane cutting the Nb (001) surface.

Fig. 46. Charge density distribution of a T1 surface state at $\underline{k} = (3/8, 1/4)\ 2\pi/a_c$ at E = 1.6 eV plotted on (a) the (110) plane and (b) the (100) plane. The charge density is normalized to 1 electron per unit cell.

Fig. 47. Charge-density contour plot of a T2 surface state at $\underline{k} = (3/8,1/4)2\pi/a_c$ at E = 0.8 eV. Plotting planes and normalization are the same as in Fig. 46.

Fig. 48. Charge-density contour plot of a T3 surface state at $\underline{k} = (3/8,1/4)2\pi/a_c$ at E = 0.4 eV. See Fig. 46 for plotting planes and normalization.

Fig. 49. Charge-density contour plot of a T4 surface state at $\underline{k} = (3/8,1/4)2\pi/a_c$ at E = -1.7 eV. See Fig. 46 for plotting planes and normalization.

Fig. 50. Charge density distribution of a T5 surface state at $\underline{k} = (3/8,1/4)2\pi/a_c$ at E = -2.0 eV plotted on the (110) plane. The charge density is normalized to one electron per unit cell.

Fig. 51. (a) Total valence charge density contours in a (110) plane. The Si atoms are indicated by dots. (b) Total valence charge density averaged parallel to the interface and plotted along the direction perpendicular to the interface. The charge densities are normalized to one electron per unit cell.

Fig. 52. (a) Contour plot of the final self-consistent potential V_{sc} in a (110) plane. (b) Final self-consistent potential averaged parallel to the interface and plotted along the direction perpendicular to the interface. The potential values are in rydbergs.

Fig. 53. Local density of states in arbitrary units as defined by Eq. (83). The regions are as shown in Fig. 51(b).

Fig. 54. Difference local density of states (DLDOS) obtained by subtracting the LDOS of region VI from that of region IV. The units are the same as in Fig. 53.

Fig. 55. Charge density contours for states with energy below -11.5 eV in the same plane and normalization as in Fig. 51(a).

Fig. 56. (a) Charge density contours for MIGS with energy between 0 and 1.2 eV in the same plane and normalization as in Fig. 51(a). (b) Charge density in (a) averaged parallel to the interface and plotted along the direction perpendicular to the interface.

Fig. 57. Schematic diagram of the bottom two bands of the Si band structure (horizontally hatched) projected to the two-dimensional Brillouin zone. Superimposed on it is the

projected Al conduction band (vertically hatched). S_K denotes the interface states discussed in the text.

Fig. 58. Charge density contours for the interface states at K in the same plane and normalization as in Fig. 51(a).

Fig. 59. Total valence charge density for the m/GaAs interface plotted in the $(1\bar{1}0)$ plane containing the (a) Ga surface atom and (b) As surface atom. The charge density has been normalized to one electron per unit cell.

Fig. 60. Total valence charge density for the m/ZnSe interface plotted in the $(1\bar{1}0)$ plane containing the (a) Zn surface atom and (b) Se surface atom. Normalization is as in Fig. 59.

Fig. 61. Total valence charge density for the m/ZnS interface plotted in the $(1\bar{1}0)$ plane containing the (a) Zn surface atom and (b) S surface atom. Normalization is as in Fig. 59.

Fig. 62. Local density of states for the m/GaAs interface in arbitrary units as defined by Eq. (83).

Fig. 63. Local density of states for the m/ZnSe interface.

Fig. 64. Local density of states for the m/ZnS interface.

Fig. 65. Charge distributions of the penetrating tails of the MIGS in the semiconductor thermal gap. $\bar{\rho}(z)$ is the total charge density for these states averaged parallel to the interface with $z = 0$ at the edge of the jellium core.

Fig. 66. Charge density of the s-like sulfur interface states in the same plane as Fig. 61(b). The charge density is again normalized to one electron per unit cell.

Fig. 67. Charge density of an interface state at M at -5.1 eV. (See text.)

Fig. 68. Charge density of an interface state at M at -4.6 eV. (See text.)

Fig. 69. Experimental values of the barrier heights for four semiconductors in contact with various metals. X_m is the electronegativity of the metal in the Pauling-Gordy scale. Data were taken from Ref. 142 (Si) and Ref. 149 (GaAs, ZnSe, ZnS).

Fig. 70. The index of interface behavior S from Ref. 137.

Fig. 71. Surface density of states as defined in Eq. (85).

Fig. 72. Structure of cubic Si (a) and an undistorted Si lattice vacancy (b).

Fig. 73. Total, self-consistent valence charge density displayed in a (110) plane for a neutral Si vacancy in an ideal, unreconstructed structure. The charge values are normalized to one electron per unit cell which extends over 53 atoms and one vacancy.

Fig. 74. (top) Crystalline density of states for Si with the position of strong resonant and vacancy levels at Γ. (bottom) Energies at Γ for the perfect 54-atom unit cell crystal using an empirical pseudopotential, for the ideal vacancy using the same empirical pseudopotential and for the ideal vacancy using the final self-consistent pseudopotential are given. Note the lowering of the vacancy level in the funcamental gap.

Fig. 75. Charge density plots in a (110) plane (area enclosed by dashed lines in Fig. 73) of (a) the vacancy states in the fundamental gap and (b) the strong resonance around -8.2 eV.

Fig. 76. Schematic energy diagram of dispersion between Γ and X and order of the Si vacancy levels in the fundamental gap as a function of different reconstruction models. For Rec I and Rec II, X is along the distorted [100] direction.

Fig. 77. Radial dependence of various Si atomic and vacancy potentials.

Fig. 78. Total self-consistent valence charge density for a neutral Si vacancy in a reconstructed environment (Rec I). The distances between the four atoms surrounding the vacancy are pair wise decreased, resulting in a [100] uniaxial distortion and a net relaxation towards the vacancy. Units are as in Fig. 73.

Fig. 79. Total self-consistent valence charge density for a neutral Si vacancy in a reconstructed environment (Rec II). The distances between the four atoms surrounding the vacancy are pair wise increased, resulting in a [100] uniaxial distortion and a net relaxation away from the vacancy. Units are as in Fig. 73.

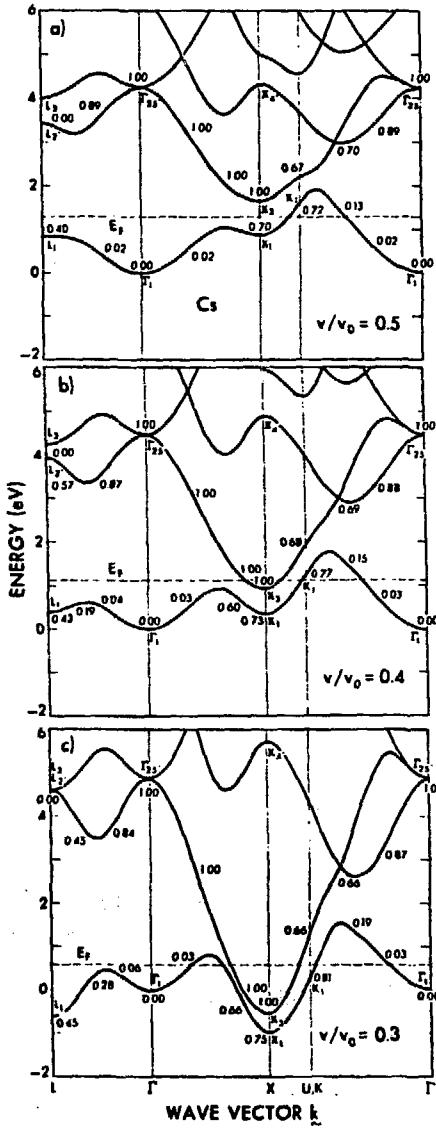
a)
b)
c)
Cs
v/v0 = 0.5
v/v0 = 0.4
v/v0 = 0.3
E_F
ENERGY (eV)
WAVE VECTOR k
L Γ X U,K Γ
XBL 769-10391

Fig. 1.

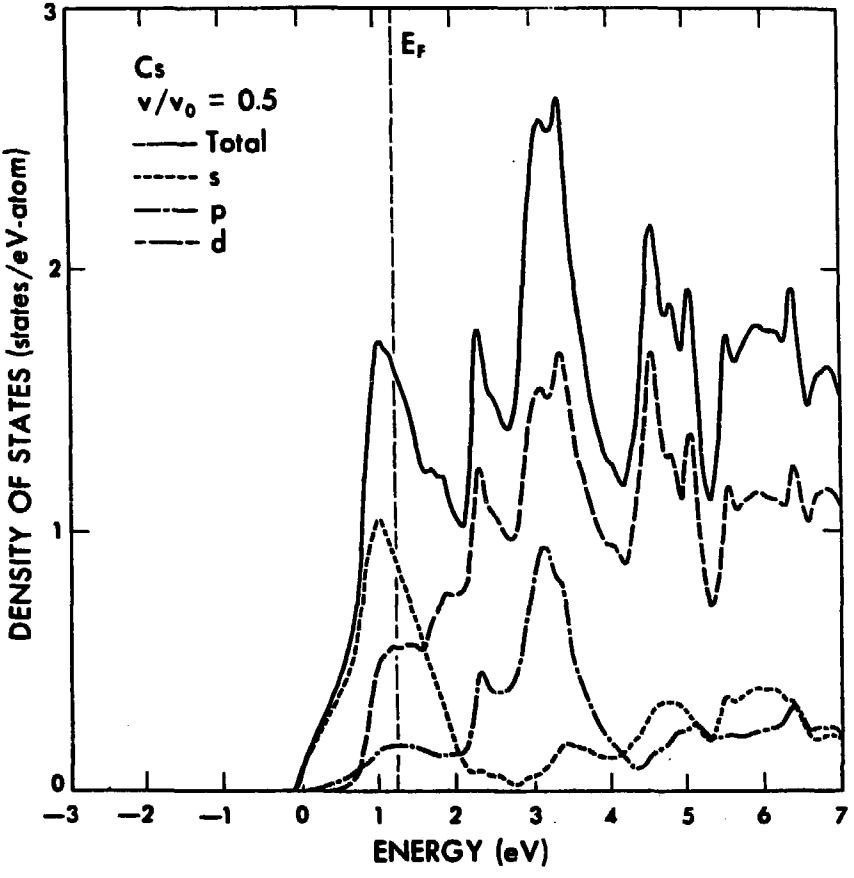

XBL 769-10377

Fig. 2.

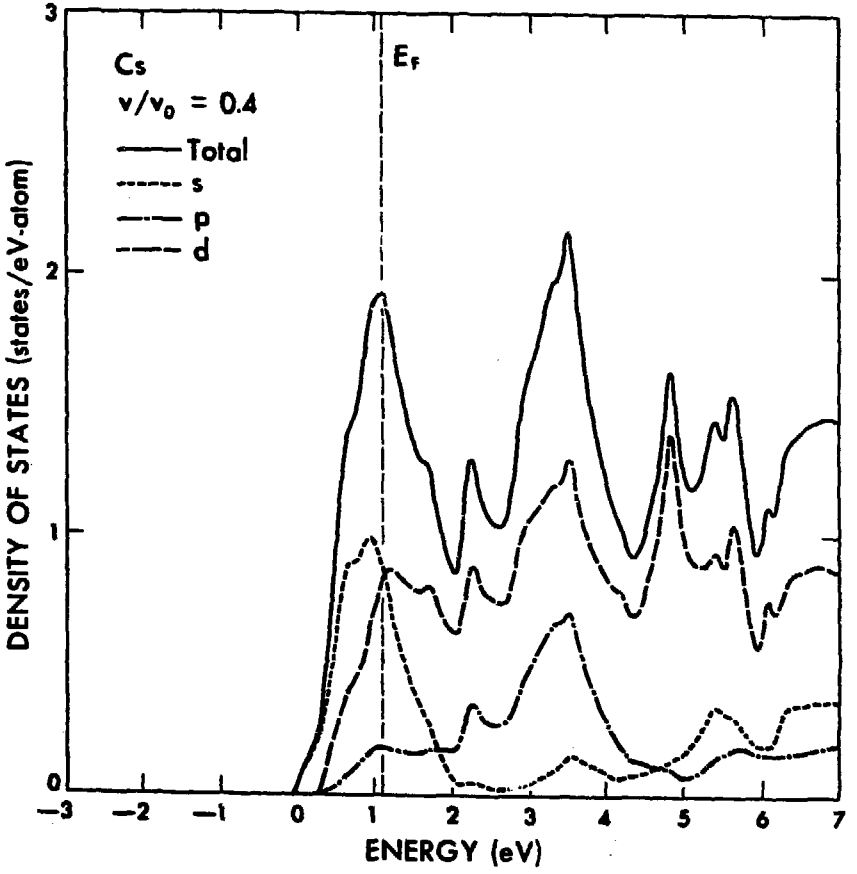
Cs
v/v0 = 0.4
Total
s
p
d
EF
DENSITY OF STATES (states/eV-atom)
ENERGY (eV)
3
2
1
0
−3
−2
−1
0
1
2
3
4
5
6
7
XBL 769-10340

Fig. 3.

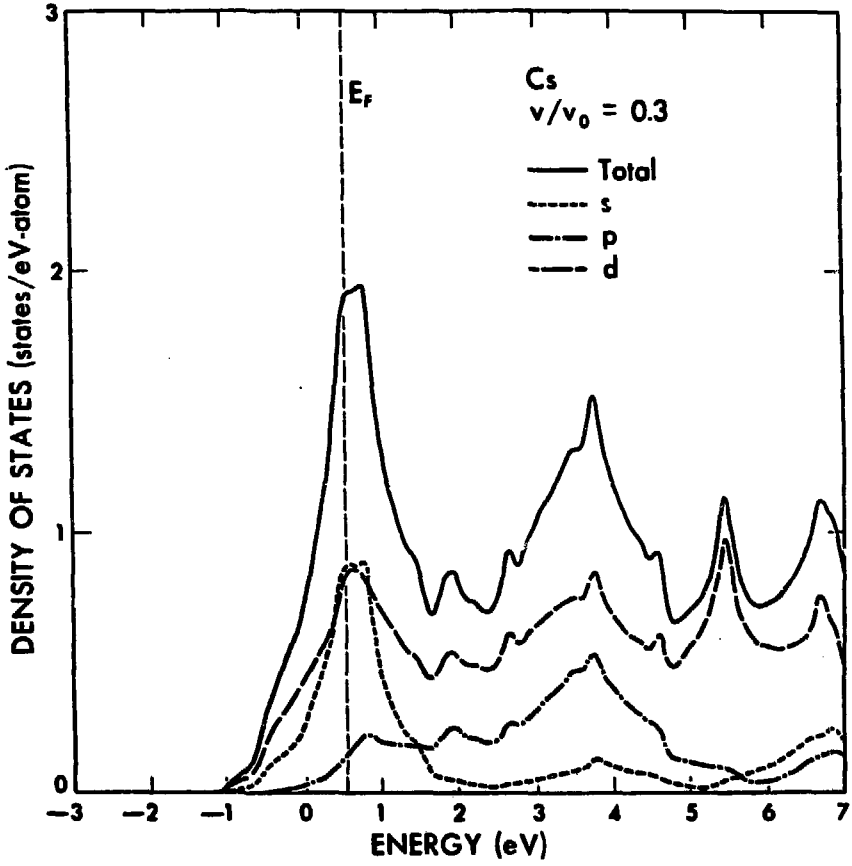

XBL 769 10388

Fig. 4.

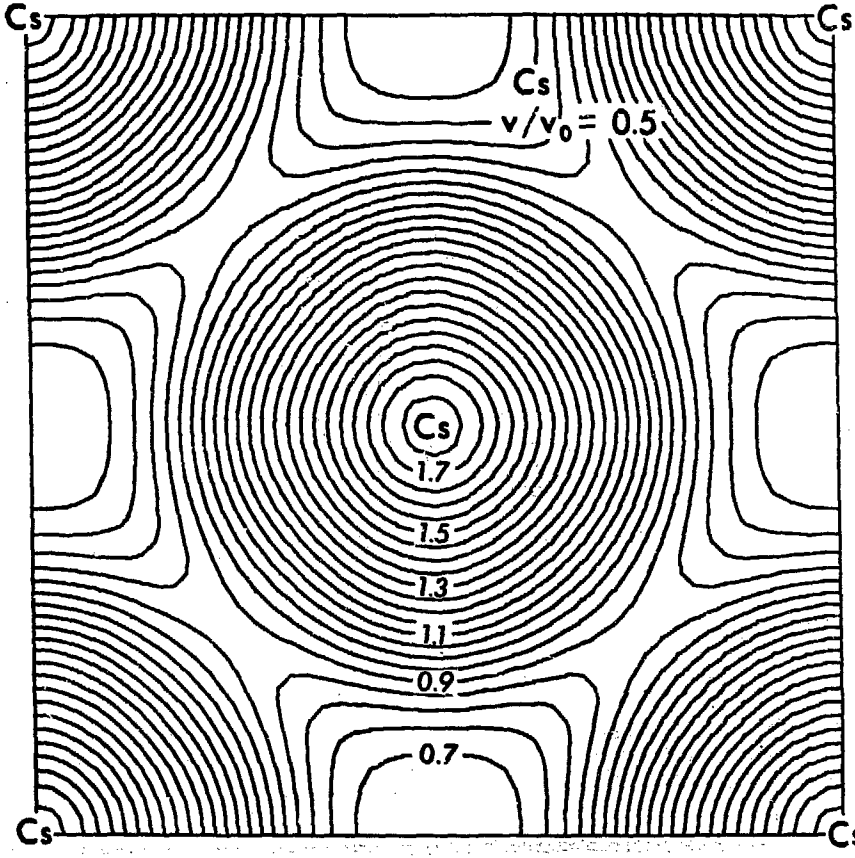

XBL 769-10379

Fig. 5.

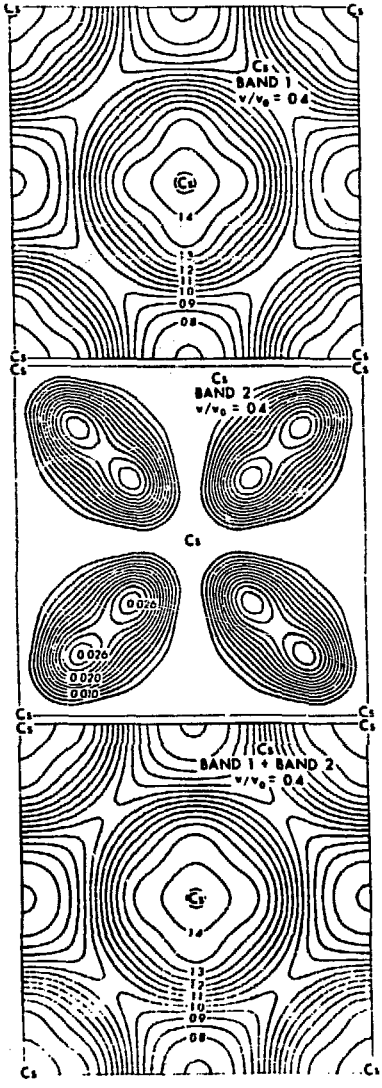

XBL 769-10384

Fig. 6.

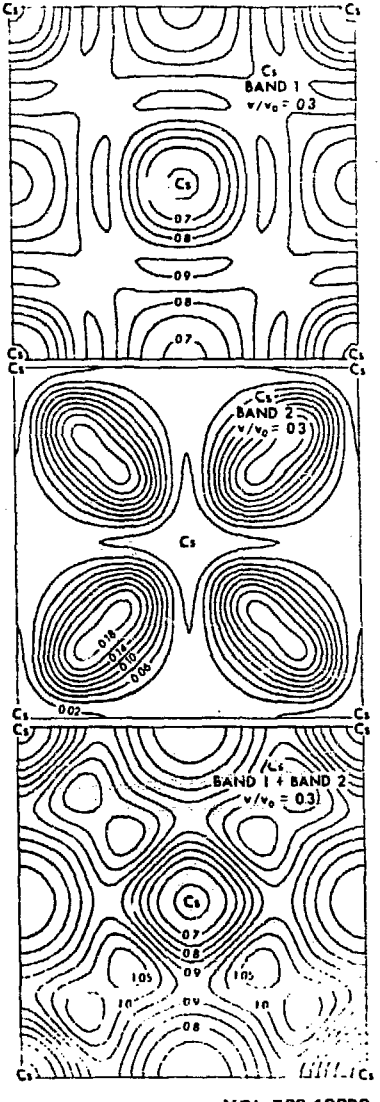

XBL 769-10390

Fig. 7.

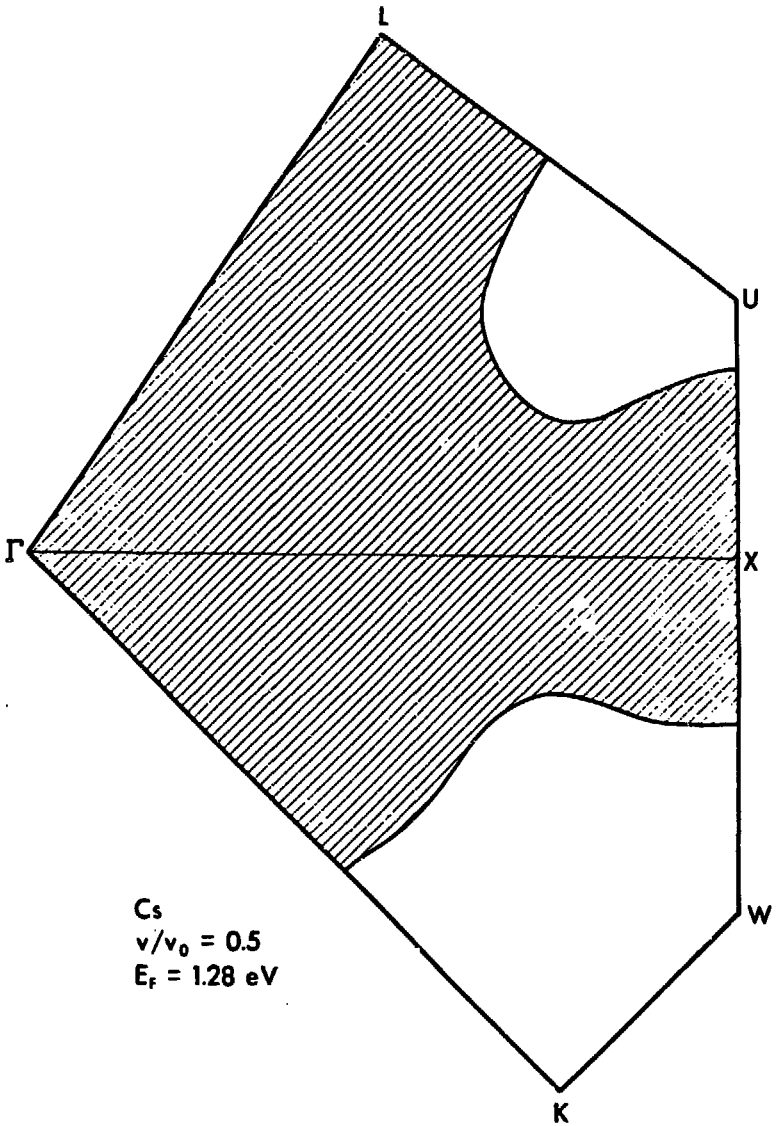

XBL 769-10367

Fig. 8.

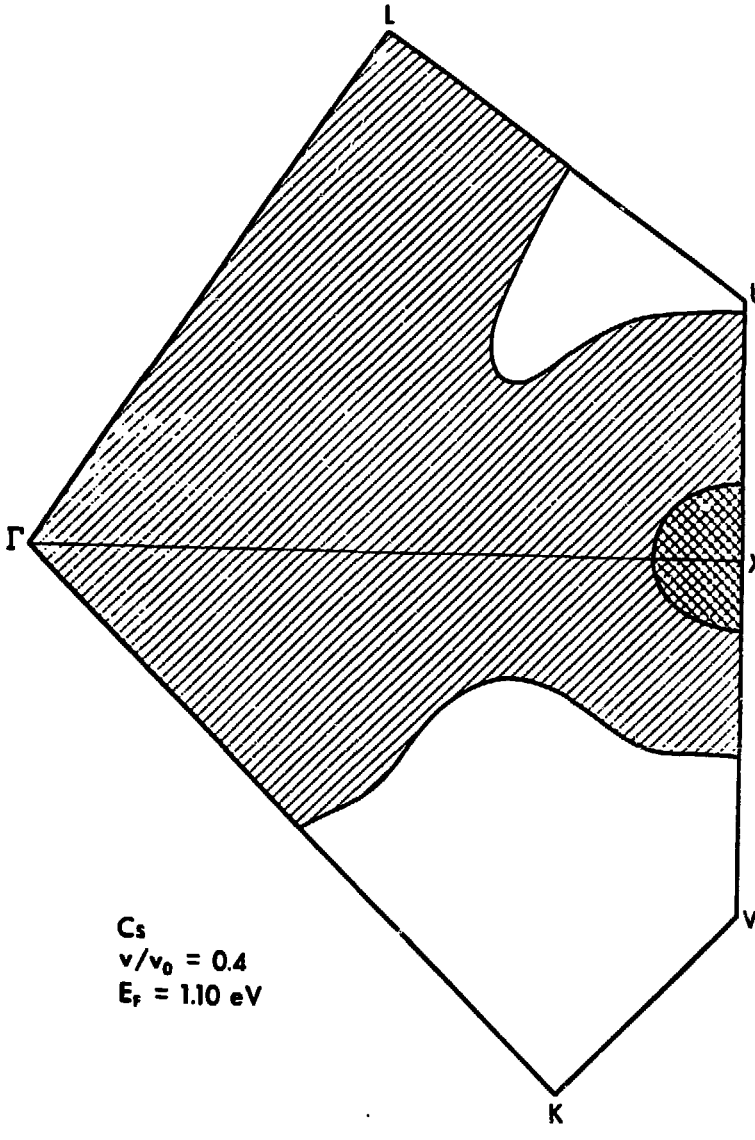

XBL 769-10352

Fig. 9.

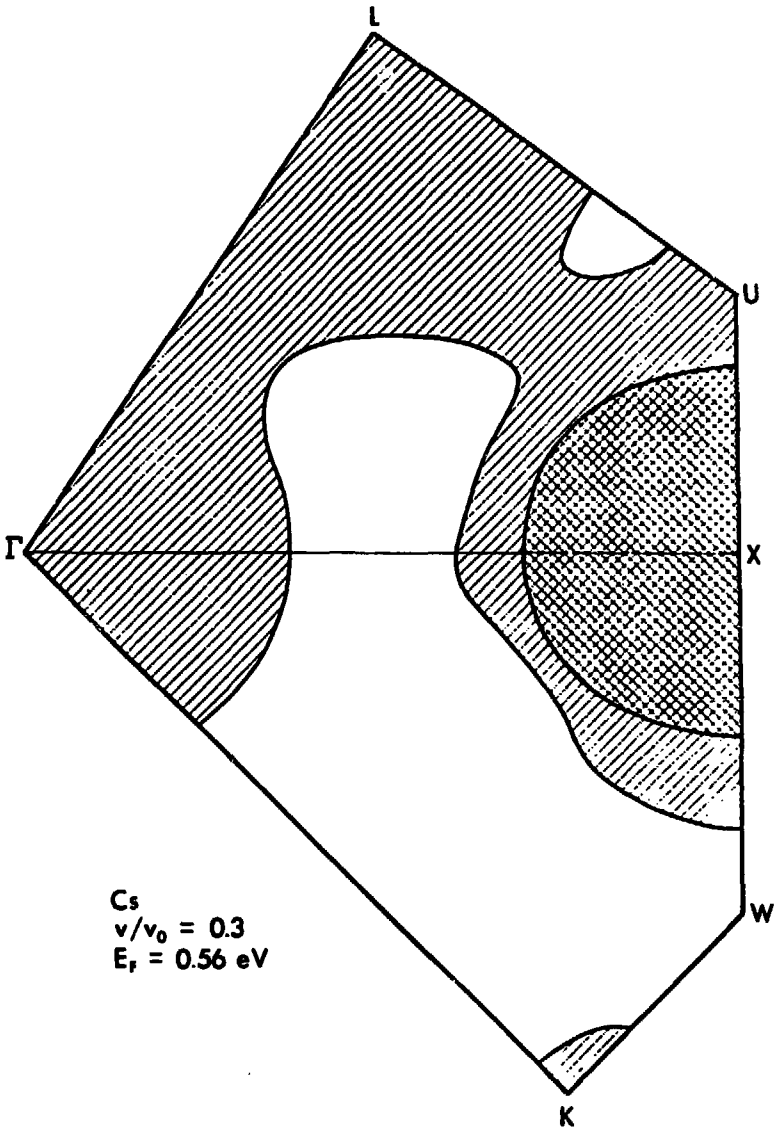

XBL 769-10342

Fig. 10.

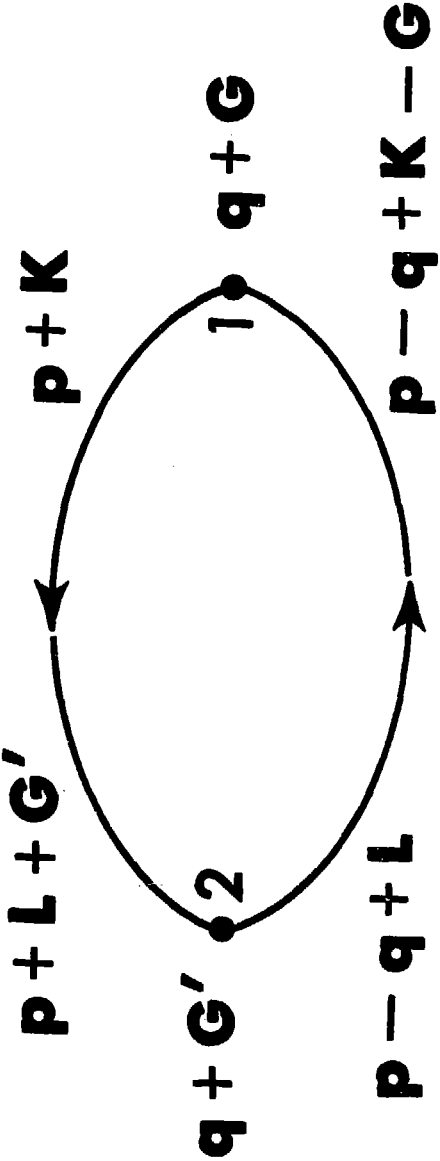

XBL 769-10376

Fig. 11.

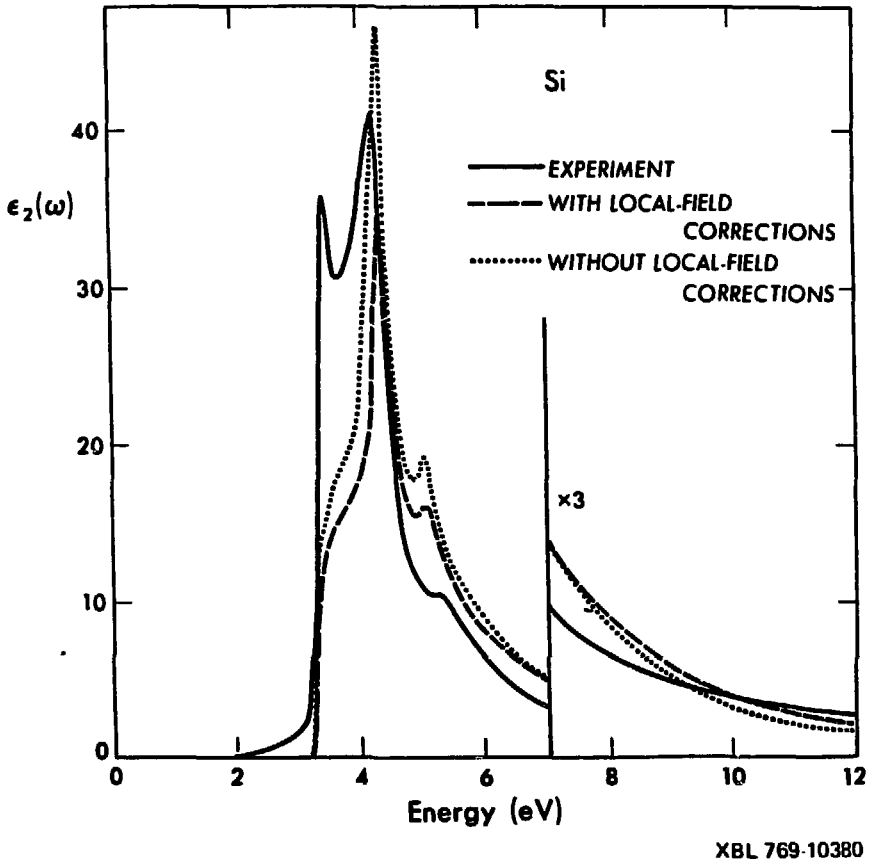
Si
EXPERIMENT
WITH LOCAL-FIELD CORRECTIONS
WITHOUT LOCAL-FIELD CORRECTIONS
×3
$\epsilon_2(\omega)$
Energy (eV)
0
10
20
30
40
0
2
4
6
8
10
12
XBL 769-10380

Fig. 12.

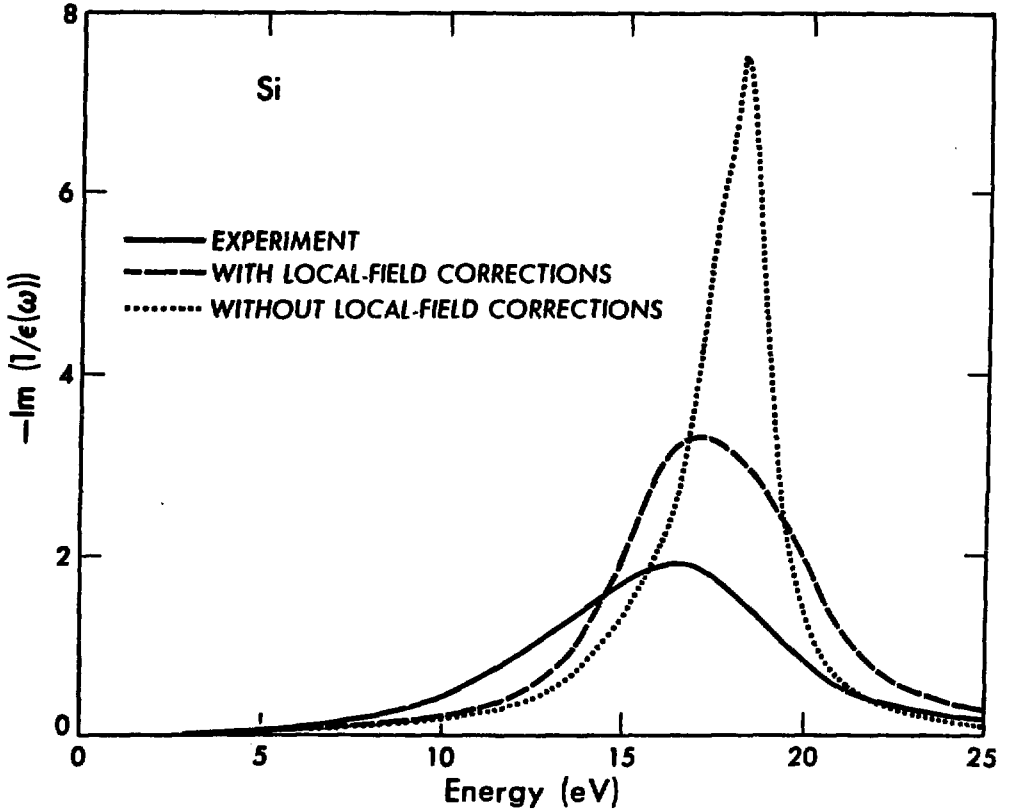

XBL 769-10372

Fig. 13.

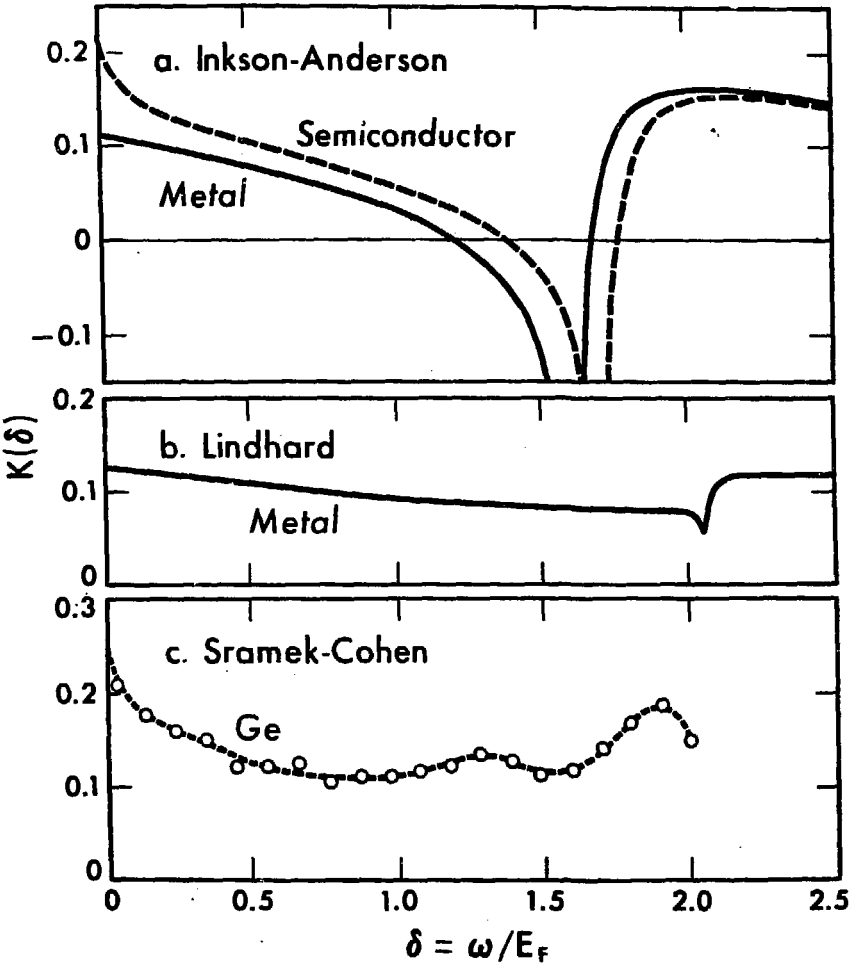

XBL 769-10381

Fig. 14.

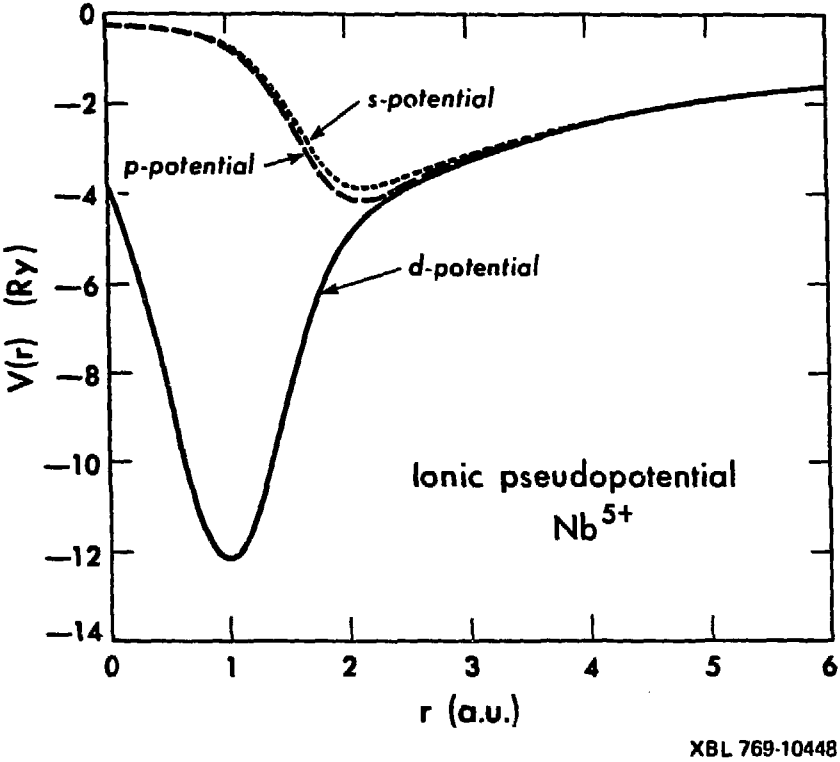
0
−2
−4
−6
−8
−10
−12
−14
V(r) (Ry)
s-potential
p-potential
d-potential
Ionic pseudopotential
Nb5+
0
1
2
3
4
5
6
r (a.u.)
XBL 769-10448

Fig. 15.

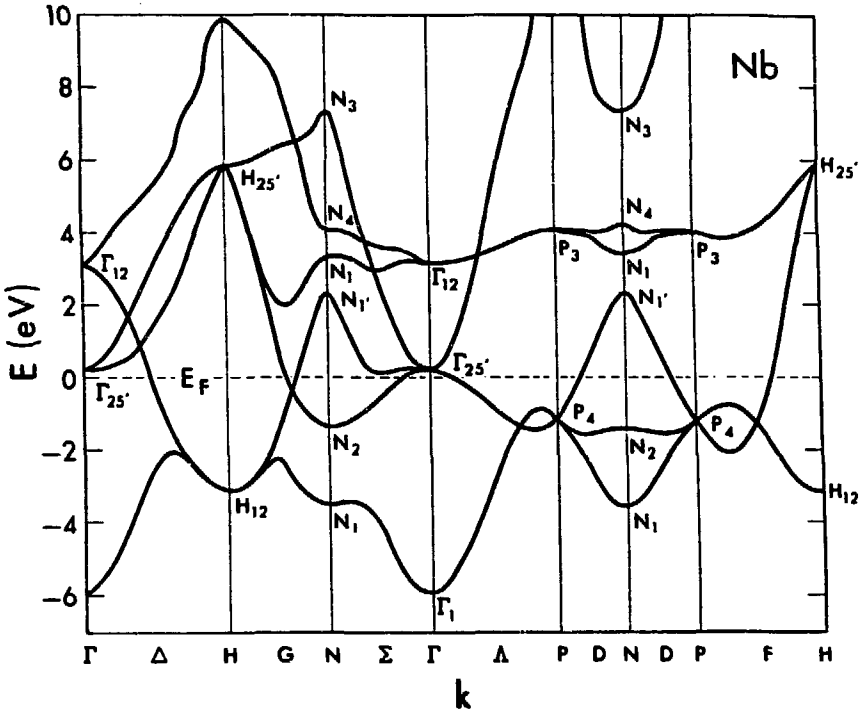

XBL 769-10447

Fig. 16.

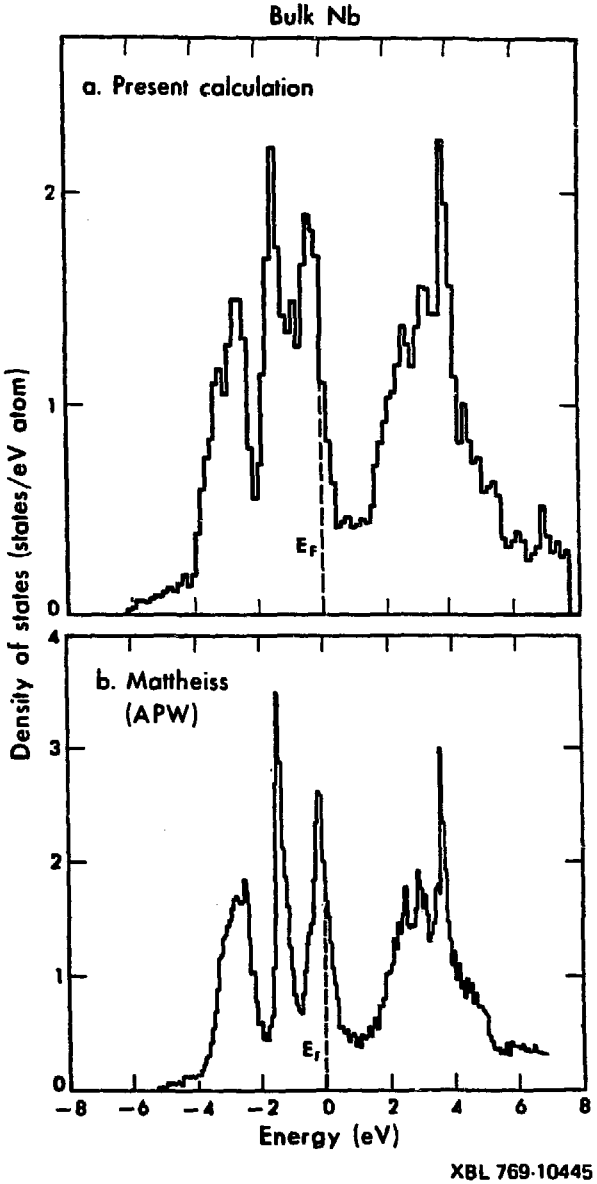
Bulk Nb
a. Present calculation
b. Mattheiss
(APW)
E_F
E_f
Density of states (states/eV atom)
Energy (eV)
XBL 769-10445

Fig. 17.

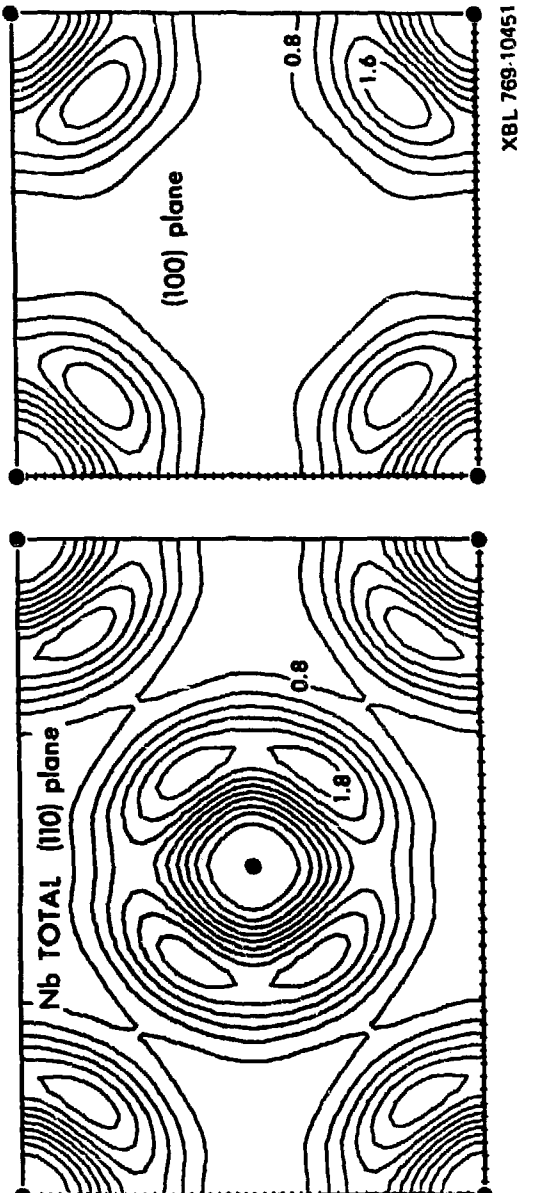

Fig. 18.

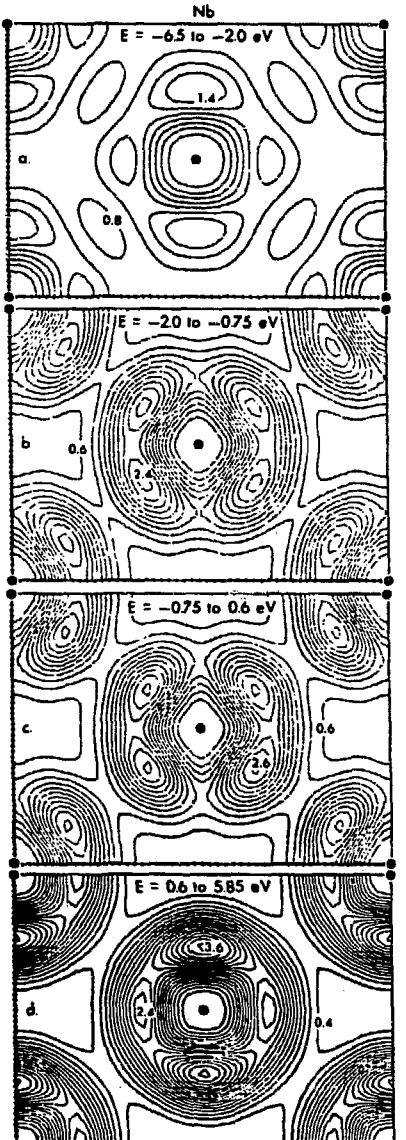

XBL 769-10444

Fig. 19.

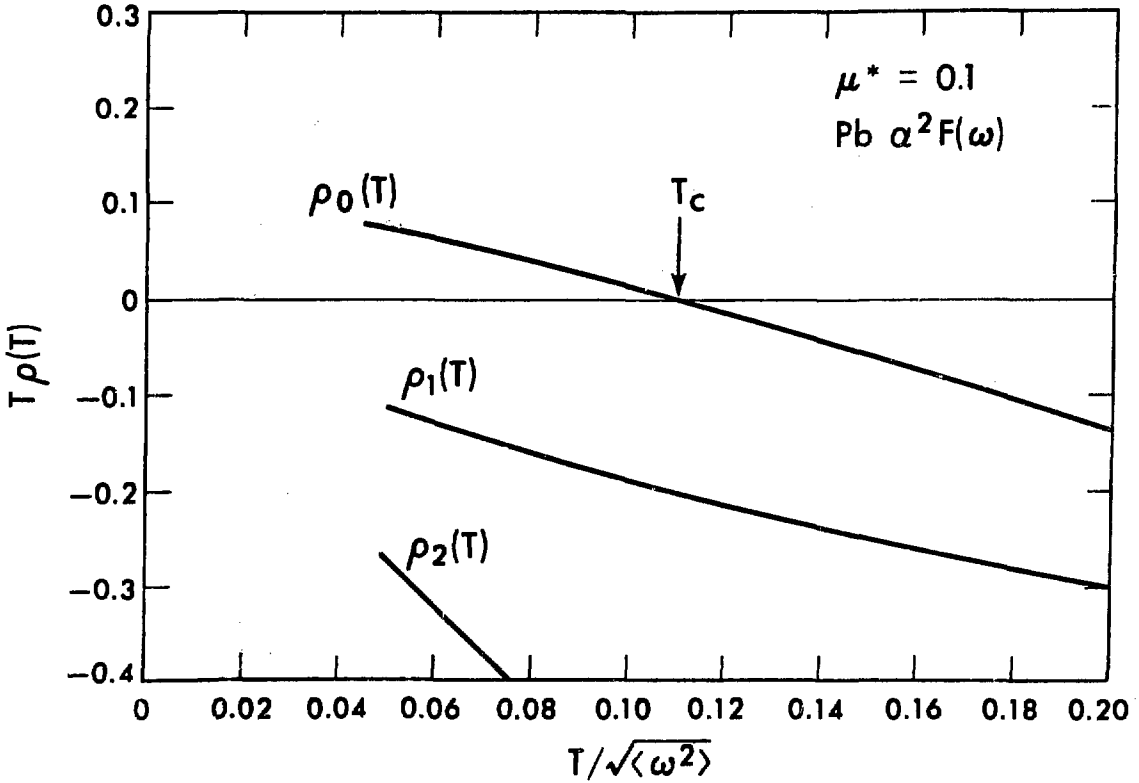

XBL 769-10354

Fig. 20.

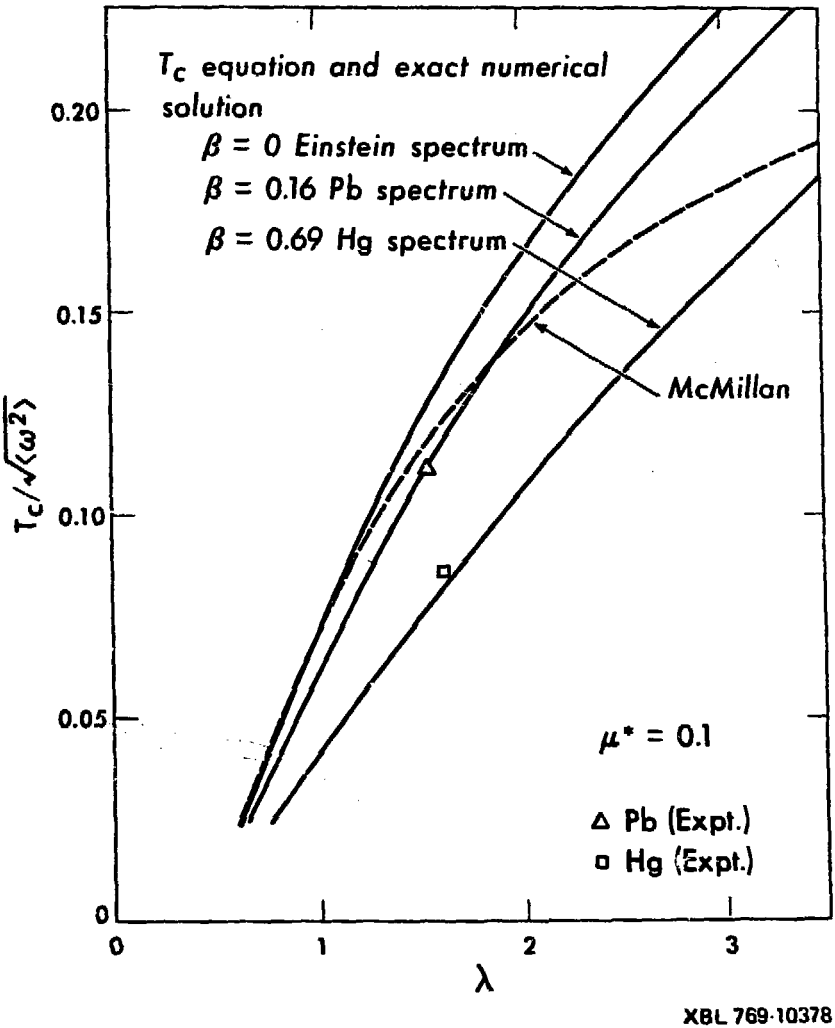
T_c equation and exact numerical solution
β = 0 Einstein spectrum
β = 0.16 Pb spectrum
β = 0.69 Hg spectrum
McMillan
μ^* = 0.1
Δ Pb (Expt.)
□ Hg (Expt.)
$T_c/\sqrt{\langle\omega^2\rangle}$
λ
0.20
0.15
0.10
0.05
0
0
1
2
3
XBL 769-10378

Fig. 21.

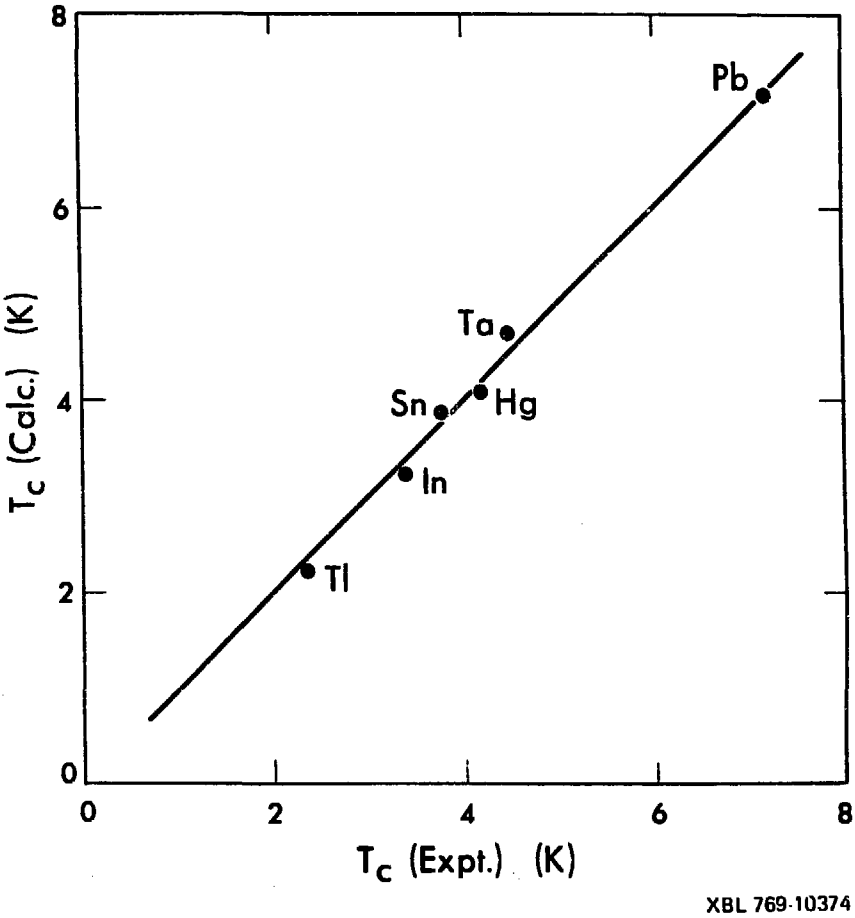

Fig. 22.

STEPS IN ACHIEVING SELF-CONSISTENCY

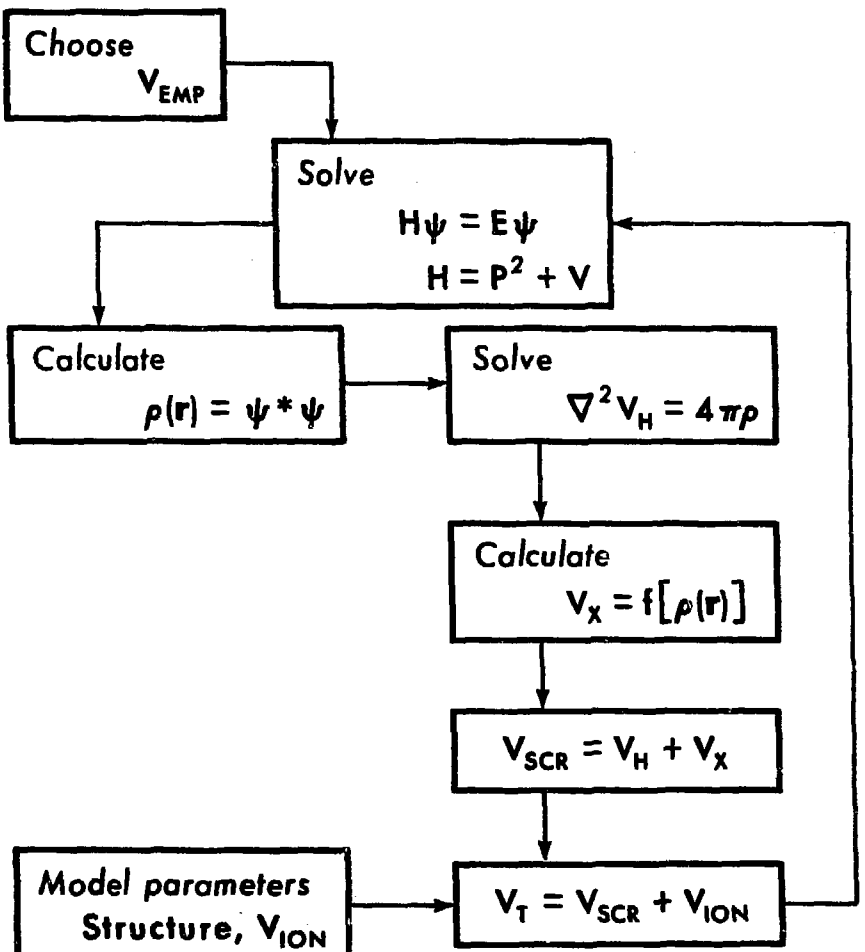

XBL 769-10369

Fig. 23.

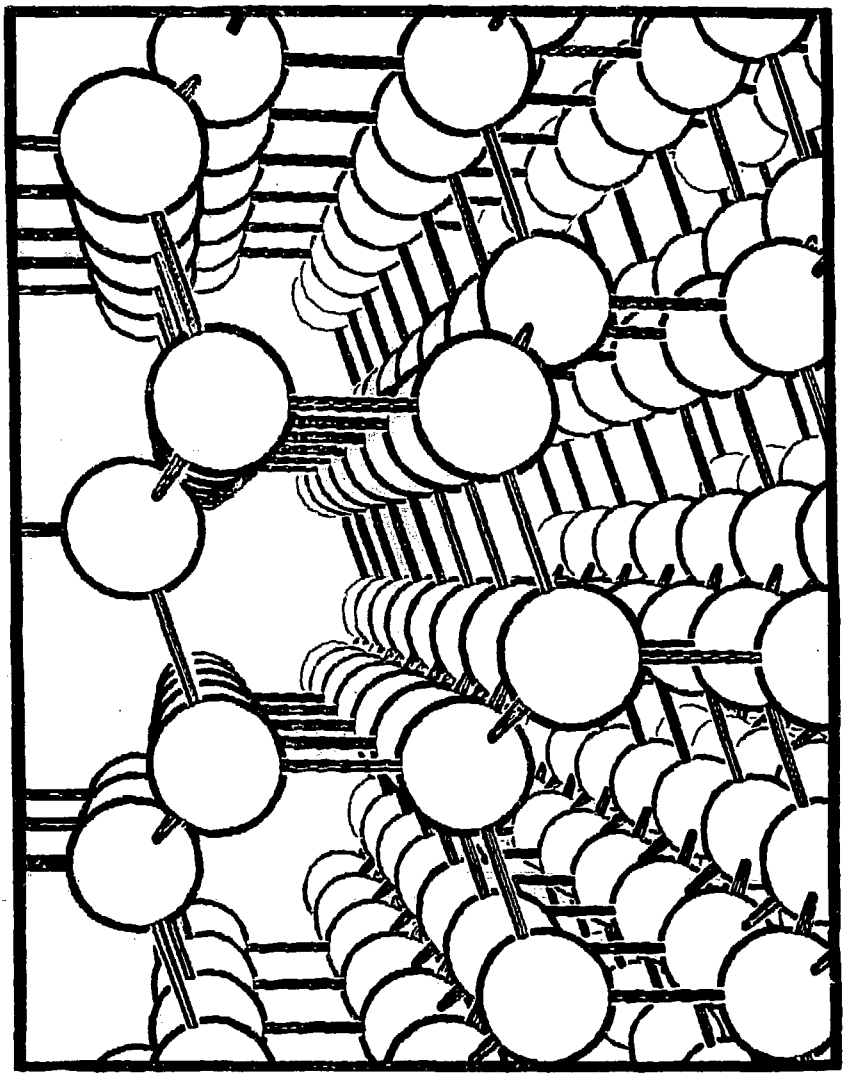

XBL 769-10339

Fig. 24.

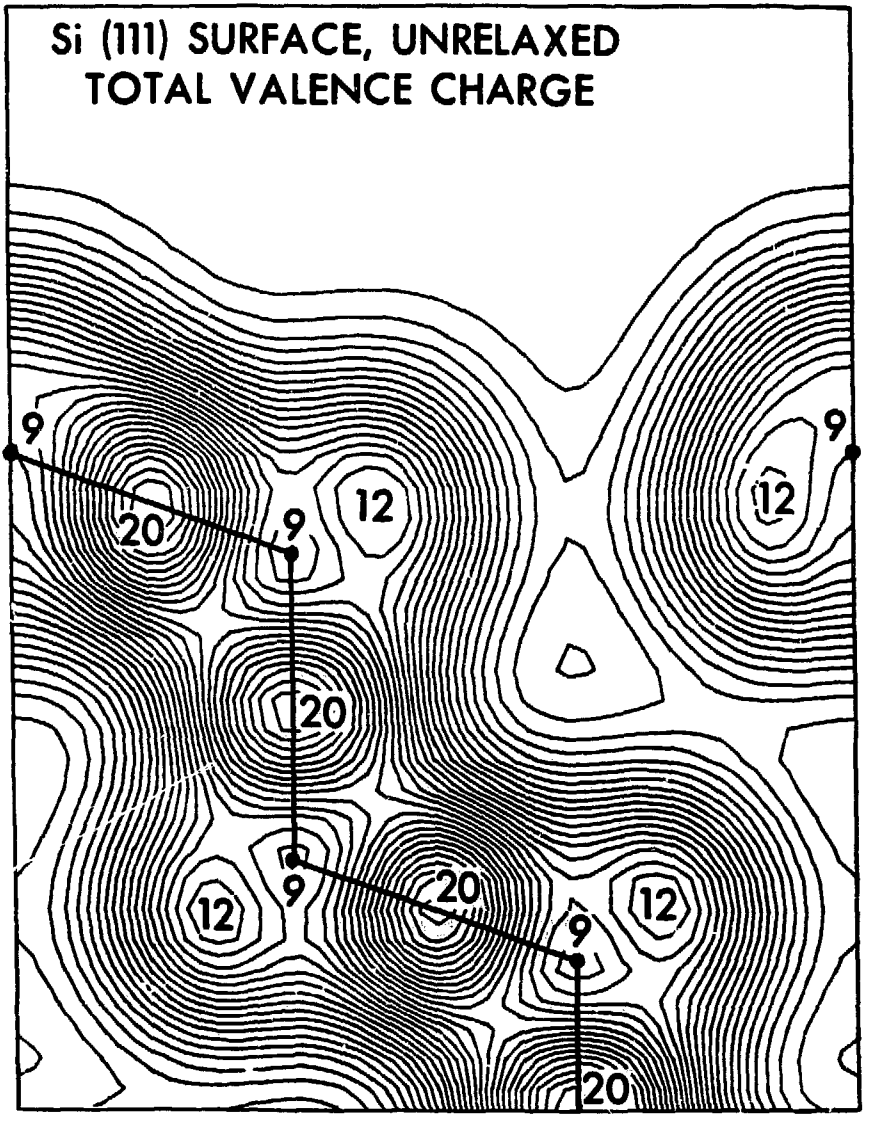

XBL 769-10371

Fig. 25.

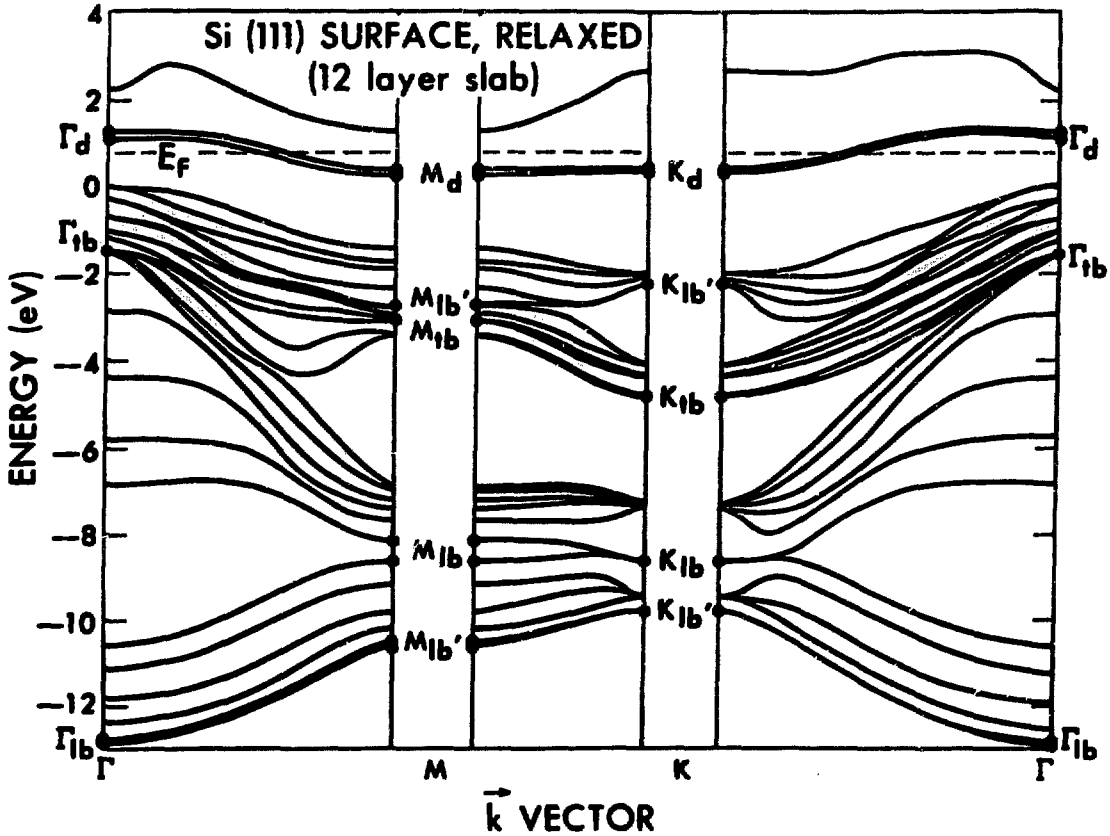

XBL 769-10348

Fig. 26.

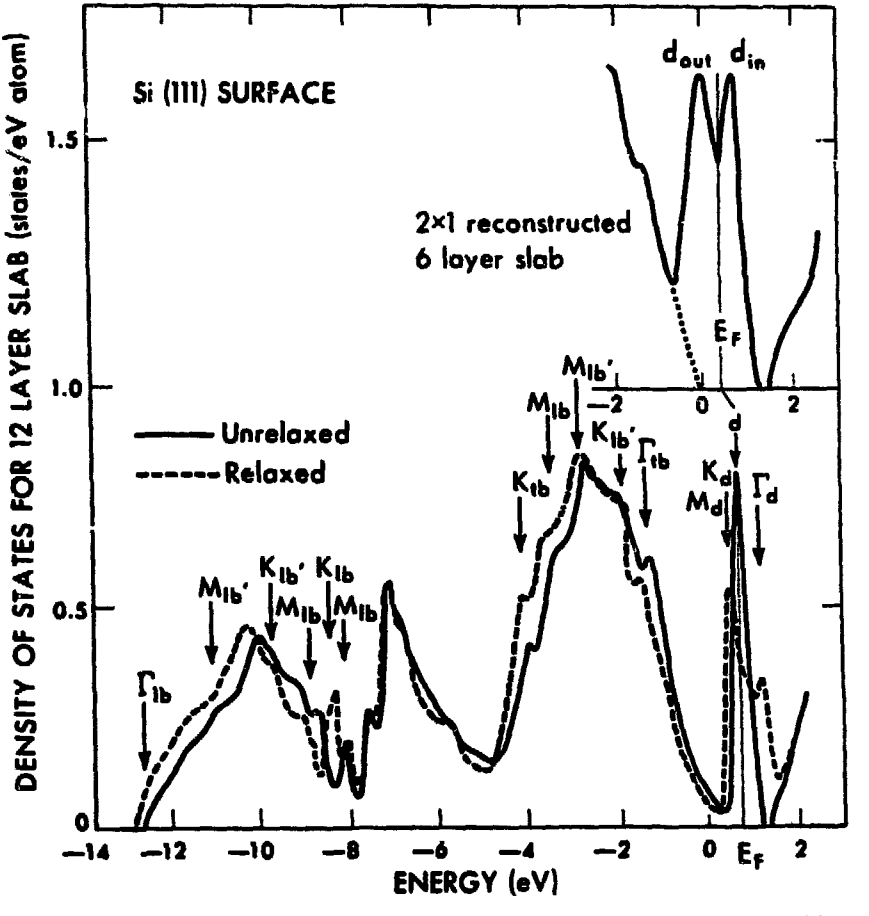

XBL 769-10385

Fig. 27.

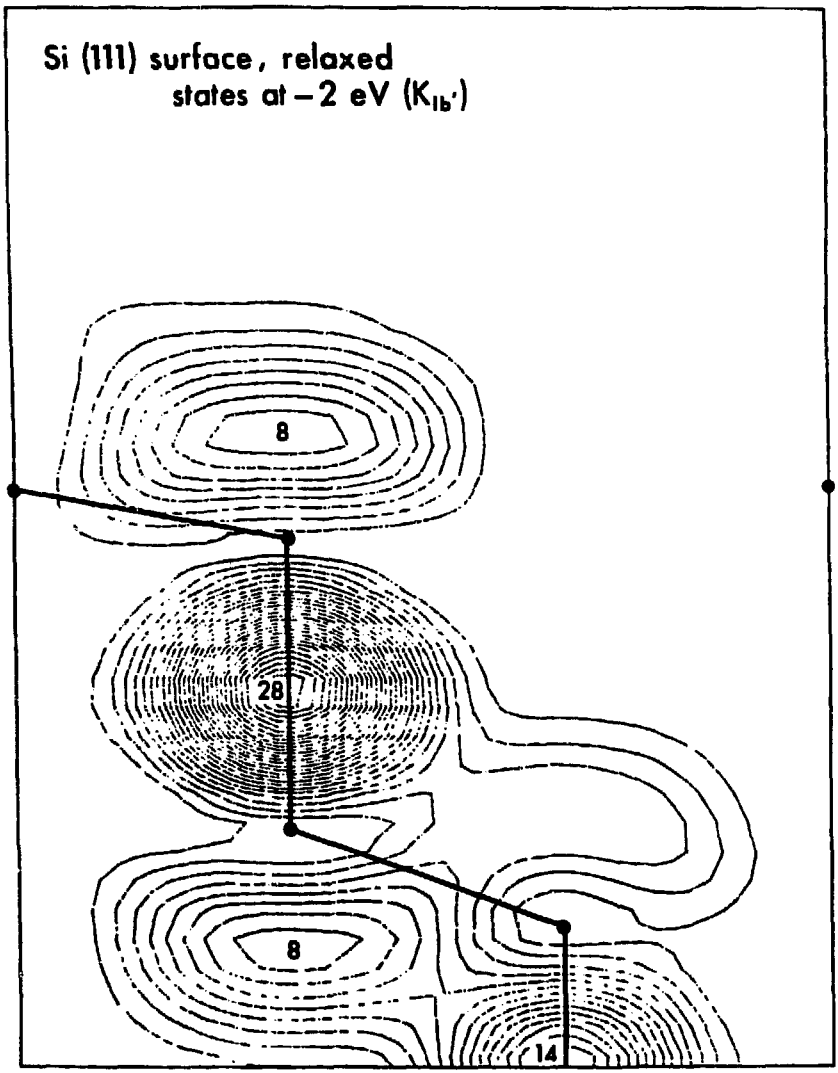

XBL 769 10338

Fig. 28.

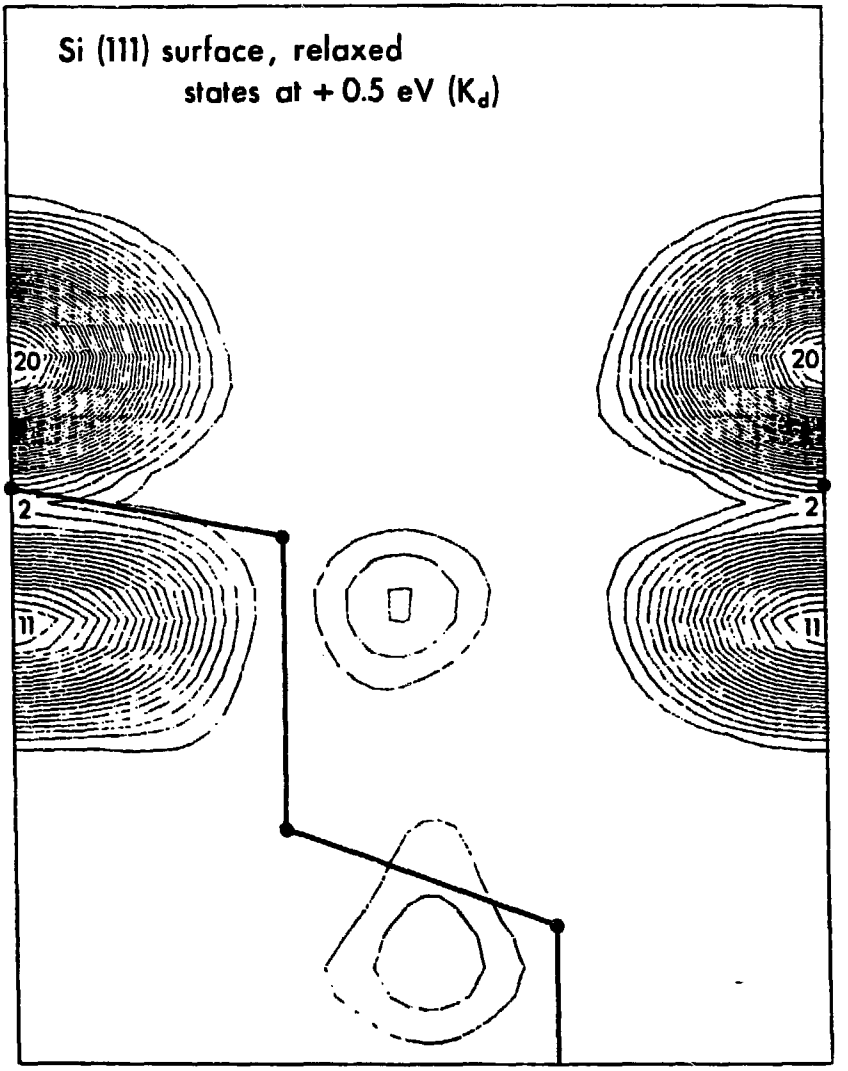

XBL 769-10356

Fig. 29.

Si (111) — 2 × 1

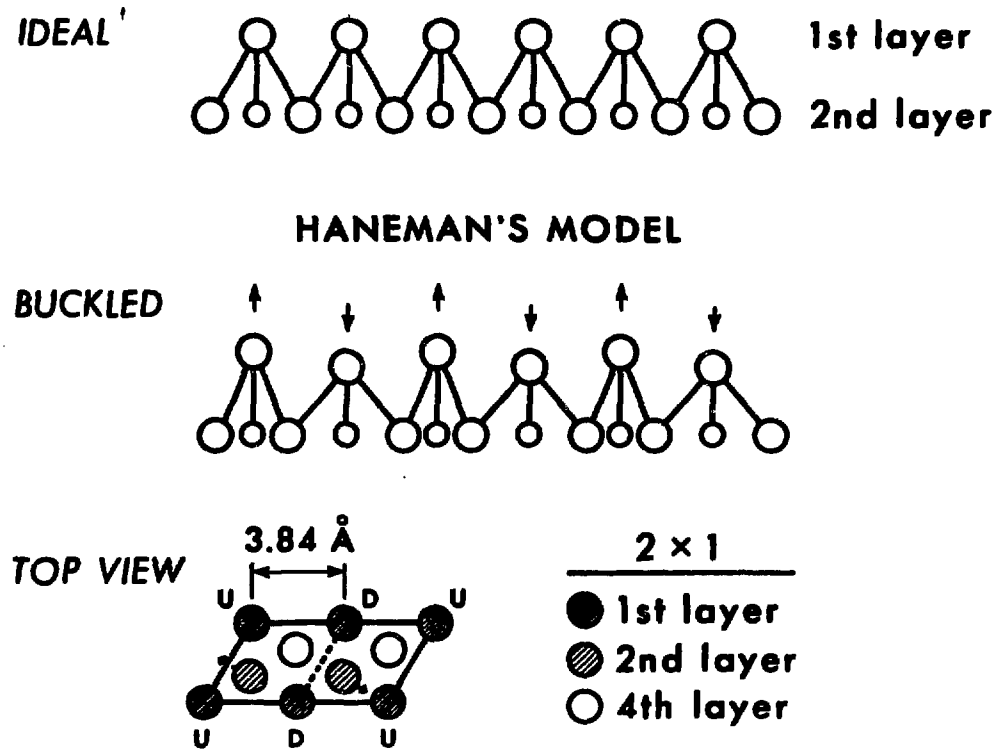

XBL 769-10349

Fig. 30.

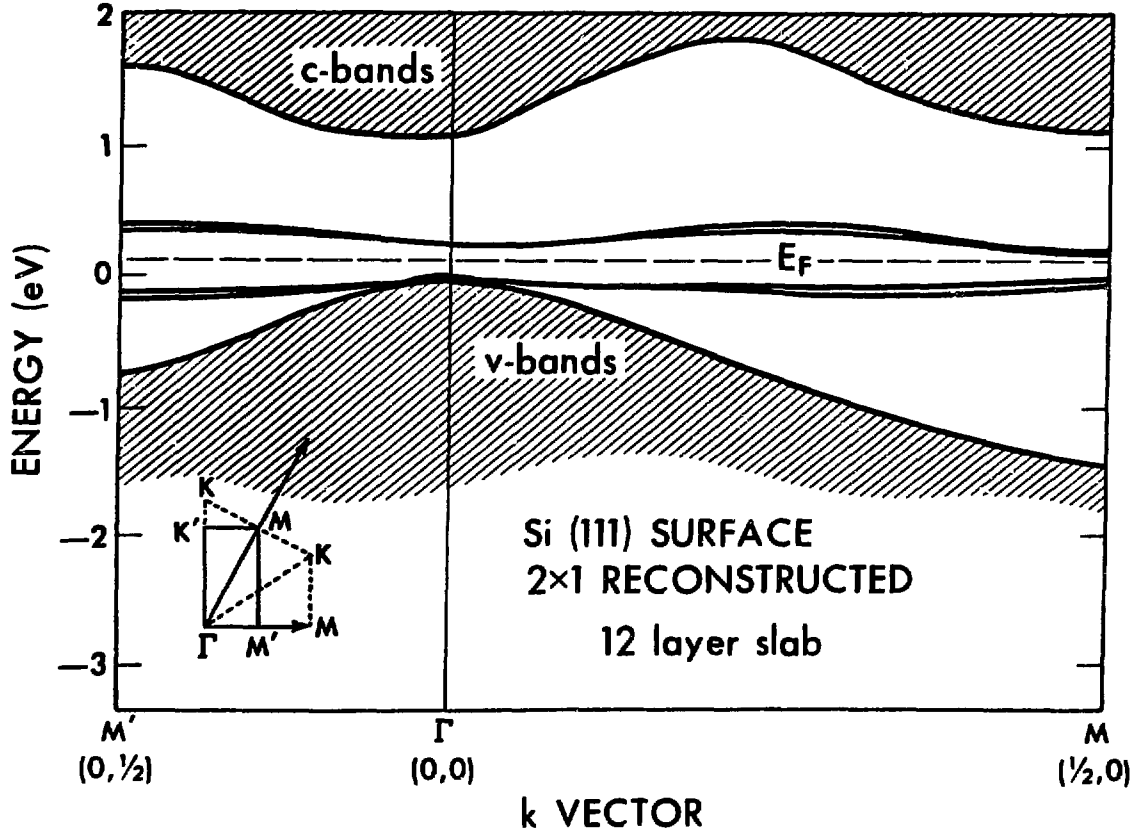

Fig. 31.

XBL 769-10355

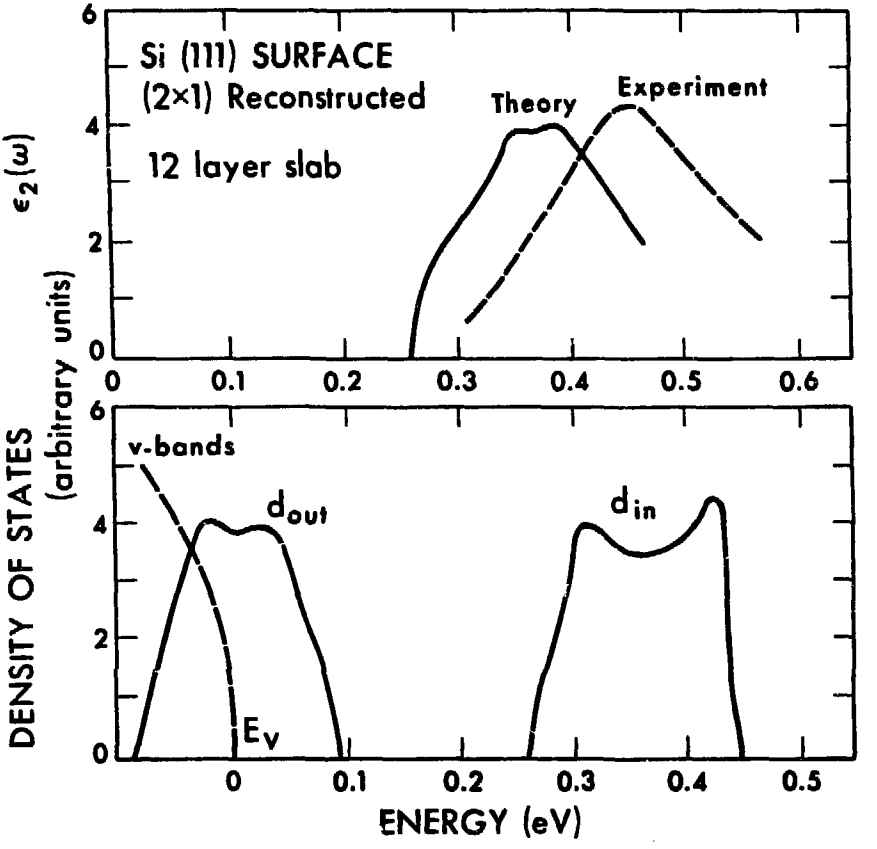
Si (111) SURFACE
(2×1) Reconstructed
12 layer slab
Theory
Experiment
$\epsilon_2(\omega)$
DENSITY OF STATES
(arbitrary units)
v-bands
d_{out}
d_{in}
E_v
ENERGY (eV)
XBL 769-10382

Fig. 32.

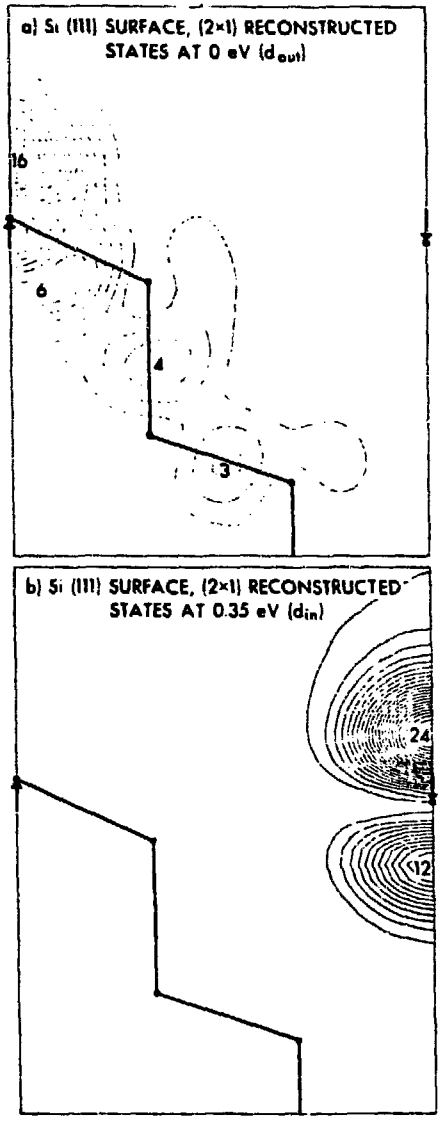

XBL 769-10334

Fig. 33.

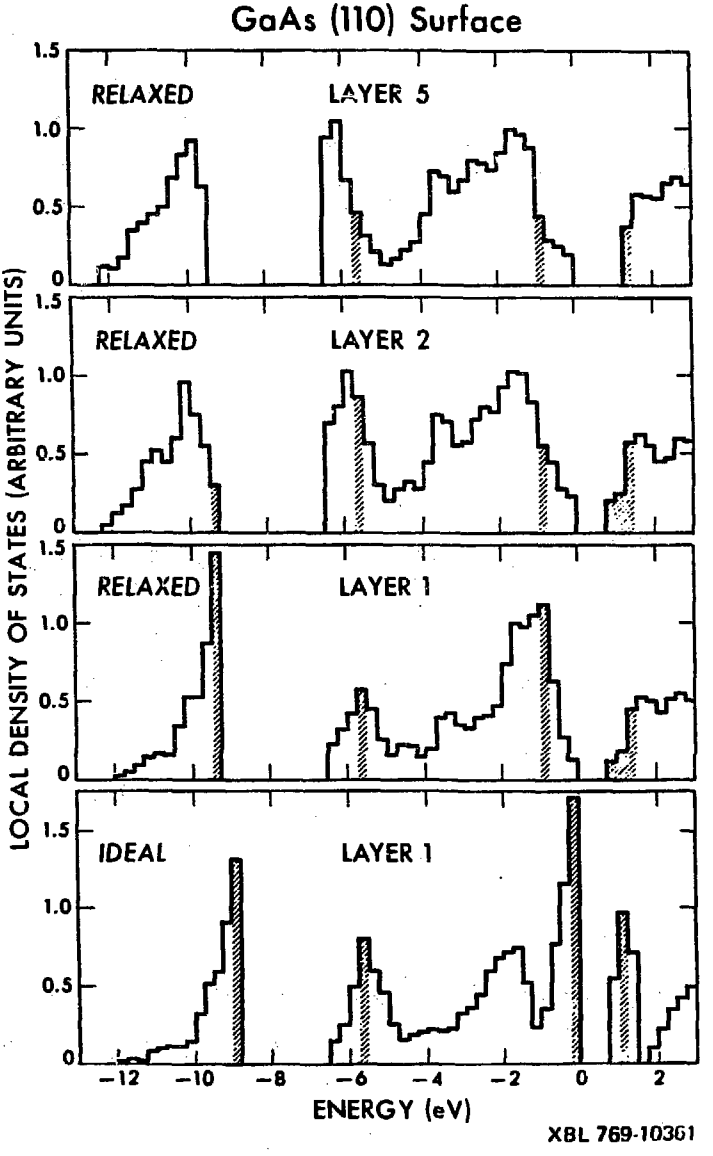
GaAs (110) Surface
RELAXED
LAYER 5
RELAXED
LAYER 2
RELAXED
LAYER 1
IDEAL
LAYER 1
LOCAL DENSITY OF STATES (ARBITRARY UNITS)
1.5
1.0
0.5
0
−12
−10
−8
−6
−4
−2
0
2
ENERGY (eV)
XBL 769-10361

Fig. 34.

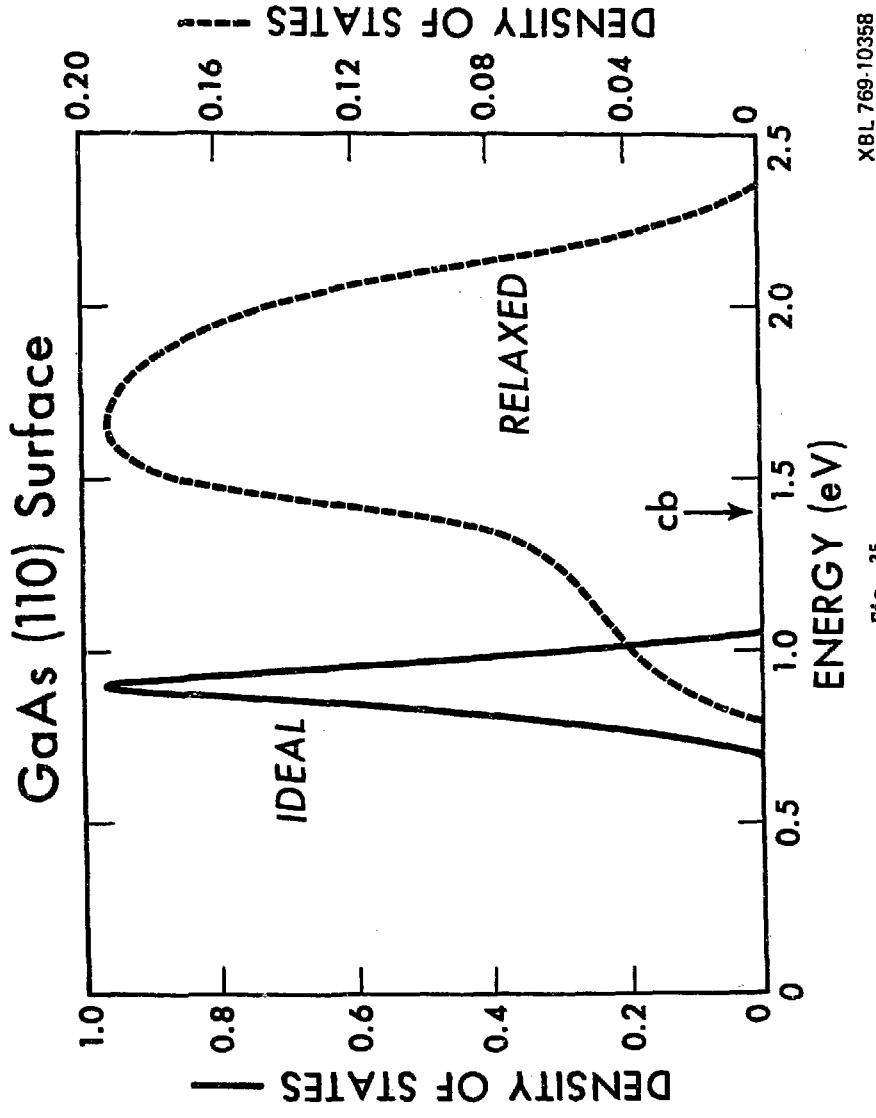

XBL 769-10358

Fig. 35.

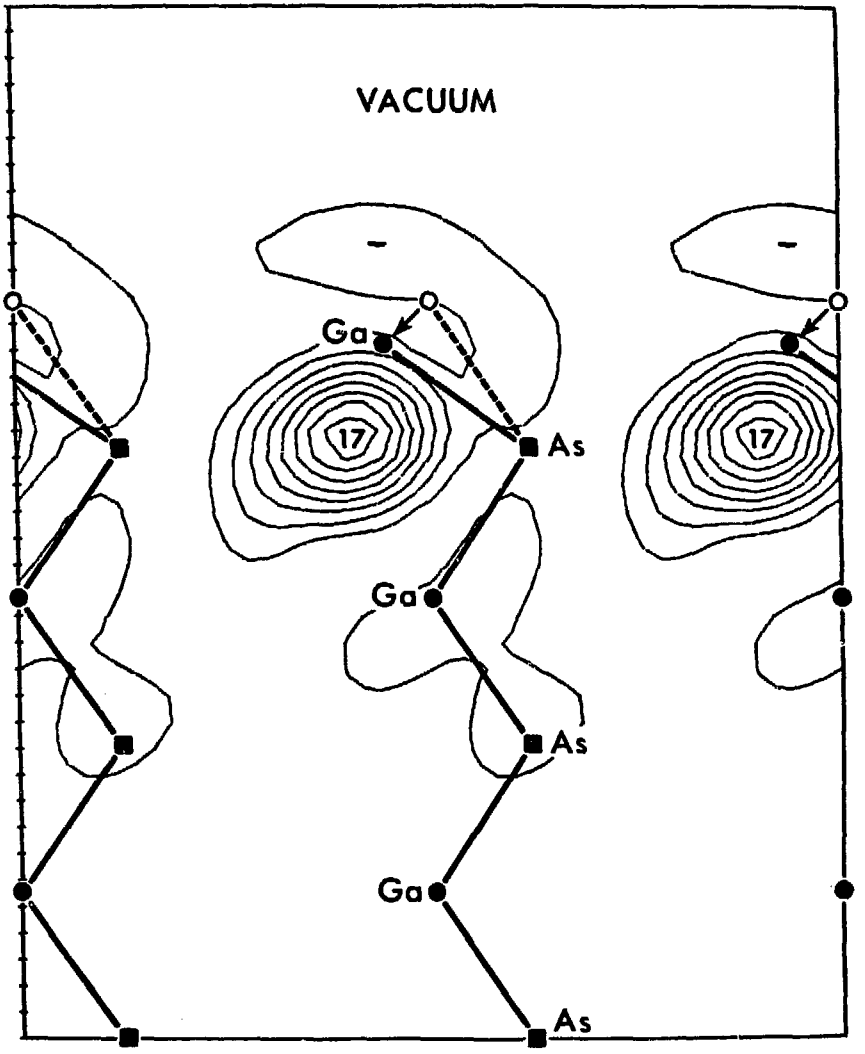

XBL 769-10363

Fig. 36.

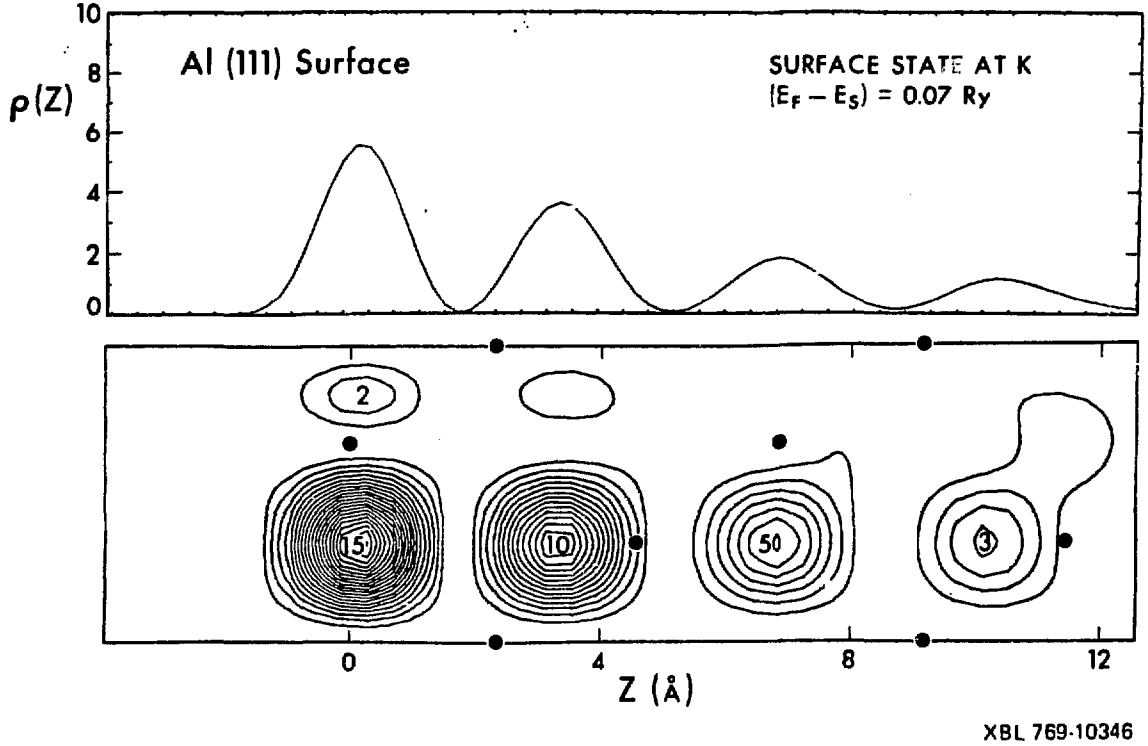
Al (111) Surface
SURFACE STATE AT K
$(E_F - E_S)$ = 0.07 Ry
ρ(Z)
10
8
6
4
2
0
2
15
10
50
3
0
4
8
12
Z (Å)
XBL 769-10346

Fig. 37.

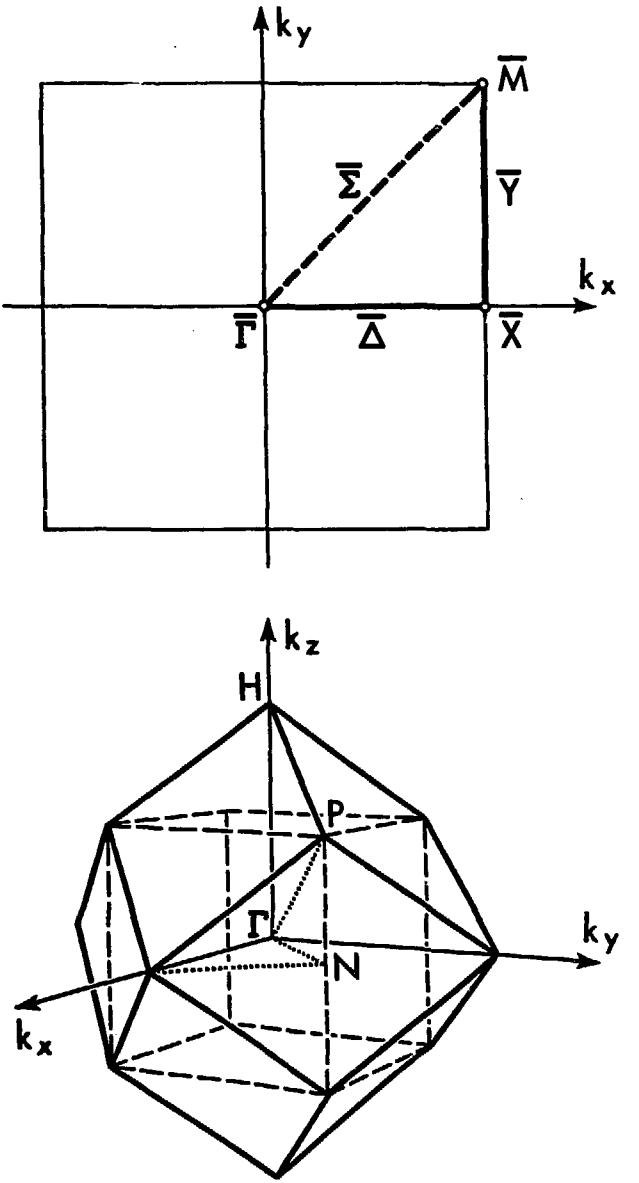

XBL 769-10446

Fig. 38.

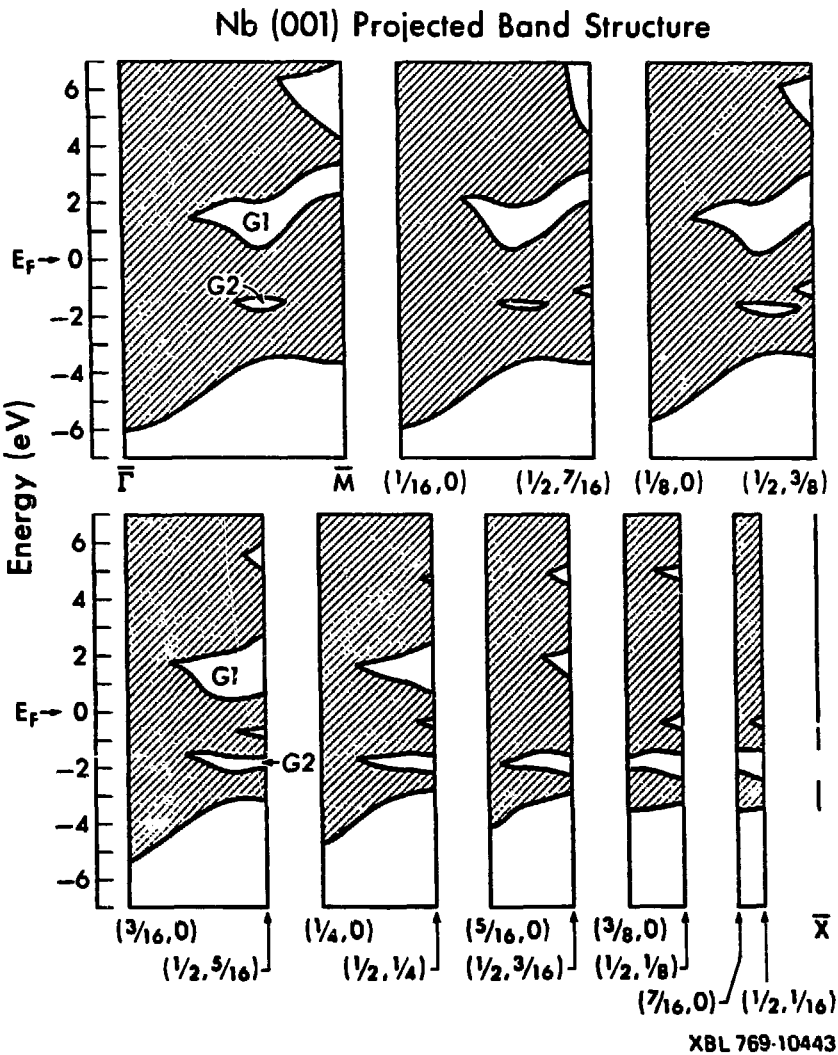
Nb (001) Projected Band Structure
Energy (eV)
6
4
2
E_F 0
−2
−4
−6
G1
G2
$\bar{\Gamma}$
$\bar{M}$
(1/16,0)
(1/2,7/16)
(1/8,0)
(1/2,3/8)
(3/16,0)
(1/2,5/16)
(1/4,0)
(1/2,1/4)
(5/16,0)
(1/2,3/16)
(3/8,0)
(1/2,1/8)
(7/16,0)
(1/2,1/16)
$\bar{X}$
XBL 769-10443

Fig. 39.

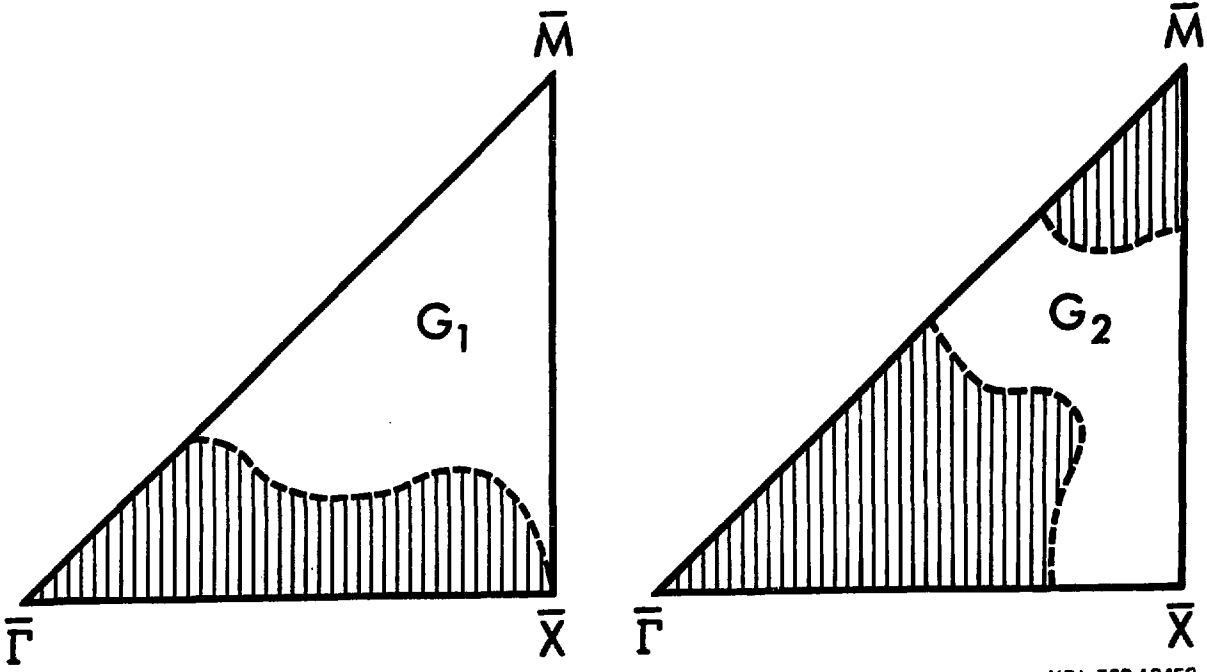

XBL 769-10452

Fig. 40.

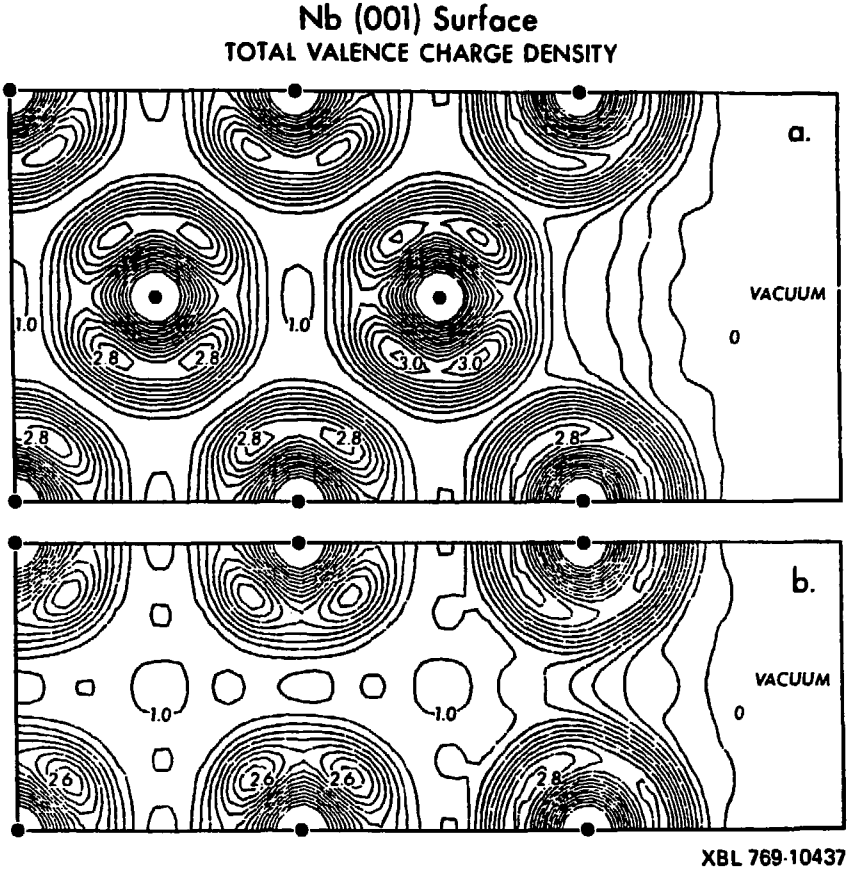
Nb (001) Surface
TOTAL VALENCE CHARGE DENSITY
a.
VACUUM
0
1.0
1.0
2.8
2.8
3.0
3.0
2.8
2.8
2.8
2.8
b.
VACUUM
0
1.0
1.0
2.6
2.6
2.6
2.8
XBL 769-10437

Fig. 41.

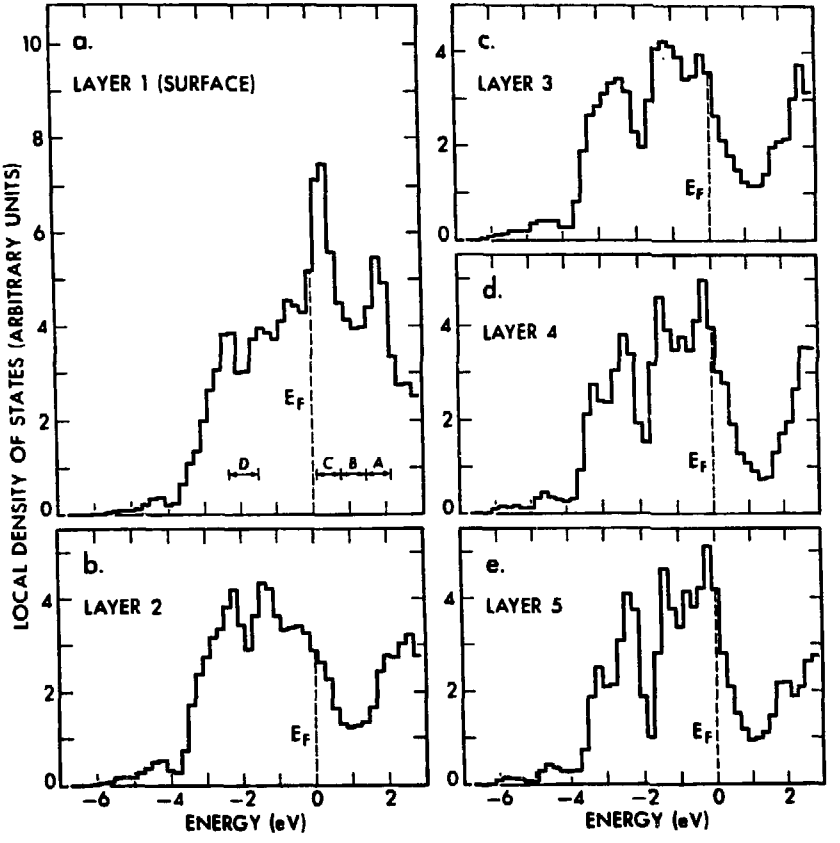

XBL 769-10439

Fig. 42.

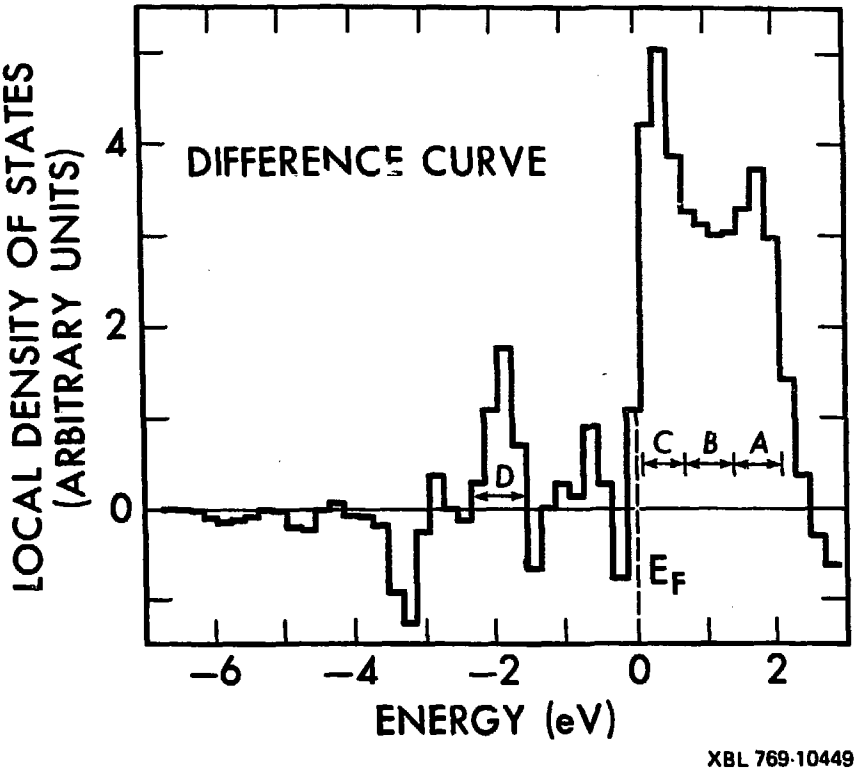
LOCAL DENSITY OF STATES
(ARBITRARY UNITS)
DIFFERENCE CURVE
4
2
0
D
C
B
A
E_F
−6
−4
−2
0
2
ENERGY (eV)
XBL 769-10449

Fig. 43.

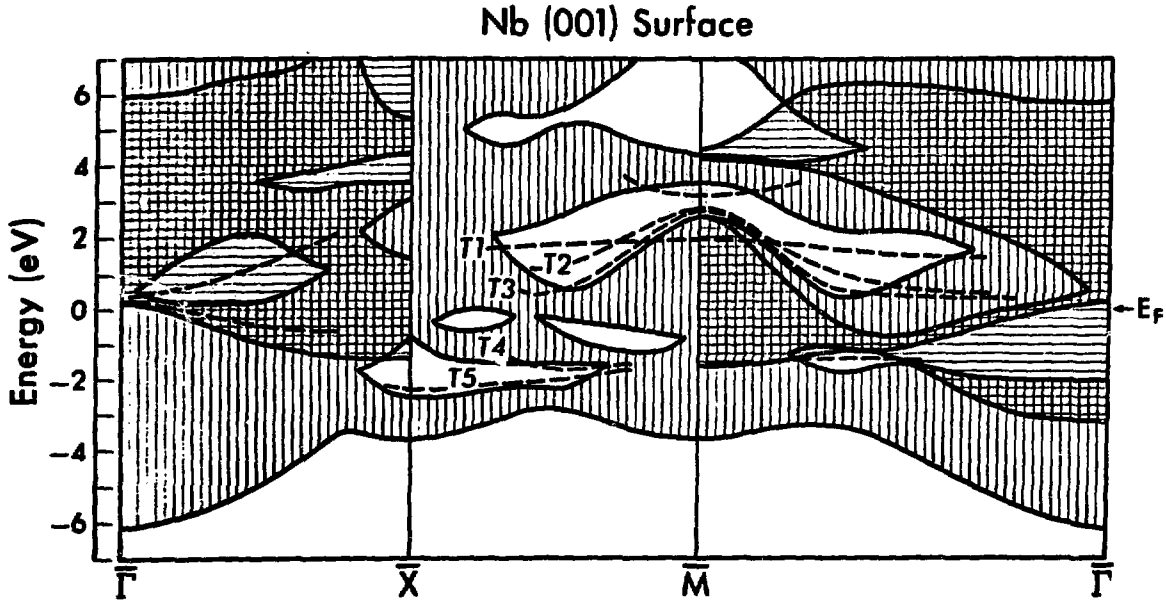

XBL 769-10450

Fig. 44.

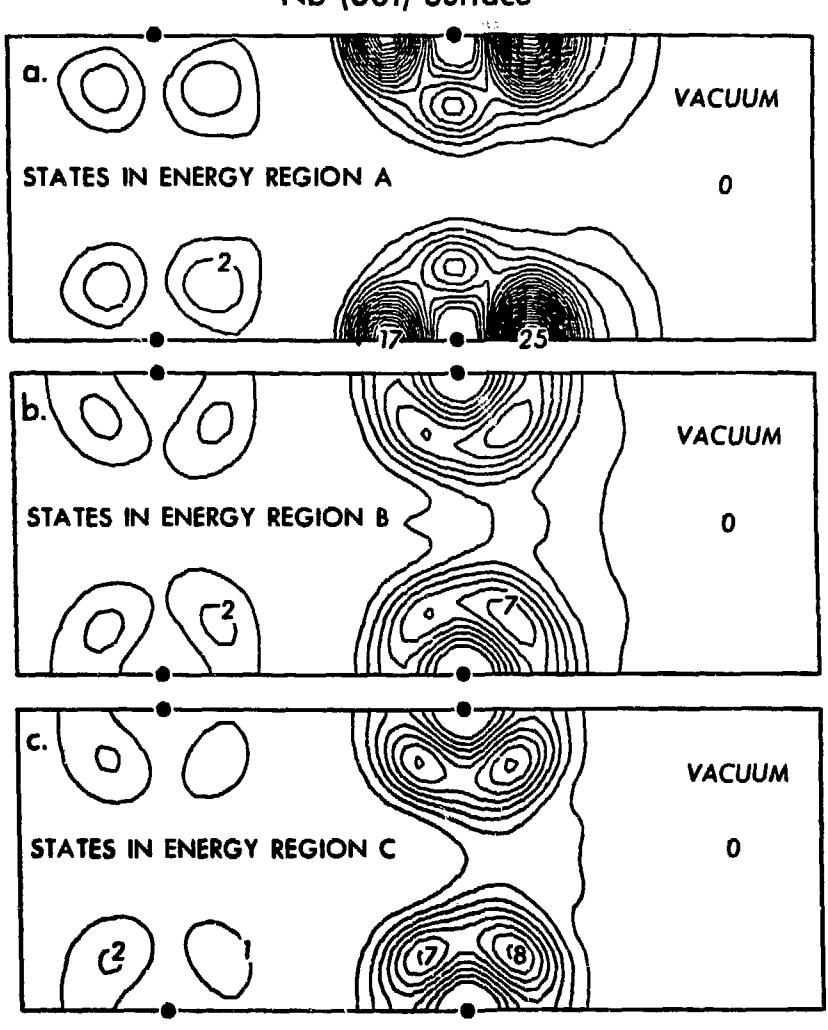

XBL 769-10360

Fig. 45.

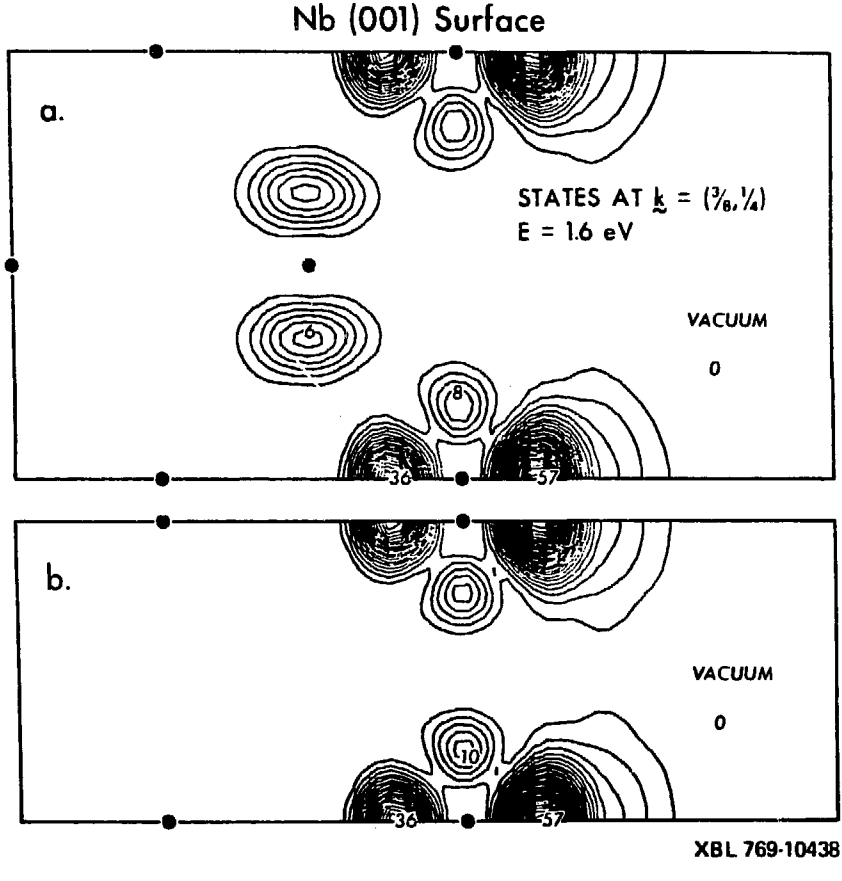
Nb (001) Surface
a.
STATES AT k = (3/8, 1/4)
E = 1.6 eV
VACUUM
0
8
36
57
b.
VACUUM
0
10
36
57
XBL 769-10438

Fig. 46.

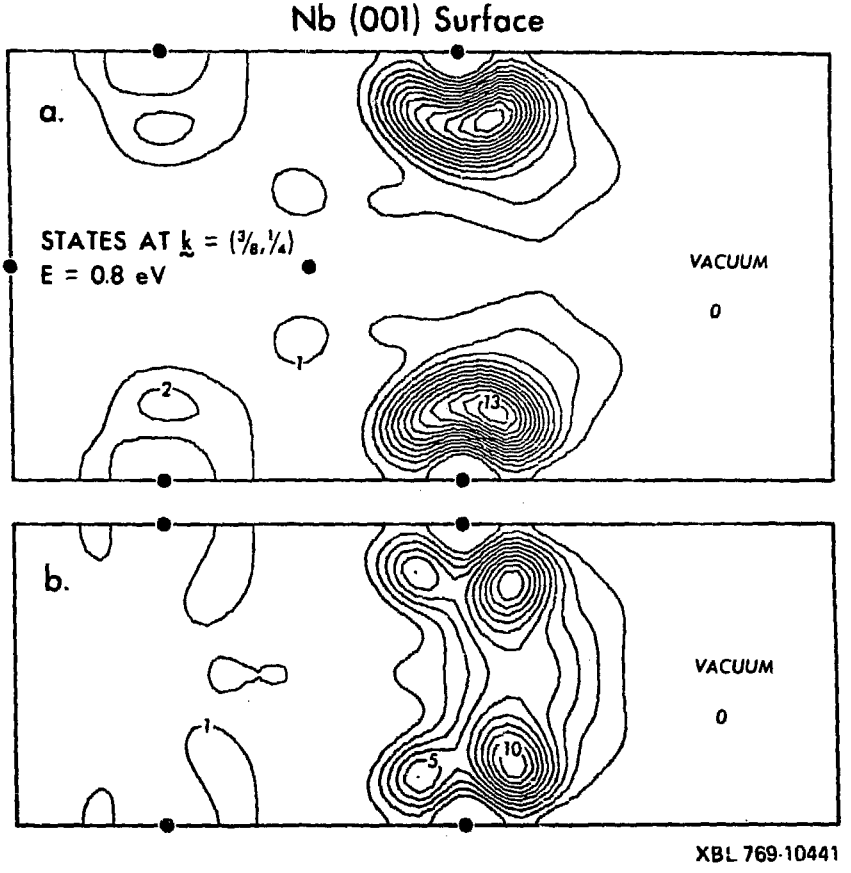
Nb (001) Surface
a.
STATES AT k = (3/8, 1/4)
E = 0.8 eV
VACUUM
0
1
2
13
b.
VACUUM
0
1
5
10
XBL 769-10441

Fig. 47.

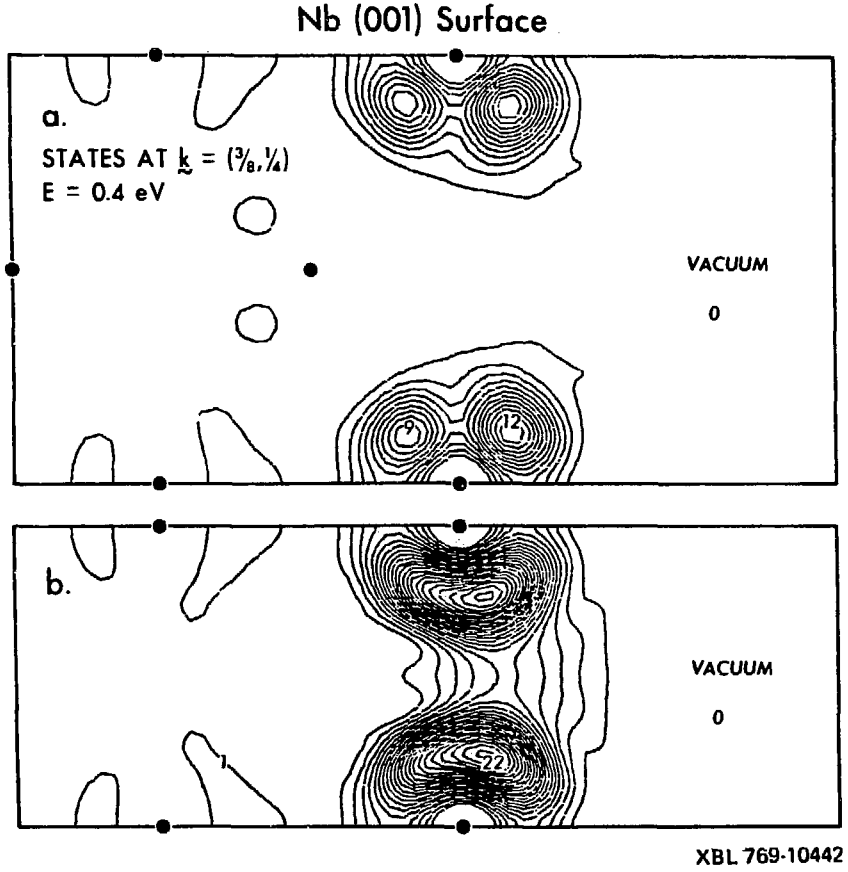
Nb (001) Surface
a.
STATES AT k = (3/8, 1/4)
E = 0.4 eV
VACUUM
0
9
12
b.
VACUUM
0
1
22
XBL 769-10442

Fig. 48.

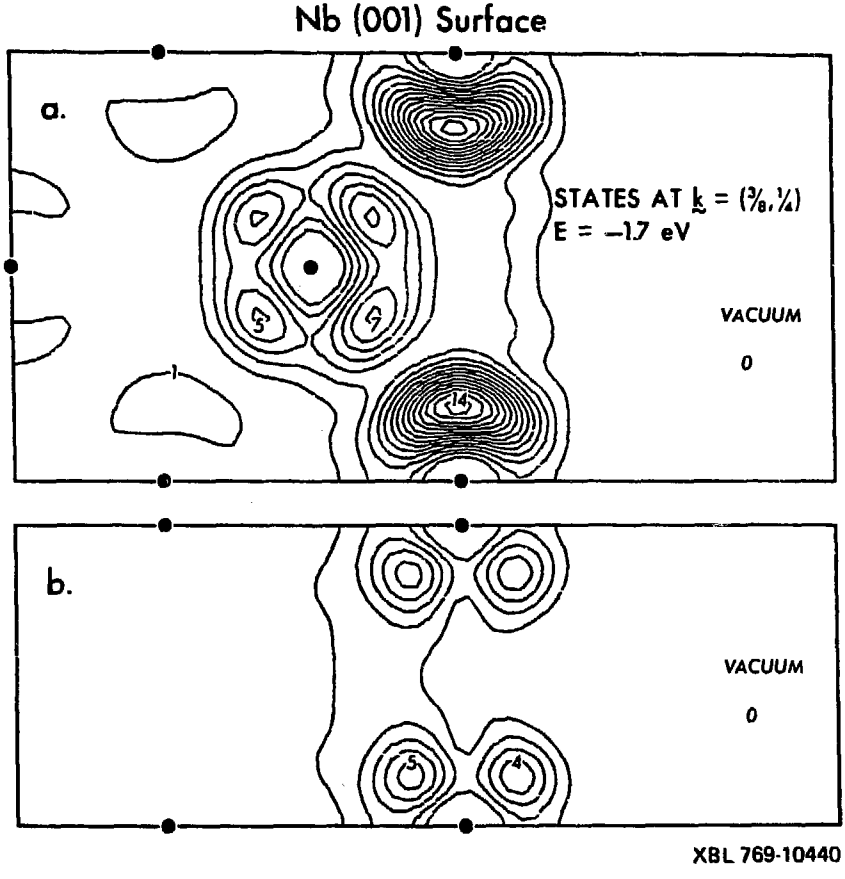
Nb (001) Surface
a.
STATES AT k = (3/8, 1/4)
E = −1.7 eV
VACUUM
0
1
5
14
b.
VACUUM
0
5
4
XBL 769-10440

Fig. 49.

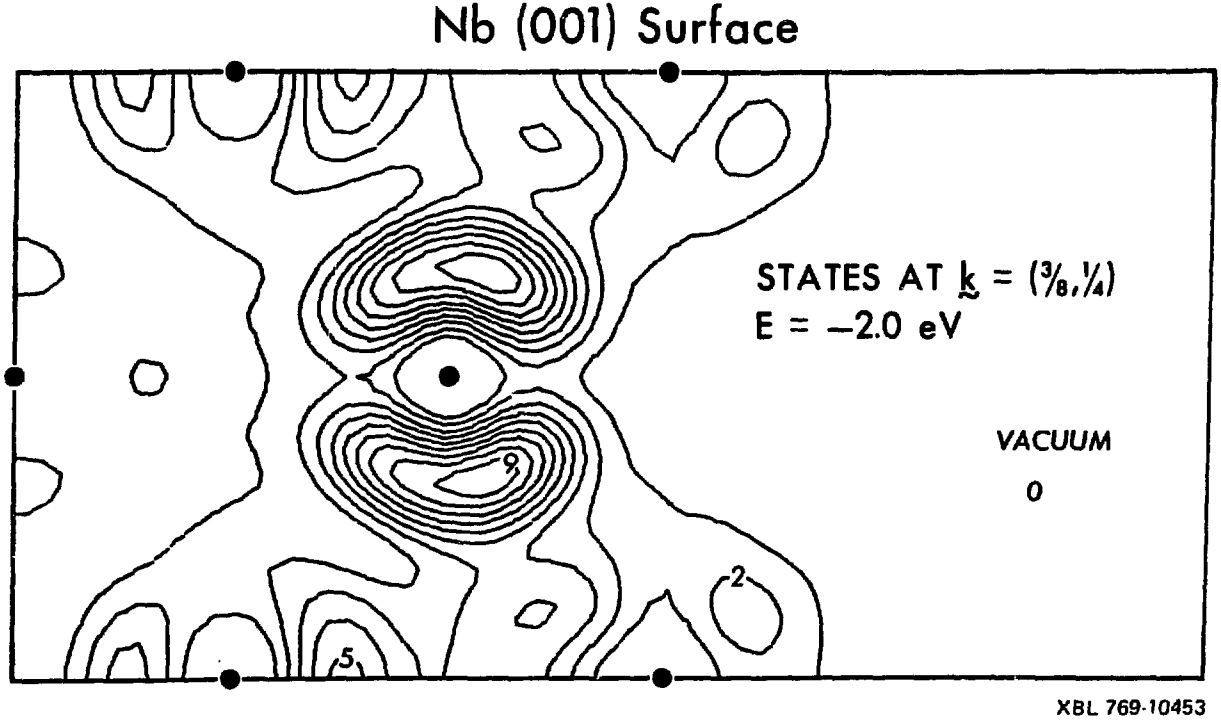
Nb (001) Surface
STATES AT k = (3/8, 1/4)
E = −2.0 eV
VACUUM
0
9
2
5
XBL 769-10453

Fig. 50.

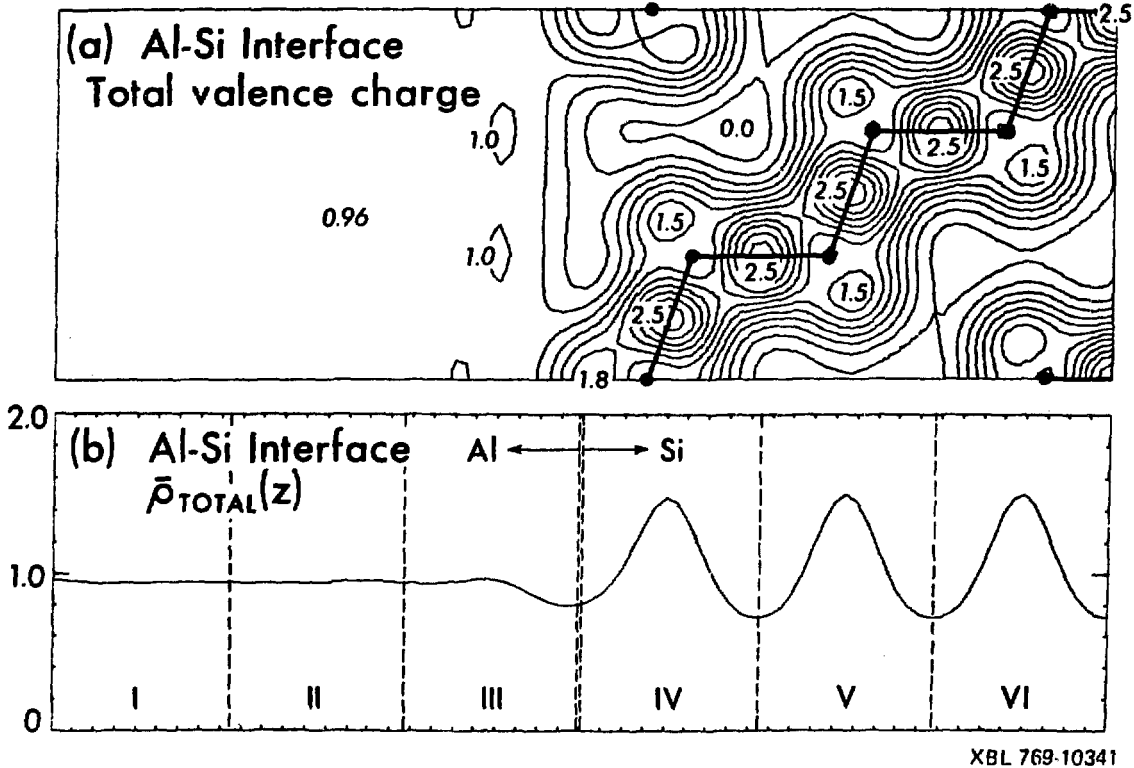
(a) Al-Si Interface
Total valence charge
0.96
1.0
1.0
0.0
1.5
2.5
2.5
2.5
1.5
2.5
1.5
2.5
1.5
2.5
2.5
1.8
(b) Al-Si Interface
$\bar{\rho}_{TOTAL}(z)$
Al ⟷ Si
2.0
1.0
0
I
II
III
IV
V
VI
XBL 769-10341

Fig. 51.

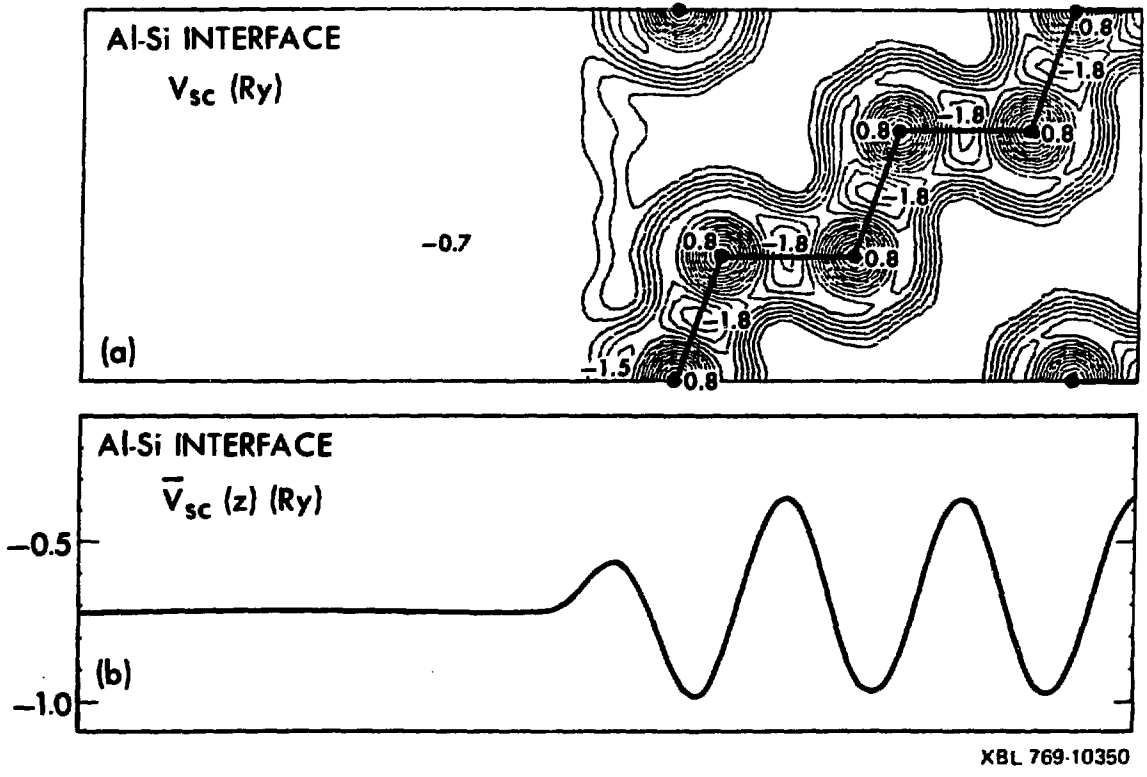
Al-Si INTERFACE
V_{sc} (Ry)
−0.7
(a)
0.8
−1.8
−1.5
Al-Si INTERFACE
$\bar{V}_{sc}$ (z) (Ry)
−0.5
−1.0
(b)
XBL 769-10350

Fig. 52.

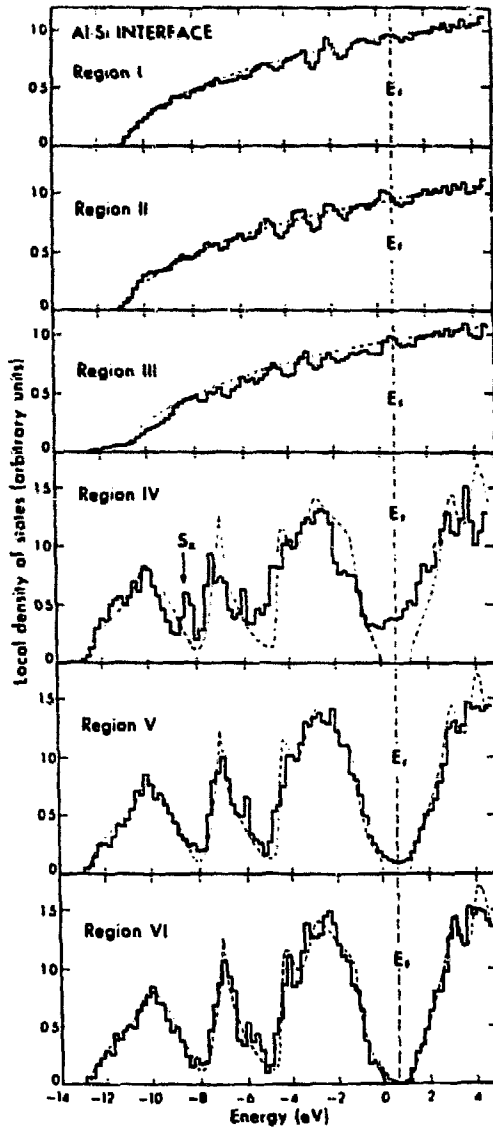
Al-Si INTERFACE
Region I
Region II
Region III
Region IV
Region V
Region VI
S_x
E_F
Local density of states (arbitrary units)
Energy (eV)
XBL 769-10389

Fig. 53.

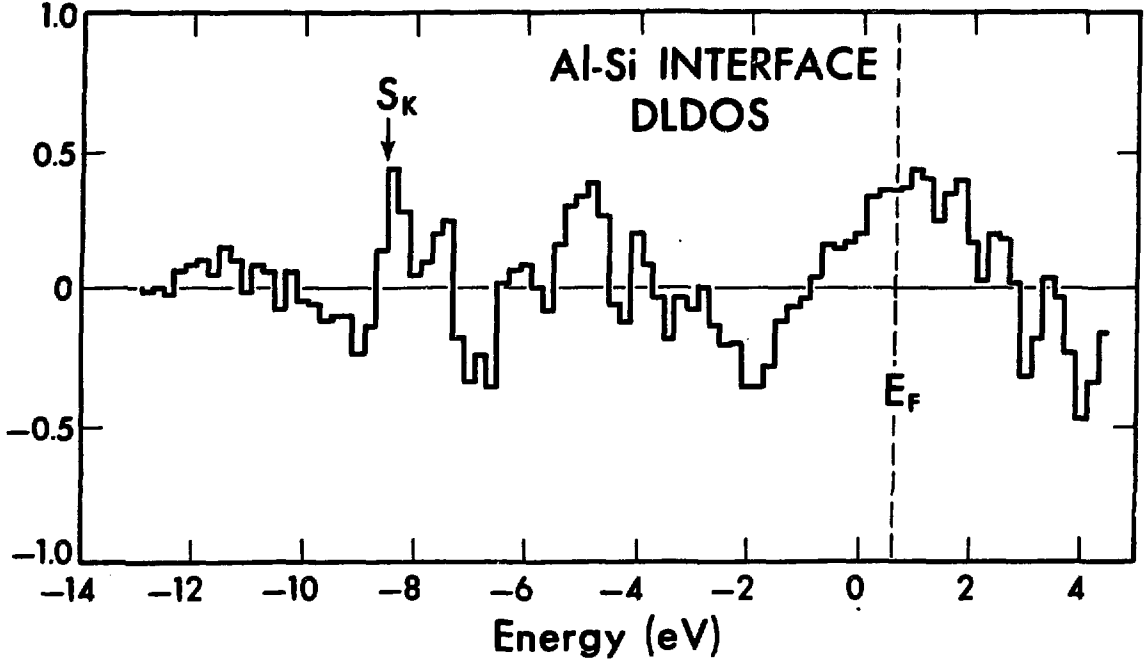

XBL 769-10359

Fig. 54.

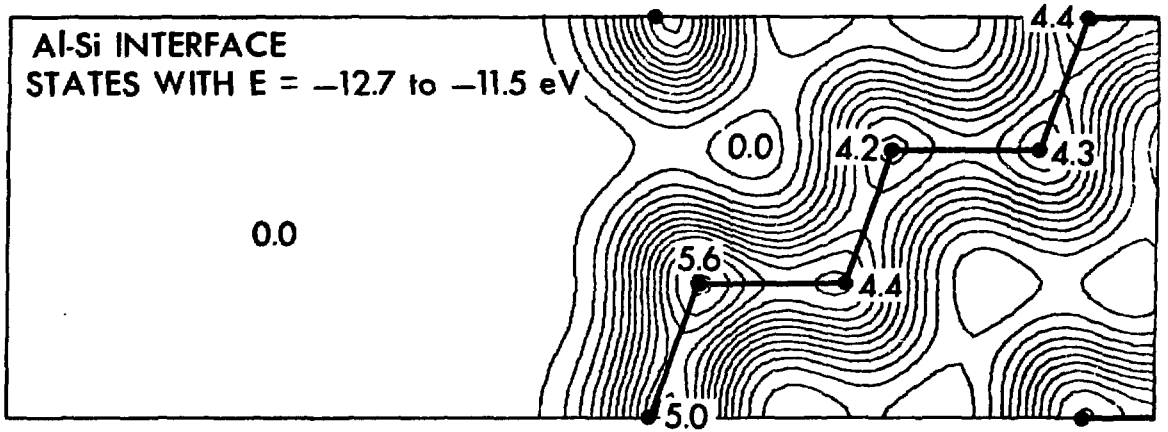

XBL 769-10357

Fig. 55.

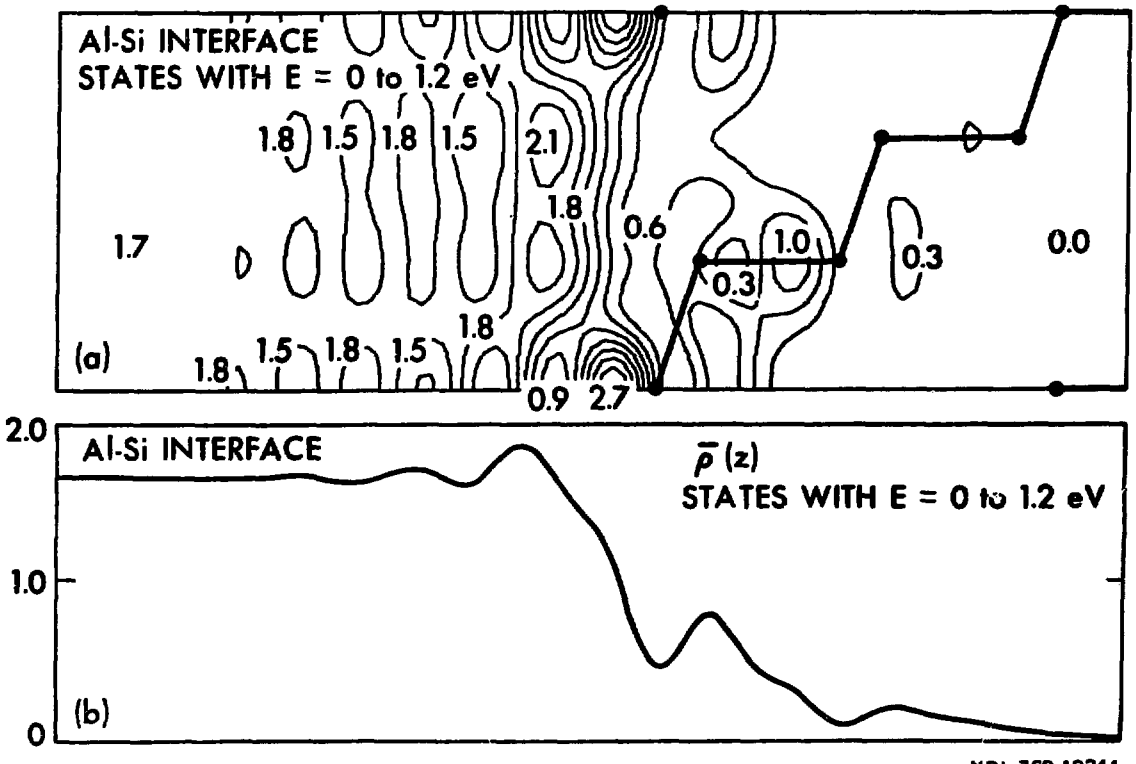
Al-Si INTERFACE
STATES WITH E = 0 to 1.2 eV
1.8
1.5
1.8
1.5
2.1
1.8
0.6
1.0
0.3
0.0
1.7
0.3
1.8
(a)
1.8
1.5
1.8
1.5
0.9
2.7
2.0
Al-Si INTERFACE
$\bar{\rho}(z)$
STATES WITH E = 0 to 1.2 eV
1.0
(b)
0
XBL 769-10344

Fig. 56.

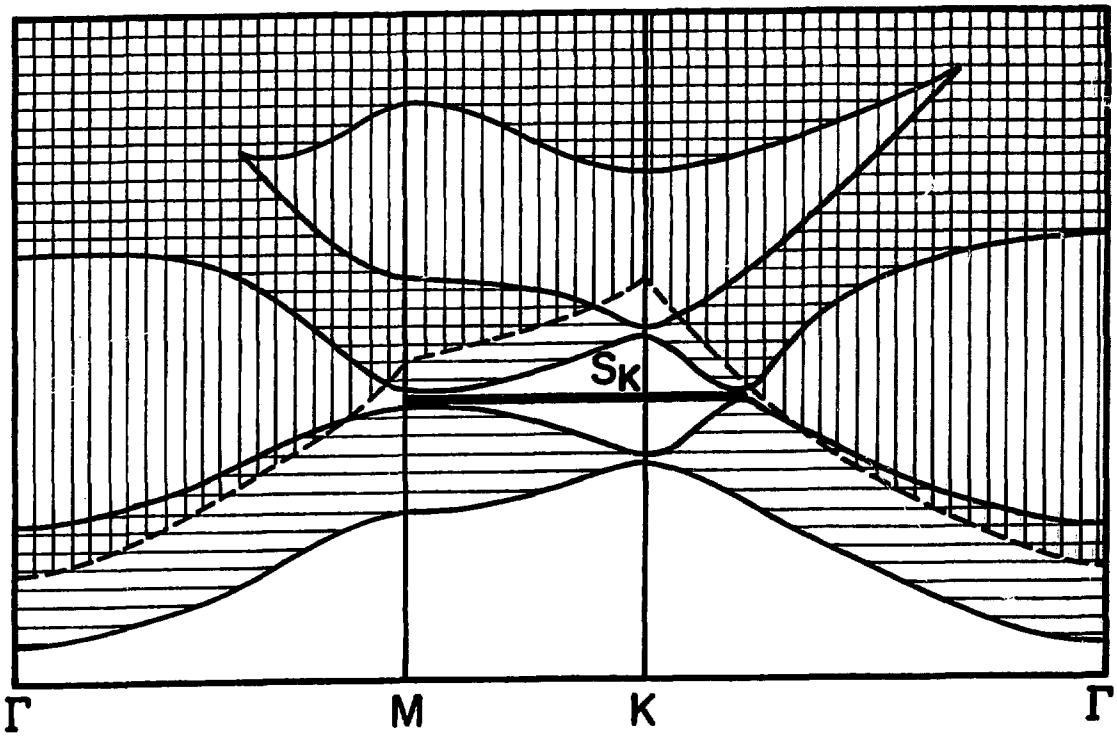

XBL 769 10343

Fig. 57.

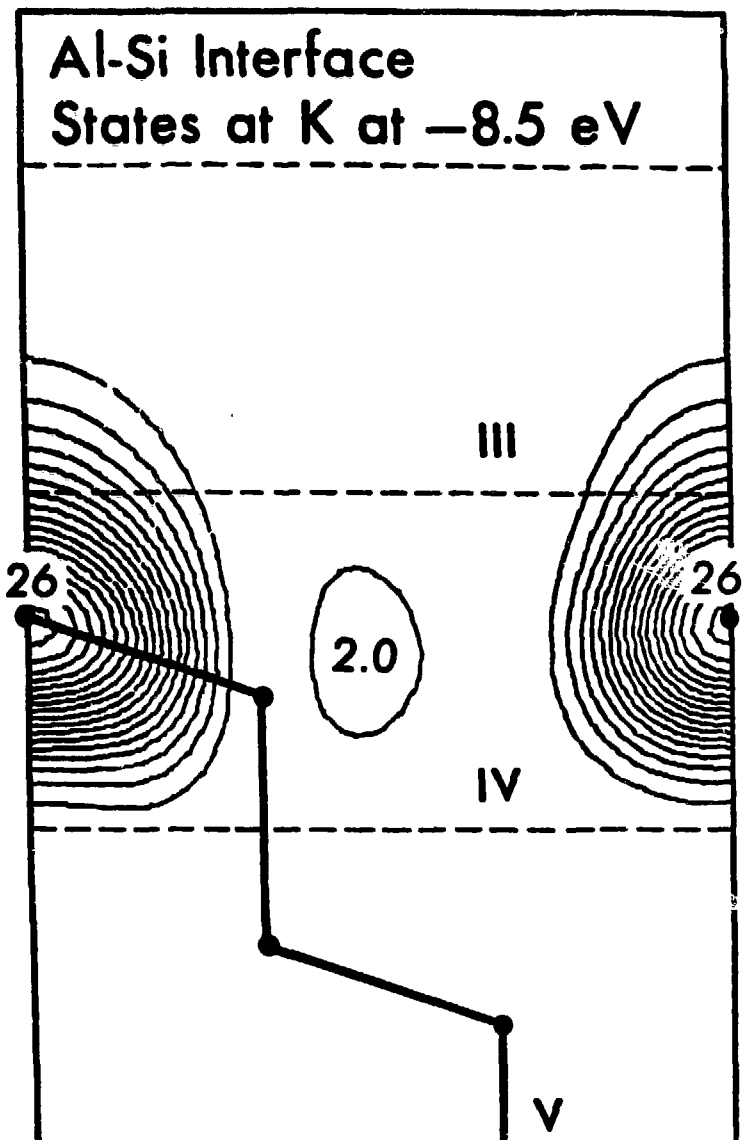

XBL 769-10362

Fig. 58.

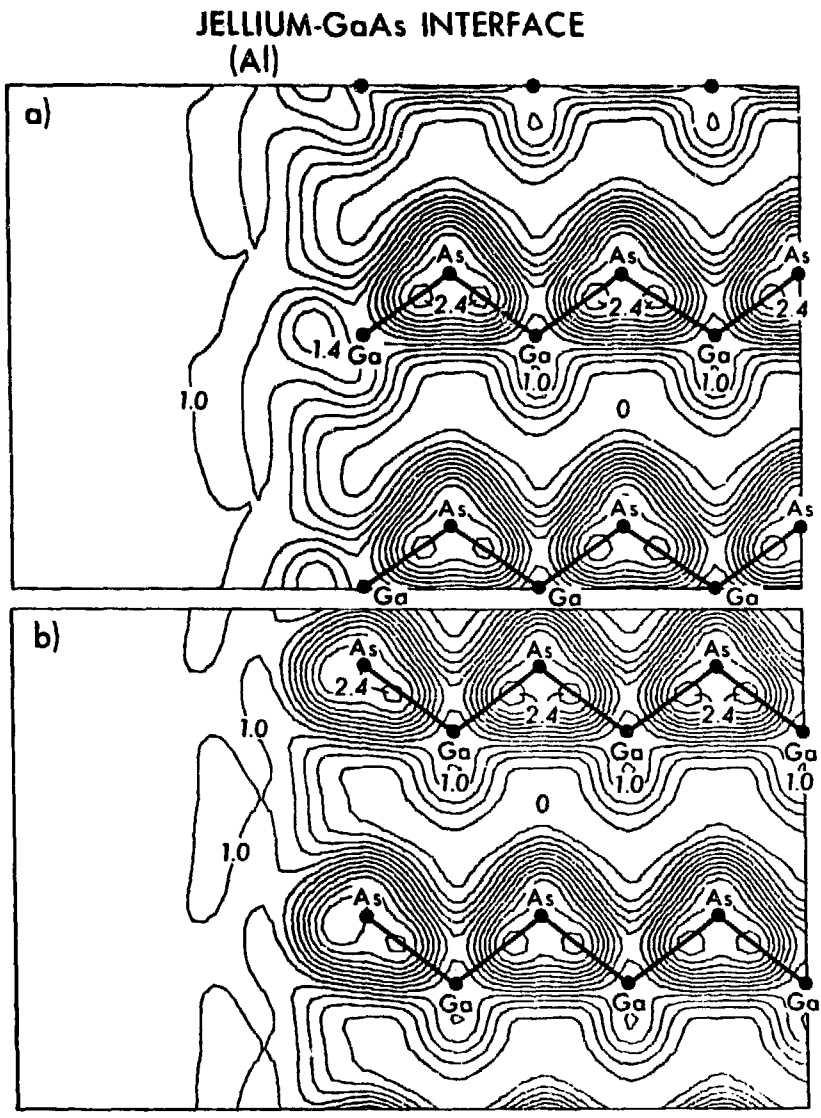

XBL 769 10335

Fig. 59.

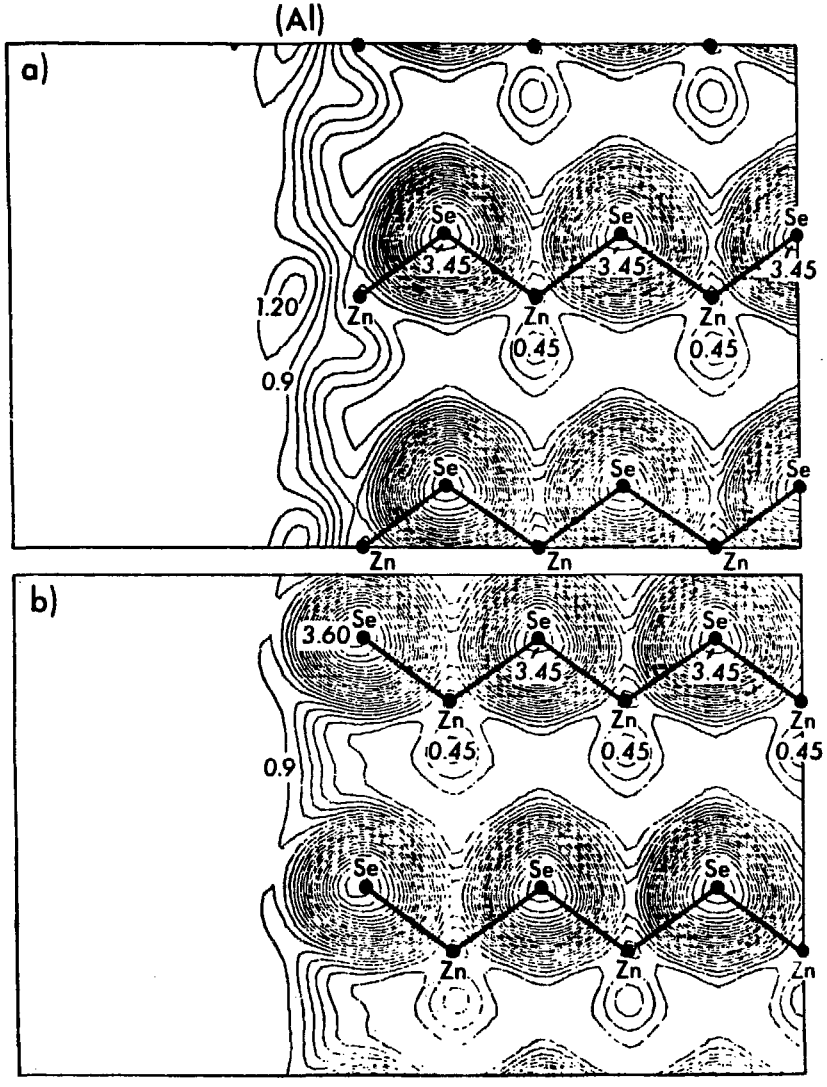
JELLIUM-ZnSe INTERFACE
(Al)
a)
Se
Zn
3.45
1.20
0.9
0.45
b)
3.60
XBL 769-10337

Fig. 60.

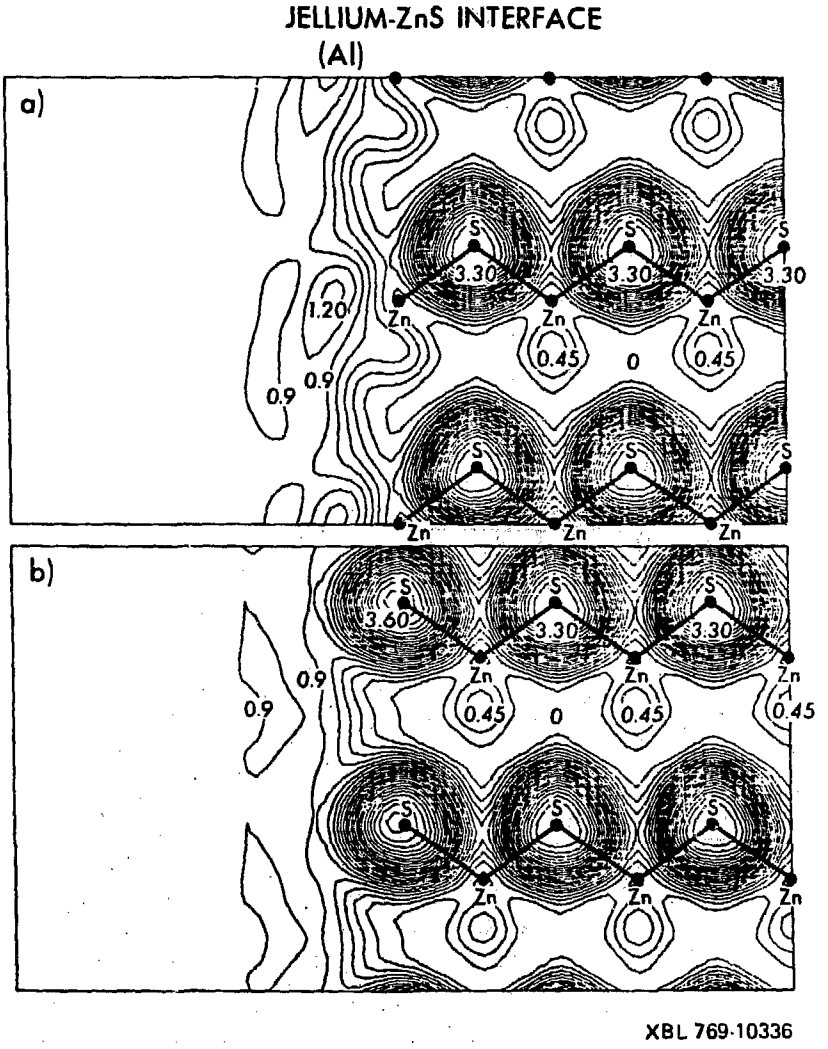
JELLIUM-ZnS INTERFACE
(Al)
a)
S
Zn
3.30
1.20
0.9
0.45
0
b)
3.60
XBL 769-10336

Fig. 61.

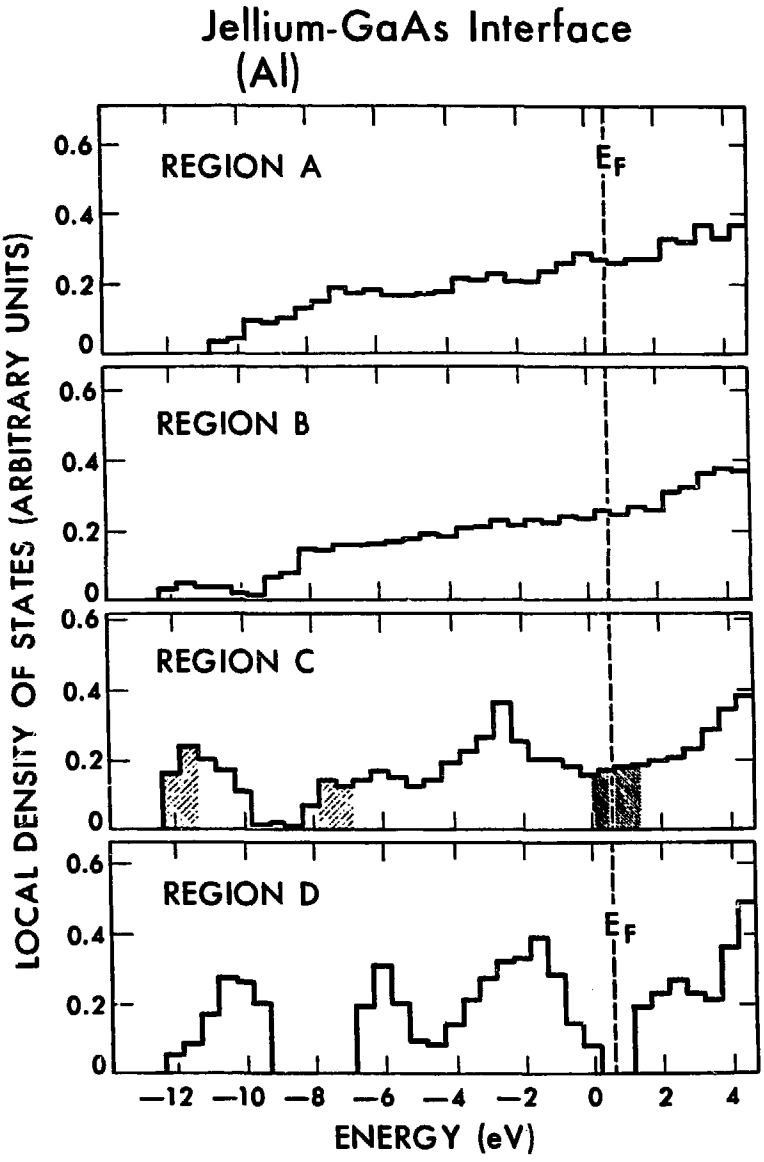
Jellium-GaAs Interface
(Al)
REGION A
REGION B
REGION C
REGION D
E_F
E_F
LOCAL DENSITY OF STATES (ARBITRARY UNITS)
0.6
0.4
0.2
0
−12 −10 −8 −6 −4 −2 0 2 4
ENERGY (eV)
XBL 769-10368

Fig. 62.

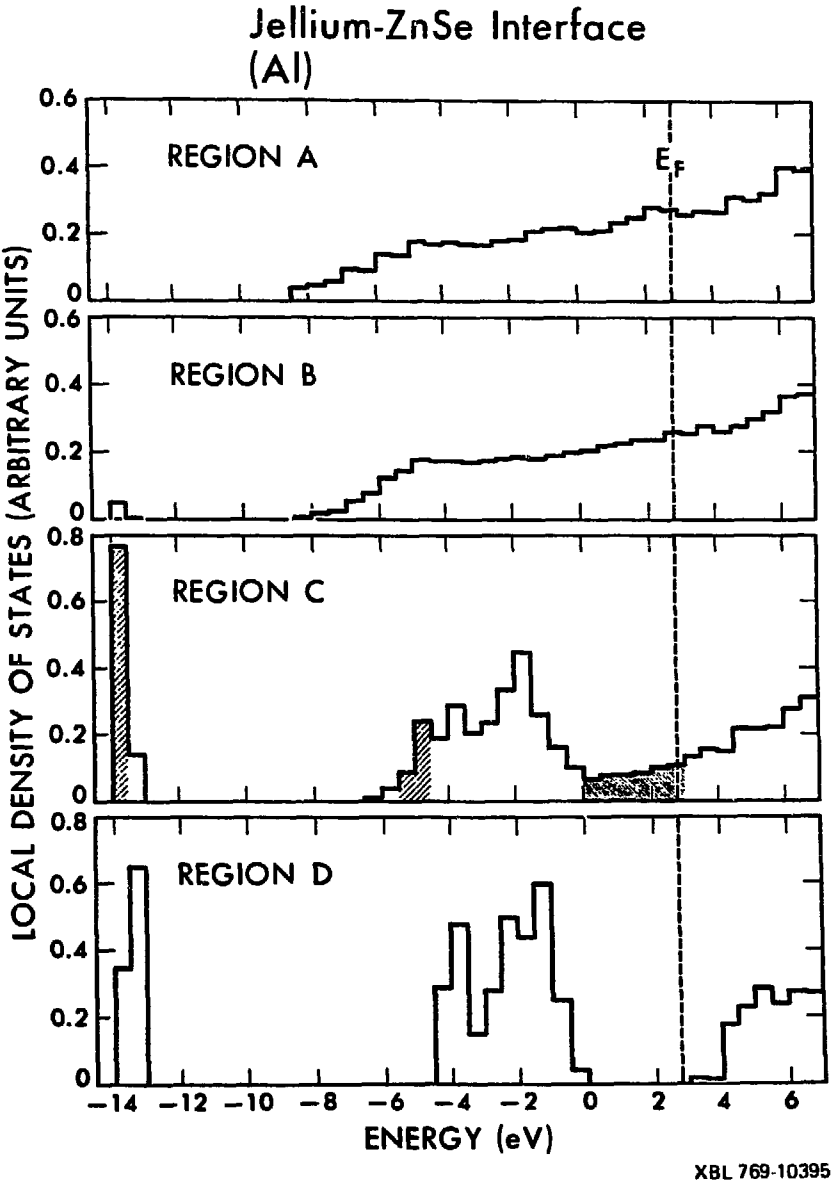

XBL 769-10395

Fig. 63.

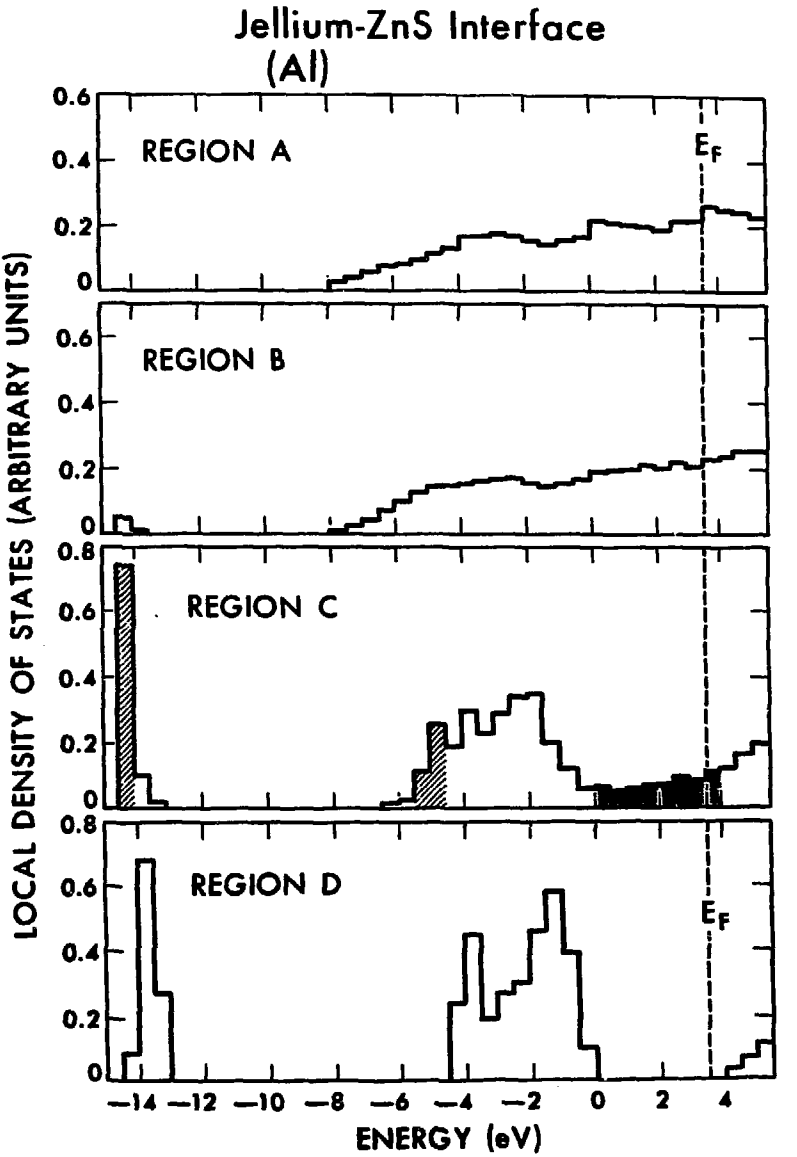
Jellium-ZnS Interface
(Al)
REGION A
REGION B
REGION C
REGION D
E_F
E_F
LOCAL DENSITY OF STATES (ARBITRARY UNITS)
ENERGY (eV)
0.6
0.4
0.2
0
0.8
−14 −12 −10 −8 −6 −4 −2 0 2 4
XBL 769-10365

Fig. 64.

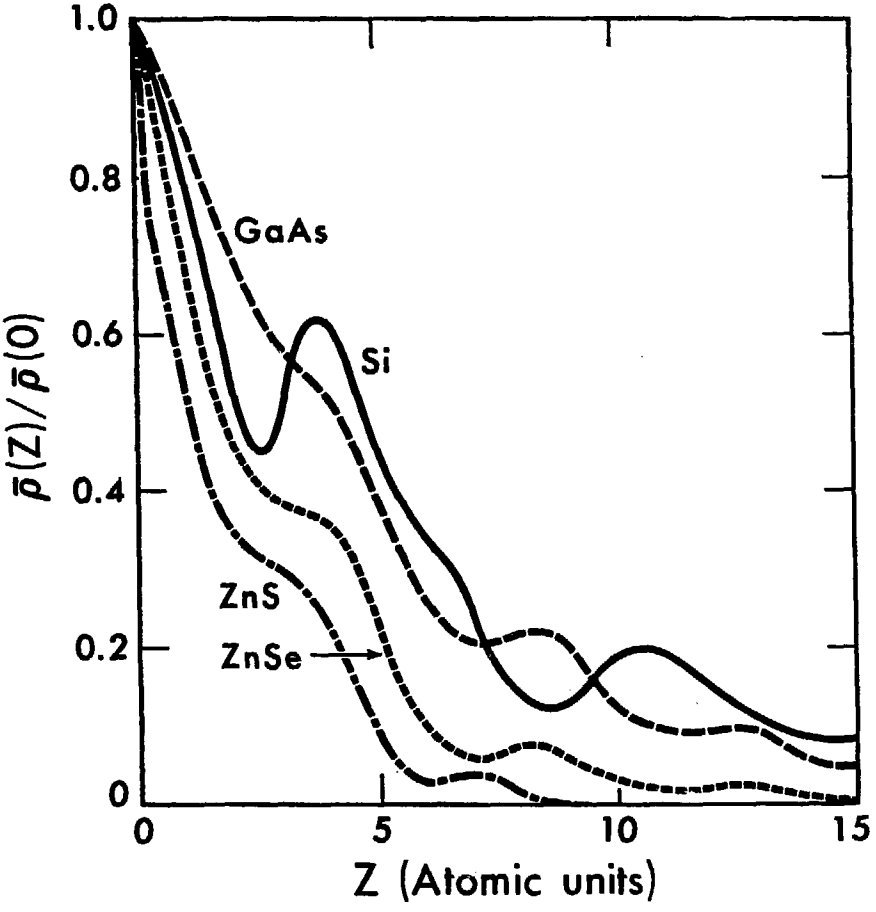

XBL 769-10373

Fig. 65.

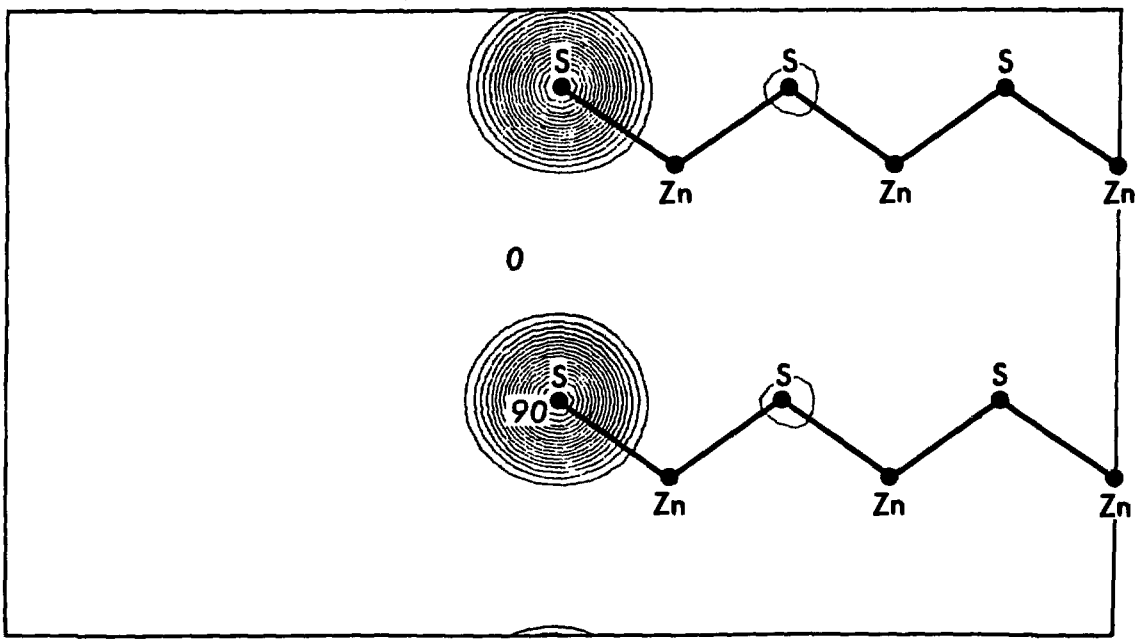
JELLIUM-ZnS INTERFACE
(Al)
S
S
S
Zn
Zn
Zn
0
S
S
S
90
Zn
Zn
Zn
XBL 769-10345

Fig. 66.

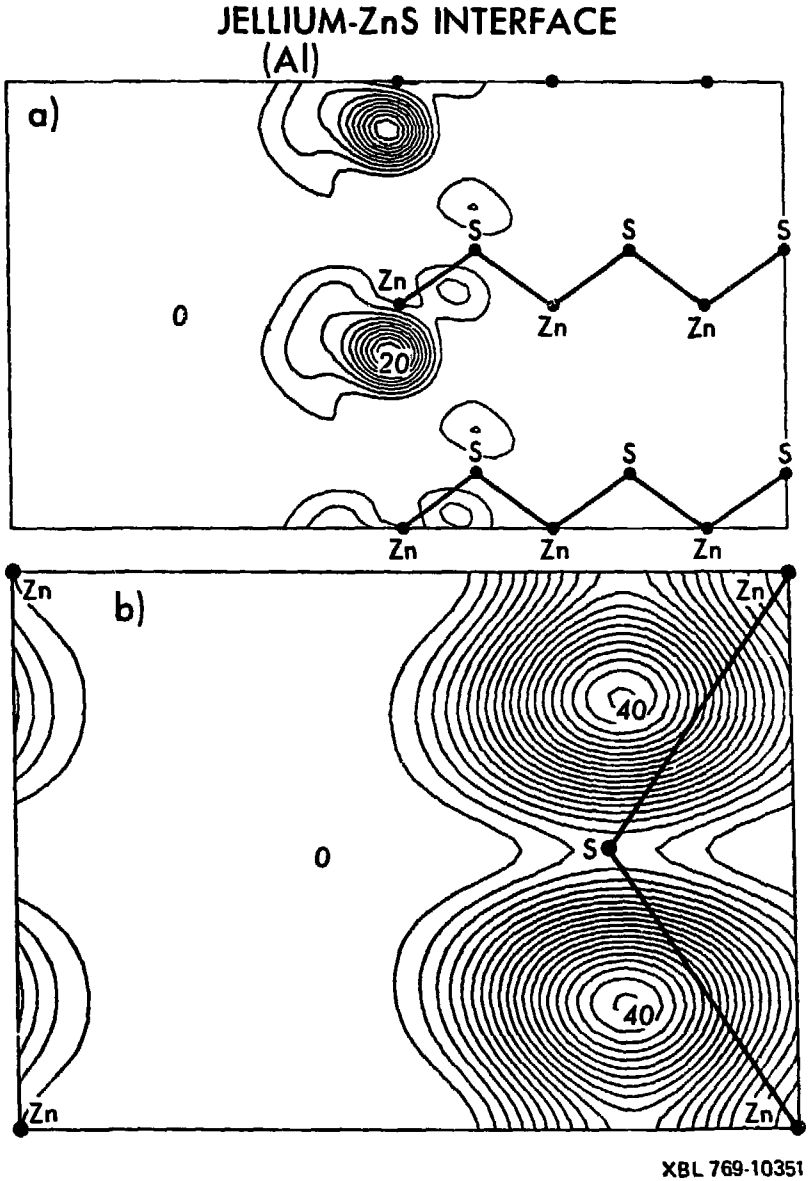

XBL 769-10351

Fig. 67.

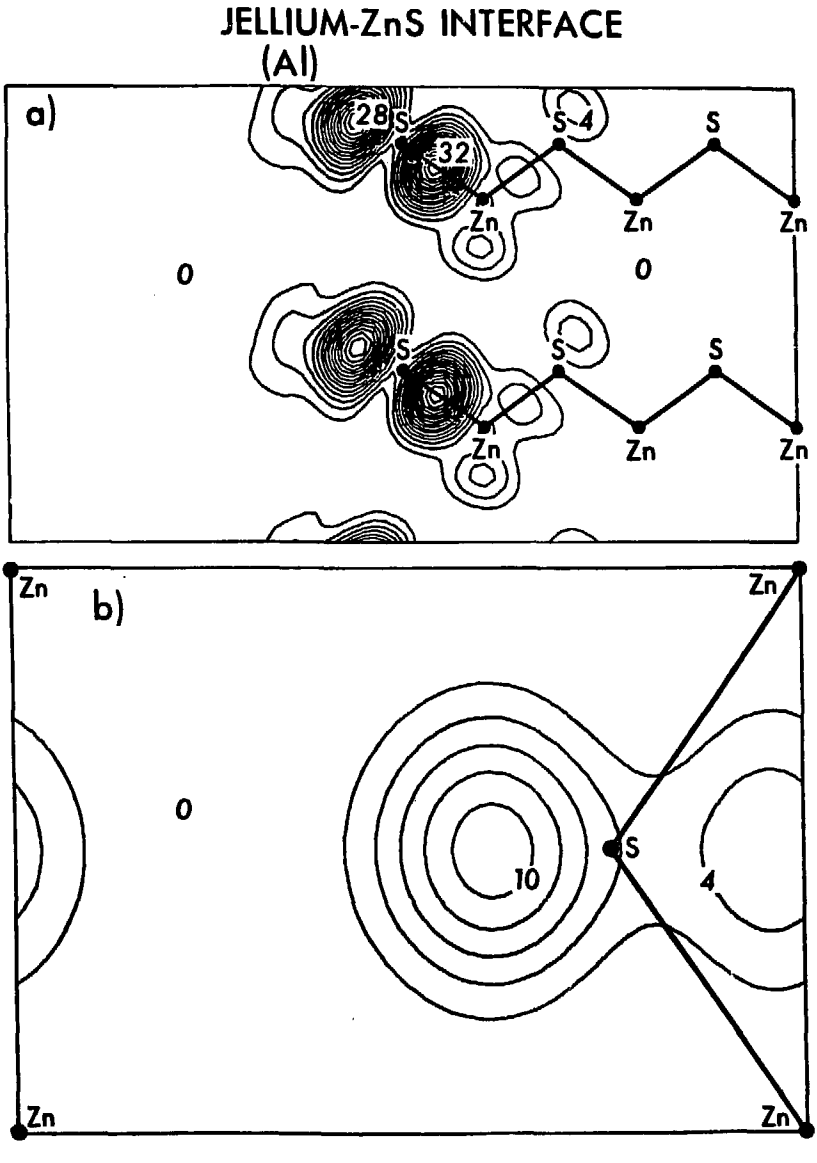
JELLIUM-ZnS INTERFACE
(Al)
a)
28
S
32
S-4
S
Zn
Zn
Zn
0
0
S
S
S
Zn
Zn
Zn
Zn
b)
Zn
Zn
0
S
10
4
Zn
Zn
XBL 769-10364

Fig. 68.

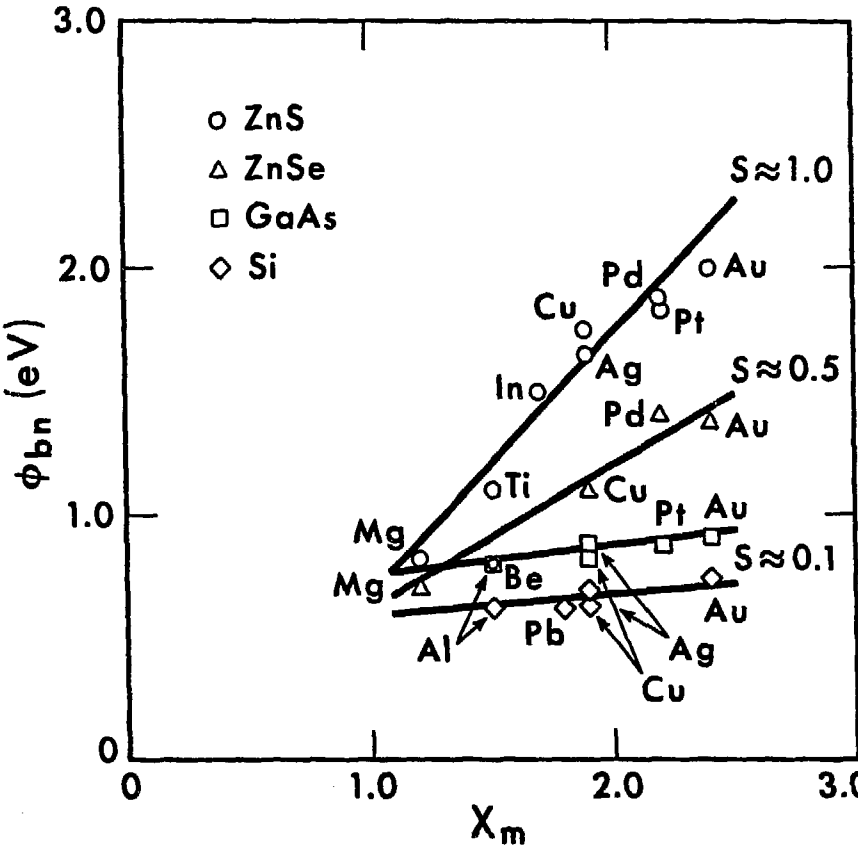

XBL 769-10375

Fig. 69.

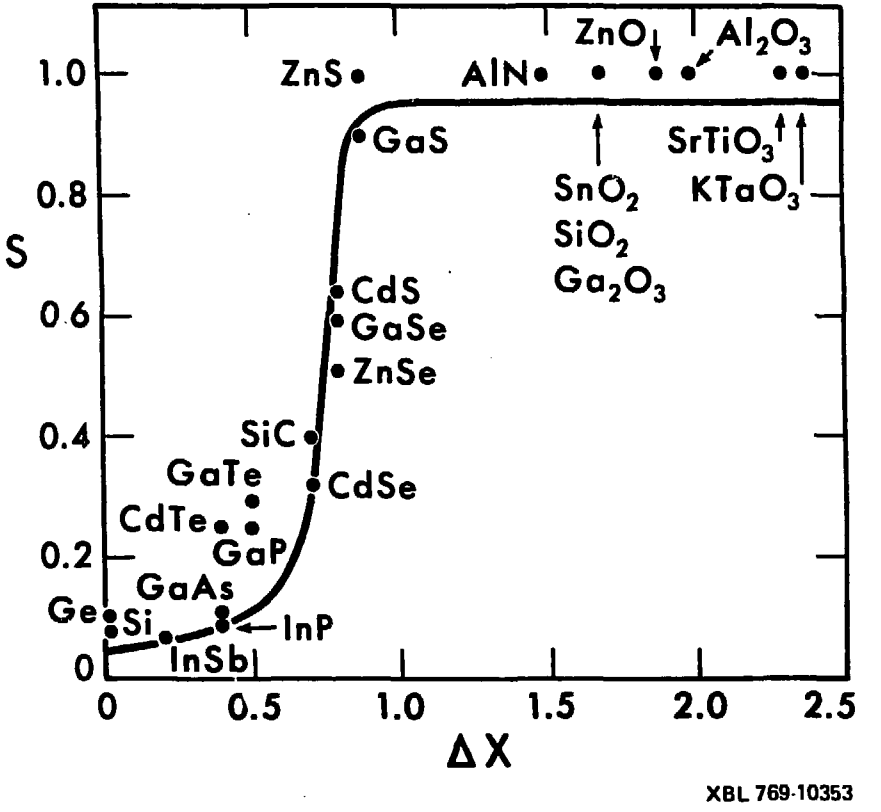
ZnO
Al2O3
1.0
ZnS
AlN
GaS
SrTiO3
SnO2
KTaO3
SiO2
Ga2O3
0.8
S
CdS
0.6
GaSe
ZnSe
0.4
SiC
GaTe
CdSe
CdTe
GaP
0.2
GaAs
Ge
Si
InP
InSb
0
0
0.5
1.0
1.5
2.0
2.5
ΔX
XBL 769-10353

Fig. 70.

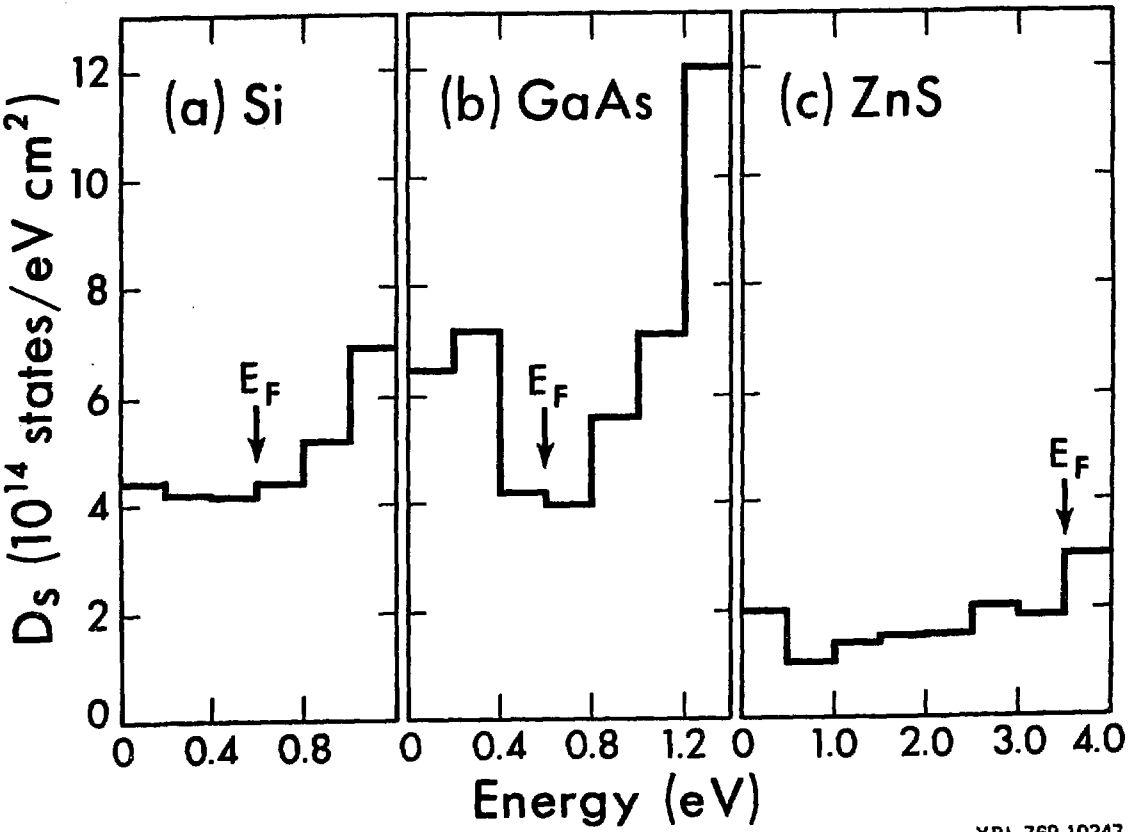

XBL 769-10347

Fig. 71.

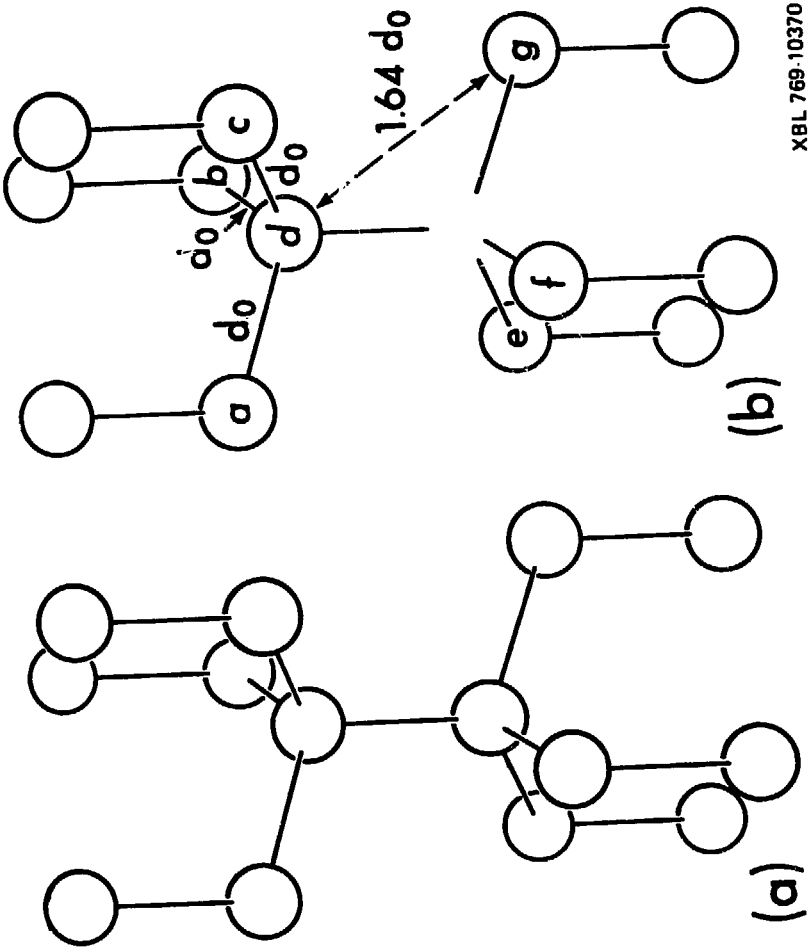

XBL 769-10370

Fig. 72.

XBL 769-10332

Fig. 73.

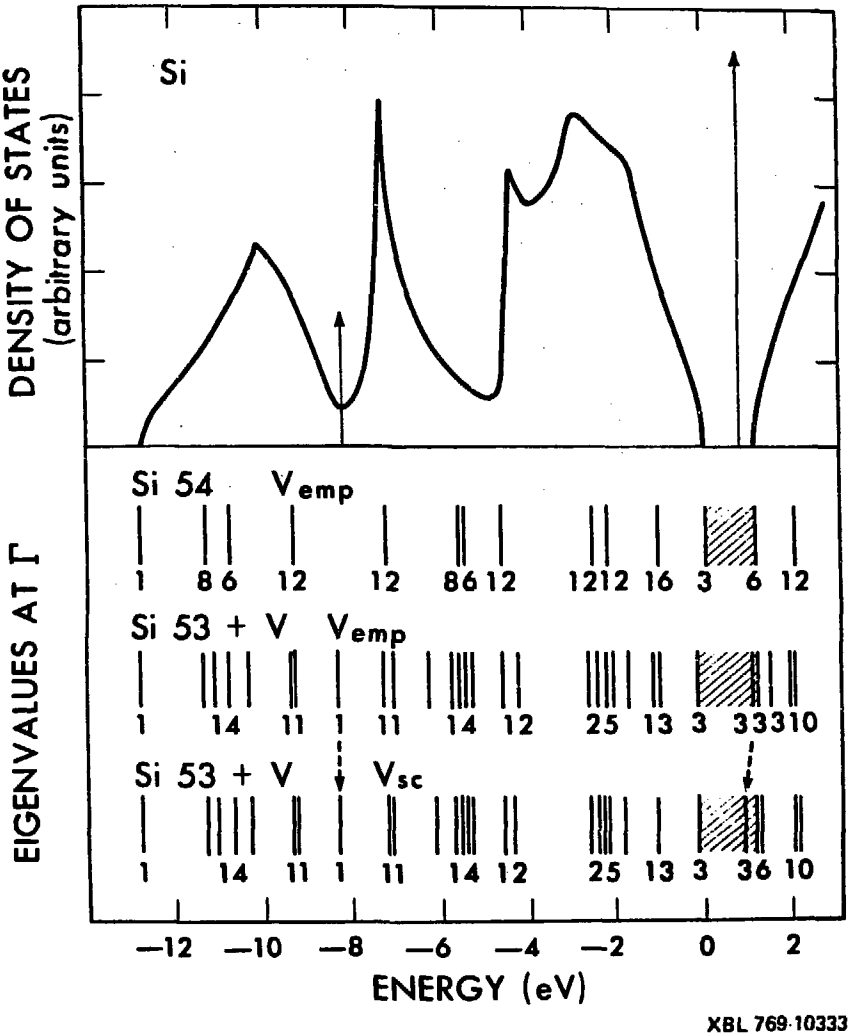
Si
DENSITY OF STATES
(arbitrary units)
EIGENVALUES AT Γ
Si 54 Vemp
1 8 6 12 12 8 6 12 12 12 16 3 6 12
Si 53 + V Vemp
1 14 11 1 11 14 12 25 13 3 33 10
Si 53 + V Vsc
1 14 11 1 11 14 12 25 13 3 36 10
−12 −10 −8 −6 −4 −2 0 2
ENERGY (eV)
XBL 769-10333

Fig. 74.

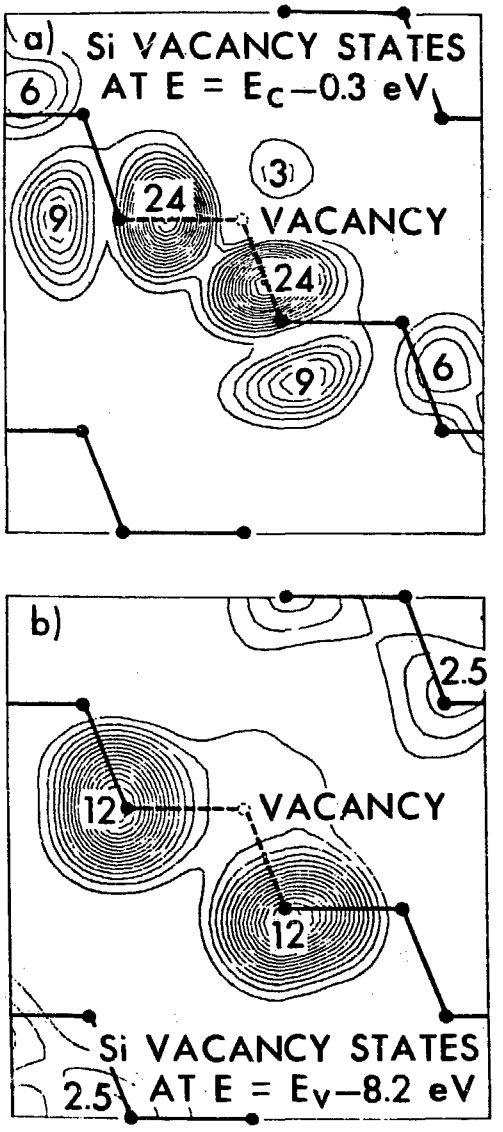

XBL 769-10331

Fig. 75.

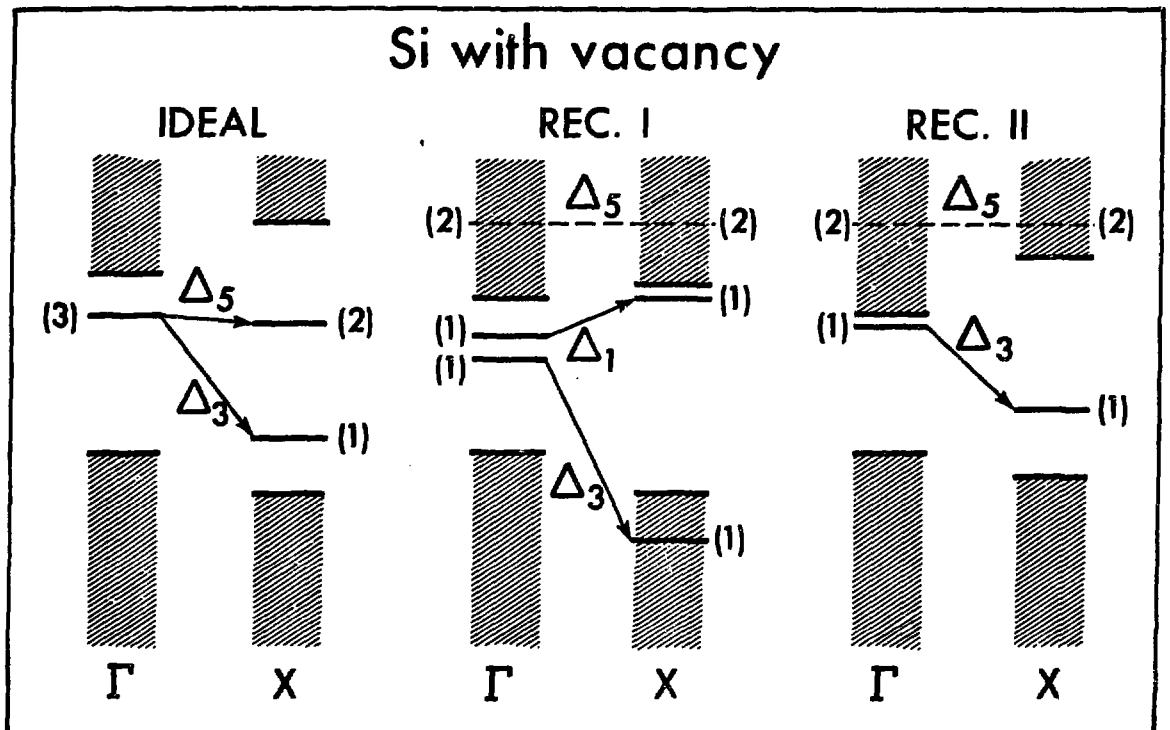

XBL 769-10366

Fig. 76.

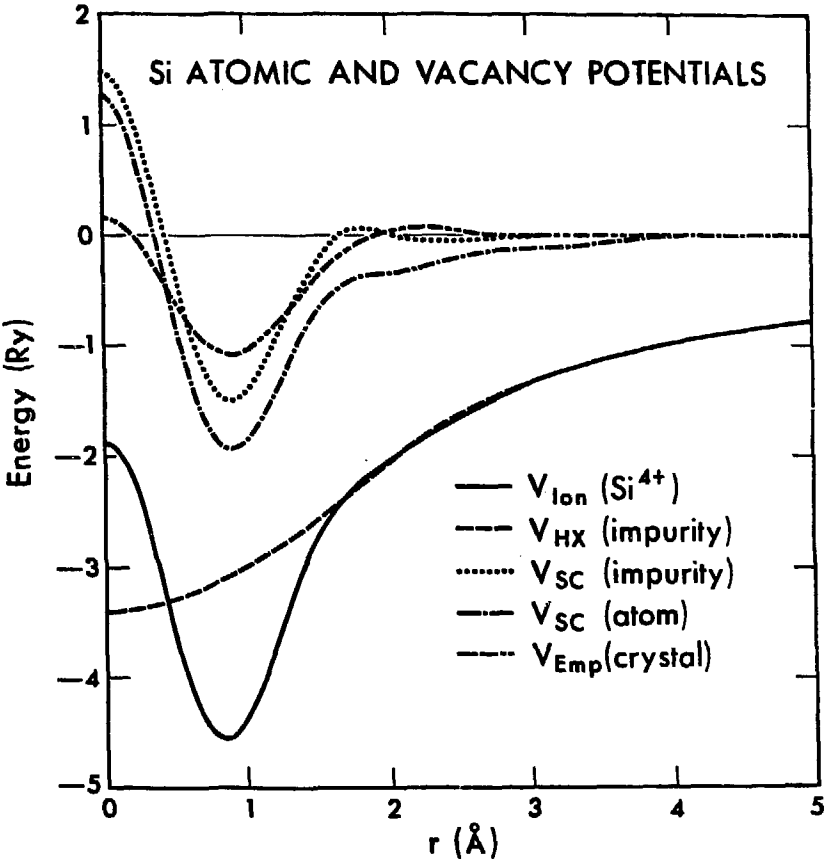
Si ATOMIC AND VACANCY POTENTIALS
Energy (Ry)
r (Å)
V_{Ion} (Si^{4+})
V_{HX} (impurity)
V_{SC} (impurity)
V_{SC} (atom)
V_{Emp}(crystal)
2
1
0
−1
−2
−3
−4
−5
0
1
2
3
4
5
XBL 769-10386

Fig. 77.

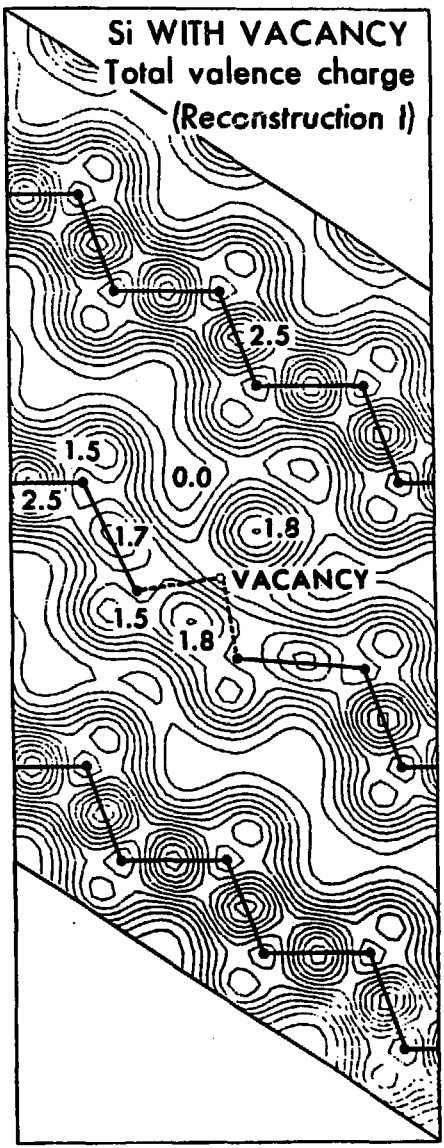

XBL 769-10383

Fig. 78.

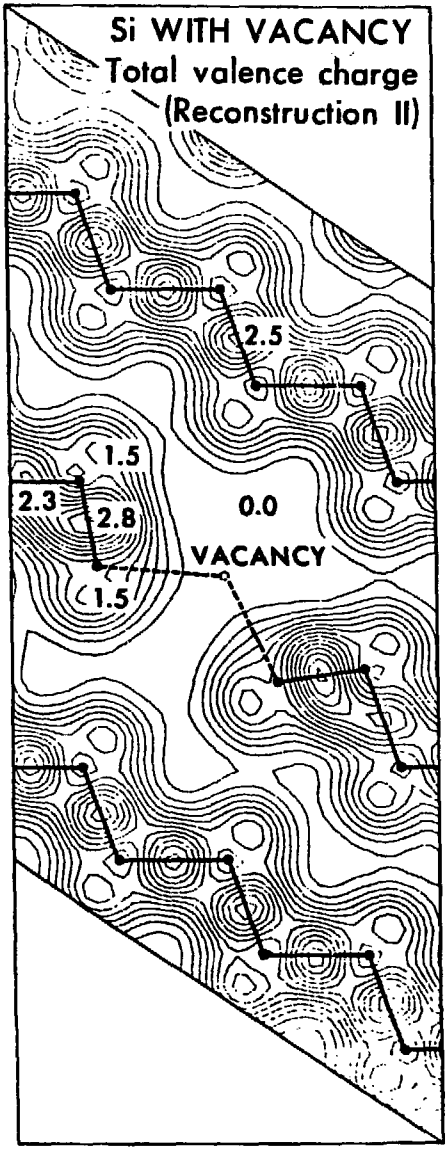

XBL 769-10387

Fig. 79.

Table I. Parameters used in the Cs calculations. Form factors (in Ry), d-well depth (in Ry), d-well radius (in Å), and lattice constants (in Å).

V/V_o	V(3)	V(4)	V(8)	V(11)	A_2	R	a
0.5	-0.0276	-0.0205	0.0011	0.0001	-3.2	1.275	6.175
0.4	-0.0314	-0.0165	0.0010	0.0000	-3.2	1.275	5.732
0.3	-0.0292	-0.0084	-0.0004	0.0000	-3.2	1.275	5.208

Table II. Cs. Calculated Fermi energies (in eV), density of states and partial densities of states at E_F, and the amount of charge distributed to s-, p- and d-states as defined in text. (The density of states is in units of states/eV-atom.)

V/V_o	0.5	0.4	0.3
E_F	1.28	1.10	0.56
$N(E_F)$	1.64	1.90	1.91
$N_s(E_F)$	0.90	0.94	0.89
$N_p(E_F)$	0.18	0.19	0.16
$N_d(E_F)$	0.56	0.77	0.86
Q_s	0.70	0.62	0.41
Q_p	0.09	0.07	0.05
Q_d	0.21	0.31	0.54

Table III. Sum rules from Eq. (26) for $\varepsilon_{\underset{\sim}{G},\underset{\sim}{G}}$ and $\varepsilon_{\underset{\sim}{G},\underset{\sim}{G}'}$ in units of $(eV)^2$ in the limit $\underset{\sim}{q}\to 0$ along the $\hat{x}$-direction.

$(\frac{a}{2\pi})\underset{\sim}{G}$	$(\frac{a}{2\pi})\underset{\sim}{G}'$	$\int\omega\ \mathrm{Im}\ \varepsilon_{\underset{\sim}{G},\underset{\sim}{G}'}d\omega$	$\frac{\pi}{2}\omega_p^2\frac{\rho(\underset{\sim}{G}-\underset{\sim}{G}')}{\rho(0)}\ \hat{e}(\underset{\sim}{q}+\underset{\sim}{G})\cdot\hat{e}(\underset{\sim}{q}+\underset{\sim}{G}')$
(000)	(000)	415.6	433.5
(111)	(111)	431.6	433.5
(200)	(200)	430.1	433.5
(220)	(220)	403.2	433.5
(311)	(311)	311.8	433.5
(222)	(222)	278.4	433.5
(000)	(111)	-50.9	-54.7
(000)	(200)	0.0	0.0
(000)	(220)	11.5	10.3
(000)	(311)	21.6	20.2
(000)	(131)	7.2	6.7
(000)	(222)	15.5	15.0

Table IV. (a) Comparison of the calculated ionic energy levels with experimental data from spectroscopy.[73] (b) Self-consistent Nb atom: A comparison of our results with those of Herman and Skillman.[74]

(a) Nb^{+4}

Level	Calculated Energy (Ry)	Experimental Energy (Ry)
4d	-3.657	-3.63
5s	-2.953	-2.95
5p	-2.448	-2.45
5d	-1.725	-1.71
6s	-1.635	-1.56

(b) Self-consistent Nb atom

	Energies (Ry) Present Calculation	Herman and Skillman
4d	0.354	0.45
5s	0.340	0.40

Postions of Maximum of rR(r) (in a.u.)

	Present calculation	Herman and Skillman
4d	1.48	1.41
5s	3.00	3.12

Table V. Comparison of energy levels between the present calculation of the Nb band structure and previous calculated results. (Energies are in eV with E_F =0.)

	Γ_1	$\Gamma_{25'}$	Γ_{12}	H_{12}	$\Gamma_{25'}$	$N_{1'}$
Predominant Character	s	d	d	d	d	p
Present Calculation	-6.06	0.15	3.07	-3.22	5.83	2.32
APW[66]	-5.30	0.41	2.80	-3.81	5.17	2.33
EPM[67]	-5.20	0.51	2.59	-3.70	5.68	2.18
Self-consisted APW[71]	-5.24	0.55	3.25	-4.24	5.97	2.25

Table VI. Principal peak positions in the calculated Nb density of states are compared with peaks in photoemission data and previous calculations.

Experiment (Photoemission)[72]	Theory		
	APW[66]	EPM[67]	Present Calculation
-2.3	-2.4	-2.6	-2.5
-1.1	-1.4	-1.4	-1.4
-0.4	-0.2	-0.4	-0.4
-	2.5	-	2.6
-	3.0	-	3.2
-	3.7	2.6	3.8

Table VII. Experimental parameters for six elemental superconductors.[84] T_c (Calc.) is calculated using Eq. (55).

Materials	(°K) W_{log}	(°K) $\sqrt{\langle\omega^2\rangle}$	β	λ	μ^*	(°K) T_c(Expt)	(°K) T_c(Calc.)
Pb	56	65	.161	1.55	0.105	7.20	7.15
In	68	89	.309	0.805	0.097	3.40	3.22
Sn	99	121	.222	0.72	0.092	3.75	3.88
Hg	29	49	0.690	1.62	0.098	4.19	4.07
Tl	52	64	0.231	0.795	0.111	2.36	2.20
Ta	132	148	0.121	0.69	0.093	4.48	4.69

Table VIII. Calculated energies of surface states and strong surface resonances of the relaxed Si (111) surface at $\bar{\Gamma}$ (center), K (corner) and M (edge midpoint) of the two-dimensional Brillouin zone. Also indicated are experimental (UPS) results for (2×1) and (7×7) reconstructed surfaces. The energy zero is taken at the bulk valence band edge E_V.

	SCLC[g]		AH[e]	PP[f]	experiment	
	(1×1) relaxed surface				(2×1)	(7×7)
$\bar{\Gamma}$	1.2	Γ_d	0.88	1.04		
	-1.5(2x)	Γ_{tb}	-1.95(2x)	-1.71(2x)	~-1.0[d]	-1.5[a]
	-12.7	Γ_{Lb}	-12.87	-12.9	-11.7[a]	-12.3[a]
K	0.5	K_d		0.11	-0.5[a] -0.45[b] -0.6[c]	0.1[a]
	-2.0	$K_{Lb'}$				
	≈4.2	K_{tb}		-5.65		
	-8.5	K_{Lb}		-8.35		-7.5[a]
	-9.8	$K_{Lb'}$		-9.6		
M	0.5	M_d	0.04	0.17		
	-2.6	$M_{Lb'}$				
	-3.1	M_{tb}	-3.55	-3.78		-3.6[a]
	-8.1 -8.7	M_{Lb}				
	-10.7	$M_{Lb'}$				

a) ref. 93(c); b) ref. 93(a); c) ref. 93(b); d) ref. 93(d); e) ref. 91; f) ref. 98; g) this work.

Table IX. Character tables and transformation of d functions in the 2-dimension square Brillouin zone.

$\bar{\Sigma}$	E	M_d	
$\bar{\Sigma}_1$	1	1	$3z^2-r^2$, xy, 3(x+y)
$\bar{\Sigma}_2$	1	-1	x^2-y^2, z(x-y)

$\bar{\Delta}$	E	M_x	
$\bar{\Delta}_1$	1	1	$3z^2-r^2$, x^2-y^2, zx
$\bar{\Delta}_2$	1	-1	xy, zy

$\bar{Y}$	E	M_y	
$\bar{Y}_1$	1	1	$3z^2-r^2$, x^2-y^2, zy
$\bar{Y}_2$	1	-1	xy, zx

Table X. Parameters entering Eqs. (71) and (81) to define the empirical and ionic Si pseudopotentials.

	V^{Si}_{emp}		V^{Si}_{ion}
a_1	0.17459	b_1	-0.57315
a_2	2.22144	b_2	0.79065
a_3	0.86334	b_3	-0.35201
a_4	1.53457	b_4	-0.01807

Table XI. The ionic core potential parameters, b_i. The potentials are normalized to an atomic volume of 152.3 (a.u.)^3. The form of the potential is given by Eq. (81). The units for v(q) are Ry if q is given in a.u. (The Ga potential is valid only for $q \leq 3$ a.u.)

	Ga	As	Zn	Se	S
b_1	-0.3384	-0.7057	-0.3056	-2.3258	-5.4101
b_2	1.3305	1.0448	1.3412	0.5283	0.3275
b_3	0.4466	0.1662	0.0802	-0.5740	-0.8169
b_4	0.0071	-0.0151	-0.0086	-0.0321	-0.0250

Table XII. The empirical starting potential parameters, a_i. Normalization and units are as in Table XI. The form of the potential is given by Eq. (71).

	Ga	As	Zn	Se	S
a_1	1.2214	0.3474	6.7008	0.2334	0.2361
a_2	2.4495	2.6203	1.4983	3.3858	3.3630
a_3	0.5445	0.9335	0.6696	0.7266	0.7243
a_4	-2.7148	1.5677	-4.7128	2.2012	2.1900

Table XIII. Theoretical and experimental values for the Schottky barrier height ϕ_b(eV) and the index of interface behavior S. D_s in units of 10^{14} states/eV-cm^2 is the surface density of states used to obtain the calculated S.

	ΔX[a]	ϕ_b(cal)	ϕ_{bn}(expt)	D_s	S(cal)	S(expt)[d]
Al-Si	0	0.6 ± 0.1	0.6[b]	4.5	0.1	0.1
Al-GaAs	0.4	0.8 ± 0.2	0.8[c]	5.0	0.1	0.1
Al-ZnSe	0.8	0.2 ± 0.2	-	2.0	0.4	0.5
Al-ZnS	0.9	0.5 ± 0.2	0.8[c]	1.4	0.7	1.0

a) Ref. 156
b) Ref. 142
c) Ref. 149
d) Ref. 137

Table XIV. Form factor parameters for the empirical Si pseudopotential V_{emp} (Eq. 92) and for the ionic Si^{4+} pseudopotential V_{ion} (Eq. 97).

V_{emp}	V_{ion}
$a_1 = 0.34270$	$b_1 = -1.12507$
$a_2 = 2.22144$	$b_2 = 0.79065$
$a_3 = 0.86334$	$b_3 = -0.35201$
$a_4 = 1.53457$	$b_4 = -0.01807$

ACKNOWLEDGEMENTS

I am deeply grateful to my thesis advisor Professor Marvin L. Cohen for his guidance and encouragement throughout all aspects of this work. His advice , interest and thoughtfulness have been most helpful and are truly appreciated.

I am also grateful to Professor A. H. Rosenfeld for his help and encouragement during the early stages of my study in physics.

I would like to thank Professors Leo Falicov, Charles Kittel, Phil Allen, D. Haneman, Y. R. Shen, Ching Fong and Dr. Dean Eastman for many stimulating discussions and helpful advice on various aspects of physics.

I am please to thank Dr. James R. Chelikowsky, Dr. Michael Schluter, and Kai-Ming Ho for their collaborations on several of the sections on non-periodic systems. I further thank my close friend Jim Chelikowsky for his collaboration on the local fields section and for numerous other fruitful interactions.

I would like to acknowledge many interesting and helpful interactions with the other members of the Solid State Theory Group. In particular, I thank Dr. F. Yndurain, Dr. D. Bullett, Dr. P. Schlottmann, Dr. M. Kelly, Dr. J. Joanopoulos, Dr. D. Chadi, Dr. N. Garcia, Dr. W. Hsu, Dr. V. T. Rajan, Dr. B. Koiller, Mr. D. Denley and Mr. R. Kittler for many stimulating discussions.

I would also like to thank Mrs. Carol Tung and Mrs. Deborah Turner for being such friendly and efficient secretaries and Ms. Alice Ramirez for her excellent typing of the manuscript.

I would also like to acknowledge financial support by a University of California fellowship for my first year and a National Science Foundation fellowship for my subsequent three years of study and research at Berkeley. Part of this work was supported by the U.S. Energy Research and Development Administration.

Finally, and most importantly, I would like to thank my parents for their support and encouragement through all these years and my wife, Jane, for her everlasting love, patience and care during my graduate years.